Chemical Vapour Deposition Growth of Large-Area Graphene on Metals



Adrian T. Murdock

St Edmund Hall

University of Oxford

A thesis submitted in partial fulfilment

of the requirements for the degree of

Doctor of Philosophy in Materials

Department of Materials

Hilary Term 2014

Acknowledgements

The past four and a half years have been an intellectually stimulating, challenging and highly rewarding journey. Many people and organisations made this possible and deserve thanks for supporting me as I completed this thesis.

Firstly, I acknowledge the financial support of the Commonwealth Scholarships Commission for a Commonwealth Postgraduate Research Scholarship, and the University of Oxford Clarendon Fund for a Clarendon Research Grant, which made studying at Oxford possible. Further assistance from the Department of Materials and St Edmund Hall was also gratefully received.

Thank you to my academic supervisor Professor Nicole Grobert for your mentoring and guidance. In particular, thank you for supporting my participation in countless conferences and personal development opportunities, and for allowing me great freedom in directing this research project. I look forward to continuing to work with you in the future.

Thank you to Dr Antal Koos for your supervision during the early stage of my research, ongoing guidance and beneficial scientific debate.

I acknowledge and am thankful for direct collaboration with many outstanding researchers during this project including Ms Jude Britton, Mr Vitaliy Babenko, Dr Shayan Meysami, Dr Rebecca Nicholls, Dr T. Ben Britton, Dr Angus Wilkinson, Dr Hugh Bishop, Dr Alison Crossley, Dr Christina Lekka, Dr Tim Batten, Dr Lothar Houben, Dr Peter Nemes-Inzce, Dr Timothy Pennycook, Dr Andrew Pollard, and all their respective coworkers.

I also recognise and am sincerely grateful for the assistance by Mrs Gabriella Chapman, Mr Greg Cook, Dr Zabeada Aslam, Dr Neil Young, Dr Gareth Hughes, Dr Colin Johnston, Mr Chris Salter, Dr Hugh Bishop and Dr T. Ben Britton in providing training in various characterisation techniques within the Department of Materials.

My sincerest thanks also to Professor Nicole Grobert, Dr Antal Koos, Dr Rebecca Nicholls and Dr Frank Dillon for reviewing my thesis.

Special mention must be given to Dr Frank Dillon, Dr Zabeada Aslam, Dr Laura Miranda Perez, Professor Peter Nellist, Professor Martin Castell, Professor Robert Whittaker, George Theodossiou and Christian Beck, who offered invaluable discussions, advice and guidance- both scientific and personal- at one time or another during this research project.

To the past and present members of Professor Nicole Grobert's Nanomaterials by Design, thank you for your friendship, many enjoyable scientific discussions and assistance over the years.

To my many new lifelong friends from St Edmund Hall and Oxford, thank you for making my time in Oxford so memorable.

My gratitude goes out to all my past science teachers and lecturers who inspired me to follow this path. Particularly Mr Kim Whisson, who first sparked my interests in chemistry and physics, and Professor Mark Ogden, who convinced me to study nanoscience, and continues to be a great mentor.

To my Mum and Dad, thank you for always being there for me. I wouldn't be where I am today without your unwavering support, advice and encouragement for each and every endeavour that I undertake. I am eternally grateful.

Finally, to my fiancée Bonnie, thank you for coming on this journey with me. This was only possible with the help of your never-ending love, encouragement, support, and understanding, through the easy times and the hard. I'm so excited for our future together, and hope we can achieve all the dreams that you have selflessly postponed for me. My love, I am forever in your debt.

Dedication

For my Mum, my Dad, and my Bonnie

and

In memory of Professor David Cockayne

Who sowed the seed of inspiration by suggesting, "Why don't you apply to Oxford?"

Abstract

Chemical Vapour Deposition Growth of Large-Area Graphene on Metals

A thesis submitted in partial fulfilment of the requirements for the degree of Doctor of Philosophy in Materials at the University of Oxford

Adrian T. Murdock

St Edmund Hall

Hilary Term 2014

Graphene has unrivalled properties and is heralded as a revolutionary material for the 21st century. Chemical vapour deposition (CVD) on metals is a promising method to produce large-area graphene. Controlling the properties of CVD graphene is vital for its integration in a wide-range of future applications. Many factors can influence the CVD growth of graphene and its properties, therefore further investigations will be beneficial to fully understand and control this technique. In this thesis I expand the knowledge about the growth of pure and heteroatom-doped graphene by low-pressure chemical vapour deposition (LPCVD) and atmospheric-pressure chemical vapour deposition (APCVD) on commercially available Cu and Pt foils. Using a range of characterisation techniques, I investigate the influence of the substrate's properties and the synthesis conditions on the growth of graphene, in pursuit of improved, controlled or optimised production, which can promote high-quality, large-area, single-layer graphene, or other as desired. By characterising the topography, surface roughness, crystallographic orientations, and chemical composition of six Cu foils, I find that their properties vary greatly and this influences the growth of CVD graphene. I elucidate that the commonly used 99.8 % Alfa Aesar Cu foil has a surface coating composed of calcium, chromium, and phosphorus,

which detrimentally influences graphene growth. Cleaning Cu foils with CH_3COOH is shown to reduce the concentration of surface contaminants, consequently reducing the nucleation density and increasing the growth rate of CVD graphene. I also demonstrate that the shape, orientation, edge-geometry and thickness of CVD graphene domains can be controlled by the Cu crystallographic orientations. Single-layer LPCVD graphene domains align with zigzag edges parallel to a single <101> direction on Cu{111} and Cu{101}, while bilayer domains align to two directions on Cu{001}. Hexagonal APCVD domains also preferentially align with edges parallel to the <101> direction(s). This discovery resolves a key challenge of controlling the orientation of individual graphene domains and opens a new avenue for tailored production of large-area CVD graphene with improved properties. By controlling the synthesis conditions of APCVD graphene on Pt foils I optimise production of ~0.5 mm single-layer graphene domains with reduced nucleation density and increased growth rate of ~100 μm/min by synthesis at 1150 ˚C, a higher temperature than previously reported. The absence of large, hexagonal, single-crystal domains on pristine Pt foil, and observation of a reaction between quartz and Pt that promotes hexagonal domains, suggests that a silicon or platinum silicide surface layer may be advantageous for improved growth of graphene. Finally, I demonstrate that the dopant concentration of nitrogen-doped graphene is increased at lower synthesis temperatures and higher NH_3 concentration, up to 1.3 %, but with an associated decrease in the growth rate. Direct visualisation, elemental confirmation, and electronic characterisation of individual nitrogen atoms is shown for the first time using aberration-corrected scanning transmission electron microscopy and electron energy loss spectroscopy. Boron-doped graphene is also synthesised. The implications of these findings, and many additional minor contributions, are wide-ranging and of considerable importance for the future understanding of CVD growth of graphene on metals, and more generally for the advancement of scientific knowledge for manufacturing large-area graphene. Collectively, these discoveries represent a significant body of work that can improve the efficiency of production and assist with controlling the properties of large-area CVD graphene.

Contents

Acknowledgements ii

Dedication iv

Abstract v

List of Tables xxiv

List of Acronyms xxv

List of Publications and Patents xxvii

1 Introduction 1

2 Literature Review 3

2.1 Defining graphene 3

2.1.1 Relation to other carbon nanomaterials and stacking 4

2.1.2 Heteroatomic doping of graphene 6

2.2 Properties of graphene 7

2.2.1 Electrical properties 7

2.2.2 Optical properties 8

2.2.3 Mechanical properties 8

2.2.4 Thermal properties 8

2.2.5 Properties of heteroatom-doped graphene 9

2.3 Potential applications of pure and heteroatom-doped graphene 10

2.4 Production of graphene 12

2.4.1 Overview of production methods 12

2.4.1.1 Micromechanical exfoliation of graphite 12

2.4.1.2 Chemical treatment of graphite 13

2.4.1.3 Epitaxial growth on SiC 13

2.4.1.4 Synthesis on metal surfaces 14

2.4.2 Influence of the production method on the type, morphology, size, and properties of graphene 15

2.4.3 Chemical vapour deposition of graphene on metals 16

2.4.3.1 Chemical vapour deposition of graphene on nickel and other metals 18

2.4.3.2 Chemical vapour deposition of graphene on copper 18

2.4.3.3 Chemical vapour deposition of graphene on platinum 20

2.4.3.4 Chemical vapour deposition of nitrogen-doped and boron-doped graphene 21

2.4.3.1 Transfer of chemical vapour deposition graphene from metals 23
2.4.4 Influence of the synthesis parameters on chemical vapour deposition growth of graphene 24
2.4.5 Influence of the Cu substrate on chemical vapour deposition growth of graphene 26
2.4.6 Influence of Cu crystallographic orientations on chemical vapour deposition growth of graphene 27
2.5 Summary and scope 29
3 Aims of research project 31
4 Experimental techniques for the characterisation of chemical vapour deposition graphene and metal substrates 33
4.1 Systematic characterisation of graphene and metal substrates 33
4.2 Optical microscopy 34
4.3 Optical profilometry 36
4.4 Raman spectroscopy 36
4.4.1 Confocal Raman microscopy 36
4.4.2 Two-dimensional Raman mapping 39
4.5 Scanning probe microscopy 40
4.5.1 Atomic force microscopy 41
4.5.2 Scanning tunnelling microscopy 42
4.6 Scanning electron microscopy 42
4.6.1 Electron backscatter diffraction 44
4.6.2 Energy-dispersive X-ray spectroscopy 45
4.7 Transmission electron microscopy 46
4.7.1 Selected area electron diffraction 47
4.7.2 Dark field TEM 48
4.7.3 High-resolution transmission electron microscopy 48
4.7.4 TEM instrumental details and operating conditions 49
4.8 Scanning transmission electron microscopy 50
4.9 Electron energy loss spectroscopy 52
4.10 X-ray photoelectron spectroscopy 53
4.11 Secondary ion mass spectrometry 54
4.12 Electrical characterisation 54

5 Low-pressure chemical vapour deposition of graphene on copper foils 56

5.1 Design, construction and safety testing of LPCVD apparatus 57

5.1.1 First prototype LPCVD apparatus 58

5.1.2 Second prototype LPCVD apparatus and investigations into contaminants within system 59

5.1.3 Third prototype LPCVD apparatus and investigations into contaminants within system 63

5.1.4 Fourth prototype LPCVD apparatus and investigations into contaminants within system 66

5.2 Investigations into the influence of synthesis parameters on LPCVD graphene growth on as-received 99.8% Alfa Aesar Cu foil 69

5.2.1 Influence of synthesis time and CH_4:H_2 flow rate ratio 72

5.3 Investigations into the influence of synthesis parameters on LPCVD graphene growth on as-received 99.999 % Alfa Aesar Cu foil 80

5.3.1 Influence of synthesis time and CH_4:H_2 flow rate ratio 80

5.4 Investigations into the influence of the side of the Cu foil 82

5.5 Investigations into the influence of the position within furnace 85

5.6 Conclusions on low-pressure chemical vapour deposition of graphene on copper foils 89

6 Atmospheric-pressure chemical vapour deposition of graphene on copper foils. 90

6.1 Benefits of APCVD 90

6.2 Construction of APCVD apparatus 91

6.3 Investigations into the influence of synthesis parameters on APCVD graphene growth on 99.8% Alfa Aesar Cu foil 91

6.4 Investigations into the influence of synthesis parameters on APCVD graphene growth on 99.9% Goodfellow Cu foil 93

6.4.1 Influence of synthesis time 93

6.4.2 Influence of CH_4:H_2 flow rate ratio 95

6.5 Pulsed APCVD graphene growth 97

6.6 Conclusions on atmospheric-pressure chemical vapour deposition of graphene on copper foils 100

7 Influence of the crystallographic orientations of copper foil on the growth and properties of chemical vapour deposition graphene domains 101

7.1 Variation of the growth of graphene on Cu crystallographic orientations..... 102

7.2 Influence of Cu crystallographic orientations on LPCVD graphene domains..... 102

7.2.1 Influence on the shape and orientation 102

7.2.2 Influence on the domain size and growth rate 109

7.2.3 Influence on the thickness 110

7.2.4 Edge geometry of aligned LPCVD graphene domains 112

7.2.5 Substrate-induced strain in LPCVD graphene domains 114

7.3 Influence of Cu crystallographic orientations on the orientation of APCVD graphene domains 117

7.3.1 Influence of crystallographic orientations of 99.999 % Alfa Aesar Cu foil 117

7.3.2 Influence of crystallographic orientations of 99.8 % Alfa Aesar Cu foil 120

7.3.3 Influence of crystallographic orientation of 99.9 % Goodfellow Cu foil 122

7.4 Variation of Cu crystallographic orientations with Cu foils 124

7.5 Computational modelling of graphene on primary Cu crystallographic orientations 125

7.6 Conclusions on the influence of Cu crystallographic orientation on the growth and properties of graphene domains 128

8 Influence of the properties of copper foils on the growth of chemical vapour deposition graphene 130

8.1 Influence of the properties of copper foils on the growth of APCVD graphene .. 130

8.1.1 Variations of copper foils due to purity and supplier 132

8.1.1.1 Surface topography and roughness of annealed copper foils via SEM and optical profilometry 133

8.1.1.2 Chemical composition and concentration of surface contaminations and dissolved impurities of as-received and annealed copper foils via XPS and SIMS 138

8.1.1.3 Crystallographic orientations and grain sizes of annealed copper foils via EBSD .. 148

8.1.1.4 Conclusions on variations of copper foils due to purity and supplier 150

8.1.2 APCVD graphene growth on annealed Alfa Aesar copper foils with varying purity 152

8.1.3 APCVD graphene growth on annealed copper foils with similar purities from different suppliers 155

8.1.4 Conclusions on influence of properties and quality of coppers foils on APCVD graphene growth 157
8.2 Influence of chemical treatment of copper foil on synthesis of graphene 158
8.2.1 Variation to copper foils by CH_3COOH cleaning 159
8.2.1.1 Surface topography of CH_3COOH cleaned and annealed copper foils via SEM and optical profilometry 159
8.2.1.2 Chemical composition and concentration of surface impurities on CH_3COOH cleaned and annealed copper foils via XPS and SIMS 163
8.2.1.3 Conclusions on influence of CH_3COOH cleaning of copper foils 169
8.2.2 Variation of CVD graphene growth by CH_3COOH cleaning of copper foils 170
8.2.2.1 Variation to APCVD graphene growth by CH_3COOH cleaning of copper foils 170
8.2.2.2 Variation to LPCVD graphene growth by CH_3COOH cleaning of copper foils 173
8.2.2.3 Conclusions on influence of CH_3COOH cleaning of copper foils on APCVD and LPCVD graphene growth 175
8.2.3 Alternative cleaning treatments 175
8.2.3.1 Variation to APCVD graphene growth by $FeNO_3$ cleaning of copper foil 176
8.2.3.2 Variation to LPCVD graphene growth by $FeNO_3$ cleaning of copper foil 177
8.2.3.3 Variation to LPCVD graphene growth by electrochemical polishing of copper foils in $K_2S_2O_8$ 178
8.2.3.4 Conclusions on alternative cleaning treatments 180
9 Atmospheric-pressure chemical vapour deposition of graphene on platinum foils 181
9.1 Investigations into the influence of synthesis parameters on APCVD graphene growth on 99.99+ % Goodfellow Pt foil 182
9.1.1 Influence of CH_4:H_2 flow rate ratio 184
9.1.2 Influence of synthesis temperature 193
9.2 Investigations into nucleation sites of APCVD graphene domains on Pt foil 196
9.2.1 Influence of surface topography on location of nucleation sites 196
9.2.2 Influence of contamination particles on location of nucleation sites 199
9.3 Conclusions on atmospheric-pressure chemical vapour deposition of graphene on platinum foils 203
10 Chemical vapour deposition of heteroatom-doped graphene on copper foils 204
10.1 CVD of nitrogen-doped graphene on copper foils 205

10.1.1 Design and construction of low-pressure CVD apparatus for doping of graphene using gaseous precursors 205
10.1.2 Investigations into the influence of synthesis parameters on LPCVD nitrogen-doped graphene growth on 99.999 % Alfa Aesar Cu foil 205
10.1.2.1 Influence of NH_3 flow rate and synthesis temperature on dopant concentration 207
10.1.2.2 Influence of NH_3 flow rate and synthesis temperature on growth rate and surface coverage 211
10.1.3 Investigations into the bonding of dopants in nitrogen-doped graphene 215
10.1.4 Investigations into the electronic structure of nitrogen-doped graphene 220
10.2 CVD of boron-doped graphene on copper foils 224
10.2.1 Design and construction of low-pressure CVD apparatus for heteroatom doping of graphene using liquid precursors 224
10.2.2 Initial experiments into synthesis of boron-doped graphene 225
10.3 Conclusions on heteroatom-doped graphene 228
11 Conclusions 229
11.1 Conclusions on the contributions and impact of research project 229
11.2 Outlook and future work 240
11.2.1 Influence of Cu crystallographic orientations on geometry of domain boundaries, and the electrical and mechanical properties of graphene 240
11.2.2 Controlling the Cu substrate's properties aiming for CVD growth on an optimised Cu substrate 241
11.2.3 Confirming the nature and influence of metal contamination particles 241
11.2.4 Influence of surface features and contamination particles on growth and nucleation of graphene on Pt foils 242
11.2.5 APCVD growth on silicidated platinum and eutectic substrates 242
11.2.6 Influence of synthesis conditions on the nitrogen-containing active species, the dopant bonding configuration, and electronic properties of nitrogen-doped graphene 243
11.2.7 Boron-doped graphene and LPCVD growth using liquid precursors 244
List of References 245
Appendix 246
EBSD data from analysis of influence of Cu crystallographic orientation on graphene 246

Representative Raman spectra from analysis of influence of Cu crystallographic orientation on LPCVD graphene 247
XPS analysis of Cu foils 248
SIMS data from analysis of Cu foils 261
Large area EBSD map of annealed 99.9999 % Alfa Aesar Cu foil 265
STEM and EELS data of nitrogen-doped graphene 265

List of Figures

Figure 1: Diagram of graphene 4

Figure 2: Graphene and related carbon nanomaterials. 4

Figure 3: Stacking configurations of graphene 5

Figure 4: Configurations of nitrogen dopants within graphene lattice 6

Figure 5: 3D band structure of graphene 7

Figure 6: Optical properties of graphene 8

Figure 7: Influence of heteroatomic doping on band structure of graphene 9

Figure 8: Graphene produced by micromechanical exfoliation 12

Figure 9: Graphene produced by chemical treatment of graphite 13

Figure 10: Graphene produced by epitaxial growth on SiC 14

Figure 11: Methods of synthesis of graphene on metals 15

Figure 12: Commercially available CVD apparatus 17

Figure 13: LPCVD growth of large-area graphene on Cu foils 19

Figure 14: APCVD growth of large-area graphene on Pt foils 21

Figure 15: Polymer transfer of CVD graphene 23

Figure 16: Variation of synthesis parameters during CVD growth 24

Figure 17: Influence of synthesis conditions on LPCVD growth of isolated graphene domains 25

Figure 18: APCVD growth of large-area graphene on Cu foils 26

Figure 19: Optical microscopy image of micromechanically exfoliated graphene on 300 nm SiO_2. 34

Figure 20: Raman spectrum of graphene and graphite 37

Figure 21: Variation of Raman 2D peak with thickness 38

Figure 22: Two-dimensional Raman mapping of LPCVD graphene 40

Figure 23: Atomic force microscopy image of graphene 41

Figure 24: Scanning electron microscopy of graphene 43

Figure 25: Electron backscatter diffraction from Cu foils 44

Figure 26: Bright-field TEM imaging of graphene 46

Figure 27: Selected area electron diffraction of graphene 47

Figure 28: DFTEM imaging of graphene 48

Figure 29: High-resolution TEM imaging of graphene 49

Figure 30: STEM imaging of graphene 51

Figure 31: ADF-STEM imaging of low Z atoms 51

Figure 32: First prototype of LPCVD apparatus 58

Figure 33: Second prototype of LPCVD apparatus 59

Figure 34: As-received 99.8% Alfa Aesar Cu foil 60

Figure 35: 99.8% Alfa Aesar Cu foil annealed in second prototype LPCVD system with 2 sccm H_2 for 60 minutes 60

Figure 36: Raman spectrum of 99.8% Alfar Aesar Cu foil annealed in second prototype LPCVD system with 2 sccm H_2 for 60 minutes 61

Figure 37: 99.8% Alfa Aesar Cu foil annealed in second prototype LPCVD system with no gas flow 62

Figure 38: Raman spectrum of 99.8% Alfa Aesar Cu foil annealed in second prototype LPCVD system 63

Figure 39: Third prototype of LPCVD apparatus 63

Figure 40: 99.8% Alfa Aesar Cu foil annealed in third prototype LPCVD system isolated from the gas manifold with no gas flow for 60 minutes. 64

Figure 41: 99.8% Alfa Aesar Cu foil annealed in third prototype LPCVD system with gas flow 64

Figure 42: Raman spectra from 99.8 % Alfa Aesar Cu annealed in third prototype LPCVD system 65

Figure 43: Fourth prototype of LPCVD apparatus 66

Figure 44: Annealing of 99.8 % Alfa Aesar Cu in fourth prototype LPCVD system with 100 sccm H_2 67

Figure 45: Annealing of 99.8 % Alfa Aesar Cu in fourth prototype LPCVD system with 100 sccm H_2 67

Figure 46: Annealing of 99.8 % Alfa Aesar Cu in fourth prototype LPCVD system with 500 sccm H_2 68

Figure 47: Variety of SEM images of LPCVD graphene on 99.8 % Alfa Aesar Cu foil .. 70

Figure 48: LPCVD graphene growth on as-received 99.8 % Cu foil with a deficit of H_2 73

Figure 49: Isolated LPCVD graphene domains formed on as-received 99.8 % Alfa Aesar Cu foil..... 75

Figure 50: LPCVD graphene domains on as-received 99.8 % Alfar Aesar Cu foil with CH_4:H_2 flow rate ratio of 1:100 for various synthesis times 76

Figure 51: LPCVD graphene domains on as-received 99.8 % Alfar Aesar Cu foil with CH_4:H_2 flow rate ratio of 1:500 for various synthesis time..... 77

Figure 52: Surface contaminant particles observed following growth procedure 78

Figure 53: Hexagon-like LPCVD graphene domains on as-received 99.8 % Alfar Aesar Cu foil with a high concentration of surface contaminations..... 80

Figure 54: LPCVD growth of graphene domains on as-received 99.999 % Alfa Aesar Cu foil with CH_4:H_2 flow rate ratio of 1:100..... 81

Figure 55: LPCVD growth of graphene domains on as-received 99.999 % Alfa Aesar Cu foil with CH_4:H_2 flow rate ratio of 1:500..... 82

Figure 56: Variation of LPCVD growth of graphene domains on different sides of Cu foil..... 83

Figure 57: Diagram of restricted space below Cu foil..... 84

Figure 58: Diagram of LPCVD experiment with Cu foil spanning length of furnace ... 86

Figure 59: Temperature profile of LPCVD furnace at 1035 ˚C set point 86

Figure 60: Variation of LPCVD graphene growth on Cu foil with position within furnace..... 87

Figure 61: Variation of average size of LPCVD graphene domains with position within furnace..... 87

Figure 62: APCVD apparatus with conical joints and acetone bubbler 91

Figure 63: APCVD graphene domains on CH_3COOH cleaned 99.8 % Alfa Aesar Cu foil 92

Figure 64: APCVD graphene domains on CH_3COOH cleaned 99.9 % Goodfellow Cu foil with varying synthesis time 94

Figure 65: APCVD graphene domains on CH_3COOH cleaned 99.9 % Goodfellow Cu foil with varying CH_4:H_2 flow rate ratio 95

Figure 66: Higher magnification of APCVD graphene domains formed on CH_3COOH cleaned 99.9 % Goodfellow Cu foiil with varying CH_4:H_2 flow rate ratio..... 96

Figure 67: Predominately single-layer APCVD graphene domains 97

Figure 68: Pulsed-APCVD graphene domains formed on CH_3COOH cleaned 99.9 % Goodfellow Cu foil 98

Figure 69: Variation of shape and orientation of LPCVD graphene domains over different Cu grains 103

Figure 70: Shape and orientation dependence of LPCVD graphene domains on polycrystalline Cu foil. 104

Figure 71: Distribution of the edge angle of graphene domains on Cu surfaces 106

Figure 72: Change of shape and orientation of LPCVD graphene domains at Cu grain boundaries..... 108

Figure 73: Influence of Cu crystallographic orientation on LPCVD graphene domain size and area 109

Figure 74: Spatially resolved Raman spectroscopy I_{2D}/I_G map of graphene on polycrystalline Cu foil 110

Figure 75: HRTEM and SAED analysis of thickness of graphene domains 112

Figure 76: TEM and SAED analysis of graphene domain edge geometry 113

Figure 77: Spatially resolved Raman spectroscopy map of 2D and G peak position map of graphene on polycrystalline Cu foil 114

Figure 78: High resolution spatially resolved Raman spectroscopy of an individual graphene domain 116

Figure 79: Schematic demonstrating variation in domain boundaries..... 117

Figure 80: Variation of orientation of isolated hexagonal APCVD graphene domains on 99.999 % Alfa Aesar Cu foil..... 118

Figure 81: Distribution of edge angle of hexagonal APCVD graphene domains on 99.999 % Alfa Aesar Cu foil, measured relative to [-110]..... 119

Figure 82: Variation of orientation of isolated hexagonal APCVD graphene domains on 99.8 % Alfa Aesar Cu foil..... 120

Figure 83: Distribution of the edge angle of hexagonal APCVD graphene domains grown on 99.8 % Alfa Aesar Cu foil, measured relative to [-110]..... 121

Figure 84: Variation of orientation of isolated hexagonal APCVD graphene domains on 99.9 % Goodfellow Cu foil 122

Figure 85: Distribution of the edge alignment of hexagonal APCVD graphene domains grown on 99.9% Goodfellow Cu foil, measured relative to [-110] 123

Figure 86: Large-area EBSD maps of crystallographic orientations of various Cu foils 124

Figure 87: Computational modelling of graphene on primary Cu crystallographic orientations 126

Figure 88: Graphene cluster C_{28} on Cu{101} oriented with armchair edge parallel to [-101] 127

Figure 89: Wavefunction representation of graphene cluster on Cu{101} 128

Figure 90: Orientation dependence of APCVD hexagonal graphene domains on polycrystalline Cu 129

Figure 91: SEM images of various Cu foils annealed at 1035 ˚C for 30 minutes under 500 sccm H_2 134

Figure 92: Optical profilometry 3D images of various Cu foils annealed 136

Figure 93: Optical profilometry measured mean surface roughness of various annealed Cu foils 137

Figure 94: Optical profilometry 3D image of annealed Uncoated 99.8 % Alfa Aesar Cu foil with cold rolling striations and grain boundaries 138

Figure 95: XPS analysis of elemental composition of various Cu foils 140

Figure 96: SIMS analysis of surface contamination on annealed Coated 99.8 % Alfa Aesar Cu foil 143

Figure 97: SIMS analysis of surface contamination on annealed Uncoated 99.8 % Alfa Aesar Cu foil 143

Figure 98: SIMS analysis of surface contamination on annealed 99.99+ % Alfa Aesar Cu foil 144

Figure 99: SIMS analysis of surface contamination on annealed 99.999 % Alfa Aesar Cu foil 144

Figure 100: SIMS analysis of surface contamination on annealed 99.9 % Goodfellow Cu foil 144

Figure 101: Depth profiling SIMS at high ion bombardment rate demonstrating penetration of surface contaminations on various annealed Cu foils 146

Figure 102: Depth profiling SIMS at low ion bombardment rate demonstrating surface contaminations on various annealed Cu foils 147

Figure 103: Variation of SIMS Ca:Ga ratio, and hence Ca concentration, for various annealed Cu foils 148

Figure 104: 900 x 900 µm EBSD maps of annealed Cu foils 149

Figure 105: SEM images of APCVD graphene growth on Alfa Aesar Cu foils of varying purity 153

Figure 106: SEM images of APCVD graphene growth on low purity Cu foils from different suppliers 156

Figure 107: Comparison of SEM images of various annealed Cu foils with and without CH_3COOH cleaning 160

Figure 108: Optical profilometry 3D images of various CH_3COOH cleaned and annealed Cu foils 162

Figure 109: Comparison of mean surface roughness measured by optical profilometry of various Cu foils with and without CH_3COOH cleaning 163

Figure 110: XPS analysis of elemental composition of Cu foils following CH_3COOH cleaning and annealing 164

Figure 111: Comparison between XPS analysis of elemental composition of annealed Cu foils with and without CH_3COOH cleaning 165

Figure 112: SIMS analysis of surface contamination on CH_3COOH cleaned and annealed Coated 99.8 % Alfa Aesar Cu foil 166

Figure 113: SIMS analysis of surface contamination on CH_3COOH cleaned and annealed Uncoated 99.8 % Alfa Aesar Cu foil 166

Figure 114: SIMS analysis of surface contamination on CH_3COOH cleaned and annealed 99.99+ % Alfa Aesar Cu foil 166

Figure 115: SIMS analysis of surface contamination on annealed 99.999 % Alfa Aesar Cu foil 167

Figure 116: SIMS analysis of surface contamination on annealed 99.9999 % Alfa Aesar Cu foil 167

Figure 117: SIMS analysis of surface contamination on CH_3COOH cleaned and annealed 99.9 % Goodfellow Cu foil. 167

Figure 118: Comparison of SIMS Ca:Ga ratio, and hence Ca concentration, for various annealed Cu foils with and without CH_3COOH cleaning 169

Figure 119: Comparison of SEM images of APCVD graphene growth on various Cu foils with and without CH_3COOH cleaning 171

Figure 120: LPCVD graphene growth on various Cu foils with and without CH_3COOH cleaning 174

Figure 121: Comparison of APCVD graphene growth on Coated 99.8 % Alfa Aesar Cu foil with CH_3COOH and $FeNO_3$ cleaning 176

Figure 122: Comparison of LPCVD graphene growth on Coated 99.8% Alfa Aesar Cu foil with CH_3COOH and $FeNO_3$ cleaning 177

Figure 123: Comparison of LPCVD graphene growth on 99.999 % Alfa Aesar Cu foil with CH_3COOH cleaning and electropolishing 179

Figure 124: APCVD graphene growth on 99.99+ % Goodfellow Pt foil at 1045˚C with 5 sccm CH_4 and 500 sccm H_2 183

Figure 125: 99.99+ % Goodfellow Pt foil annealed at 1045 ˚C for 30 minutes 184

Figure 126: APCVD graphene growth at 1045˚C on Pt foil with 500 sccm H_2 and varying CH_4 flow rate 185

Figure 127: APCVD graphene growth on Pt foil at 1045˚C with 4 sccm CH_4 and varying H_2 flow rate 186

Figure 128: Hexagonal single-layer APCVD graphene domains on Pt foil 188

Figure 129: Bilayer and few-layer regions with the shape and orientation varying over grains of Pt foil 188

Figure 130: Damage to edge of Pt foil due to reaction with quartz tube 189

Figure 131: APCVD graphene growth at 1045˚C on ceramic-plate-supported Pt foil with 500 sccm H_2 and varying CH_4 flow rate 189

Figure 132: APCVD graphene growth at 1045˚C on ceramic-plate-supported Pt foil with 600 sccm H_2 and varying CH_4 flow rate 190

Figure 133: APCVD graphene growth at 1045˚C on ceramic-plate-supported Pt foil with 4.5 sccm CH_4 and varying H_2 flow rate 191

Figure 134: Hexagonal-like domains formed near the edges of unsupported Pt foils 193

Figure 135: APCVD graphene growth on Pt foil with 4 sccm CH_4 and 500 sccm H_2 at varying synthesis temperature 194

Figure 136: APCVD graphene growth on Pt foil at 1150 ˚C with 500 sccm H_2 and varying CH_4 195

Figure 137: Low magnification SEM composite images of APCVD graphene growth on Pt foil after primary and secondary synthesis 197

Figure 138: APCVD graphene growth following primary and secondary synthesis on the same region of Pt foil. 198

Figure 139: APCVD graphene domains formed on 1 x 1 cm^2 Pt foil with contamination particles 199

Figure 140: APCVD graphene domains formed on 1 x 1 cm^2 Pt foil without significant contamination particles 200

Figure 141: EDX spectrum and SEM images of contamination particles on APCVD graphene domains grown on Pt foil. 201

Figure 142: EDX spectrum and SEM images of contamination particles on APCVD graphene domains grown on Pt foil. 202

Figure 143: LPCVD apparatus for synthesis of nitrogen-doped graphene using $NH_3$205

Figure 144: Raman spectra of nitrogen-doped and raw graphene domains on Cu foil. 207

Figure 145: XPS analysis of nitrogen-doped graphene synthesised at 900 ˚C with 0.5 sccm NH_3 210

Figure 146: LPCVD nitrogen-doped graphene growth with 5 sccm CH_4, 500 sccm H_2 and 0.1 sccm NH_3, varying synthesis temperature 212

Figure 147: LPCVD nitrogen-doped graphene growth with 5 sccm CH_4 and 500 sccm H_2, varying NH_3 213

Figure 148: Damaged LPCVD nitrogen-doped graphene growth at 900 ˚C with 0.5 sccm NH_3 214

Figure 149: STM of LPCVD nitrogen-doped graphene on Cu foil 216

Figure 150: MAADF-STEM of LPCVD nitrogen-doped graphene 218

Figure 151: High-resolution MAADF-STEM of nitrogen dopant in single-layer LPCVD nitrogen-doped graphene 219

Figure 152: STM and CITS of LPCVD nitrogen-doped graphene on Cu foil 220

Figure 153: MAADF-STEM and EELS of LPCVD nitrogen-doped graphene 221

Figure 154: Computational EELS simulation of nitrogen-doped graphene 222

Figure 155: Comparison between experimental and simulated EELS spectra from pristine and nitrogen-doped graphene. 223

Figure 156: LPCVD apparatus for heteroatom doping using liquid precursors 224

Figure 157: LPCVD pure and boron-doped graphene synthesised on 99.999 % Alfa Aesar Cu foil using liquid precursors 225

Figure 158: Raman spectra of LPCVD pure and boron-doped graphene 226

List of Tables

Table 1: Details of Cu foils used for graphene growth 131

Table 2: Details of rebranded Cu foils used for graphene growth..... 131

Table 3: XPS analysis of elemental composition of various Cu foils 139

Table 4: XPS analysis of elemental composition of untreated and CH_3COOH cleaned and annealed Cu foils 164

List of Acronyms

Chemical vapour deposition ..... CVD

Low-pressure CVD ..... LPCVD

Atmospheric-pressure CVD ..... APCVD

Optical microscopy ..... OM

Scanning probe microscopy ..... SPM

Atomic force microscopy ..... AFM

Scanning tunnelling microscopy ..... STM

Current imaging tunnelling spectroscopy ..... CITS

Scanning electron microscopy ..... SEM

Electron backscatter diffraction ..... EBSD

Transmission electron microscopy ..... TEM

Dark-field TEM ..... DFTEM

High-resolution TEM ..... HRTEM

Selected-area electron diffraction ..... SAED

Scanning transmission electron microscopy ..... STEM

Annular dark-field STEM ..... ADF-STEM

High-angle annular dark-field STEM ..... HAADF-STEM

Medium-angle annular dark-field STEM ..... MAADF-STEM

Electron energy loss spectroscopy ..... EELS

Energy-loss near edge structure ..... ELNES

Extended energy-loss fine structure ..... EXELFS

Energy-dispersive X-ray spectroscopy ..... EDX

Secondary ion mass spectrometry ..... SIMS

X-ray photoelectron spectroscopy .....XPS

Low energy electron microscopy.....LEEM

Low energy electron diffraction .....LEED

Ultra-high vacuum .....UHV

Ion bombardment .....IB

Poly(methyl methacrylate) .....PMMA

Field effect transistors .....FETs

Carbon nanotube.....CNT

Multi-walled CNT.....MWCNT

Density functional theory .....DFT

Surface roughness .....S_a

List of Publications and Patents

Sections of this thesis have been published in peer-reviewed journal articles:

- Murdock, A.T., Koos, A., Britton, T.B., Houben, L., Batten, T., Zhang, T., Wilkinson, A.J., Dunin-Borkowski, R.E., Lekka, C.E., Grobert, N., Controlling the orientation, edge geometry, and thickness of chemical vapor deposition graphene, *ACS Nano*, 2013, 7, 1351-1359[1]
- Koos, A.A., Murdock, A.T., Nemes-Incze, P., Nicholls, R.J., Pollard, A.J., Spencer, S.J., Shard, A.G., Roy, D., Biro, L.P., Grobert, N. Effects of temperature and ammonia flow rate on the chemical vapour deposition growth of nitrogen-doped graphene, *Physical chemistry chemical physics*, 2014, DOI:10.1039/C4CP02132K[2]
- Nicholls, R.J., Murdock, A.T., Tsang, J., Britton, J., Pennycook, T.J., Koos, A.A., Nellist, P.D., Grobert, N., Yates, J.R., Probing the bonding in nitrogen-doped graphene using electron energy loss spectroscopy, *ACS Nano*, 2013, 7, 7145-7150[3]
- Kertesz, K., Koos, A.A., Murdock, A.T., Vertesy, Z., Nemes-Incze, P., Szabo, P.J., Horvath, Z.E., Tapszto, L., Hwang, C., Grobert, N., Biro, L.P., Polarized light microscopy of chemical-vapor-deposition-grown graphene, *Applied Physics Letters*, 2012, 100, 213103[4]

Sections of this thesis are currently in preparation for submission to peer-reviewed journals:

- Murdock, A.T., Britton, J., van Engers, C., Babenko, V., Lane, G., Bishop, H., Crossley, A., Koos, A.A., Grobert, N., Effect of metal contaminations and copper cleaning procedures on the CVD growth of graphene and hexagonal boron nitride, *2D materials*
- Murdock, A.T., Babenko, V., Britton, J., Koos, A.A., Grobert, N., Influence of the synthesis parameters on the growth of polycrystalline chemical vapour deposition graphene domains on Pt foils, *Nanoscale*

- Babenko, V., Murdock, A.T., Koos, A.A., Britton, J., Crossley, A., Holdway, P., Moffat, J., Alexander-Webber, J., Huang, N., Nicholas, R., Grobert, N., Rapid, epitaxy-free graphene synthesis on silicidated polycrystalline platinum, *Nature Materials*

Sections of this thesis have been filed as a GB (EU) and US patent:

- Grobert, N., Murdock, A.T., Koos, A.A., Producing two-dimensional nanomaterials (graphene) by chemical vapor deposition, used in e.g. display, comprises contacting substrate with flow of hydrogen and flow of precursor such that precursor forms material on surface of substrate, Patent number WO2013144640-A1[5]

1 Introduction

This thesis presents investigations into the chemical vapour deposition growth of large-area graphene on metals, encompassing a body of research aiming towards a Doctor of Philosophy (DPhil) in Materials at The University of Oxford. Research was conducted between 5 October 2009 and 25 April 2014 in the Department of Materials under the supervisor of Professor Nicole Grobert. During this period a student internship on the growth of two-dimensional nanomaterials was also completed at the Samsung Advanced Institute of Technology, Giheung, South Korea, between July and September 2013. The majority of experimental investigations were conducted between October 2010 and May 2013.

The thesis begins with a review of the literature describing graphene, its properties, potential applications, and production methods in Chapter 2. The historical development of chemical vapour deposition growth of graphene on metals is covered, specifically using copper and platinum foils. Production of heteroatom-doped graphene by chemical vapour deposition is also outlined. Literature on the influence of synthesis conditions and metal substrates on the growth of graphene is reviewed in detail, with attention drawn to specific areas where further investigations are necessary for improved understanding. This review provides a case for the experimental investigations presented in this thesis, with specific research aims outlined in Chapter 3.

Owing to the breadth of research into graphene and metal surfaces, many experimental and characterisation techniques are required for thorough analysis. The range of techniques presented in this thesis are outline in Chapter 4.

Chapter 5 and Chapter 6 present investigations into low-pressure and atmospheric-pressure chemical vapour deposition growth of graphene on copper foils. The design and production of low-pressure synthesis apparatus is covered in detail, owing to the significant amount of time this involved. Investigations into the influence of synthesis conditions on graphene growth demonstrate the importance of individual

parameters, and the uniformity and reproducibility needed in the experimental setup.

Chapter 7 and Chapter 8 present detailed investigations into the influence of various properties of the Cu substrate on graphene growth. The Cu crystallographic orientation is shown to control the orientation of individual graphene domains. The influence of the topography, surface roughness and chemical purity of Cu foils on graphene growth is investigated. A variety of cleaning treatments to modify the Cu surface and improve graphene growth are investigated.

In Chapter 9 attention is shifted to atmospheric-pressure chemical vapour deposition growth of large-area graphene on platinum foils. Optimising the synthesis conditions promotes growth of ~0.5 mm single-layer graphene domains at a growth rate of ~100 μm/min. The importance of the surface topography and metal contamination particles in dictating the nucleation of graphene on platinum is also investigated.

Chapter 10 presents final investigations into the growth of heteroatom-doped graphene. The chapter focuses on low-pressure chemical vapour deposition growth and characterisation of nitrogen-doped graphene. Synthesis conditions are shown to play an important role in controlling the growth and dopant concentration of nitrogen-doped graphene. Noteworthy scanning transmission electron microscopy presents the first direct imaging and analysis of nitrogen dopant atoms within the graphene lattice. Initial investigations into the low-pressure chemical vapour deposition growth of boron-doped graphene are also presented

The thesis concludes with a summary of the significant discoveries made during the course of the research project and the implications to the field at large. Future investigations that may be helpful to further advance the field are outlined.

2 Literature Review

This chapter provides a summary of literature relating to graphene, its properties and production methods, aiming to place my research in context of the field at large and justify the areas of investigation during my DPhil. Owing to the explosion of interest in the field, the volume of literature has grown considerably since October 2009, and continues to expand. As such, a caveat is necessary. The literature presented focuses on publications prior to January 2013, with a significant portion of from prior to January 2012. This review is therefore a representation of the scientific knowledge and extent of the field as and when I planned and conducted investigations. Of course, countless articles were published during the course of my research, and these new developments were used to guide and redirect my investigations. However, I have attempted to separate the journal articles that did not significantly impact on my scientific judgement, or which were published after my investigations were complete. Any such articles of significance are therefore mentioned in the discussion and conclusion sections of the relevant chapter. In some cases these new journal articles present similar investigations, and while this may somewhat reduce the novelty of results, it also validates my initial decision to investigate these topics.

2.1 Defining graphene

Graphene is a one-atom-thick nanomaterial composed of sp^2 hybridized carbon atoms in a hexagonal planar arrangement. The C-C interatomic distance is 1.42 Å. Each atom provides one 2s and two 2p orbital electrons for in-plane bonding, and one perpendicular 2p orbital electron remains[6]. Two interpenetrating triangle sub-lattices can be envisaged to construct the hexagonal graphene lattice, with atoms on the vertex of one sub-lattice located at the triangles' centre of the alternate sub-lattice. This equates to two carbon atoms existing per unit cell, with basis vectors of $|\mathbf{a1}|=|\mathbf{a2}|=2.461$ Å and a separation angle of 60˚, Figure 1. Graphene can exhibit ideal zigzag and armchair edges, or reconstructed zigzag configurations[7, 8].

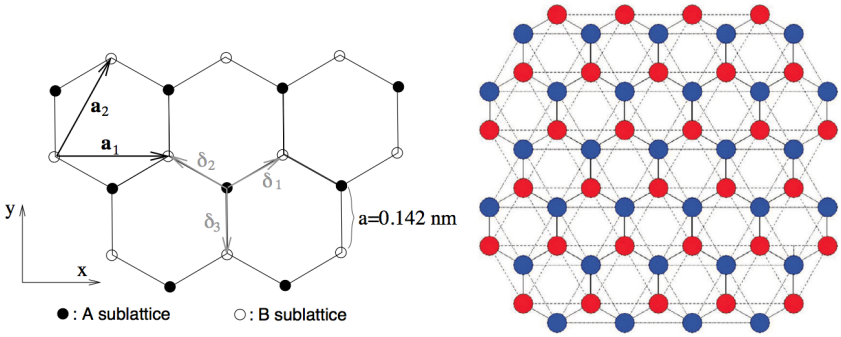


Figure 1: Diagram of graphene

(a) Graphene, a single-layer of carbon atoms in a hexagonal network, with basis vectors and dimensions of the graphene unit cell, (b) Two interpenetrating triangular sub-lattices of graphene, represented by red and blue atoms. Zigzag (horizontal edges) and armchair (vertical edges) edge configurations are visible. Reproduced with permission from (a) Goerbig[9] and (b) Castro Neto[10]

2.1.1 Relation to other carbon nanomaterials and stacking

If viewed as either a single layer of graphite, an unrolled carbon nanotube, or a carbon net of a fullerene, graphene can be considered as the fundamental theoretical template of all other graphitic carbon allotropes[11], Figure 2.

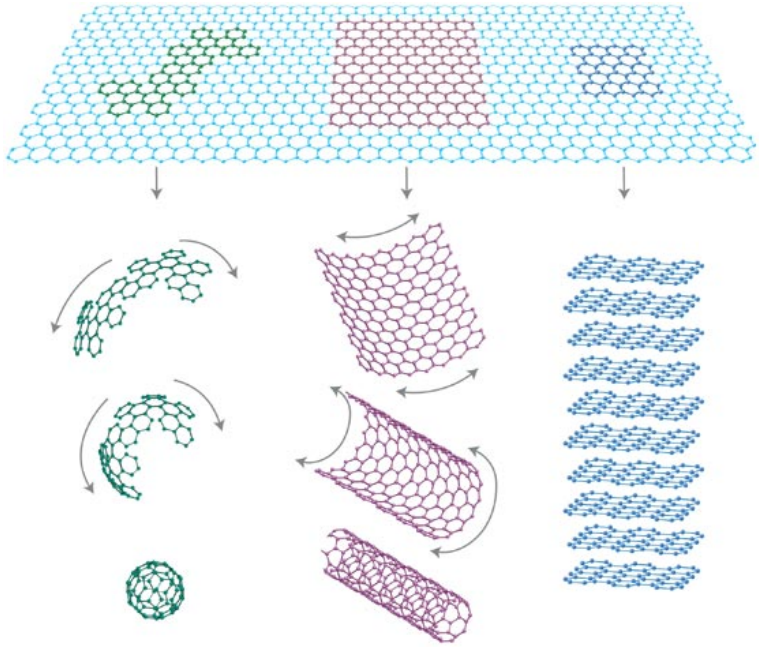


Figure 2: Graphene and related carbon nanomaterials.

Reproduced with permission from Geim et al.[11]

Graphene can exist in a variety of configurations from that of an ideal, isolated graphite sheet. For consistency, single-layer (monolayer) graphene, bilayer graphene, trilayer, and few-layer graphene (3 - <10 layers)- all which exhibit distinct

and characteristic electronic qualities- should be uniquely identified from each other, and certainly viewed as separate entities to graphite (≥10 layers)[11]. However, multilayer graphene is often used to collectively refer to bilayer and few-layer graphene. Multiple graphene layers can stack with a variety of different configurations: either oriented, with no rotation between layers, Figure 3, or misoriented, with rotation and a misorientation angle between layers. Oriented stacking includes AB Bernal (where the atoms of the second layer are located above the centre of hexagons of the first layers, and this is repeated), ABC rhombohedral (where the first two layers replicate AB Bernal stacking, but the third layer is shifted so that this layer also displays Bernal stacking with respect to the first layer), and the relatively uncommon AA stacking (where the atoms of the second layer are located directly above the atoms of the first layer). Misoriented stacking, often referred to as turbostratic, occurs when there is no correlation between the orientation of multiple layers, and instead layers adopt a random alignment. The interlayer distance between multiple layers of graphene is dependent on the stacking configuration, being near to 3.35 Å as shown by graphite[12]. The stacking configuration is also important as it can influence the electrical, optical and mechanical properties of multilayer graphene[13-16].

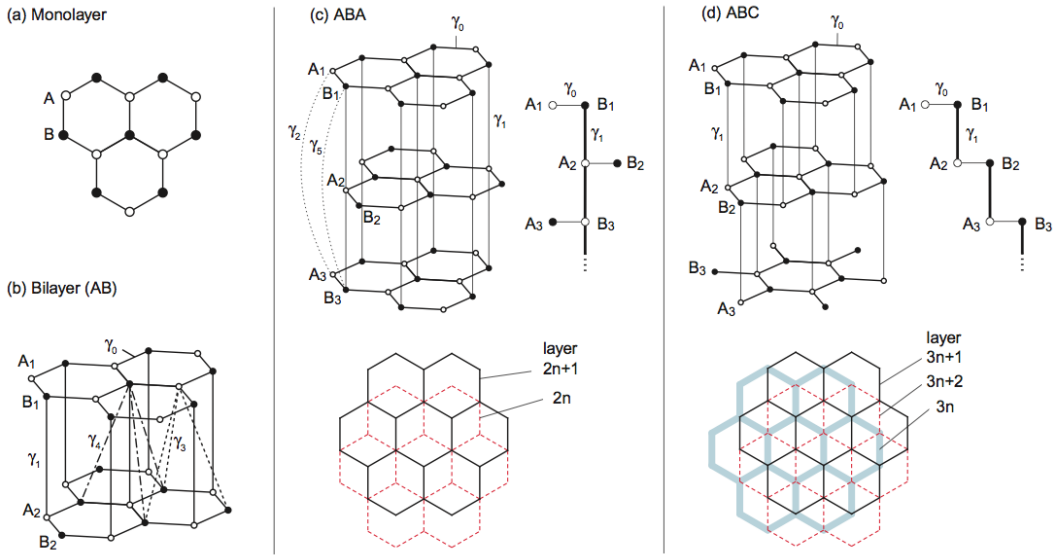


Figure 3: Stacking configurations of graphene

(a) monolayer, (b) bilayer AB stacking, (c) AB Bernal stacking, (d) ABC rhombohedral stacking. Reproduced with permission from Koshino et al.[17]

2.1.2 Heteroatomic doping of graphene

The concept of chemically doping carbon nanomaterials, notably carbon nanotubes, has been around for decades[18-21]. Heteroatomic doping- the introduction of non-carbon atoms, for instance N, B, P, S, Cl, or Br into a molecular structure- is distinguished from electrical doping, which may be promoted by an external applied voltage, and surface transfer doping due to adsorbed molecules. Heteroatom doping provides the opportunity to modify and control the electronic, chemical and mechanical properties[20, 22, 23]. This opens the possibility for a wide range of highly specific applications, for instance, in gas sensors and catalysts, which are outlined in more detail in Chapter 2.3. It is for these reasons that investigations into the synthesis of heteroatom-doped graphene are an important field for advancement. Nitrogen and boron heteroatoms are particularly promising candidates due to their similar atomic radius and preference for chemical bonding with carbon. Nitrogen atoms can be introduced into the graphene lattice with three noteworthy bonding arrangements, namely substitutional (or graphitic), pyridinic and pyrrolic[22, 24], Figure 4.

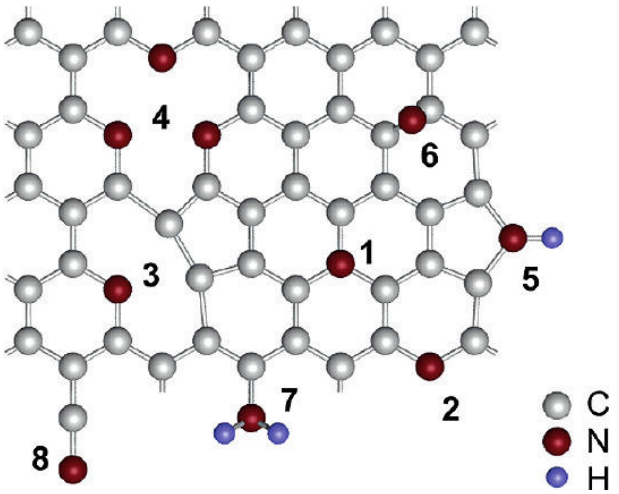


Figure 4: Configurations of nitrogen dopants within graphene lattice including (1) substitutional (or graphitic), (2) pyridinic-like, (3) single N pyridinic vacancy, (4) triple N pyridinic vacancy, (5) pyrrole-like, (6) interstitial N or adatom, (7) amine, (8) nitrile

Reproduced with permission from Usachov et al.[25]. Copyright (2011) American Chemical Society.

2.2 Properties of graphene

2.2.1 Electrical properties

Intrinsic graphene is described as a zero-gap semiconductor (or zero-overlap semimetal)[11]. Graphene has a unique bandstructure, dictated by the C atom's remaining unbonded p orbital which hybridises to form the π (valence) and π* (conduction) bands[6], Figure 5. These bands touch at corners of the Brillouin zone at Dirac points (K points). At low energies the bands have approximately linear energy-momentum dispersion and can be viewed as two touching cones. From this band structure the charge carriers can be described to have relativistic-like behaviour with zero effective mass [26, 27]. This has led to the observation of a half-integer quantum Hall effect[26-28].

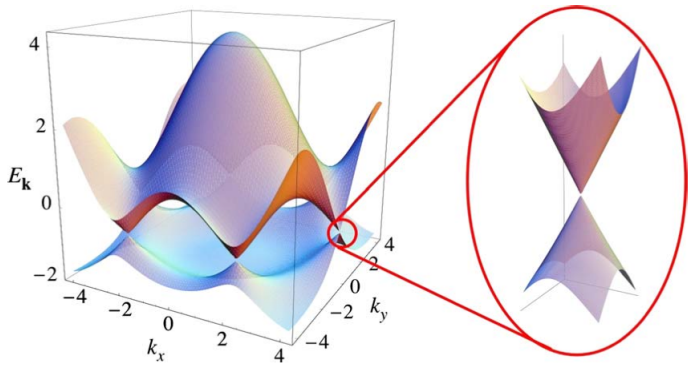


Figure 5: 3D band structure of graphene

Two surfaces representing the π and π bands (valence and conduction bands, respectively). Zoom illustrates the low energy band structure approximated as two cones touching at the Dirac point. Reproduced with permission from Castro Neto et al.[29]*

As a consequence of this band structure, graphene shows very high electrical conductivity, with both electrons and holes able to act as charge carriers. Charge carriers display extremely high mobilities, up to 250,000 $cm^2 V^{-1} s^{-1}$ in an ideal case[28, 30, 31]. Suspended graphene can show a mean free path greater than 1 µm, resulting in the possibility for ballistic conduction[30, 32]. While substrate interaction, impurity scattering, defects and disorder can limit this transport, a very recent study using epitaxial graphene nanoribbons shows a mean free path greater than 10 µm and ballistic transport[33] . The current density in graphene can also be extremely high, at 5 x 10^8 A cm^{-2}, up to a million times greater than observed with copper[34, 35].

2.2.2 Optical properties

A single layer of pristine graphene exhibits 97.7% transmittance (2.3 % absorption) in the visible spectrum[36]. Each layer thereafter cumulatively reduces the transmittance by 2.3%, Figure 6a. This is a fundamental property due to the electrical nature of graphene and is directly related to the fine-structure constant. Graphene has a flat absorption spectrum from 300 to 2,500 nm, with only a small peak at ~270 nm in the ultraviolet region[37], Figure 6b.

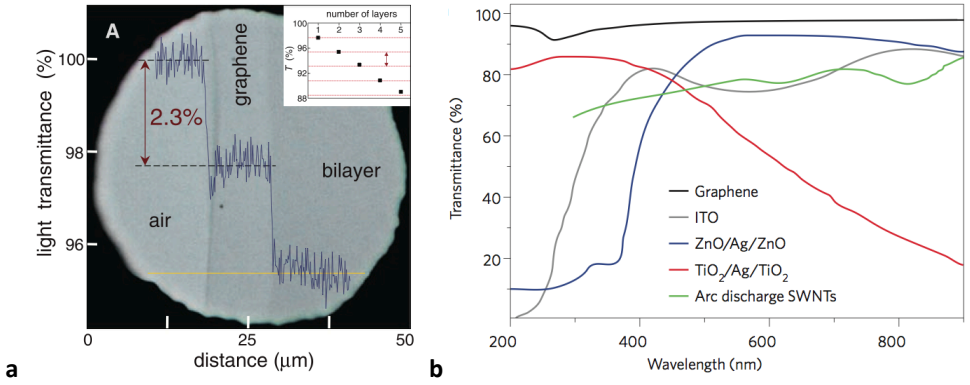


Figure 6: Optical properties of graphene

(a) Variation of optical transmittance with the number of graphene layers. (b) Variation of transmittance of graphene at different wavelengths, compared to common transparent conductors. Images reproduced and modified with permission from (a) Nair et al.[36] (b) Bonaccorso et al.[37]

2.2.3 Mechanical properties

With unrivalled mechanical stiffness, pristine defect-free graphene displays a Young's modulus of ~1 TPa, breaking strength of 42 Nm^{-1} and intrinsic strength of 130 GPa[38]. This makes pristine graphene the strongest material ever measured. However, graphene still shows flexibility, and elasticity, being able to absorb 20% strain[38]. These properties have led to some scientists to claim, somewhat jocularly, that a hypothetical 1 m^2 hammock made of pristine graphene could thus hold up to 4 kg without breaking, capable of supporting a cat[39], or potentially even a small *Velociraptor mongoliensis*[40].

2.2.4 Thermal properties

Graphene has a high in-plane thermal conductivity- greater than copper, diamond, and one of the highest ever measured- with ~2000-4000 $Wm^{-1}K^{-1}$ for suspended

flakes[41-43]. This is due to the covalent sp^2 bonding between the carbon atoms[44]. However, thermal conductivity decreases significantly when graphene is in contact substrates, to ~600 W $m^{-1}K^{-1}$ on SiO_2[45]. Defects and disorder in the graphene lattice will also cause similar reductions. Due to its two-dimensional geometry, graphene also shows over 100-fold anisotropy when comparing heat flow in the in-plane and interplanar directions[46]. Out-of-plane thermal conductivity of graphite is only ~6 W m^{-1} K^{-1}.

2.2.5 Properties of heteroatom-doped graphene

The introduction of heteroatoms that posses either an excess (five) or deficiency (three) of valence electrons into the graphitic network can modify the electronic band structure. An energy gap can open between the valence and conduction bands, and the Fermi level is shifted, resulting in p-type or n-type behaviour, Figure 7[47-49].

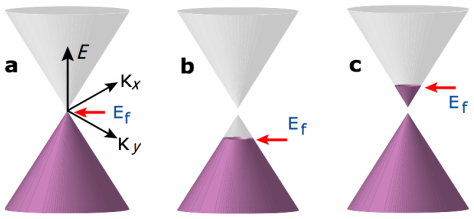


Figure 7: Influence of heteroatomic doping on band structure of graphene
(a) Cone-shaped band structure of pristine graphene with zero band gap and Fermi level at cross-over point. (b) Band structure of p-type graphene, with band gap and E_f in valence band, as predicted for boron-doped graphene, (c) Band structure of n-type graphene, with band gap and E_f in conduction band, as predicted for substitutional nitrogen-doped graphene. Reproduced from Guo et al.[49]

Heteroatom-doping of graphene with substitutional atoms has been theoretically[50-54] and experimentally[24, 50, 54-56] demonstrated to modify and control the electronic properties of graphene. Different configurations of nitrogen dopants, highlighted previously in Figure 4, affect the electronic properties of nitrogen-doped graphene differently[25]. Substitutional nitrogen dopants cause n-type doping, while pyridinic and pyrrolic dopants cause p-type doping[25, 57]. Substitutional nitrogen-doped graphene with n-type semiconducting behaviour was demonstrated by fabrication of field-effect transistors (FETs), which show a shift in the neutrality point toward negative gate voltages[20, 48, 50, 54, 58, 59], and angle-resolve photoemission spectroscopy,

measuring a band gap of ~0.2 eV and a shift of the Fermi level by ~300 meV (measured after Au intercalation)[25].

The introduction of substitutional heteroatoms into the graphitic lattice also provides defect sites from which specific chemical activity can be tailored[18, 53, 60]. Dopant atoms will show chemical reactivity of their own accord. Additionally, dopants will influence the electron charge distribution of neighbouring carbon atoms, producing an activated region[61]. Adsorbents, including individual atoms and molecules, functional groups, and nanoparticles, will be attracted to the vicinity of dopant atoms and the activated region, which can act as a location for preferential chemical functionality. Chemical reactions may be possible at these sites with increased kinetic efficiency, or lower activation energy requirements. Doping can therefore be used to improve and control the chemical properties of graphene.

2.3 Potential applications of pure and heteroatom-doped graphene

With such extraordinary properties there have been widespread applications proposed to utilise graphene. These applications aim to harness at least one, and often multiple properties for improved performance of a device or material. Graphene is envisaged as a champion of future carbon-based nanoscale electronics, with publications demonstrating its application in high-frequency transistors[62, 63] and tunable ultrafast mode-locked lasers[64]. With extremely high carrier mobility and low optical absorption, graphene could be used as a transparent conductive electrode to replace brittle indium tin oxide in solar cells, touch screens and liquid crystal displays[65,66,67]. Flexible, stretchable and wearable electronics may also be possible using graphene due to its improved mechanical flexibility[68-70]. With an ultra-fast response and efficient detection across a broad spectrum, graphene-based photodetectors may improve optical communications and revolutionise personal computers by enabling optical fibre signal transmission[71, 72]. Graphene also has a high surface area, meaning it may find use in energy conversion and storage devices, as electrodes in Li ion batteries or as supercapacitors[73, 74]. Additionally, with its high thermal conductivity graphene appears as a candidate material for heat sinks[46]. As an ideal two-dimensional material, graphene can be used as a protective, chemically inert surface coating, with potential applications in reducing oxidation of metal

surfaces[75]. The graphene surface additionally shows potential as a support surface for electron microscopy[76, 77], surface enhanced Raman spectroscopy[78], as a template for controlled cluster and atom dispersions[79, 80], and as chemical sensors for detection of individual gas molecules[81]. Utilising graphene's exceptional strength and large surface area, nanocomposites made by the addition of graphene to polymer matrices or other materials are reinforced and have improved mechanical properties[82-84]. These lightweight, ultra-strong materials may be particularly useful for aeronautical applications. Graphene nanocomposites may also have improved electrical or thermal conductivity, so that conducting polymers can be produced[85].

Heteroatomic doping of graphene expands its capabilities and potential applications. As pristine graphene is a zero gap semiconductor with an inert surface, changing its electronic properties or surface chemistry through doping may be beneficial for particular applications. The primary application where doped graphene is predicted to show significant advantages is in nanoelectronics, where the opening of a band gap and production of large-area semiconducting sheets would herald graphene's suitability to supersede Si in transistors and electronic devices. Initial studies have demonstrated the capability of nitrogen doping to alter the electronic properties of graphene to n-type semiconducting behaviour[48, 86], however issues relating to a low on/off ratio, reduced carrier mobility, and tunability of the band gap are still unresolved. Doped graphene also appears promising for improved catalysts, sensors and energy storage materials due to the increased chemical reactivity from dopants. Nitrogen-doped graphene has shown better performance than pristine graphene as a metal-free catalyst for oxygen reduction reactions in fuel cells[55] and bioelectrochemical systems[87], and as a biosensor[87]. Li-ion intercalation and reversible discharge capacity has also been improved by using nitrogen-doped graphene electrodes in lithium batteries[88]. A four-times improvement in capacitance of supercapacitors using nitrogen-doped graphene rather than pristine graphene has also been demonstrated[89]. Heteroatomic doping, particularly nitrogen and boron doping, expands upon the wide-range of possible applications of graphene, and specifically provides the researcher with the ability to control both electrical and chemical properties which would otherwise be unachievable.

2.4 Production of graphene

2.4.1 Overview of production methods

Since its isolation in 2004, significant progress has occurred in the controlled synthesis of graphene[6, 11, 90-92]. Developments have occurred through a variety of production methods, including:

- Micromechanical exfoliation of graphite, Chapter 2.4.1.1,
- Chemical treatment of graphite, Chapter 2.4.1.2,
- Epitaxial growth on silicon carbide, Chapter 2.4.1.3, and
- Synthesis on metal surfaces, Chapter 2.4.1.4.

2.4.1.1 Micromechanical exfoliation of graphite

Andre Geim and co-workers from Manchester University produced isolated graphene for the first time through the mechanical exfoliation of bulk graphite[12]. Through the use of Scotch® tape, bulk graphite layers were repeatedly peeled and separated until single layers of graphene up to 10 µm in width were isolated. Bilayer and few-layer graphene can also be produced. The micromechanical exfoliation technique relies on the fact that graphite is composed of many stacked sheets of graphene, held together by weak Van der Waals forces. Through fine-tuning this process, high-quality graphene up to 100 µm in size is readily available[11], Figure 8.



Figure 8: Graphene produced by micromechanical exfoliation

Optical image of a large monolayer on 90 nm SiO_2. Reproduced from grapheneindustries.com[93]

2.4.1.2 Chemical treatment of graphite

Chemical treatment of graphite can produce colloidal suspensions of graphene and graphite-based derivatives. Numerous routes exist[91, 94-98], primarily through the intercalation of bulk graphite to form graphite oxide via Brodie's or (modified) Hummer's[99] methods. Chemical species are often added to resulting solutions to aid stabilisation, before chemical reduction is performed (commonly through use of hydrazine) to produce chemically reduced graphene oxide, Figure 9[95, 100]. Alternatively, sonicating graphite in solvents selected for preferential dissolution (e.g N-methyl-pyrrolidone) has proven to be a successful method to form graphene[97]. These solutions can be deposited on surfaces to form thin deposits or coatings, and the solvent can be evaporated to produce powdered graphene.

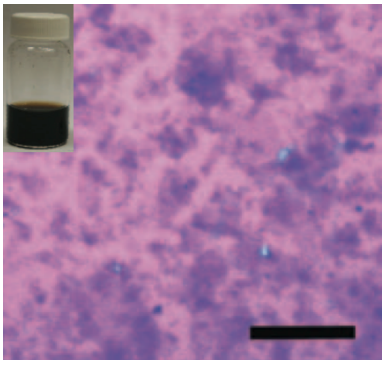


Figure 9: Graphene produced by chemical treatment of graphite

Optical image (scale bar: 20 µm) of reduced graphene oxide thin film deposited on 300 nm SiO_2 with variable thickness. Inset shows a typical dispersion. Reproduced with permission from Eda et al.[95]

2.4.1.3 Epitaxial growth on SiC

Single and few-layer graphene can form on silicon carbide substrates through a process of thermal decomposition, Si sublimation, and epitaxial growth, Figure 10[101-104]. Samples are annealed at high temperatures, 1300 °C, and typically under ultrahigh vacuum (UHV) to initially promote sublimation of silicon. Carbon remaining in the surface can subsequently undergo graphitisation if the appropriate conditions are provided, and with careful control the process can be limited to the formation of single and few-layer graphene.

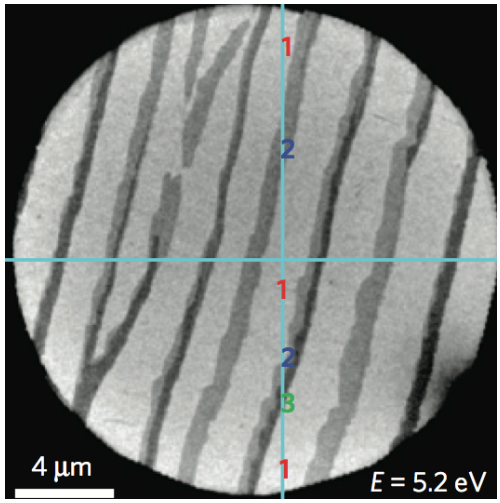


Figure 10: Graphene produced by epitaxial growth on SiC

LEED image showing monolayer coverage (light grey) with bilayer and tri-layers (dark grey) on step edges. Reproduced with permission from Emtsev et al.[104]

2.4.1.4 Synthesis on metal surfaces

Graphene can also be synthesised on catalytic transition metal substrates, Figure 11. Three related processes have been identified in the literature:

- Carbon surface segregation[105-107]: carbon atoms dissolved in a metal substrate segregate to the surface (or to grain boundaries and later to the surface) as the stable concentration of dissolved carbon decreases and supersaturation is induced with variations to cooling rates and substrate temperature. By carefully controlling the cooling rate while lowering substrate temperature the formation of single and few-layer graphene can be promoted. This method can be combined with chemical vapour deposition, which provides the initial carbon atoms to dissolve into the metallic substrate[108].
- Chemical vapour deposition (CVD)[109-112]: carbon-containing gases are passed over a hot catalytic metal surface. The gases absorb specifically on the surface or near-surface region of the metal, decompose, and graphitisation occurs.
- Thermal decomposition of surface adsorbed species[59, 79, 113-116]: hydrocarbons are adsorbed onto a metal surface at room temperature, which is subsequently heated to promote thermal decomposition and graphitisation.

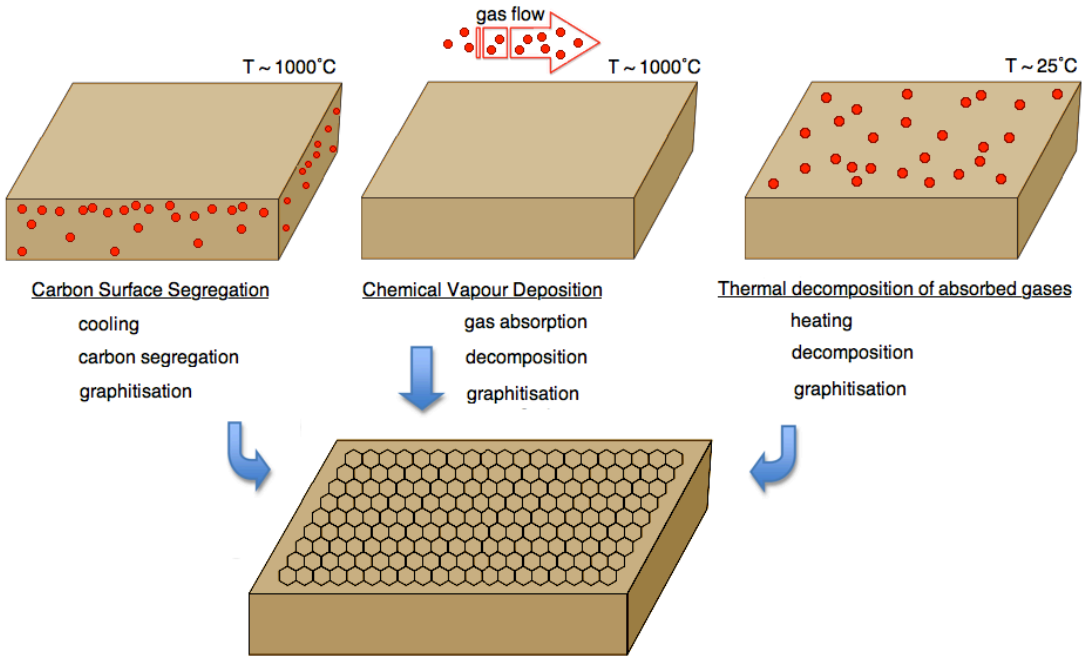


Figure 11: Methods of synthesis of graphene on metals

Though the terminology used to describe these processes varies between publications (particularly if published before 2009), and irrespective of other differences, they all ultimately rely on the same key element: a metallic surface acts as a catalytic substrate for the preferential agglomeration and alignment of carbon atoms, promoting the formation of the graphene network. The graphene growth is strongly influenced by the surface characteristics of the underlying substrate. Indeed, it is the added interaction between the graphene layer and the surface before, during, and after growth that distinguishes these methods from other synthesis techniques[117].

2.4.2 Influence of the production method on the type, morphology, size, and properties of graphene

The production method has a direct influence on the type and quality of graphene that is formed. While each method produces "graphene" of a sort, the dimensions, morphology, quantity, and properties vary significantly. Each production method exhibits both benefits and shortcomings, with a common limitation being a lack of potential for production of large areas with high-quality mechanical and electrical properties. While the micromechanical exfoliation process generated the current research interests into the field, and unquestionably produces the highest quality

graphene suitable for fundamental scientific studies[12, 118], the technique is inherently restricted to the small-scale production of graphene flakes with uncontrollable thickness, size and shape. This rules out micromechanical exfoliation for mass production. Conversely, the majority of the chemical treatments are indeed scalable to mass quantities of powders or solutions of graphene[91], suitable for surface coatings or integration within composite materials. However, the use of chemicals for intercalation, reduction, stabilising agents or other processing in the extraction from the bulk graphite and derivatives[91] means residual defects and functional groups often persist in the final graphene material causing diminished properties[6]. Furthermore, the dimensions and thickness of graphene in powders and solutions vary greatly. While chemical treatments have scope for some future applications, they are not viable for producing uniform, large-area graphene with a controlled thickness. Epitaxial growth on SiC provides large-area samples of potentially high quality graphene. Unfortunately, an expensive substrate, high synthesis temperature, and ultra-high vacuum conditions lead to high production costs, limiting its potential for specialised applications. Synthesis on metal surfaces overcomes many of the drawbacks the other production methods suffer from by producing large-areas of graphene, with maximum dimensions limited only by the size of the metal substrate. Of the techniques highlighted in Figure 11, CVD provides the greatest opportunity for controlling the properties and thickness of graphene by optimising the flow of reactant gases. As such, CVD is considered the likely candidate for synthesising large-areas of high-quality single, bilayer and few-layer graphene.

2.4.3 Chemical vapour deposition of graphene on metals

CVD of graphene relies on exposing a heated metal surface to a gas mixture including hydrocarbon species (commonly CH_4), often hydrogen, and sometimes a carrier species (commonly Ar). Additional gases, such as NH_3, can be added to the gas mixture to promote *in-situ* doping of the graphene[24, 119]. CVD is commonly achieved by placing the metal substrate within a cylindrical quartz (borosilicate glass) tube, located within a temperature-controlled cylindrical tube furnace, Figure 12. CVD can also be conducted in box furnaces, or cold-walled systems with resistive heating stages (which show significant differences to hot-walled counterparts).



Figure 12: Commercially available CVD apparatus

Cylindrical quartz tube within a cylindrical tube furnace. Image reproduced from mtixtl.com[120]

The exact CVD growth mechanism of graphene is still an active area of investigation. The basic process consists of a number of stages[121-123], including:

(i) Chemisorption of hydrocarbons onto the metal surface to form an adsorbed species,

(ii) Dissociation of the adsorbed species into absorbed carbon atoms, dimmers, radicals or few-atom clusters,

(iii) Surface diffusion of the carbon atoms, through or over the metal,

(iv) Breaking of metal-C bonds, to release carbon atoms which nucleate to form a stable graphene nuclei, often occurring when a critical supersaturation level is achieved, or where surface features stimulate nucleation by providing a lower energy barrier for monomer attachment, and/or lower size of critical nuclei,

(v) Growth of graphene nuclei, which may involve edge reconstruction, depending on the degree of supersaturation, to form micron-sized graphene flakes- referred to as domains;

(vi) Merging and coalescence of neighbouring graphene domains into a continuous polycrystalline layer covering the metal surface, providing that sufficient surface carbon is available.

Competing processes simultaneously occur alongside this growth mechanism including:

(i) Etching of graphene domains by H_2 gas, the reverse of hydrocarbon decomposition

(ii) Evaporation of metal atoms from the surface, particularly under low-pressure conditions, or when the synthesis temperature approaches the melting point of the metal.

2.4.3.1 Chemical vapour deposition of graphene on nickel and other metals

The surface science community reported on the synthesis of graphene on metal surfaces over 40 years ago[6, 117, 124], including single-layer graphene through carbon segregation on Ni[105, 125], and few-layer graphite on Pt through a process akin to ethylene CVD[126]. Graphene was grown on Co[114], Ir[79, 80, 112, 127-130], Ni[109, 111, 131], Pt[113, 116, 132] and Ru[106, 133-138], often using single-crystal substrates and UHV conditions. In 2009, independent studies conclusively demonstrated that few-layer graphene formed via low-pressure CVD (LPCVD) on thin films of Ni on silicon, and polycrystalline Ni foils, with dimensions larger than square centimetres[69, 108, 139-141]. However, the homogeneity of the graphene films varied, with production of few-layer graphene common due to the high solubility of carbon in Ni (~0.6 wt % for Ni at 1326 ˚C[122]) causing uncontrolled surface segregation. This made Ni an undesirable substrate for CVD growth of graphene. More recent studies[142, 143] have proposed counter measures to improve the uniformity of graphene, for instance, a reduction in synthesis temperature, meaning CVD growth on Ni shows promise for the future.

2.4.3.2 Chemical vapour deposition of graphene on copper

Following the seminal publication by Li *et al.*[144] in May 2009, significant attention shifted to the CVD growth of graphene on Cu[42, 77, 119, 145-164]. The Ruoff group demonstrated that predominately monolayer graphene could be synthesised via LPCVD of CH_4 on polycrystalline Cu foils, 25 μm thick, 99.8 % purity, sourced from Alfa Aesar, Figure 13.

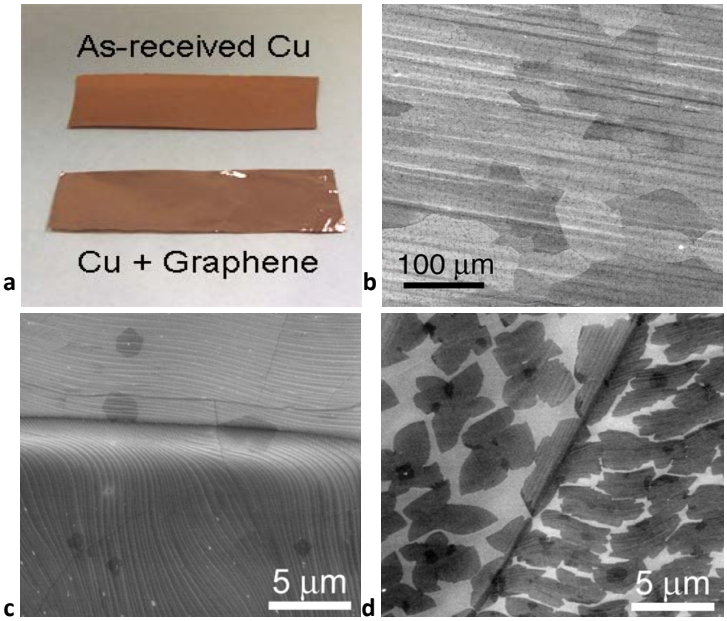


Figure 13: LPCVD growth of large-area graphene on Cu foils

(a) Cu foils before and after graphene growth, (b) Low magnification SEM image of graphene on Cu foil, (c) High magnification SEM image of graphene fully covering Cu foil, (d) High magnification SEM image of isolated graphene domains. Reproduced with permission from Li et al.[144]

While growth of graphene on Cu was known[24, 165, 166], Li *et al.*[144]'s article provided the first revelation that relatively cheap and commercially available Cu foils could be used for production of large-areas of single-layer graphene. Using Cu also overcame the inherent challenges of small grain sizes and high carbon solubility for Ni (only 0.001-0.008 wt % at 1084˚C for Cu[122]). Growth on Cu was claimed to be a self-limiting surface mediated process, predominately forming single layer micron-sized domains.

These advances, combined with the high profile exposure and timely nature of the publication, undoubtedly stirred the field. Within 12 months of the publication appearing in excess of 20 publications describing graphene grown through CVD using Cu proliferated the field[, 42, 68, 70, 77, 119, 145, 148, 150-152, 154-159, 161-164]. Advances included:

- Increase in the size of Cu foil and resultant graphene, up to 30-inch diagonal[68],
- Investigations into the influence of synthesis conditions to reduce multilayer regions and nucleation density, and increase domain size[167, 168],

- Demonstration of atmospheric-pressure CVD (APCVD) growth of graphene on Cu[147, 150, 152, 167, 169],
- Alternative carbon sources to CH_4, including ethylene gas[151, 156, 159, 162, 170], liquid hexane[157], and solid polymers[59],
- Alternative Cu substrates, including thin films of Cu on silicon[148, 155, 171],
- Cu foil treatments, including cleaning [148, 158] and annealing procedures[119, 149-151, 153, 154, 157, 158, 160, 162, 163].

These developments indicated that CVD growth of graphene on Cu was viable for large-area production. However, even with this rapid progress, by 2011 only limited systematic investigations were published demonstrating the influence of the CVD synthesis conditions. Similarly, few reports specifically investigated the influence of the Cu substrate on graphene growth. While multiple types of substrates were used within some publications, no comparison was made between the different types of graphene that formed and the substrate's influence. These are two key areas identified for further scientific investigation that would provide a deeper understanding of how the quality of graphene grown can be improved, rather than simply reiterating that the process could be achieved. Conclusions through systematic investigations would provide improvements that could be replicated across the field to individual CVD setups and procedures. This would have a significant improvement on the resultant graphene produced, and the quality of future research, worldwide.

2.4.3.3 Chemical vapour deposition of graphene on platinum

Pt was one of the first metals upon which the formation of graphene was observed[113, 117, 126, 172]. Pt shows a relatively low carbon solubility[123], low thermal expansion coefficient and high melting point making it a likely candidate for producing high-quality graphene. More recent studies in 2009 using ethylene in UHV on single crystals showed epitaxial growth on Pt(111), although multiple preferential orientations were identified[173, 174]. However, graphene growth on Pt did not receive considerable interest in the following years, presumably due to the high costs associated with the single crystal substrate. Interests were reignited in 2011 when APCVD graphene growth was demonstrated on commercial polycrystalline Pt foils[175].

Gao *et al.*[176]'s publication in early 2012 demonstrating APCVD growth of millimetre sized hexagonal single-crystal graphene confirmed the benefits of using polycrystalline Pt foils, Figure 14.

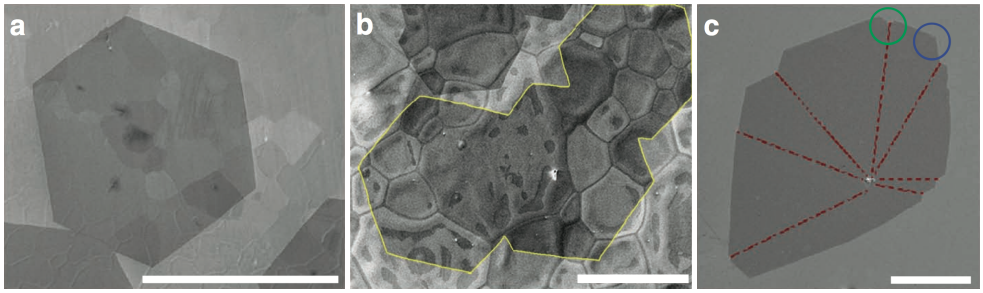


Figure 14: APCVD growth of large-area graphene on Pt foils

(a) SEM image of large-area single-crystal hexagonal graphene domain, scale bar 1 mm, (b) Merging of single-crystal hexagonal domains, scale bar 400 µm, (c) Irregular shaped graphene domain, with reflex angles representative of polycrystal. Reproduced with permission from Gao et al.[176]

Crucially, Gao *et al.*[176] demonstrated a non-destructive electrolytic 'bubbling transfer' of graphene, claiming the Pt foil can be reused over 1000 times. This significantly reduces the costs associated with using Pt. While minor investigations were reported in this publication on optimising the synthesis conditions to reduce multilayers and increase the domain size, a complete understanding of graphene growth on Pt is still lacking. Further investigations into the APCVD growth of graphene on Pt foils offer a great opportunity for improved production of large-area graphene.

2.4.3.4 Chemical vapour deposition of nitrogen-doped and boron-doped graphene

Nitrogen-doped graphene can be produced by direct production methods or by post-production treatment of the various types of graphene. Nitrogen-doping has been achieved through treatment of graphene by annealing in NH_3[48, 50], exposure to N-containing plasma[87, 89, 177, 178], and low-energy N bombardment[179], but the distribution of the dopants through these post-production treatments is inherently inhomogeneous. Direct production methods have included arc-discharge in nitrogen-containing gas[23, 54] and a solvothermal synthesis[180]- both which are unsuitable for large-area production- as well as growth on metal surfaces by methods including annealing of nitrogen-containing polymers[59], segregation of

dissolved carbon and nitrogen[107], and CVD using a variety of carbon and nitrogen reactants. In the CVD procedure NH_3 gas is commonly added to the reactant gas mixture, either simultaneously with the carbon source at the synthesis temperature[24, 57, 181], or while cooling at low temperatures[88, 182, 183]. Single-source liquid precursors have also been used including acetonitrile[88], pyridine[184, 185], s-triazine[25] and dimethylformamide[186]. However, all these CVD studies are similar in simply reporting the production of N-doped graphene- albeit often through a new method- rather than optimising the doping procedure. Instead, focus to date has generally been on measuring an improved property and application due to nitrogen doping. X-ray photoelectron spectroscopy, high-resolution transmission electron microscopy and scanning tunnelling microscopy studies have investigated the bonding configuration of dopants, for instance, substitutional[86, 183, 187] versus pyridinic[57], but by early 2011 few publications had systematically investigated the effect of synthesis conditions on the concentration of dopants and the growth of the nitrogen-doped graphene domains. Noteworthy studies have claimed that the NH_3:CH_4 flow rate ratio controls dopant concentrations up to 8.9 %[24] and 16 %[57], but in both cases the XPS chemical analysis was not presented. Zhao *et al.*[86] demonstrated growth with increasing NH_3 partial pressure, however Raman spectroscopy peak shifts- representative of dopant concentration[188]- showed a broad distribution and did not consistently increase with increasing NH_3 concentration. In late 2012 Lv *et al.*[183] published a more detailed study on the variation of dopant concentration with the temperature and duration of NH_3 exposure while cooling APCVD graphene. However, the dopant concentration and graphene growth may also be influenced by other synthesis conditions, including the system pressure, growth temperature, and Cu surface[185, 189]. Therefore, detailed and systematic parameter studies are important to determine the influence of individual synthesis conditions so that doping can be controlled and optimised to promote desirable properties.

The production of boron-doped graphene has received significantly less attention than nitrogen-doped graphene. Post-synthesis methods have produced powders of boron-doped graphene through annealing in boron oxide[190], and exposure to a

B-containing plasma[191]. Direct synthesis of powders of boron-doped graphene was demonstrated by arc-discharge in diborane[54], and solvothermal synthesis between tetrachloromethane and boron tribromide[192]. CVD growth of large-area boron-doped graphene on Cu was first demonstrated in 2012 independently by Wu *et al.*[193] and Li *et al.*[194]. By varying the mass of the solid precursors (polystyrene and boric acid), Wu *et al.*[193] controlled the dopant concentration up to 4.3 %[193]. Li *et al.*[194]'s procedure used liquid ethanol and a surface coating of boron powder to achieve doping to 0.5 %. The first CVD synthesis with entirely gaseous precursors was achieved by Cattelan *et al.*[195] using CH_4 and diborane in early 2013. This method has since been reproduced with a thorough STM study by Zhao *et al.*[196] directly visualising individual boron dopants. The field of boron-doped graphene is therefore just developing, demonstrating the necessity for further investigations to control and understand the influence of synthesis conditions on the growth and dopant concentration.

2.4.3.1 Transfer of chemical vapour deposition graphene from metals

Following CVD synthesis a transfer procedure is necessary to separate the graphene from the metal substrate and place it on a target surface. In 2009 Reina *et al.*[139] demonstrated a novel and reproducible process for transferring graphene onto arbitrary surfaces. By coating with a temporary poly(methyl methacrylate) (PMMA) support, chemically dissolving the metal substrate, washing, and placing onto an alternative desirable substrate, CVD graphene can be manipulated, Figure 15.

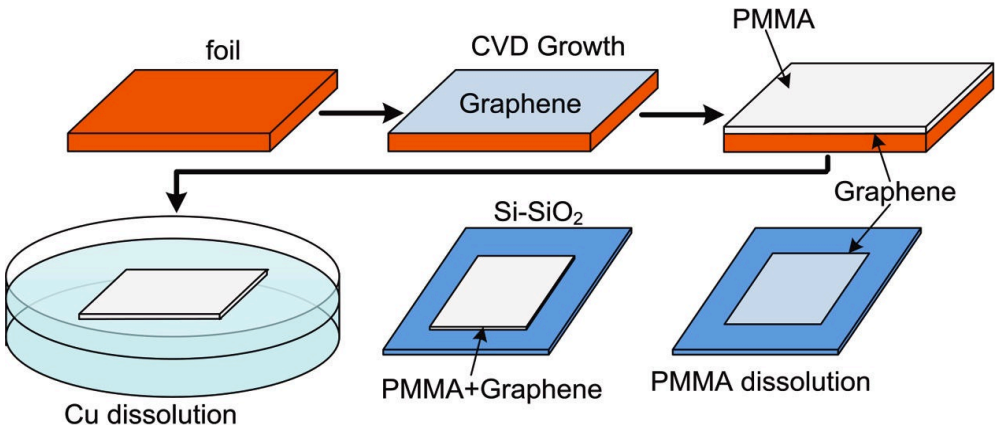


Figure 15: Polymer transfer of CVD graphene

Reproduced and modified with permission from Srivastava et al.[157]

Copyright (2010) American Chemical Society

Polymer residues left on graphene from the transfer procedure are an unresolved problem, with alternative polymers, *e.g.* cellulose acetate butyrate[197], and post-transfer annealing and cleaning somewhat reducing residues compared to the original procedure[77, 146, 161]. A 'bubbling transfer' by electrochemical delamination resolved some of the issues and costs from dissolving the substrate[176, 198].

2.4.4 Influence of the synthesis parameters on chemical vapour deposition growth of graphene

The synthesis conditions have a paramount importance in dictating the CVD growth of graphene. Factors include:

- Gas mixture composition, particularly the carbon-containing reactant,
- Gas concentrations, or flow rate ratios,
- Total gas flow rate,
- System pressure,
- Synthesis temperature,
- Synthesis time,
- Cooling rate, and
- Substrate

Many of these can be considered to vary during the synthesis procedure, Figure 16.

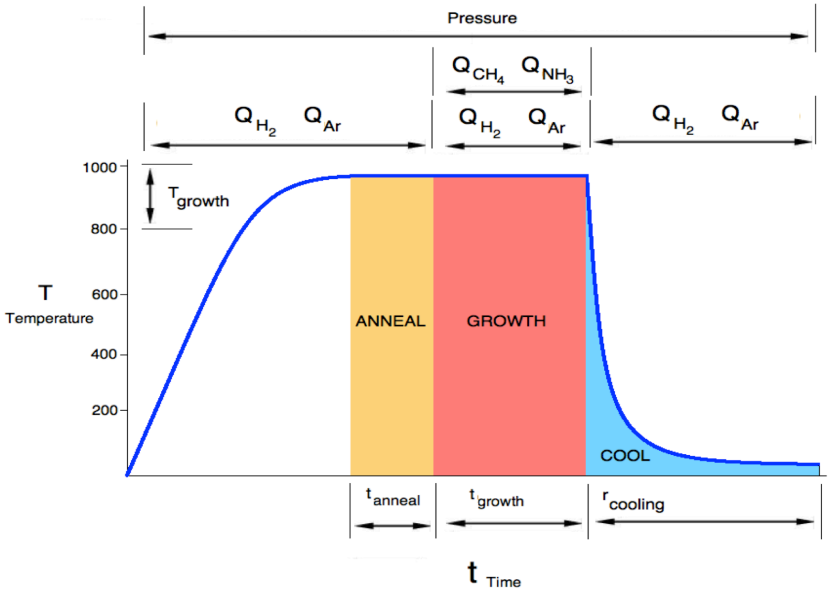


Figure 16: Variation of synthesis parameters during CVD growth

Q=flow rate, T=temperature, t=time, r=rate. Original diagram concept from Li et al.[144]

One strategy for improving the quality of large-area graphene is to reduce the number of domain boundaries by increasing the size of constituent domains and reducing the nucleation density. From 2011 to 2013 studies into the synthesis conditions advanced this aim beyond expectations. Systematic investigations demonstrated that increasing the synthesis temperature and synthesis time, and reducing the CH_4 concentration and synthesis pressure promotes growth of larger LPCVD domains at a lower nucleation density with fewer multilayer regions, Figure 17a-d[167, 168, 189, 199-204]. This increased the domain size from less than 5 microns[144] to tens of micrometers[167]. Using a copper enclosure LPCVD domain sizes were further increased to hundreds of micrometers, Figure 17e[205, 206].

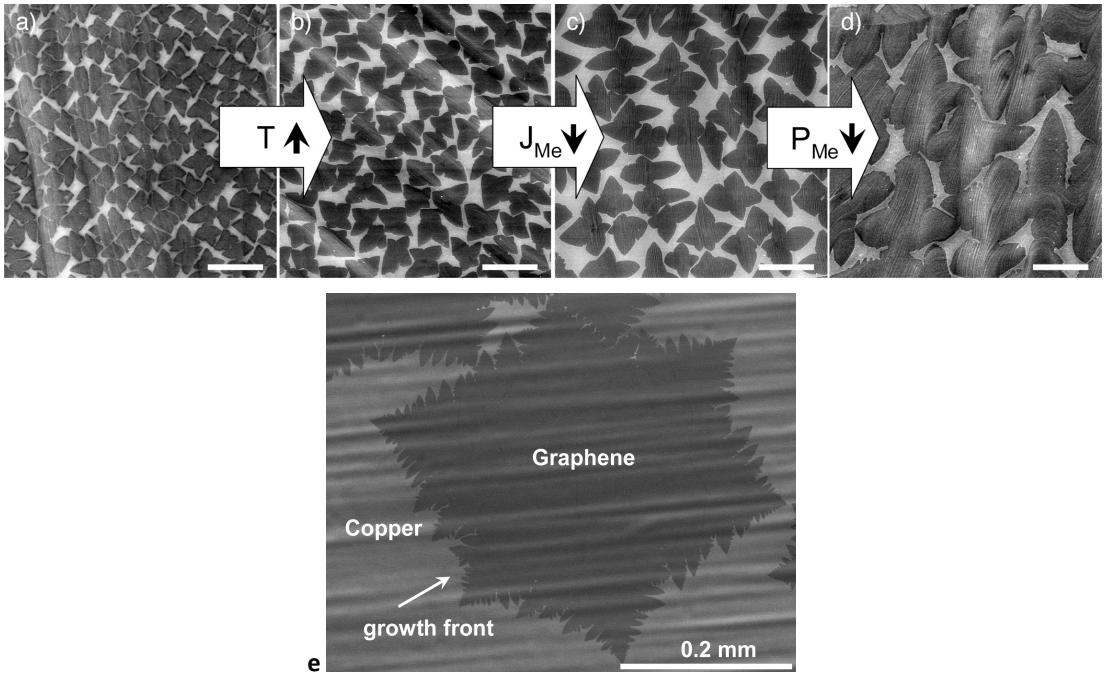


Figure 17: Influence of synthesis conditions on LPCVD growth of isolated graphene domains (a)(b)(c)(d) Varying synthesis temperature (T), CH_4 flow rate (J_{Me}) and CH_4 partial pressure(P_{Me}), respectively, causing a reduction in nucleation density and increase in domain size, scale bars 10 µm, (e) Large-area single-crystal LPCVD graphene domain produced using copper foil enclosures. Reproduced with permission from (a)(b)(c)(d) Li et al.[168], and (e) Li et al.[205].

While LPCVD domains were originally shown to have defined lobes[207] with dendritic shape[205], increasing the H_2 concentration varied the shape[208] and promoted domains with improved hexagonality[209]. Concurrent advances in APCVD growth showed that hexagonal graphene domains form preferentially under common synthesis conditions[210, 211] with the edges displaying zigzag geometry, Figure 18[211, 212].

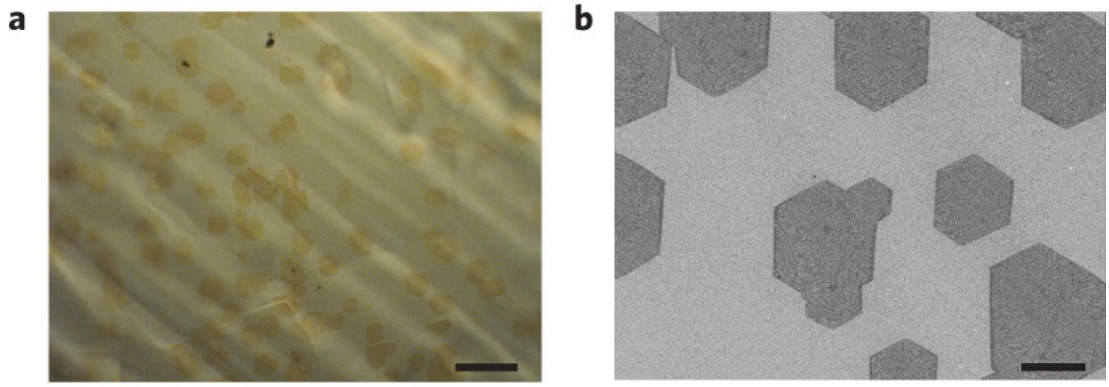


Figure 18: APCVD growth of large-area graphene on Cu foils

(a) Optical microscope image of hexagonal graphene domains on Cu foil, 25 µm scale bar, (b) SEM image of isolated and merged single-crystal hexagonal graphene domains on Cu foil. Reproduced with permission from Yu et al.[211]

Systematic investigations again demonstrated that the synthesis conditions could be optimised to promote larger single-layer domain[203, 204], with the H_2 concentration again found to play a crucial role in reducing multilayers and dictating the APCVD domain shape[199, 213]. APCVD studies at synthesis temperatures above the Cu melting point have shown that uniform hexagonal graphene can grow on liquid Cu, resulting in a significant increase in domain sizes to 50 - 100 µm[214, 215].

2.4.5 Influence of the Cu substrate on chemical vapour deposition growth of graphene

Concurrent to the developments on the influence of synthesis conditions, research also focussed on the importance of the metal substrate for controlling graphene growth. Although the commercially available 99.8 % Alfa Aesar Cu foils were frequently used in an untreated, as-received condition[42, 77, 144, 146, 152, 161, 216-221], graphene was also grown on higher purity foils[189, 207, 220, 222, 223], and thin Cu films made by electron-beam evaporation[119, 150, 155, 224], thermal evaporation[148], and sputtering[151]. However, early studies frequently overlooked any variations in graphene growth and did not draw conclusions about the substrate's importance. In many publications an annealing step was used prior to CVD to increase grain sizes of polycrystalline Cu foil from a few micrometers to ~100 µm[119, 149-151, 153, 154, 157, 158, 160, 162, 163]. This was claimed to produce higher quality graphene[149]. A correlation between annealing time and a reduction in the nucleation density was eventually

shown by Wang *et al.*[219] with the synthesis of sub-millimetre domains following three hours high-temperature annealing. Surface topography and surface roughness were subsequently shown to influence the nucleation density and thickness of graphene, with increased nucleation observed on surface scratches, grain boundaries, and striations from the cold-rolling extrusion during manufacturing[121, 189, 225, 226]. Surface chemical impurities were also shown to act as heteronuclei that increase the density of graphene domains[219, 222, 227]. Chemical treatments, mechanical polishing, and electropolishing have therefore been proposed to reduce these features and particles, with the aim of suppressing nucleation and multilayers. Levendorf *et al.*[143] reported one of the first cleaning procedures aiming to improve the Cu foil prior to graphene growth, using acetic acid to remove copper oxides[148, 228]. Acetic acid treatment has been frequently adopted in subsequent literature[121, 158, 212, 224, 225, 229, 230], but no studies provide evidence showing its benefit for graphene growth. $FeCl_3$ treatment[222], mechanical polishing[226] and electropolishing[222, 225, 231] were also demonstrated to reduce the surface roughness and remove surface contaminants. In late 2012 Vlassiouk *et al.*[222] published one of the most thorough studies into the influence of Cu foils on graphene growth. The roughness and presence of contamination particles were investigated for different Cu foil purities (99.8 % and 99.999 %) from different suppliers (Alfa Aesar and Nimrod Hall) and with different cleaning treatments (HNO_3, $FeCl_4$, electropolishing in H_3PO_4, and acetic acid). The influence of these properties on the subsequent graphene was then investigated. However, while many conclusions were claimed, evidence throughout the publication was limited. Furthermore, while roughness variations were analysed, no chemical analysis was conducted for the different foils with and without treatments. Detailed and systematic studies are therefore an important area for further investigation.

2.4.6 Influence of Cu crystallographic orientations on chemical vapour deposition growth of graphene

Studies have also demonstrated that the Cu crystallographic orientation influences the growth and quality of graphene. Wood *et al.*[232] demonstrated that the Cu crystallographic orientations influence the thickness, growth rate and nucleation

density of graphene domains, showing for their synthesis parameters that single layer graphene forms on Cu(111) with a high growth rate, while multilayer graphene forms on Cu(001) with a slower growth rate. A high nucleation density and growth rate was also observed on high index grains. Growth on Cu(111) has since been recognised for producing high-quality graphene[233, 234]. These studies suggest that the growth mechanism is influenced by the crystallographic orientation, perhaps due to a lower energy barrier for nucleation, increased supersaturation, or reduced Cu evaporation.

The Cu crystallographic orientations may also provide another method to improve the quality of large-area graphene by reducing the defects that form at domain boundaries when adjacent domains merge. Rotation between domains will cause a mismatch between the graphene lattices, causing a line of defects and disorder along the boundary[217, 235, 236]. Low-angle rotation and alignment of domains, through influences of the substrate's crystallographic orientation, will reduce these defects and may result in seamless bonding between the adjacent domains.

Investigations by the surface science community into the orientation of graphene lattices on single crystal metal substrates have been conducted for some years[109, 113, 117, 237]. More recently, low energy electron microscopy (LEEM) and low energy electron diffraction (LEED) were used to investigate the surface crystallography and relative orientation of the graphene lattice on Cu single crystals[227, 238], heteroeptiaxial thin films of Cu on SiO_2/sapphire/MgO[239, 240], and polycrystalline Cu foils[207]. High-resolution STM imaging and analysis of Moire patterns[241-244] also demonstrates the relative alignment of graphene on the Cu substrate. These studies demonstrated that full coverage of graphene can form epitaxially on Cu surfaces as the graphene lattice is in registry with the underlying Cu crystallographic orientation. However, results often vary between publications. In an early study, Gao *et al.*[244] found that graphene formed epitaxially on Cu(111) with at least two predominant orientations of 0˚ and 7˚ between the graphene zigzag edge and the [110] direction on Cu(111). A follow up study by the group on Cu(001) found two orientations of 0˚ and 6˚[216]. Zhao *et al.*[243]'s independent studies confirmed an alignment of 0˚ on Cu(111). They also demonstrated two preferential alignments on Cu(001) of 0˚ and

90˚ with a large spread of +/-7˚, although some graphene was detected with random orientation. However, Rasool *et al.*[242] found a variety of orientations on Cu(001). Subsequent studies by Ogawa *et al.*[239] and Orofeo *et al.*[245] confirmed one orientation of 0˚ on Cu(111), and two orientations of 0˚ and 30˚ on Cu(001) - equivalent to the 90˚ rotation observed by Zhao *et al.*[243].

However, the correlation between these epitaxial studies with the shape, orientation and edge geometry of individual micron-scale graphene domains has not been thoroughly investigated. Wofford *et al*.[207] notably demonstrated with LEEM and LEED that the lobes of LPCVD graphene domains grown on polycrystalline foil with Cu(001) orientation align along the Cu<001>, representing two equivalent graphene orientations. Recently, aligned hexagonal domains were demonstrated using liquid Cu[214, 215] but the orientation relationship between graphene domains and the many different grains that compose a Cu foil (e.g. Cu(001), Cu(111), Cu(101) and high index surface orientations) remains unclear. Indeed, under particular synthesis conditions, researchers have claimed that no epitaxial relationship exists because graphene domains misorient within one Cu grain[209, 210] and show invariant orientation across Cu grain boundaries[208, 209, 211, 212]. However, in some instances- and even within the same publications claiming that no epitaxy exists- aligned domains are observed[211, 231, 246]. These inconsistencies and uncertainty demonstrate the need for greater investigation into the influence of the Cu crystallographic orientations on the growth and orientation of graphene domains. The ability to control the thickness and orientation of individual graphene domains is a key challenge that needs to be addressed for CVD graphene to be used in future applications[27].

2.5 Summary and scope

In summary, graphene shows exceptional properties and a plethora of potential applications. Graphene can be produced by a number of different production methods that dictate its properties and potential uses, with CVD on metals showing promise for the production of large-area single-layer sheets. A variety of synthesis conditions and substrates can be used, including LPCVD and APCVD synthesis; growth with gaseous, liquid and solid carbon precursors; growth on Ni, Cu and Pt commercial foils, thin films and single crystals; and growth with heteroatom doping

precursors. With only a handful of publications before 2011 the importance of synthesis conditions and substrates on the growth and properties of graphene domains was relatively unknown, and therefore further studies were needed to elucidate the influence and importance of these factors. Between 2011 and 2013, concurrent with this research project, the field received a significant amount of interest. Nonetheless, a complete understanding of the influence of the synthesis parameters and experimental setup, and the properties and crystallographic orientation of the metal substrate on CVD growth of pristine and heteroatom-doped graphene is still lacking. With this motivation the aims for the research project outlined in Chapter 3 were developed.

3 Aims of research project

The broad aim of the research project can be defined as:

To investigate the chemical vapour deposition growth of graphene on metals.

This aim can be elaborated as:

To expand the knowledge of low-pressure and atmospheric-pressure chemical vapour deposition growth of pure and hetero-atom doped graphene on metals, notably Cu and Pt foils. To advance the understanding of the influence of the synthesis conditions and the substrate's properties in pursuit of improved, controlled or optimised growth, which can promote high-quality, large-area graphene or other as desired.

In this context '*large-area*' refers to the overall size of graphene films, which is dictated by the size of the metal substrate and, arbitrarily, should be at least 1 cm^2. However, by extension, the size of individual constituent graphene domains should be as large as possible and, arbitrarily, at least 1 μm^2. *'High-quality'* can be interpreted multiple ways. In the ideal case, for which the majority of research strives to obtain, 'high-quality' graphene will be single-layer with a low defect density and properties with little variation from the experimental or theoretical optimum. However, in other applications multilayer graphene, or graphene with modified properties, may be desired. In such cases a 'high-quality' material will have only specific properties optimised when compared to the ideal. Therefore, the aim to control and understand the factors influencing growth is paramount.

With respect to the production of high-quality, large-area, single-layer graphene, a number of specific aims can be identified to be pursued:

- Increase the size of graphene domains,
- Reduce the size and quantity of multilayer regions,
- Reduce the nucleation density of graphene domains,
- Control the location of nucleation sites of graphene domains,

- Control the orientation of graphene domains,
- Promote the growth of graphene domains with a defined shape and edge geometry,
- Improve the homogeneity of graphene domains across the substrate,
- Improve the reproducibility of growth between experiments.

To achieve the overall research goal and promote these specific aims a wide-range of investigations were conducted, systematically varying individual synthesis conditions and substrate properties to determine their respective influence on graphene growth. Factors varied included:

- Low-pressure and atmospheric-pressure conditions,
- Reactant gas flow rate ratios,
- Addition of NH_3 dopant reactant gas,
- Synthesis time,
- Synthesis temperature,
- Cu and Pt foil,
- Side of the substrate,
- Position of substrate within the synthesis apparatus,
- Crystallographic orientation of substrate,
- Topography and surface roughness of substrate,
- Chemical impurities on the surface, and supplier-stated purity of substrate,
- Supplier of substrate,
- Cleaning treatments of substrate.

The influence of these factors on the growth of graphene was investigated through systematic characterisation and analysis, using techniques outlined in Chapter 4, and allowed trends and correlations to be ascertained which are presented in Chapters 5 to 10.

4 Experimental techniques for the characterisation of chemical vapour deposition graphene and metal substrates

4.1 Systematic characterisation of graphene and metal substrates

Systematic characterisation of graphene samples and metal substrates is essential to elucidate their quality and relate this to synthesis conditions. Through systematic characterisation the CVD reaction conditions and metal substrates can be optimised to reproducibly grow high-quality graphene. The primary experimental techniques used for characterising graphene are optical microscopy, Raman spectroscopy, atomic force microscopy, scanning electron microscopy, and transmission electron microscopy[6, 247, 248]. These techniques provide straightforward and definitive confirmation of the nature of a graphene sample. Individually, they can categorically reveal whether a sample is single layer, bilayer, few-layer or graphite. The techniques can also provide an indication of the disorder in a sample, while detecting the presence of domain boundaries, wrinkles, and edge structures, amongst other features. Collectively, the techniques can provide a thorough assessment of a sample's quality from the atomic to macroscopic scale. Many of these characterisation techniques are also appropriate for analysis of the surface morphology and chemical composition of metal substrates, particularly scanning electron microscopy. Additionally, surface specific analysis through optical profilometry, electron backscatter diffraction, X-ray photoelectron spectroscopy and energy-dispersive X-ray spectroscopy provides invaluable details about the surface roughness, crystallographic orientations, grain sizes and chemical composition of the substrate and surface contamination particles. Complementary techniques also can provide further information about the graphene's chemical composition, electrical properties, or mechanical properties, for example, X-ray photoelectron spectroscopy, electron energy loss spectroscopy, and four-point probe electrical measurements.

In this chapter the fundamental principles of characterisation of graphene and metal substrates with different experimental techniques are outlined. Attention is given to the specific properties of the sample that can be determined by using a technique, as well as its limitations. Instrumental details and operating conditions used during the research project are summarised.

4.2 Optical microscopy

Optical microscopy (OM) is a useful technique to characterise graphene and metal substrates. Characterisation of graphene is possible on specifically selected substrates due to interference-like optical contrast[11]. This effect was fortuitously discovered when silicon substrates with a 300 nm SiO_2 surface coating were used by Geim *et al*.[12] in their original publication on the isolation of graphene, Figure 19.

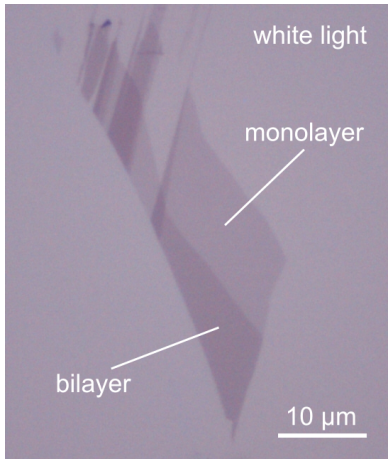


Figure 19: Optical microscopy image of micromechanically exfoliated graphene on 300 nm SiO_2. Reproduced and modified from grapheneindustries.com[93]

The magnitude of contrast interference depends not only on the thickness of the graphene; the thickness and optical properties of the oxide layer, and the wavelength and incidence angle of irradiating light are also influential. 72 nm thick Al_2O_3 on Si has an improved contrast compared to standard SiO_2[249, 250], while blue light can also be used in conjunction with 68 nm Si_3N_4 on Si[251]. CVD graphene synthesised on metal substrates can be transferred onto the desired substrate, using procedures outlined in Chapter 2.4.3.1. Sample thickness can then be identified by contrast variations. By spatially monitoring the contrast intensity of regions with different thickness a sample can be quantitatively analysed to determine the percentage composition of single, bilayer and few-layer graphene[144]. Wrinkles, folds

and tears in the graphene, as well as surface contamination particles can also be identified. However, in this work OM characterisation of graphene on SiO_2 was rarely conducted due to the time required to transfer graphene, and the associated contamination and damage this procedure may cause.

OM can be used to characterise CVD graphene directly on metals, with the caveat that the substrate ideally oxidises in air. Graphene provides some protection to the underlying metal by reducing the oxidation rate and consequently enhances the contrast between bare and covered regions[75]. CVD graphene on Cu or Ni can therefore be imaged by OM, whereas graphene on Au and Pt is not visible. OM provides a quick and effective method of confirming the presence of graphene on the metal surface, however the thickness cannot be accurately determined. Using polarized light microscope improves contrast variations, as was demonstrated by Kertesz *et al.*[4] using samples of LPCVD graphene grown during this research project, as discussed in Chapter 5.

OM is also a quick technique for characterising the surface topography and grain sizes of polycrystalline metallic substrates. Bae *et al.*[160] illustrated its potential by conducting OM before and after annealing procedures and in combination with grain boundary etching by acid treatment.

Of course, the spatial resolution of OM is inherently limited by the wavelength of the irradiating light. The small depth of field of OM can be beneficial to highlight variations in surface topography, but generally this is detrimental and necessitates the grinding and polishing of metal substrates, thereby making unrepresentative surfaces. As such, OM was only infrequently used to visualise the variations of surface topography of the metal substrates prior to more thorough investigation with SEM. During this research project a Reichart Polyvar MET optical microscope was used with 5x - 100x objective lens.

4.3 Optical profilometry

Non-contact optical profilometry characterisation of a metal surface is possible using confocal microscopy. The technique works by permitting only light reflected from the sample at the focal plane to reach a CCD camera at a specific height. A composite stacked image of ~400 individual images is formed by precise vertical displacement of the sample relative to the objective lens, with each image representing a horizontal slice of the topography of the sample[252]. Using optical profilometry true 3D measurement is possible with high Z-resolution, down to ~ 1nm. Surface topography maps and quantative surface roughness values can also be produced. The technique is non-destructive, requires no sample preparation, and rapid, with scans completed in ~1 minute. As such, optical profilometry was used as the primary characterisation technique for analysing the topography and surface roughness of Cu foils. During this research project a Nanofocus µSurf explorer confocal optical profiler was used with a 50x objective lens.

4.4 Raman spectroscopy

4.4.1 Confocal Raman microscopy

As a non-destructive, rapid and facile characterisation technique, confocal Raman microscopy (often called Raman microscopy) reliably indicates the presence and quality of single-layer, bilayer and few-layer graphene or graphite in a sample[253-256]. The technique relies on the Raman effect; the irradiation of a specimen with monochromatic light results in a frequency shift of inelastically scattered light that is representative of the vibrational, rotational and phonon active modes of the specimen's constituent atoms and molecules. The Raman spectrum of micromechanically exfoliated graphene on SiO_2 was described by Ferrari *et al.*[253, 256] and independently validated, Figure 20[254, 255, 257].

Characteristic identification peaks include:

- G band from stretching of sp^2 C-C bonds (~1580 cm^{-1}),
- 2D (or G') band from second-order phonon modes (2640-2720 cm^{-1}), and
- D band, representative of sample disorder due to phonons scattering from defects[258] (1320-1380 cm^{-1}).

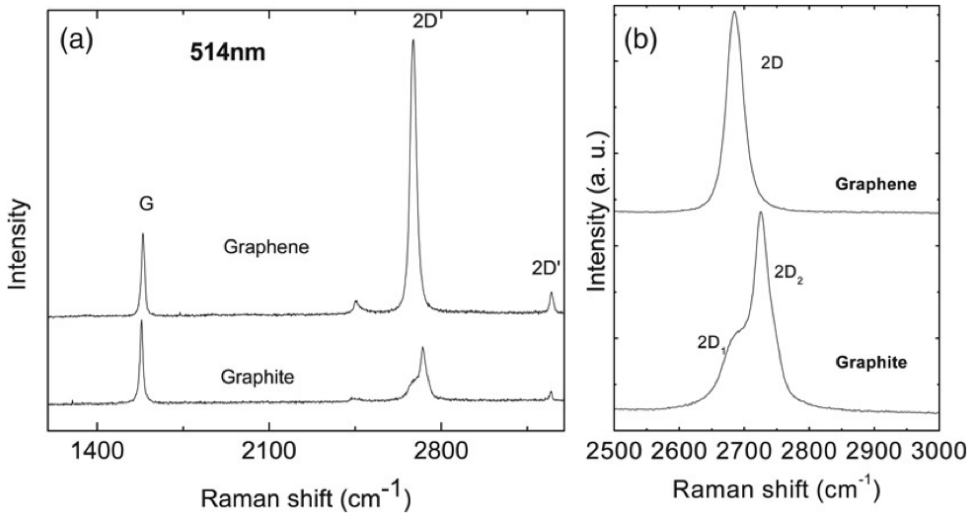


Figure 20: Raman spectrum of graphene and graphite

(a) Full spectrum showing G and 2D peaks, (b) Comparison of shape of 2D peak. Reproduced with permission from Ferrari, 2007[256]

The 2D peak's shape and FWHM provides an indication of the number of graphene layers. Single layer graphene shows a symmetrical Lorentzian shape and small FWHM (~30 cm^{-1}). Up-shifting and broadening occurs for bilayer graphene as the single Lorentzian splits into four components due to electronic band structure splitting for multilayers. By approximately 5 graphene layers the spectrum converges towards, and is essentially indistinguishable from, that of bulk graphite, Figure 21[253, 256, 259].

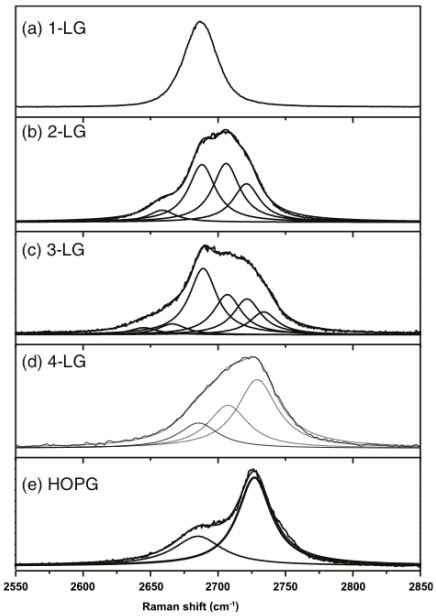


Figure 21: Variation of Raman 2D peak with thickness

Reproduced with permission from Malard et al.[259]

The peak intensity ratio of the 2D and G bands, I_G/I_{2D} (or I_{2D}/I_G), is also indicative of the number of layers for CVD graphene[139], with single-layer, bilayer, and few-layer graphene showing ratios of <0.2, 0.35 and >1.5 respectively (or >2, $1<I_{2D}/I_G<2$, and <1). This ratio therefore provides a quantitative value that experimentalists can use to measure the thickness of graphene samples. The intensity of the D peak increases with defects in the graphene[2] including atomic vacancies[260], Stone-Wales defects, dislocations, heteroatomic dopants[48, 261], and edge states[262]. The D peak intensity can therefore be used to measure and compare the quality of samples.

Changes in the Raman spectrum of graphene are also possible due to variations in the surrounding environment and external stimulus. For example, changes in the substrate[263, 264], atmosphere, temperature[265], as well as the presence of surface particles, metallic contacts, electrical doping[188] or externally induced mechanical strain[266] can cause either electronic doping or strain to the graphene, resulting in frequency shifts or broadening of the Raman peak positions. Changes in the position of the G and 2D peaks can also indicate n-type or p-type doping due to the influence of substitutional nitrogen dopants[86]. In addition, heteroatom-doped samples typically show a strong D peak, and also exhibit an additional peak at 1620 cm^{-1} (known as the D' band) due to the inter-valley and intra-valley double resonance process in graphene[267, 268]. This means that measurements must always be

compared like with like, as CVD graphene transferred onto SiO_2 will have peaks shifted from the position as measured on Cu.

Instrument and operational parameters- such as the laser energy, exposure time, focus, or polarization- will also influence the intensity, position and width of the Raman bands. To ensure systematic characterisation of samples the instrument and operational parameters should be kept constant.

I used a JY Horiba Labram confocal Raman microscope equipped with a 532 nm laser. Unless otherwise stated I used a 50x objective lens, 300 µm slit, 150 µm hole and 1800 l/mm grating. Typical exposure was 50 % power for 10 seconds with three accumulations average. Measurements were obtained in air. Background and peak spikes were removed using Horiba software.

4.4.2 Two-dimensional Raman mapping

Through incrementally scanning a surface and obtaining a Raman spectrum at each location a large-area two-dimensional Raman map of a surface can be produced, Figure 22. Spatial analysis of the thickness and defects in a graphene sample are possible through the use of I_{2D}/I_G and the I_D peak. Comparison of such maps with OM or SEM can localise defects at wrinkles using I_D, and bilayer and trilayer regions with increased contrast using I_{2D}/I_G.

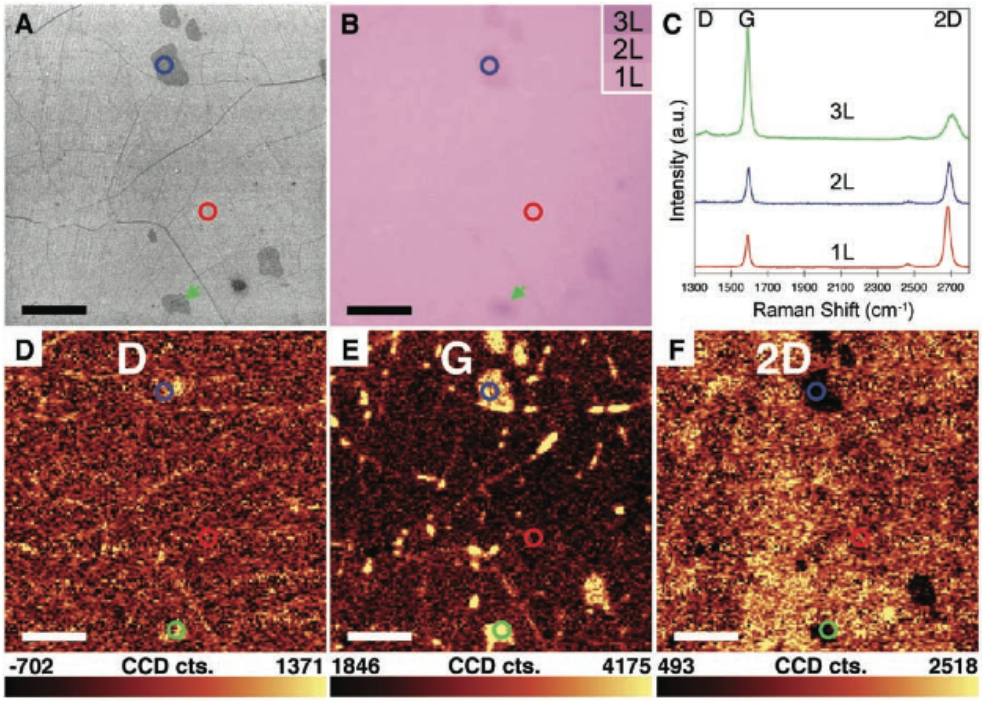


Figure 22: Two-dimensional Raman mapping of LPCVD graphene

(a) SEM image of graphene on SiO_2, (b) OM image of the same region, showing single-layer, bilayer and trilayer regions, (c) Raman spectra from the corresponding coloured circles, (d)(e)(f) Raman maps of the D, G, and 2D bands. Scale bars 5 µm. Reproduced with permission from Li et al.[144]

Recognising the benefit of high-resolution two-dimensional Raman mapping for thorough characterisation of isolated graphene domains, a new collaboration with Renishaw PLC was established during this research project. Two-dimensional Raman mapping was conducted using a Renishaw inVia Raman spectrometer operated in StreamLineHR ultra high-resolution mode with a 532 nm laser, 2400 l/mm grating, 50x and 100x objective lenses.

4.5 Scanning probe microscopy

With exceptional height resolution, lateral resolution and surface specific analysis, scanning probe microscopy (SPM) is a powerful branch of microscopy for characterising graphene and metal substrates. SPM includes the primary characterisation techniques of atomic force microscopy (AFM) and scanning tunnelling microscopy (STM).

4.5.1 Atomic force microscopy

AFM can accurately measure at the edge of a sample the number of graphene layers, the interlayer spacing, and the step height of layers, Figure 23a. AFM can also be used to provide general topographical information about a specimen through large-area scanning, Figure 23b, to observe defects, domain boundaries, wrinkles and folding[160, 269]. Mechanical measurements by nanoindentation can also be performed[38]. AFM is limited by inherently low throughput, taking ~5 - 10 minutes per image depending on scan rate.

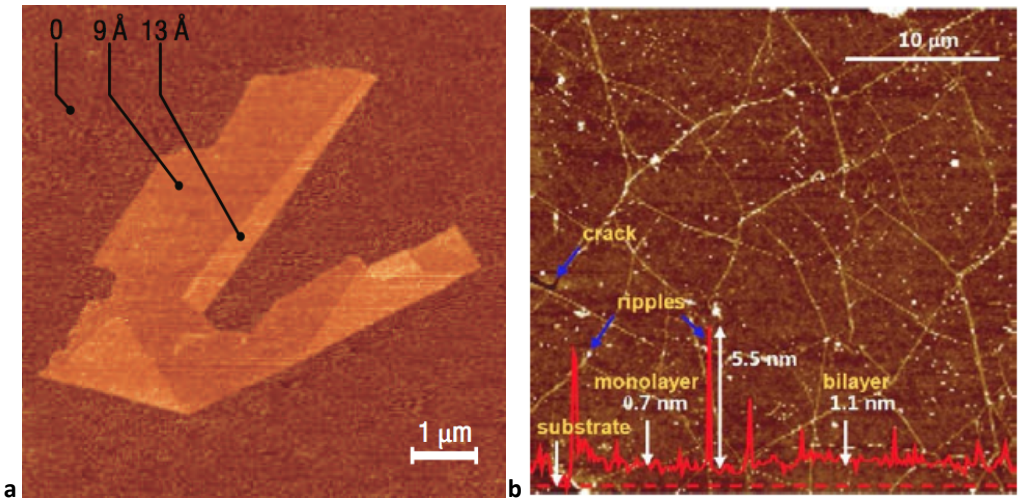


Figure 23: Atomic force microscopy image of graphene

(a) AFM image of single and bilayer exfoliated graphene, (b) AFM image of CVD grown graphene on Cu, indicating cracks and ripples in the graphene film, with a line height profile along the dashed red line. Reproduced with permission from (a) Geim & Novoselov[11], and (b) Bae et al.[160]

AFM can also provide unparalleled characterisation of the metal surface topography. Surface topographies can be mapped for qualitative comparison between samples, while RMS roughness, lattice step heights, and grain boundary density can be used as reliable figures for quantitative measurements. However, the slow speed and relatively small imaging size of AFM outweighs these benefits, meaning AFM is low throughput and often unrepresentative. As a consequence AFM was infrequently used for analysis of the surface topography and roughness of the metal substrates.

4.5.2 Scanning tunnelling microscopy

STM provides improved surface imaging of graphene and metal surfaces compared to AFM owing to image formation by measuring a tunnelling current between the sample and the tip. Low magnification STM imaging has demonstrated the continuity of graphene over Cu lattice steps and terraces[241, 244]. High-resolution STM imaging and analysis of Moire patterns[241-244] also demonstrates the relative alignment of graphene on the Cu substrate.

High-resolution STM can also visualise individual nitrogen dopants[86, 183], which appear as bright spots or triangle patterns, depending on the dopant configuration[47, 56]. The electronic properties of nitrogen-doped graphene can be analysed using scanning tunnelling spectroscopy (STS)[86, 183], which probes the local density of states by measuring the current between the sample and the tip as a function of varying the voltage when held at constant height. Current imaging tunnelling spectroscopy (CITS) measures such an I-V curve at each point of an STM map.

During this research STM/STS/CITS was conducted with a Veeco Nanoscope E in air at 500 pA and 100 mV using Pt90/Ir10 tips. Consecutive scans removed physisorbed contaminations, and images were recorded once consecutive scans stabilised.

4.6 Scanning electron microscopy

Scanning electron microscopy (SEM) is a powerful technique for characterising CVD graphene on metal substrates, Figure 24. Minor contrast variations mean single, bilayer and few-layer regions can be distinguished when graphene completely covers the Cu surface. More significant contrast exists between graphene and the exposed metal surface meaning isolated domains, wrinkles and tears, and surface contamination particles can be visualised. The shape, size, nucleation density and orientation of isolated graphene domains can also be quantitatively analysed using image analysis software. SEM was somewhat under-utilised during the initial years of research into CVD graphene, with only a few examples before September 2010[144, 146, 155, 157].

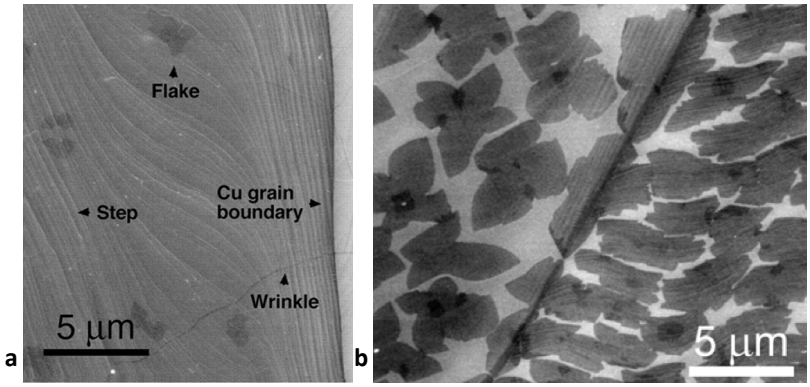


Figure 24: Scanning electron microscopy of graphene

(a) SEM image of full coverage of graphene on Cu, highlighting bilayers, wrinkles, Cu grain boundary and steps, (b) SEM image of isolated LPCVD graphene domains on Cu. Reproduced with permission from Li et al.[144]

SEM is also the primary technique for characterising the surface topography of metal substrates. Grain boundaries, surface defects and contamination particles can be visualised. Although imaging contrast is reduced for high purity samples of a single elements - such as the metal substrates used for graphene synthesis - variation still arises through electron channelling and edge effects. No sample preparation is required for characterisation of CVD graphene and metal substrates via SEM, so a high throughput of specimens can be achieved. Due to the technique's large depth of field and improved resolution compared to OM, SEM is particularly useful for imaging graphene domains on undulating metal substrates, large surface particles, or electronic devices and other fabricated products that use graphene[247].

During this research a JEOL JSM-6500F field emission SEM was used at 5 kV using low to medium current, the smallest aperture, and a short working distance to increase surface sensitivity and spatial resolution. Samples were imaged in secondary electron imaging mode at magnifications of 100x, 250x, 500x, 1000x, 2000x, 5000x and 10,000x. Multiple locations were inspected to ensure images were representative of the sample. A liquid nitrogen cold trap assisted with minimising electron-beam-induced deposition of amorphous carbon, which otherwise built up over scanned regions and hindered observation of graphene. By reducing the exposure time of the electron beam on the surface, and always imaging on an unexposed region, the issue of electron-beam-induced deposition could be reduced.

4.6.1 Electron backscatter diffraction

The microstructure and crystallinity of metal substrates can be investigated by electron backscatter diffraction (EBSD) in an SEM. EBSD patterns, Figure 25a, form due to the diffraction of the electron beam by a crystalline sample to form Kikuchi diffraction. The EBSD pattern is intrinsically related to the sample's crystal structure and its alignment under the electron beam- the crystallographic orientation[270]. Crystal orientation maps (EBSD maps) are formed by rastering the electron beam across a surface and obtaining point-by-point measurements[271]. EBSD maps are colour coded and provide unambiguous quantitative analysis of a polycrystalline substrate's crystallographic orientations, grain size and grain boundaries. The influence of different properties (e.g purity) or treatments (e.g. annealing) on the sample's microstructure can be determined through EBSD. Correlation between EBSD maps and SEM imaging can relate the substrate's properties to variations in graphene growth. By September 2010 no publications were identified using EBSD for analysis of metal substrates for graphene growth. Since then, EBSD was used by Wood *et al.*[232], Orofeo *et al*[245] and others[223] for analysing Cu foils, Figure 25b and c.

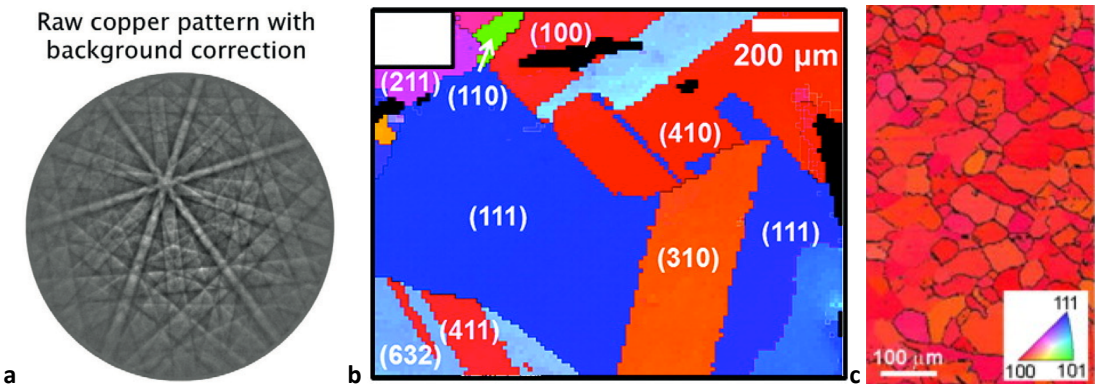


Figure 25: Electron backscatter diffraction from Cu foils

(a) Electron backscatter diffraction pattern from Cu, (b) EBSD map of 99.9 % Cu foil sourced from Basic Copper, (c) EBSD map of 99.8 % Cu foil sourced from Alfa Aesar, inset showing standard EBSD colour key. Reproduced with permission from (a) Wilkinson et al.[271], (b) Wood et al.[232], (c) Orofeo et al.[245]

During this research EBSD was conducted in a JEOL JSM-6500F field emission SEM at 15 kV using an EDAX Digiview II CCD detector. 900 x 900 µm areas were mapped with steps of 1 - 4 µm. Hough-based analysis was conducted using EDAX OIM™ Data Analysis software to index patterns and generate crystal orientation maps.

4.6.2 Energy-dispersive X-ray spectroscopy

The elemental composition of metals can be investigated by energy-dispersive X-ray spectroscopy (EDX) in an SEM. Interaction of the SEM electron beam causes ionisation of the sample's inner shell electron, leaving a void which is subsequently replaced by transition of a higher energy electron. This transition simultaneously emits an x-ray with characteristic energy equal to the difference between the two energy levels, which is intrinsically related to the elements present in the sample. An EDX spectrum provides qualitative analysis of the constituent elements by the energy of characterisation X-ray peaks on the detected spectrum. Quantitative measurements through EDX are possible, though difficult. Semi-quantitative analysis is more common by comparing relative variations between samples.

The purity and elemental composition of metal substrates and surface contamination particles can be determined using EDX. The influence of annealing, chemical treatments, and variations from one purchased substrate to the next can therefore be investigation. The primary benefit of EDX is that it can be conducted simultaneously with SEM imaging on submicron regions of a surface, in comparison to x-ray photoelectron spectroscopy analysis, which is limited to square-centimetre areas, and electron energy loss spectroscopy analysis, which is restricted to nanoscale areas on electron transparent samples in a transmission electron microscope. EDX is limited for detecting low Z elements, and has low surface sensitivity with a spatial resolution or 1 μm^3 due to the excitation volume.

EDX is also possible in a TEM, and can be useful to determine the elemental composition of contamination particles on transferred graphene[272].

During this research an EDX X-ray detector was used in the JEOL JSM-6500F SEM operated at 15 kV accelerating voltage. EDAX Genesis software was used for characteristic peak identification and elemental assignment.

4.7 Transmission electron microscopy

Transmission electron microscopy (TEM) is a powerful technique for characterising graphene, with imaging capabilities from the micrometer scale through to atomic resolution. TEM provides the opportunity for thickness determination, orientation and single crystallinity analysis, and visualisation of defects, bonding and edge geometries. Bright field imaging, selected area electron diffraction, dark-field imaging, and high-resolution TEM each provide complimentary analysis.

Single, bilayer, and few-layer graphene regions can be identified in bright-field TEM due to contrast variations across a sample, Figure 26.

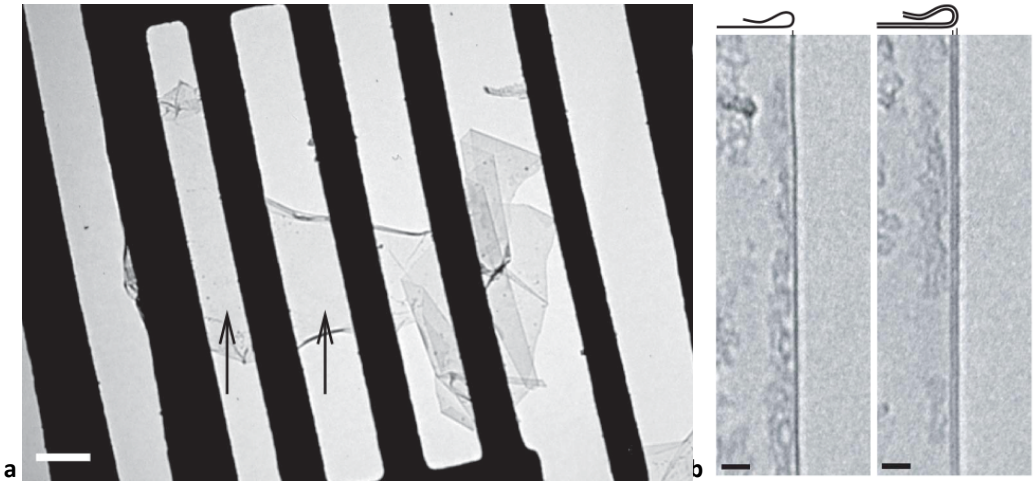


Figure 26: Bright-field TEM imaging of graphene

(a) Low magnification bright-field TEM image of suspended graphene, with arrows indicating homogenous and featureless region, scale bar: 500 nm, (b) TEM image of folded edge contrast for single and bilayer graphene. Reproduced with permission from Meyer et al.[273]

However, in general graphene flakes appear predominately homogenous and featureless in the TEM[273]. Imaging contrast is strongly dependent on focus conditions and the presence of folds, wrinkles, edges, domain boundaries and surface impurities. Contrast fringes at the edges of suspended flakes vary with the number of graphene layers, Figure 26b. Single-layer graphene appears as a single dark edge, bilayer graphene shows two parallel fringes, and this trend continues with additional layers. However, using this method alone to determine the thickness is not recommended, as incorrect classification is possible due to misleading features.

4.7.1 Selected area electron diffraction

Selected area electron diffraction (SAED) allows analysis of electron diffraction patterns from a specific area of a crystalline sample by inserting an aperture at the image plane of the objective lens. SAED of single-layer and bilayer graphene produces a characteristic hexagonal electron diffraction pattern, Figure 27. Single and bilayer graphene can be unambiguously distinguished using SAED by rotating the specimen and observing variations in the relative intensity of spots in the electron diffraction patterns[273, 274].

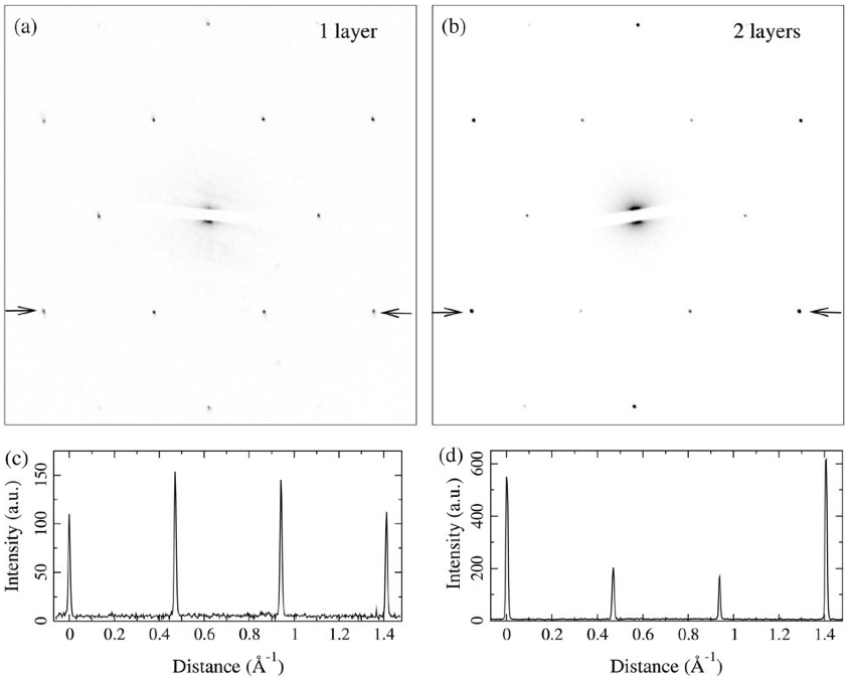


Figure 27: Selected area electron diffraction of graphene

(a) SAED of single-layer graphene. (b) SAED pattern of bilayer graphene, (c)(d) Intensity profiles between arrows in (a) and (b), indicating respective profiles of single-layer and bilayer graphene. Reproduced with permission from Meyer et al.[274]

The orientation of the SAED pattern is dictated by the graphene lattice, and will rotate between misorientated domains within a polycrystalline sample. Large-area crystallinity of graphene domains can therefore be investigated by SAED, with invariant orientation indicating a single-crystal domain[214, 215, 219, 275]. If multiple orientations of graphene are present within the area of the selected area aperture, through turbostratic stacking or overlapping domain boundaries, then extra sets of hexagonal diffraction spots will appear in the SAED pattern.

4.7.2 Dark field TEM

Dark field TEM (DFTEM) imaging produces images from the diffracted electrons by insertion of an objective aperture at the back focal plane so that the image originates from a specific diffraction spot. DFTEM can be used to characterise individual polycrystalline graphene domains and large areas composed of merged domains by selecting each constituent diffraction spot in turn and imaging the corresponding region at a specific lattice orientation[217, 218, 276]. Maps of complex graphene domain structure are formed by overlaying colour-coded images from repeated DFTEM imaging, Figure 28.

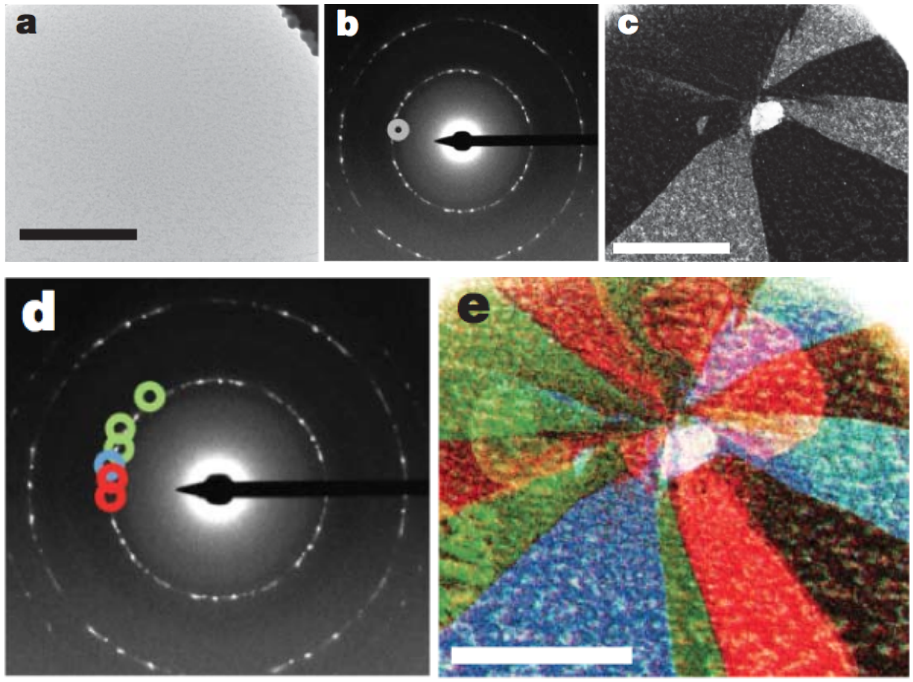


Figure 28: DFTEM imaging of graphene

(a) Bright-field TEM image of graphene domain, (b) Associated diffraction pattern demonstrating polycrystallinity, (c) DFTEM image corresponding to filtered diffraction spot selected by aperture, (d) Filtering of different diffraction spots by moving aperture, (e) Colour-coded DFTEM image depicting shapes and orientations of polycrystalline domain. Reproduced with permission from Huang et al.[217]

4.7.3 High-resolution transmission electron microscopy

High-resolution TEM (HRTEM) offers characterisation of graphene at the atomic-scale by imaging with low accelerating voltages (e.g 80 kV), to reduce knock-on damage, and with spherical and chromatic aberration correction, to maximise resolution[273, 274, 277-279]. HRTEM imaging needs careful interpretation as it

relies on phase-contrast imaging, compared to standard bright-field TEM imaging, which uses intensity variations. HRTEM imaging of graphene can visualise individual atoms, and bonding can be inferred, allowing investigations of thickness variations, stacking configurations, zigzag and armchair edge configurations, domain boundary bonding, defects and vacancies, heteroatom dopants, adatoms and adsorbed species, Figure 29[8, 76, 187, 218, 278, 280-285]. When complemented with investigations into the electrical conductivity or mechanical strength, HRTEM analysis can correlate graphene's atomic structure with its properties.

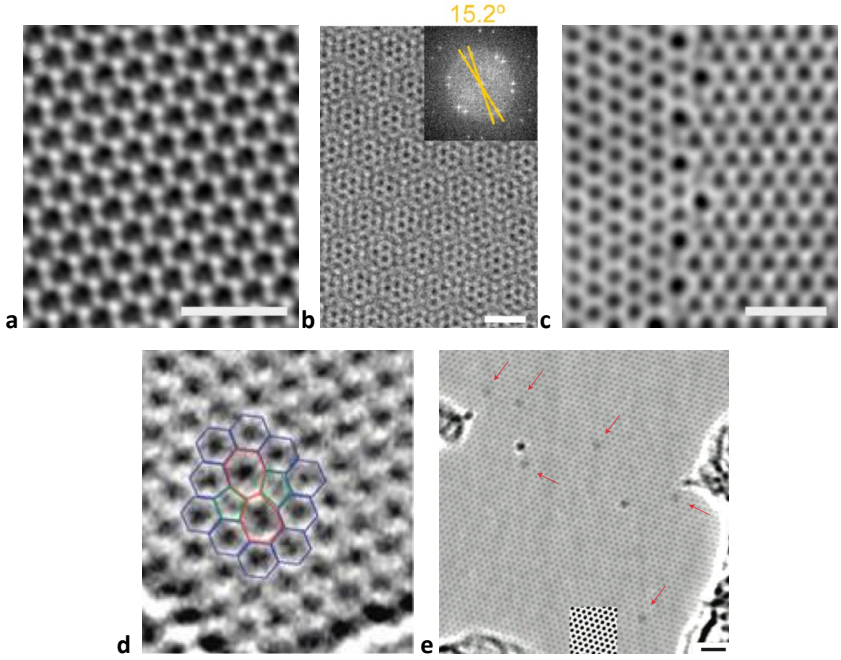


Figure 29: High-resolution TEM imaging of graphene

(a) single-layer graphene, (b) turbostratic bilayer graphene, (c) domain boundary bonding, (d) Stone Wales rotation defection, (e) individual dopants in nitrogen-doped graphene (highlighted by red arrows). Scale bars (a) 0.8 nm, (b) 1 nm, (c) 0.8 nn (d) 0.2 nm, (e) 1 nm. Reproduced with permission from (a) Rasool et al.[284], (b) Lu et al.[283], (c) Rasool et al.[284] (d) Meyer et al.[278], (e) Meyer et al.[187]

4.7.4 TEM instrumental details and operating conditions

TEM is inherently a low-throughput characterisation technique. CVD graphene also requires transfer from the metal substrate to a TEM grid prior to analysis. Subsequently, TEM shows limited utility for characterisation at low magnification and with large quantities of samples. Scale and representability of atomic-scale analysis should also be considered, particularly if quantitative information about the bulk sample is required. For instance, while the bonding of heteroatom dopants can

be investigated by HRTEM, the concentration of dopants in a large-area sample cannot be reliably measured. The representability of such observations for the bulk sample is then debatable.

Despite this, the information gained from bright-field TEM, SAED, DFTEM and HRTEM analysis of a sample means that TEM is vital for comprehensive characterisation of a graphene.

During this research a range of TEMs were used. A JEOL 2000FX operated at 200 kV provided general low magnification imaging and analysis of SAED patterns over large areas. A JEOL 2010 operated at 200 kV provided improved resolution. High-resolution imaging was conducted with an aberration-corrected JEOL 2200 MCO operated at 80 kV, and a Titan G2 60-300 operated at 80 kV.

4.8 Scanning transmission electron microscopy

Scanning transmission electron microscopy (STEM) differs from conventional TEM by using a focussed electron beam that is rastered over the sample. This fine probe means some of the highest resolution atomic structure images have been obtained by aberration-correction STEM[286]. STEM is commonly operated in annular dark-field imaging mode (ADF-STEM) in which scattered and diffracted electrons are collected by an annular detector surrounding the primary beam between specific radii. The detector measures the total electron intensity from a particular point of the sample, with scattering proportional to thickness and atomic number squared (Z^2). ADF-STEM therefore produces Z-contrast images, particularly when imaging atomically thin specimens, with heavier elements appearing brighter due to greater scattering. High-angle annular dark-field STEM (HAADF-STEM) uses a large radius detector so scattered electrons are primarily detected rather than diffracted electrons. One further advantage of STEM over TEM is that multiple detectors can be operated simultaneously, for instance, bright-field and ADF. Chemical analysis can also be conducted simultaneously with ADF-STEM imaging by directing the transmitted electron beam to EDX or EELS detectors (discussed in Chapter 4.9)[287]. Atomic-resolution ADF-STEM imaging by Huang *et al.*[217] provided the first images of the bonding of graphene domain boundaries, Figure 30.

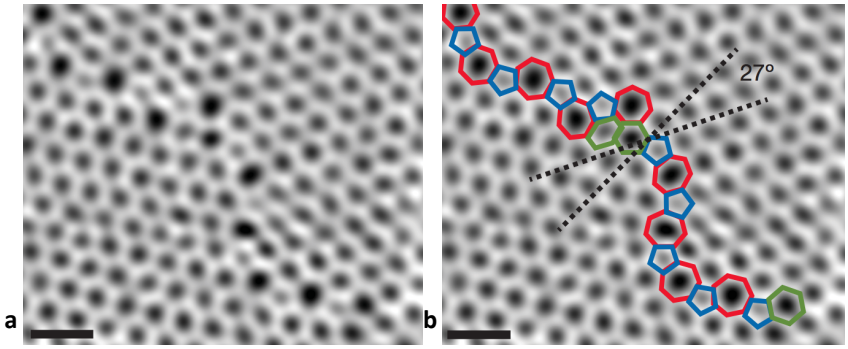


Figure 30: STEM imaging of graphene

(a) Atomic-resolution of graphene domain boundary by aberration-corrected ADF-STEM, (b) Bonding configuration at domain boundary colour-coded for pentagons (blue), heptagons (red) and distorted hexagons (green). Scale bars in (a)(b) 5Å. Reproduced with permission from Huang et al.[217]

Z-contrast in ADF-STEM makes it an unparalleled technique for characterising heteroatom dopants, adatoms and adsorbents in graphene. Individual low Z atoms- including boron, carbon, nitrogen and oxygen- were imaged and identified by Krivanek *et al.*[288] using intensity variations of aberration-corrected STEM images, Figure 31. Silicon dopants in graphene have also been imaged by HAADF-STEM with simultaneous spectroscopic confirmation and bonding analysis via EELS[289, 290].

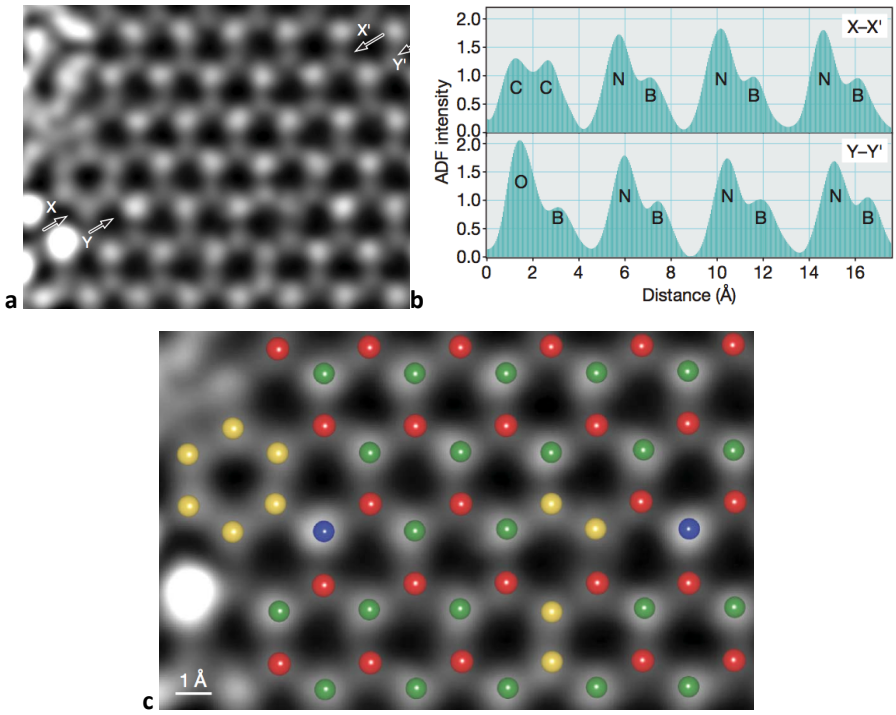


Figure 31: ADF-STEM imaging of low Z atoms

(a) ADF-STEM image of monolayer BN, (b) Line profiles showing image intensity between X-X' and Y-Y' in part (a), and identified chemical elements, (c) Colour-coded atomic structure based on intensity analysis, red:B; green: N; yellow: C; blue: O. Reproduced with permission from Krivanek et al.[288]

During this research STEM analysis was conducted at SuperSTEM, the EPSRC UK National Facility for aberration-corrected STEM using an aberration-corrected Nion UltraSTEM 100, operated at 60 kV to prevent knock-on damage. A medium-angle annular dark field (MAADF) detector, with inner and outer detector angles of 41.1 and 195 mrad, was used for imaging. The UltraSTEM was equipped with a cold field emission electron source, a corrector capable of neutralizing up to fifth order aberrations, and an EnFina EEL spectrometer.

4.9 Electron energy loss spectroscopy

Electron energy-loss spectroscopy (EELS) is an analysis technique for determining structural and chemical information by measuring the change in kinetic energy of an approximately monoenergetic electron beam after transmission through a specimen and inelastic scattering with the atomic electrons. The incident electrons lose a characteristic amount of energy representative of specific properties and electronic transitions of the atoms of the sample, including inner-shell ionization, phonon and plasmon excitations, inter and intra band transitions[291, 292]. Electron energy-loss spectra therefore reveal information about the atomic composition, coordination, chemical bonding, and electronic properties of the valence and conduction bands (including band-gap measurement and density of states). Key features of the EELS spectra are ionization edges from inelastic scattering causing excitation of inner-shell electrons e.g. K, L, M and N edges. The sharp edge ionization threshold represents the binding energy of the corresponding atomic shell for the specific element, e.g. C-K edge is ~284-290 eV. Fine structure over the ionization edges, including energy-loss near edge structure (ELNES) and extended energy-loss fine structure (EXELFS), are influenced by the electronic structure and chemical bonding of the atom. EELS can be used as a fingerprint identifier by direct comparison of experimentally recorded spectra with that of known standards or simulated spectra. Qualitative elemental composition of specimens can by determined by the identification of ionization edges in the EELS spectrum. Two-dimensional elemental mapping with high spatial resolution is possible by combining this edge identification with TEM or STEM. Such analysis has demonstrated inhomogenous distribution of heteroatom dopants in multiwalled carbon nanotubes[293]. As mentioned in Chapter 4.9, EELS was

used for simultaneous spectroscopy confirmation and analysis of substitutional Si atoms in graphene imaged by HAADF-STEM[289, 290].

During this research EELS analysis was conducted at the SuperSTEM facility using an EnFina EEL spectrometer with an aberration-correction Nion UltraSTEM 100, operated at 60 kV.

4.10 X-ray photoelectron spectroscopy

X-ray photoelectron spectroscopy (XPS) provides surface-sensitive elemental composition analysis by measuring the quantity and energy of photoelectrons emitted from a sample after monochromatic X-ray irradiation. Chemical bonding and elemental electronic states can also be determined. Peaks at characteristic energies in the XPS energy spectrum correspond to specific elements and their electron configurations. Quantitative percentage composition is calculated using peak areas, with all elements of Z > 3 detectable and ~0.1 atomic % detection limit.

XPS is inherently a surface-sensitive technique as photoelectrons emit from atoms within the top 10 nm, corresponding to the upper two to eight monolayers of the sample. XPS can provide powerful analysis of the specific catalytic environment of the metal substrate used for CVD growth of graphene, including the chemical reactivity of surface impurities. This makes XPS advantageous when compared to other elemental characterisation techniques such as EDX. The influence of annealing and cleaning treatments of metals can also be analysed by XPS. A more representative measurement of the elemental composition of the sample surface is possible by using ion bombardment and milling of the upper surface of a sample. The concentration of impurities can also be measured and depth profiled.

XPS can also be used for analysing graphene. In-situ graphene growth and XPS analysis is a powerful method to investigate the reaction mechanisms that dictate graphene growth[294]. Studies have also been conducted simultaneously with STM studies of graphene growth[117]. XPS can measure dopant concentrations and electronic states of heteroatom-doped graphene[50, 55, 87, 295].

During this research XPS analysis of Cu foils was conducted in an ion pumped VG Microtech CLAM 4 MCD analyser system using 200 Watt unmonochromated Mg Kα

X-ray radiation of 1253.6 eV. XPS analysis of dopant concentrations in nitrogen-doped graphene was conducted using a Kratos AXIS Ultra DLD with monochromated Al Kα excitation. Samples were exposed to air on removal from the CVD apparatus, stored under Ar atmosphere, and exposed to air a second time prior to insertion into the XPS chamber. Peak fitting and quantification was conducted using software, and is by a weighted average of composition of the surface layer, with the outer surface making the largest contribution.

4.11 Secondary ion mass spectrometry

Secondary ion mass spectrometry (SIMS) provides highly sensitive, surface-specific analysis of chemical composition by using a rastered focussed ion beam to sputter the sample surface[296]. Ejected secondary ions are separated by a mass spectrometer by their mass-to-charge ratio. SIMS analyses the outermost ~2nm of the surface, is capable of depth profiling, and can detect elemental compositions to parts per billion. SIMS is also capable of two-dimensional mapping to demonstrate the spatial distribution of elemental signal intensities on a surface. With improved detection limits, SIMS analysis is complimentary to XPS. However, SIMS is a qualitative analysis technique due to variations in ionisation and detection efficiency between elements. SIMS yields vary by several orders of magnitude for different elements. Alkali and alkaline earth metals have high yields, while noble metals have very low yields. Metals in the elemental state have much greater yield compared to metal oxides. Nonetheless, a basic, relative measure of the elemental concentration between two samples is possible by comparing one element's characteristic signal intensity with the intensity from the implanted primary ions.

During this research SIMS was performed using a gallium microprobe system MM1212 with quadrupole mass spectrometer.

4.12 Electrical characterisation

Electrical characterisation of graphene is possible by a variety of techniques, including lithography-based fabrication of graphene FETs, and in-situ TEM electrical measurements using a nanofactory^{TM} holder[144, 150, 157]. Sheet resistivity can be measured by bench top four-point probe devices[162, 163], however fabrication of

graphene Hall bar devices is still preferential[69, 152, 160]. Angle-resolved photoemission spectroscopy (ARPES) examines graphene's electronic structure to calculate energy band diagrams by analysing the kinetic energy and angular distribution of photoelectrons after exposure to high-energy radiation[6, 297]. ARPES finds particular use in determining the electronic band gap of heteroatom-doped graphene[298].

Ideally, every graphene sample produced would receive some form of electrical characterisation. In practice, this is far from possible. Indeed, due to the time and expertise associated with performing such measurements, electrical characterisation was not a significant part of this research project.

5 Low-pressure chemical vapour deposition of graphene on copper foils

This chapter outlines investigations into LPCVD growth of graphene on Cu foils. Work progresses from the initial development of the LPCVD synthesis apparatus and concludes with investigations on the influence of synthesis parameters. These investigations provided the groundwork for all the future research that I conducted, ranging from the investigations into the influence of Cu crystallographic orientations on graphene growth that is presented in Chapter 7, through to the heteroatomic doping of graphene presented in Chapter 10. Furthermore, this work led to the establishment of graphene research within Professor Nicole Grobert's Nanomaterials by Design research group where many DPhil and part II students are currently continuing this research. Sections of the work in this chapter were completed in collaboration with a number of researchers; Dr Antal Koos (Department of Materials, University of Oxford) and I jointly designed and constructed the LPCVD apparatus, and conducted experiments into the influence of synthesis parameters on the growth of LPCVD graphene, and Dr Shayan Meysami (Department of Materials, University of Oxford) provided assistance with mass spectrometry during leak testing.

Parts of this chapter have been published in:

Kertesz, K., Koos, A.A., Murdock, A.T., Vertesy, Z., Nemes-Incze, P., Szabo, P.J., Horvath, Z.E., Tapszto, L., Hwang, C., Grobert, N., Biro, L.P., Polarized light microscopy of chemical-vapor-deposition-grown graphene, *Applied Physics Letters*, 2012, 100, 213103[4]

5.1 Design, construction and safety testing of LPCVD apparatus

Rather than purchase an expensive commercial LPCVD apparatus[120], I designed, constructed and safety tested a custom-made hot-walled LPCVD reaction system.

Li *et al.*[144]'s reaction conditions outlined the key requirements of the system:

- Supply of reactant and purging gases with laminar flow, including CH_4, H_2, Ar,
- Control and measurement of gas flow rates from 1 - 1000 sccm,
- Control and measurement of temperature from 800 - 1100 ˚C,
- Control and measurement of pressure from 0.1 - 10 Torr.

Additional desirable capabilities that I identified included:

- Ability to maintain a stable base pressure, indicative of minimal atmospheric leaks and a safe, oxygen-free reaction chamber,
- Ability to remove, clean, and replace the reaction chamber, repeatedly, without damage to system,
- Ability to quickly heat and cool substrates,
- Accommodating of substrates up to 1 square inch,
- Large zone of reaction chamber with uniform temperature (>10 cm with <± 5˚C variation),
- Free of contaminations, which may influence the production of graphene.

In total, four different systems were in turn designed and produced to eventually fulfil these requirements. Each of the four designs is discussed, as the evolution of the system from the initial first prototype to the final system was only possible through the testing and improvements that occurred with each upgraded system. I conducted leak testing of the systems to investigate whether (i) they were safe to be used for experiments, and (ii) they provided an environment with insignificant oxygen concentration suitable for the reaction. Leaks were investigated by (i) flowing Ar or He gas (for improved sensitivity) over connections and measuring changes in gas composition at the rotary-vane pump exhaust by mass spectrometer, (ii) measuring an increase in static pressure over isolated components of the system when removing the rotary-vane pump.

5.1.1 First prototype LPCVD apparatus

The first prototype LPCVD system, Figure 32, used components adapted from a standard atmospheric-pressure MWCNT CVD reaction system: a 58 cm long hot-walled Elite cylindrical tube furnace with large uniform temperature zone, a 1 inch diameter cylindrical quartz tube that could be freely moved within the cylindrical tube furnace for quick heating and cooling and removed for cleaning, and a gas manifold capable of providing CH_4, H_2 and Ar with 1 - 1000 sccm flow rate.

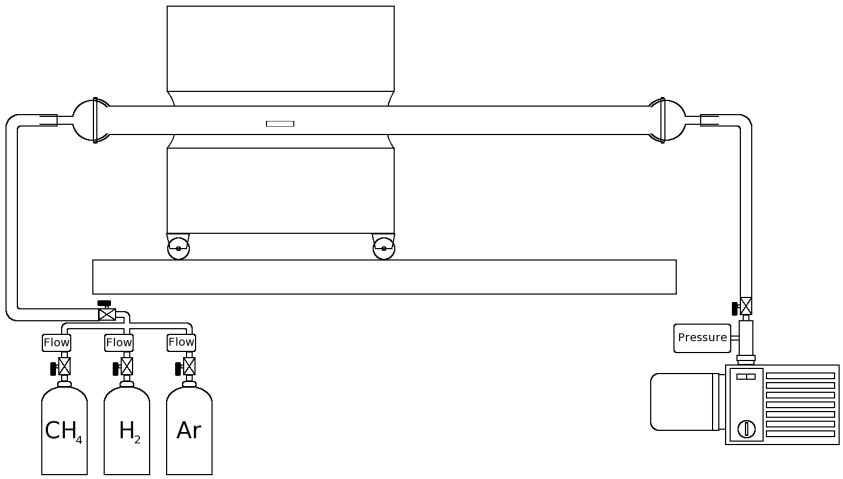


Figure 32: First prototype of LPCVD apparatus
with ball-and-socket joints and Edwards RV12 rotary-vane pump

I modified this system to permit low-pressure conditions: an Edwards RV12 rotary-vane pump, capable of an ultimate pressure of 0.0015 Torr (a medium vaccum), was connected with PVC tubing downstream of the furnace; a pressure gauge was added; custom-made ball-and-socket joints replaced fragile conical joints to connect the quartz tube; and vacuum grease and clamps were used to seal joints.

This system failed leak testing at the ball-and-socket joints, and at the connection between PVC tubing and the rotary-vane pump inlet; an increase in Ar signal intensity was detected using mass spectrometry, from a background value of 8.0×10^{-9} to 8.5×10^{-8}, when Ar gas was flowed over the ball-and-socket joints.

5.1.2 Second prototype LPCVD apparatus and investigations into contaminants within system

The second prototype LPCVD system, Figure 33, used Swagelok ultra-Torr vacuum fittings for improved connection between the cylindrical quartz tube and gas line. I selected these fittings as they provide repeatable low-pressure sealing with a temperature rating up to 204 ˚C. Nylon tubing and ferrule-sealed stainless steel Swagelok connections were used for gas lines between the gas manifold, the quartz tube and the rotary-vane pump.

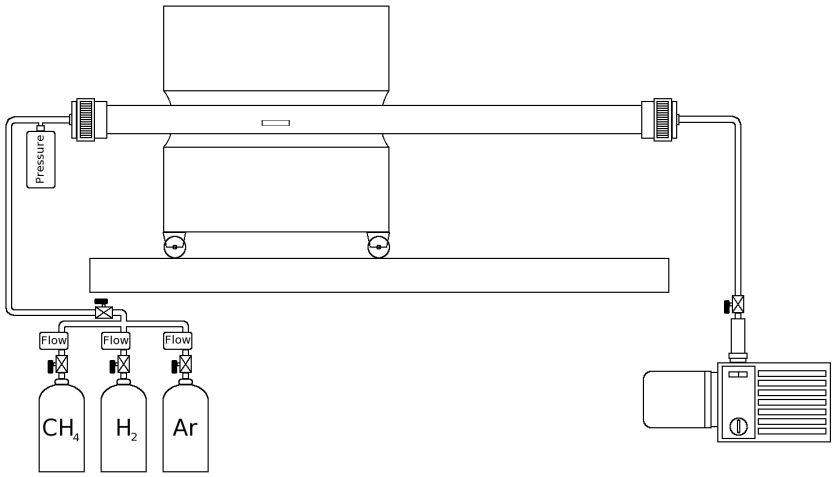


Figure 33: Second prototype of LPCVD apparatus with Swagelok ultra-Torr vacuum fittings and nylon tubing

Leak testing with Ar gas demonstrated that cleanliness and adequate compression were vital for sealing of the Swagelok ultra-Torr fittings, while leak testing with static pressure identified leaks at over-tightened Swagelok connections. The system also failed leak testing due to fracturing of the cylindrical quartz tube, which was resolved by shaping edges to a bevel, flame sealing and polishing.

Once these faulty components were replaced this system passed leak testing with He gas at all connection points. I concluded that modifications to the system effectively removed atmospheric leaks, and that the system was safe, with an environment suitable for experiments with insignificant O_2 concentration.

Using this system I investigated contaminations within the reaction system by annealing Cu foils. Parallel processing lines and contamination particles were visible on the surface of the as-received Cu foil prior to annealing, Figure 34.

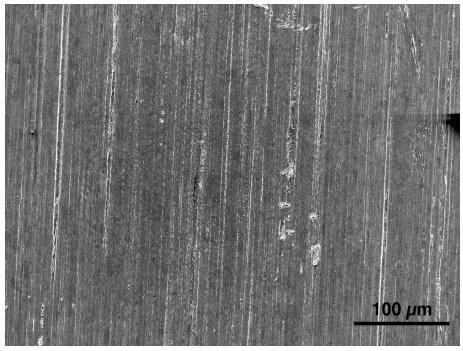


Figure 34: As-received 99.8% Alfa Aesar Cu foil

Modifying Li *et al.*[144] and Bae *et al.*[68]'s procedures, I annealed a sample of Cu foil (15 x 25 mm, 99.8 % Alfa Aesar) in a reducing atmosphere of 2 sccm H_2 (P=0.096 Torr) for 60 minutes at 1035 ˚C. The sample was placed in direct contact with the quartz tube and heated by quickly shifting into the centre of the hot cylindrical tube furnace (29 cm from the furnace edge) by moving the quartz tube or the furnace itself. The terms of "annealing time" and "synthesis time" therefore refer to the time between shifting the foil into and out of the furnace, or the time between changing gas flow rates using the flow meter controller. The foil dimensions, its location in the furnace, and the quick shifting procedure were used for all annealing and CVD experiments in this thesis unless otherwise stated. The surface appears smoother with visible grains, Figure 35a, however, white spherical particles and a high density of black speckling also formed after annealing, Figure 35b. I address the nature of the white particles in Chapter 5.2 and Chapter 8.

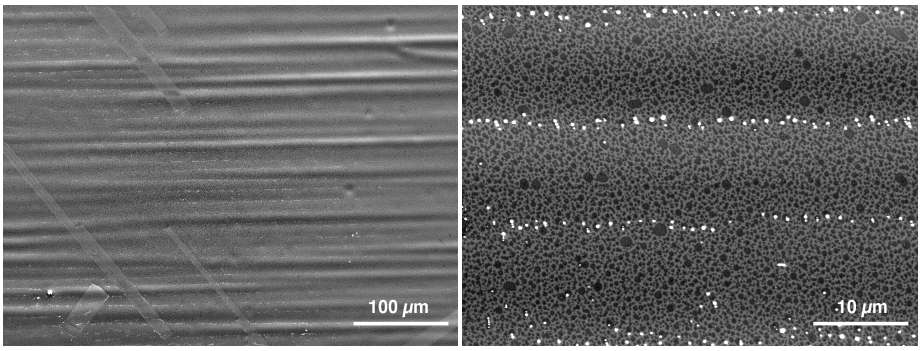


Figure 35: 99.8% Alfa Aesar Cu foil annealed in second prototype LPCVD system with 2 sccm H_2, 0.096 Torr, for 60 minutes

The presence of a broad D peak (~1350 cm^{-1}) and broad G peak (~1600 cm^{-1}) detected by Raman spectroscopy, Figure 36, suggested that the black speckling on the Cu foil's surface was an amorphous carbon contamination.

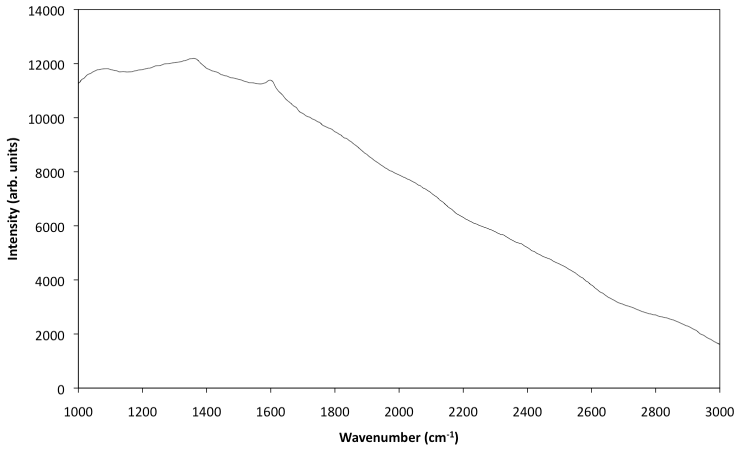


Figure 36: Raman spectrum of 99.8% Alfar Aesar Cu foil annealed in second prototype LPCVD system with 2 sccm H_2, 0.096 Torr, for 60 minutes

I proposed a number of possible sources to explain the origin of this carbon contamination, including:

- Carbon-containing surface adsorbates on the nylon gas lines,
- Carbon contaminants of low concentration within the H_2 gas supply,
- Carbon-containing residues on the quartz tube from previous experiments,
- Back-flow of oil mist from the rotary-vane vacuum pump.
- Carbon contaminants adsorbed on the surface, or dissolved within, the Cu foil,
- A combination of the above.

I investigated the origin of the carbon contamination by systematically removing these possible sources from the system. I determined that the source of carbon was from either (i) back-flow of oil mist from the rotary-vane vacuum pump, and/or (ii) carbon contaminants from the Cu foil because a carbon contamination was still detected on annealed Cu foil when the gas manifold and nylon tubing were removed from the system, and residues on the quartz tubes were excluded as a source by using a cleaned new quartz tube, Figure 37.

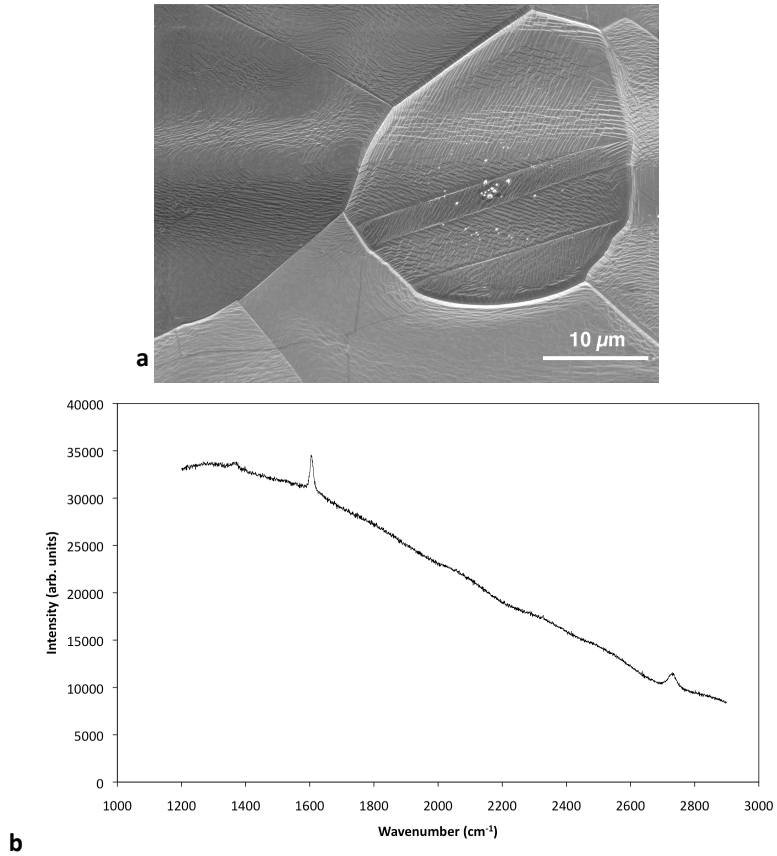


Figure 37: 99.8% Alfa Aesar Cu foil annealed in second prototype LPCVD system with no gas flow and isolated from the gas manifold, 0.004 Torr, with new cleaned quartz tube, for 60 minutes, . (a) SEM imaging, (b) Raman spectrum

Although free of black speckling, the faint wrinkles on the surface, Figure 37a, are indicative of graphitic coverage (to be discussed in detail in Chapter 5.2) and Raman spectroscopy confirmed the presence of graphitic carbon, Figure 37b.

Carbon contaminations were still detected by Raman spectroscopy after I installed a foreline trap to attempt to remove any influence of oil back-flow mist vapour, Figure 38. This result did not conclusively demonstrate that the origin of the carbon source was the Cu foil, as the effectiveness of the foreline trap in removing oil mist back-flow could vary. As an unequivocal test, I removed the rotary-vane vacuum pump from the system to eliminate any possibility of oil mist back-flow, discussed in Chapter 5.1.3.

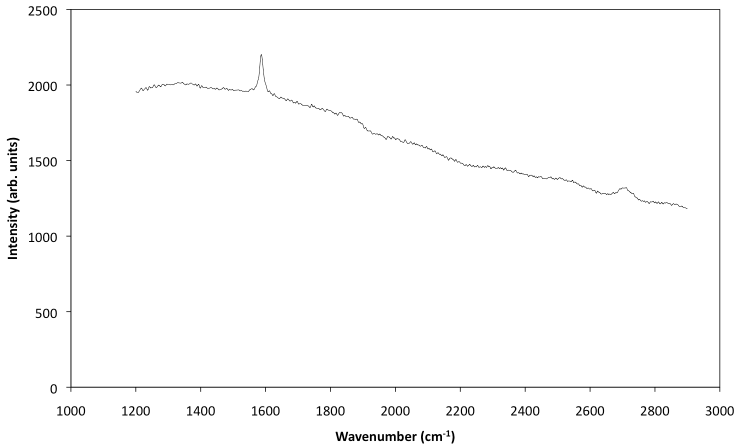


Figure 38: Raman spectrum of 99.8% Alfa Aesar Cu foil annealed in second prototype LPCVD system for 60 minutes, isolated from the gas manifold, with no gas flow, and with foreline trap installed. P = X Torr

5.1.3 Third prototype LPCVD apparatus and investigations into contaminants within system

The third prototype LPCVD system, Figure 39, used an oil-free Edwards XDS-10 scroll pump.

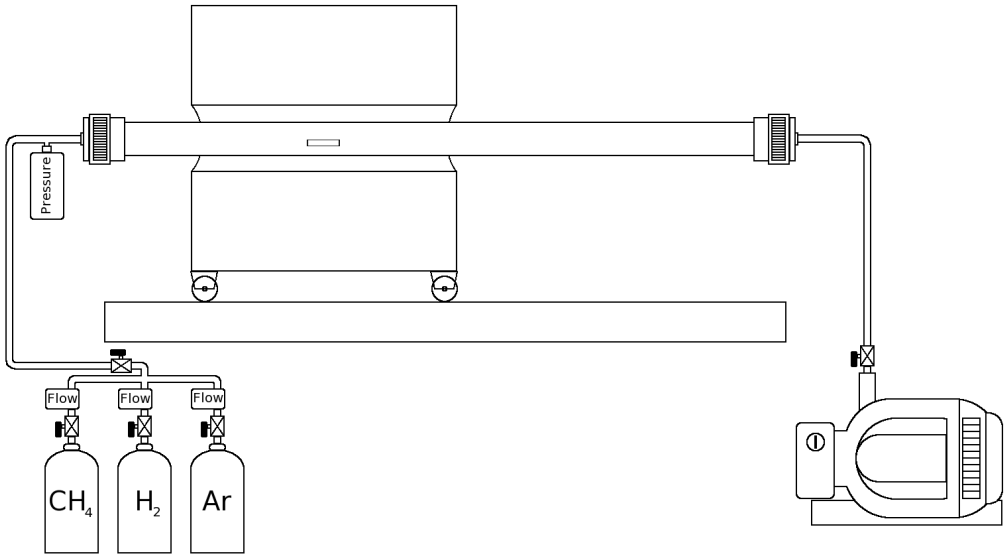


Figure 39: Third prototype of LPCVD apparatus with Swagelok ultra-Torr vacuum fittings, nylon tubing and Edwards XDS-10 scroll pump

No carbon contamination was visible by SEM, Figure 40, or detected by Raman analysis for Cu foil annealed in this system under a medium vacuum of 0.006 Torr, with no gas flow and isolated from the gas manifold.

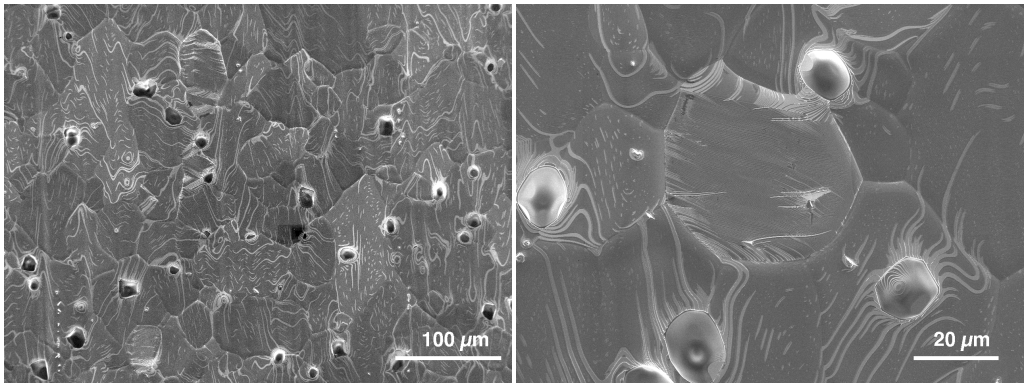


Figure 40: 99.8% Alfa Aesar Cu foil annealed in third prototype LPCVD system isolated from the gas manifold with no gas flow, 0.006 Torr, for 60 minutes. No obvious features can be interpreted as carbon contaminations; the contrast present appears due to topographical features. P= X Torr

I concluded that back-flow of oil mist from the rotary-vane vacuum pump was a source of carbon contamination. Furthermore, this contamination was completely removed by using an oil-free scroll pump.

I investigated whether other carbon contaminations were in the system by reintroducing the potential sources- the nylon gas lines, the gas manifold, or the Cu foil- back into the system. Carbon contaminations were again visible, Figure 41.

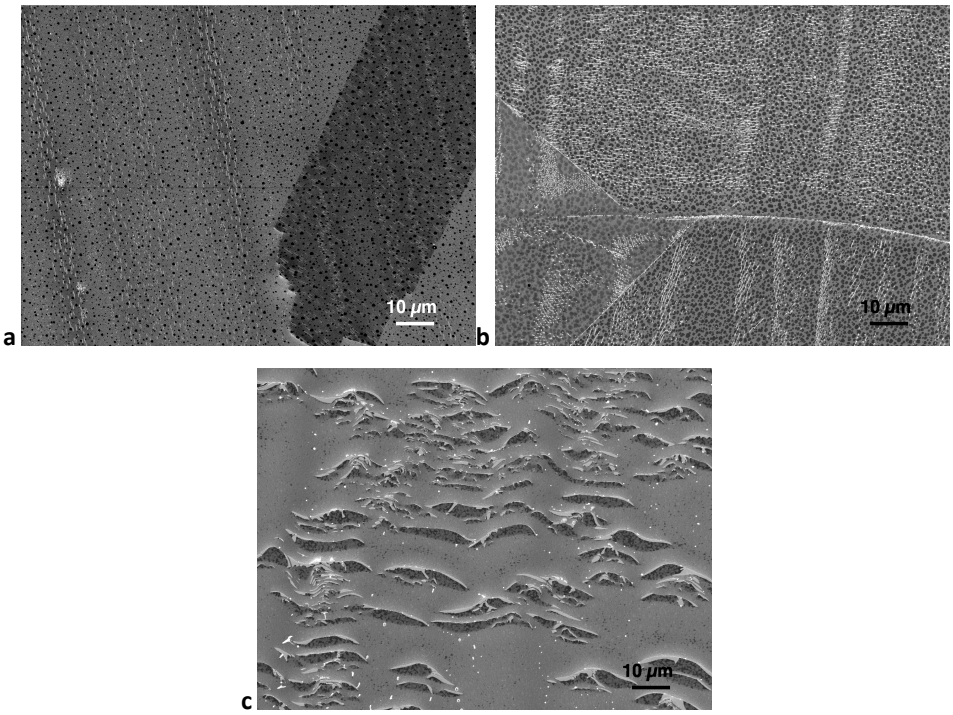


Figure 41: 99.8% Alfa Aesar Cu foil annealed in third prototype LPCVD system with gas flow for 60 minutes with (a) 5 sccm H_2, 0.23 Torr, (b) 100 sccm H_2, 1.43 Torr, and (c) 100 sccm Ar, 2.20 Torr, respectively.

Raman spectra also confirmed the reintroduction of carbon contaminations, Figure 42.

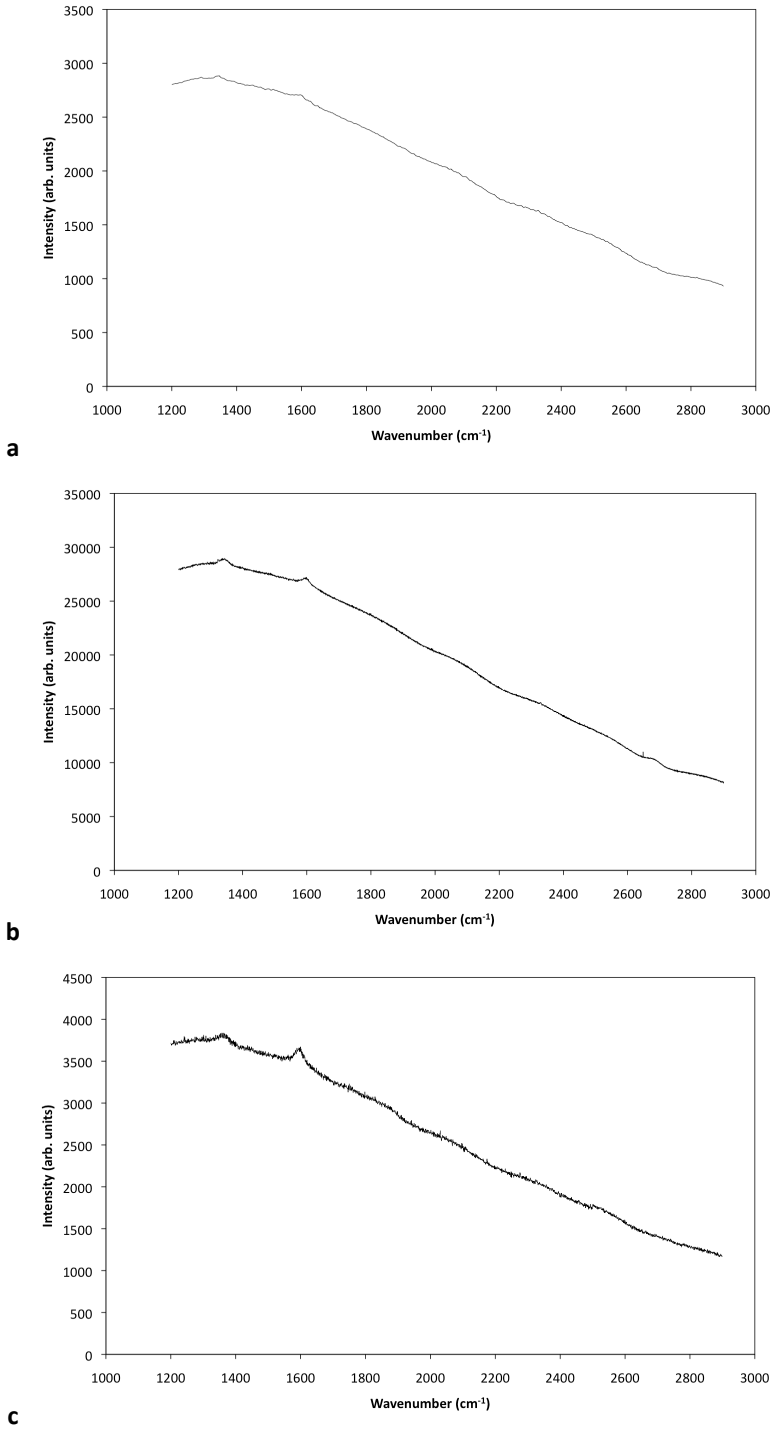


Figure 42: Raman spectra from 99.8 % Alfa Aesar Cu annealed in third prototype LPCVD system for 60 minutes with (a) 5 sccm H_2, 0.23 Torr, (b) 100 sccm H_2, 1.43 Torr, (c) 100 sccm Ar, 2.20 Torr

I concluded that a secondary contamination source was still present in the system even after removing the rotary-vane pump, originating from either the nylon gas lines or the gas manifold. However, I noted that the density of black speckling had

decreased following replacement of the rotary vane pump (comparing Figure 41a with Figure 35b), representative of the reduction in carbon contamination by removing oil-mist back-flow through replacing the rotary-vane vacuum pump with the scroll pump

5.1.4 Fourth prototype LPCVD apparatus and investigations into contaminants within system

The fourth and final prototype LPCVD system, Figure 43, used stainless steel tubing in place of nylon tubing.

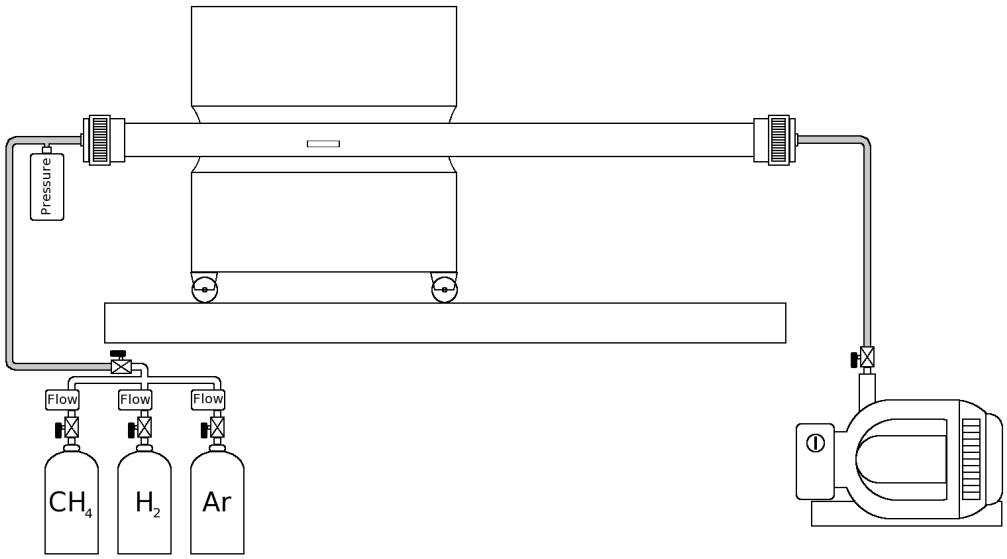


Figure 43: Fourth prototype of LPCVD apparatus

with Swagelok ultra-Torr vacuum fittings, stainless steel tubing (shaded grey) and XDS-10 scroll pump

Cu foil annealed in this system with 100 sccm Ar gas flow (2.18 Torr) appears clean and devoid of the carbon contaminations, Figure 44, in contrast to the surface after annealing in equivalent conditions in the third prototype, Figure 41c and Figure 42c. I concluded that the nylon tubing was a secondary contamination source.

While the results from annealing under Ar suggested that the system was completely free of carbon contaminations, on repeating the annealing experiments using 100 sccm H_2 (1.43 Torr) a carbon contamination was once again visible and detected by Raman on the Cu surface, Figure 45.

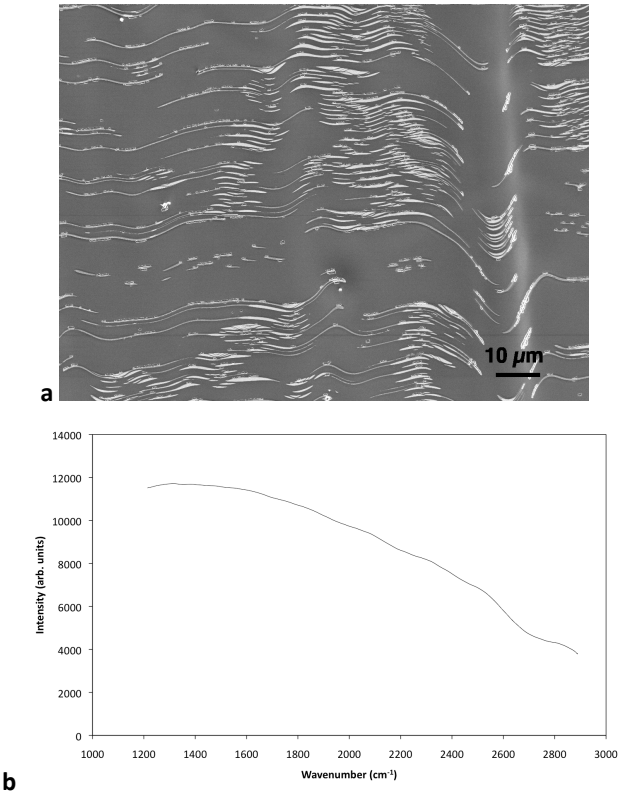


Figure 44: Annealing of 99.8 % Alfa Aesar Cu in fourth prototype LPCVD system with Ar sccm H_2 2.18 Torr, for 60 minutes, (a) SEM image, and (b) Raman spectra

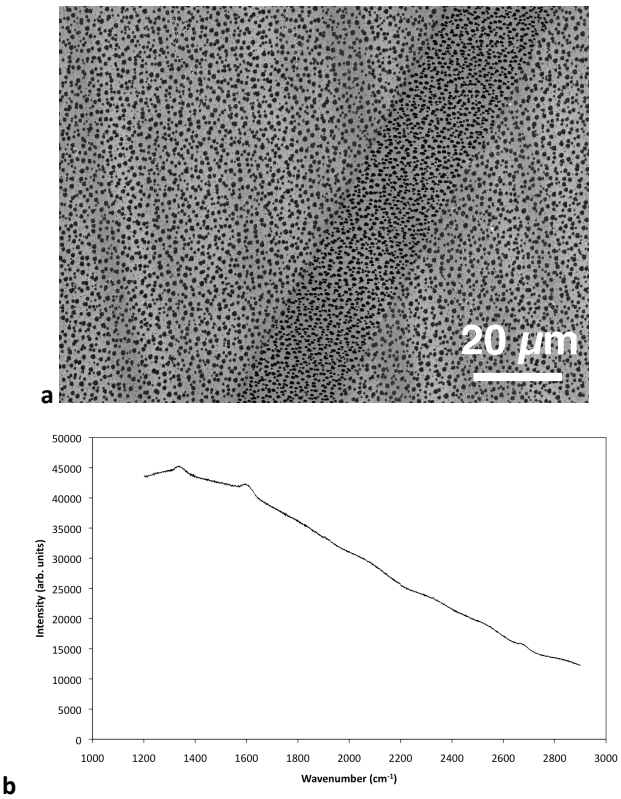


Figure 45: Annealing of 99.8 % Alfa Aesar Cu in fourth prototype LPCVD system with 100 sccm H_2 1.43 Torr, for 60 minutes, (a) SEM image, and (b) Raman spectra

Rather than view this contamination as originating from a low-percentage impurity in the H_2 gas supply, I hypothesised that it originated from adsorbed and dissolved C on the Cu foil, and that the H_2 atmosphere was an ideal environment to promote graphene formation. To confirm that a low-percentage impurity in the H_2 gas supply was not the carbon source I repeated the annealing with a higher H_2 gas flow, 500 sccm; if the carbon originated from a low-percentage impurity in the H_2 gas then increasing the gas flow would increase the contamination. SEM imaging and Raman spectroscopy of this sample revealed that, in fact, annealing with 500 sccm H_2 (4.06 Torr) produced a surface free of carbon contaminants, Figure 46.

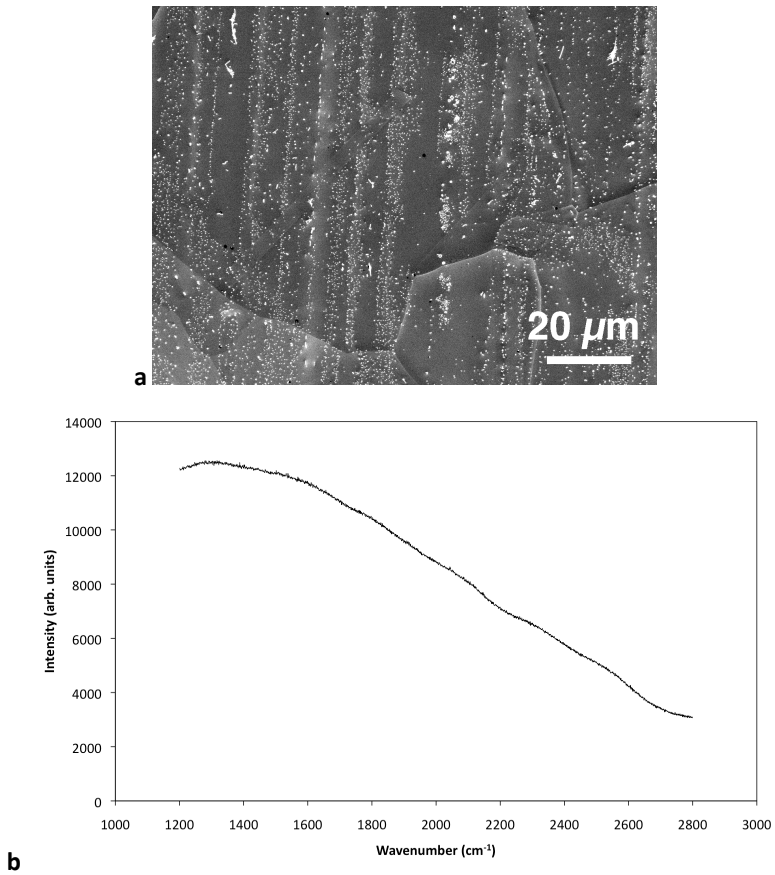


Figure 46: Annealing of 99.8 % Alfa Aesar Cu in fourth prototype LPCVD system with 500 sccm H_2 4.06 Torr, for 60 minutes, (a) SEM image, and (b) Raman spectra

This result indicates the complex dual role that H_2 plays in the system; H_2 is an activator of surface bound carbon and an etching reagent[209, 299], promoting both the growth and etching of graphene, with the dominant role dependant on the concentration in the system. This experiment demonstrates that annealing Cu foils in

LPCVD conditions with 500 sccm H_2 in the fourth prototype apparatus results in etching of any residual carbon contaminants leaving a clean Cu surface.

In summary, through a systematic investigative procedure of repeated annealing and analysis of Cu foils using SEM and Raman spectroscopy, and isolation of system components, I progressively modified and improved the LPCVD prototype apparatus to reduce atmospheric leaks and carbon contaminations in the system thereby satisfying the conditions listed in Chapter 5.1 and suitable for controlled graphene synthesis. Unless otherwise stated the annealing treatment at 1035 ˚C for 60 minutes in 500 sccm H_2 was replicated for all future LPCVD experiments using Cu foils.

5.2 Investigations into the influence of synthesis parameters on LPCVD graphene growth on as-received 99.8% Alfa Aesar Cu foil

The first experiments I conducted that aimed to synthesis LPCVD graphene used 99.8% Alfa Aesar Cu foils as received from the supplier. As discussed in Chapter 5.1.2, this Cu foil, and the absence of a surface cleaning pre-treatment prior to LPCVD, was selected to replicate the conditions suggested by Li *et al.*[144]. In a similar manner, I selected similar reactant gas flow rates and concentrations of 35 sccm CH_4 and 2 sccm H_2. Following the conclusions from annealing experiments presented in Chapter 5.1.4, the Cu foil was initially annealed for 60 minutes in 500 sccm H_2 to remove carbon contaminants and increase the Cu grain size. I used SEM as the primary technique to investigate the growth of graphene on the Cu foils following initial growth experiments. It is noteworthy that during this initial analysis there was limited prior literature available for guiding the interpretation of features and contrast in SEM images of graphene on metal surfaces. A number of factors influence the contrast variation observed in the SEM images including (i) variations in signal between regions with different number of graphene layers, (ii) variations in signal between exposed (oxidised) Cu and graphene-covered Cu (unoxidised or partially oxidised Cu), (iii) topographical features (including graphene-induced restructuring of the Cu surface) producing an edge enhancement effect. A range of SEM images from initial experiments are presented in Figure 47.

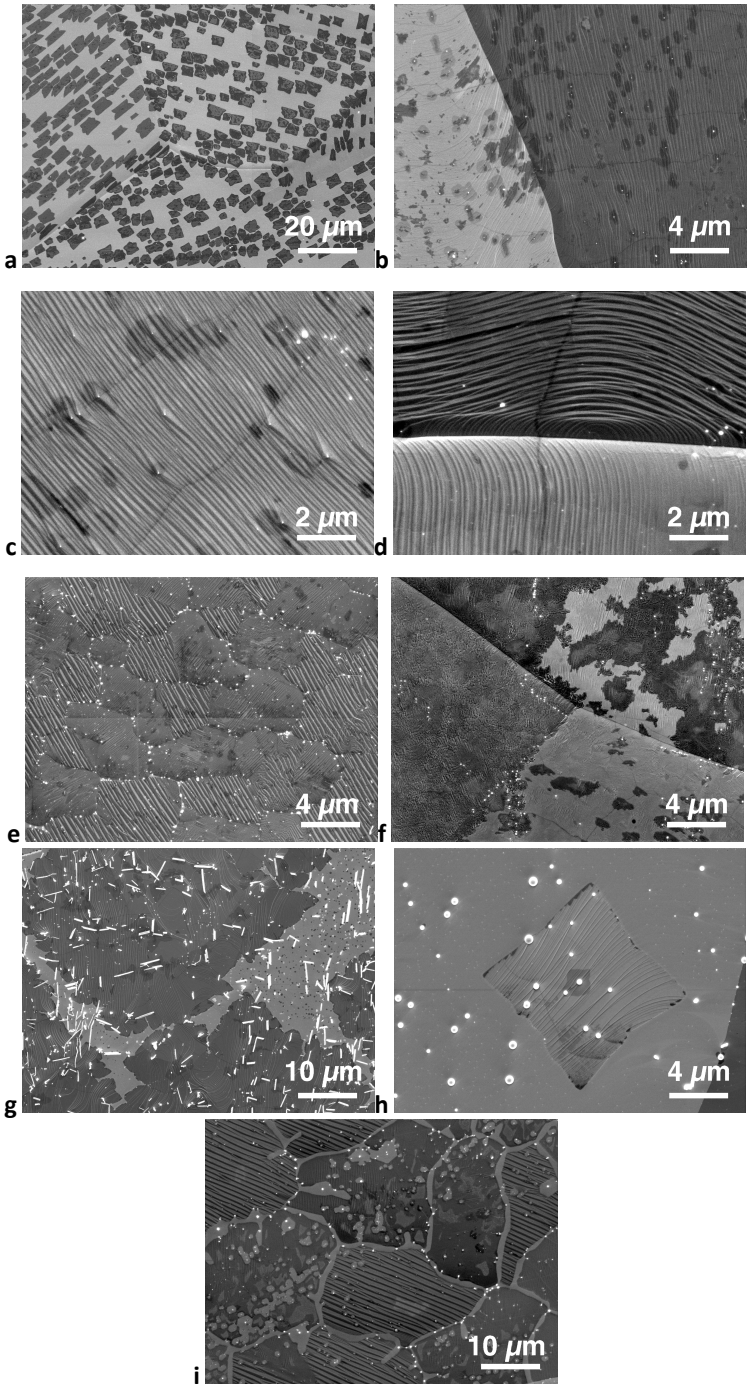


Figure 47: Variety of SEM images of LPCVD graphene on 99.8 % Alfa Aesar Cu foil (a) Isolated graphene domains (b) Full coverage of Cu surface by graphene, with darker contrast few-layer regions (c) Higher resolution of full coverage of graphene with multilayer regions and surface restructuring of Cu foil, (d) Surface restructuring of Cu to form lattice steps across a Cu grain boundary, (e) Multiple orientations of surface restructuring of Cu within one grain, (f) Dark contrast regions of disordered multilayer or amorphous carbon, (g) Edge of graphene domain with surface contaminations, (h) Isolated domain and bare Cu surface, with contaminations particles and bilayer region visible at nucleation site at centre of domain, (i) Etching of edges of graphene domains by surface contamination particles

After I gained experience with SEM imaging of graphene, and the field developed, many of the features visible in Figure 47 are easily identified including:

(i) Isolated graphene domains- dark-contrast shapes (graphene domains) on light-contrast background (copper) (Figure 47a),

(ii) Full coverage of the Cu by graphene (Figure 47b, a Cu grain boundary bisects the image),

(iii) Regions of few-layer graphene and full coverage (Figure 47b and c, with few-layer patches showing darker contrast),

(iv) Restructuring of Cu to produce Cu lattice steps (repeated parallel lines in Figure 47c and Figure 47d), sometimes with multiple orientations within a Cu grain (Figure 47e),

(v) Wrinkles in graphene (two faint diagonal wrinkles in Figure 47c, and one perpendicular wrinkle in Figure 47d),

(vi) Disordered multilayer graphene, or amorphous carbon (dark patches in Figure 47f)

(vii) Domain edges and exposed Cu (Figure 47g and Figure 47h)

(viii) Surface contamination particles (white rods in Figure 47g, and white spherical particles in Figure 47h)

(ix) Nucleation points and bilayers (centre of domain in Figure 47h)

(x) Etching of graphene by contamination particles (lighter contrast between domains in Figure 47i)

However, initially these features provided considerable uncertainty and difficulty as I interpreted SEM images and made conclusions on the influence of synthesis parameters.

Nonetheless, I conducted a systematic investigation into the influence of the synthesis parameters on the growth of LPCVD graphene on as-received 99.8 % Alfa Aesar Cu foil. The aim of this investigation was to (i) promote single layer domains, (ii) increase the size of domains, and (iii) decrease the density of domains. I varied the reactant gas concentrations, reactant gas flow rates, and synthesis times so that graphene growth varied from the maxima- a fully covered Cu surface- to the minima- no visible growth- and drew conclusions based on trends.

5.2.1 Influence of synthesis time and CH_4:H_2 flow rate ratio

I conducted an initial series of experiments based on the conditions used by Li *et al.*[144]: 35 sccm CH_4 and 2 sccm H_2 for 10 minutes synthesis time, while following procedures outlined in Chapter 5.1.2. By systematically decreasing the CH_4 flow rate between different experiments from 35 sccm to 1 sccm (e.g. 35, 20, 15, 10, 5, 2, and 1 sccm CH_4), while keeping H_2 flow constant and in deficit at a flow rate of 2 sccm, I aimed to determine the minimum CH_4 flow rate necessary to produce graphene. This variation is equivalent to a concentration change, with the CH_4:H_2 flow rate ratio varying between 17.5:1 and 0.5:1, and a change in system pressure from 0.94 Torr to 0.08 Torr. In all LPCVD experiments the conditions outlined in the scroll pump was used at full capacity to provide medium vacuum conditions (base pressure of ~0.001 Torr), resulting in the system pressure varying due to the CH_4 and H_2 flow rates. Through SEM analysis I determined, somewhat unexpectedly, that all these experiments resulted in the Cu foil being fully covered by graphene, irrespective of the reactant concentrations, Figure 48. Additional experiments for shorter duration (e.g. 3 minutes) using the lowest CH_4 flow rate set point achievable, 1 sccm, and 2 sccm H_2 also resulted in full coverage of the Cu foil with graphene, Figure 48e. In all cases bilayers and wrinkles were visible, and there appears to be a decrease in the density of these features as the CH_4:H_2 flow rate ratio decreases.

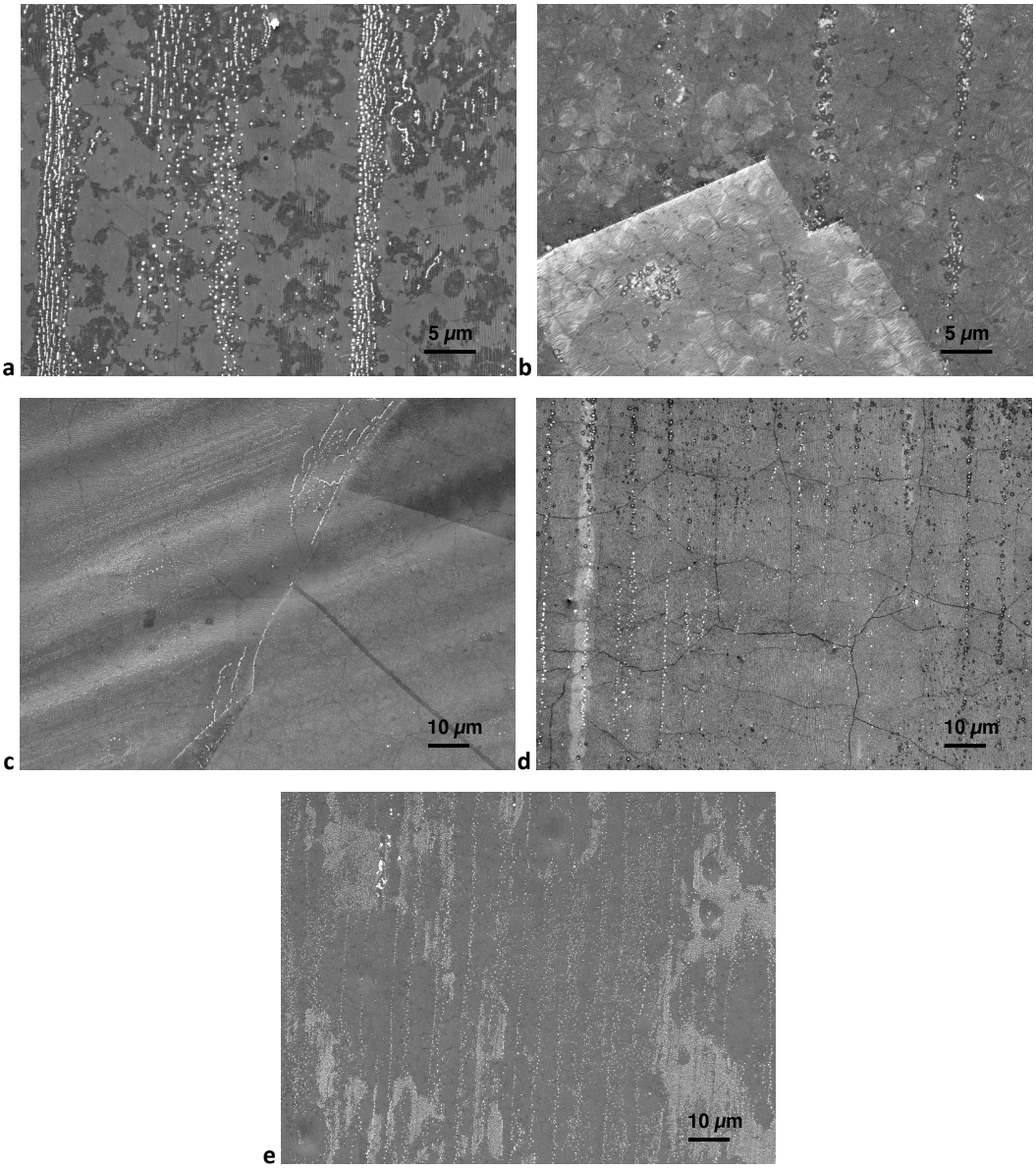


Figure 48: LPCVD graphene growth on as-received 99.8 % Cu foil with a deficit of H_2 for 10 minutes synthesis time. 2 sccm or 5 sccm H_2, with CH_4:H_2 flow rate ratio of (a) 17.5:1,0.94 Torr, (b) 7:1, 0.92 Torr, (c) 2.5:1, 0.38 Torr, (d) 1:1, 0.24 Torr, (e) 0.5:1, 0.08 Torr, for 3 minutes synthesis time

As a consequence, no definitive conclusions could be drawn from these experiments about the influence of varying the CH_4:H_2 ratio on graphene growth when there is a deficit of H_2. Furthermore, these results were somewhat contradictory to the work by Li *et al.*[168], whose experiments demonstrated that decreasing the CH_4:H_2 flow rate ratio, or reducing the synthesis time, resulted in growth of isolated graphene domains on the Cu surface. The difference between my observation and Li *et al.*[168]'s can be justified due to subtle variations in furnace dimensions, system pressures,

and experimental technique. This series of experiments did indicate that our system required finely tuned conditions for synthesis of isolated graphene flakes: namely a lower CH_4:H_2 flow rate ratio than 0.5:1, a lower concentration/partial pressure of CH_4 or increased concentration/partial pressure of H_2, or synthesis time less than 3 minutes. This experiment therefore provided upper boundaries for suitable conditions in our LPCVD system, from which future investigations were planned.

As a consequence of these results I shifted my investigations to focus on growth conditions with an excess of H_2 in order to promote the growth of isolated graphene domains with well-defined shapes. This direction followed work that was at the time newly published by Vlassiouk *et al.*[209] demonstrating the effect of hydrogen as an etching reagent to control the morphology of graphene domains and promote single layer hexagonal domains when in excess.

Using an excess of H_2, I conducted experiments to investigate the synthesis with CH_4:H_2 flow rate ratios between 1:500 and 1:100, with a constant H_2 flow rate of 500 sccm. SEM demonstrated that isolated graphene domains were synthesised with distinct shapes, Figure 49.

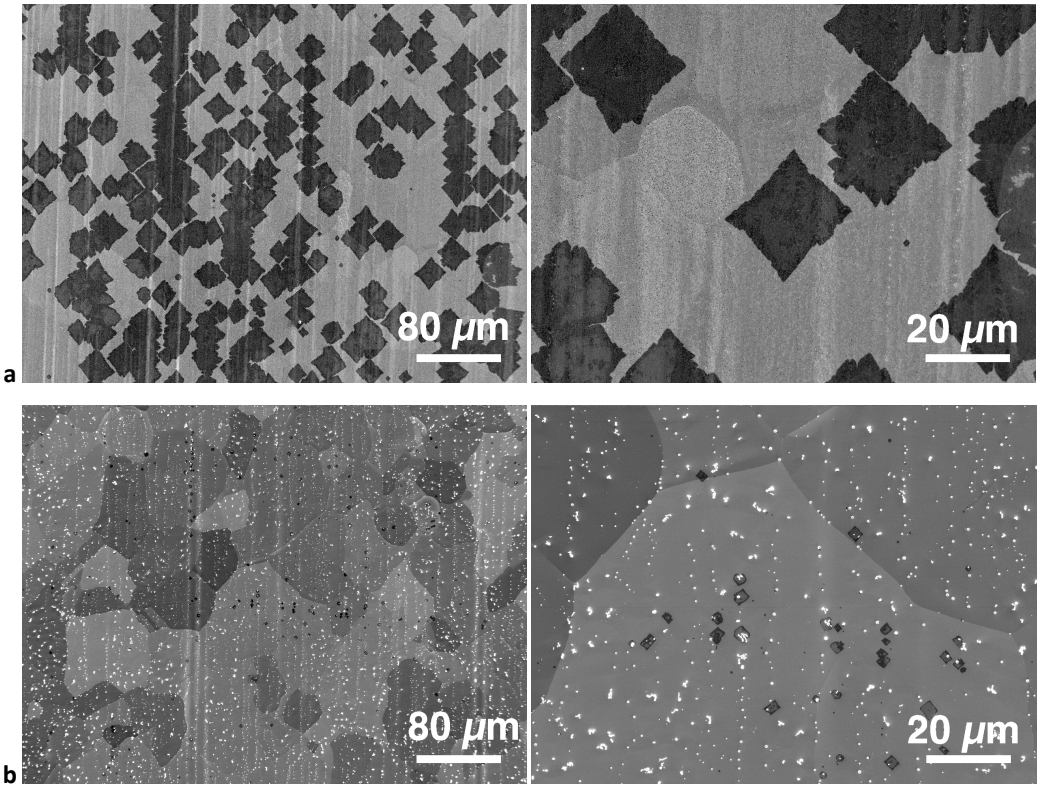


Figure 49: Isolated LPCVD graphene domains formed on as-received 99.8 % Alfa Aesar Cu foil after 5 minutes with an excess of H_2, 500 sccm, and CH_4:H_2 flow rate ratios of (a) 1:100, (b) 1:500.

The isolated graphene domains in Figure 49 were the first indication that the synthesis conditions (5 sccm CH_4, 500 sccm H_2, 5 minutes, 1035 ˚C) were suitable for the LPCVD system to produce graphene on Cu foils. To investigate this further I conducted a series of experiments varying the synthesis time, aiming to determine the time required for the graphene domains to merge and cover the entire Cu surface for CH_4:H_2 flow rate ratios of 1:100, Figure 50, and 1:500, Figure 51, with a H_2 flow rate of 500 sccm.

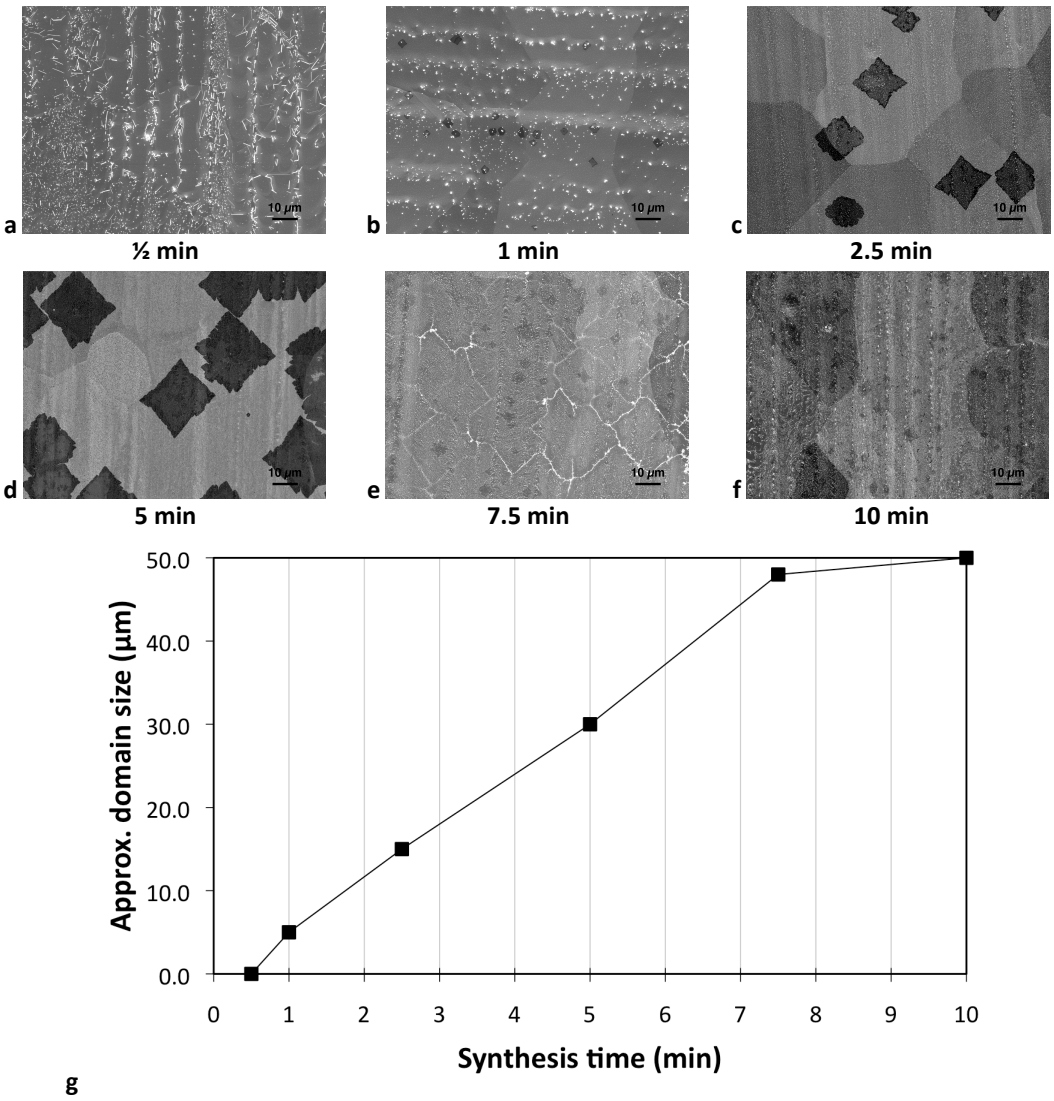


Figure 50: LPCVD graphene domains on as-received 99.8 % Alfar Aesar Cu foil with CH_4:H_2 flow rate ratio of 1:100 for various synthesis times

5 sccm CH_4 and 500 sccm H_2 for synthesis times of (a) ½ min, (b) 1 min, (c) 2.5 min, (d) 5 min, (e) 7.5 min, (f) 10 min. (g) Plot demonstrating variation in approximate domain size with synthesis time

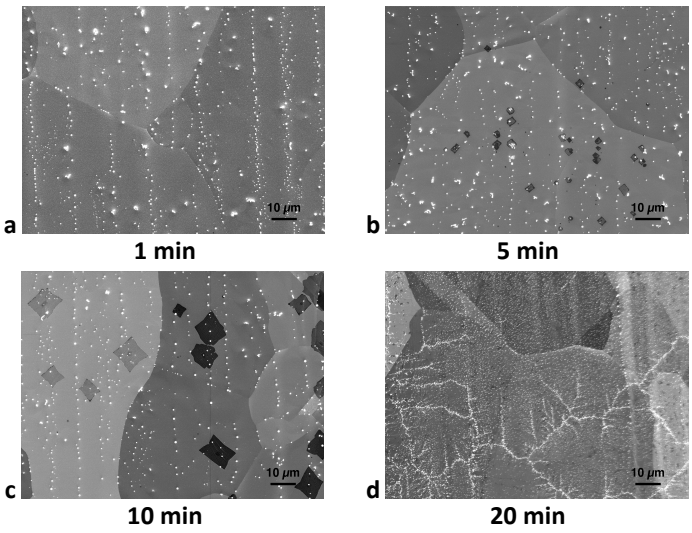


Figure 51: LPCVD graphene domains on as-received 99.8 % Alfar Aesar Cu foil with CH_4:H_2 flow rate ratio of 1:500 for various synthesis time

1 sccm CH_4 and 500 sccm H_2 for synthesis times of (a) 1 min, (b) 5 min, (c) 10 min, (d) 20 min

With a CH_4:H_2 flow rate ratio of 1:100, using 5 sccm CH_4 and 500 sccm H_2, 3 - 5 µm graphene domains are first observed after 1 minute synthesis time, Figure 50b. For shorter synthesis times no graphene domains were visible, Figure 50a. Increasing the synthesis time to 2.5 and 5 minutes the domain size increased accordingly to ~15 µm and ~20 - 30 µm, Figure 50c and Figure 50d. By 7.5 minutes synthesis time ~30 - 50 µm domains nearly covered the Cu surface entirely, Figure 50e, and after 10 minutes the individual domains merge together so that the Cu surface is fully covered by graphene, Figure 50f.

In contrast, after 10 minutes synthesis time with a CH_4:H_2 flow rate ratio of 1:500 graphene domains are still isolated, ~10 µm in size, Figure 51c. Extending the synthesis time further for 1:500 CH_4:H_2 flow rate ratio resulted in the domains merging after 20 minutes. Comparing Figure 50 and Figure 51 demonstrates that a 5x decrease in the CH_4:H_2 flow rate ratio, from 1:100 to 1:500, caused a decrease in the graphene growth rate from ~3 - 6 µm min^{-1} to ~0.2 - 1 µm min^{-1}. For the higher CH_4 gas flow ratio the domain edges appear rough, and irregular variations in the contrast can be identified across the domains, Figure 50d. In comparison, for the lower gas flow ratio the domain edges appear sharper, Figure 51. The contrast across these domains appears more uniform, although distinct regions can be identified

which exhibit lighter and darker contrast. I hypothesised that these different regions are due to bilayers/multilayers, which I commonly observed at the centre of graphene domains, and excess amorphous carbon, notable when located on the edge of the graphene domains.

During these experiments it became evident that surface contaminations were forming on the 99.8 % Alfa Aesar Cu foil during the growth procedure, visible in many instances in Figure 46 - Figure 53. This contamination was visible in SEM images as either white particles (< 500 nm in diameter) widely dispersed across the Cu surface, micron long white rods, or larger agglomerates and particles, Figure 52. The contamination varied greatly in morphology, quantity and distribution from one sample to the next.

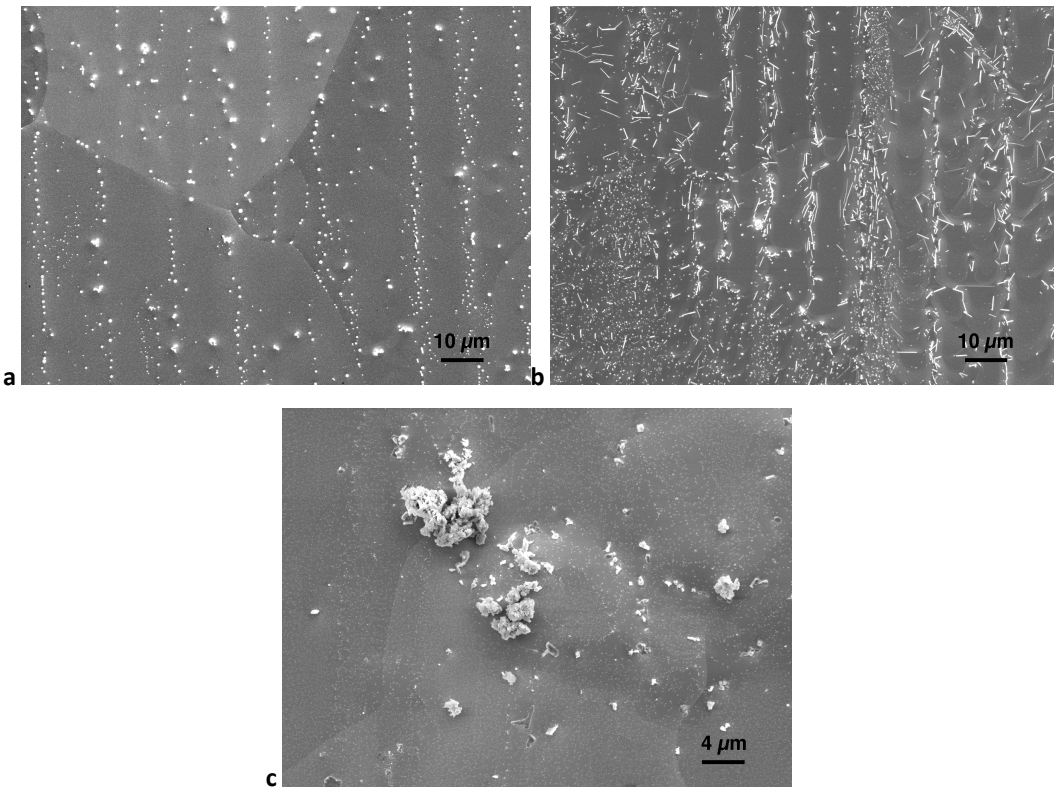


Figure 52: Surface contaminant particles observed following growth procedure
(a) Fine particles, <500 nm, widely dispersed, (b) Micron long rods, (c) Large agglomerates

Initially I hypothesised that the contamination must be due to impurities that were unique to the LPCVD system rather than originating from the Cu foil itself, as this contamination was not visible in prior work in the literature using 99.8 % Alfa Aesar Cu foil. Potential contamination sources proposed included the quartz tube, the gas

line, the sealant of gas manifold tapes, or residues in gas bottles. Due to the variation of these impurities between samples a significant investigation was required to determine that in fact the contamination predominately originated from a surface coating applied by Alfa Aesar on the 99.8 % Cu foil. The investigation leading to this conclusion is presented in Chapter 8 alongside other investigations into the influence of the properties of Cu foils on graphene growth, and methods for removal of this surface contamination.

In some instances using a low gas flow ratio resulted in the morphology of graphene domains changing to exhibit rounded edges and hexagonal-like shapes, Figure 53. These observations are in agreement with the conclusions made in the literature that a high H_2 concentration (lower CH_4 concentration) promotes the etching of graphene to hexagonal-shaped domains[208, 209]. However, in these experiments the graphene domains failed to completely cover the Cu surface even after extended synthesis time (e.g. 30 minutes). An abnormally high density of contamination rods was observed on the surface of the samples when full coverage was not achieved. This was the first indication that contamination particles may facilitate or influence the etching of graphene domains, restricting the growth of large-area sheets of graphene. Furthermore, these experiments demonstrate how the concentration of contamination particles could vary from one sample of Cu foil to the next.

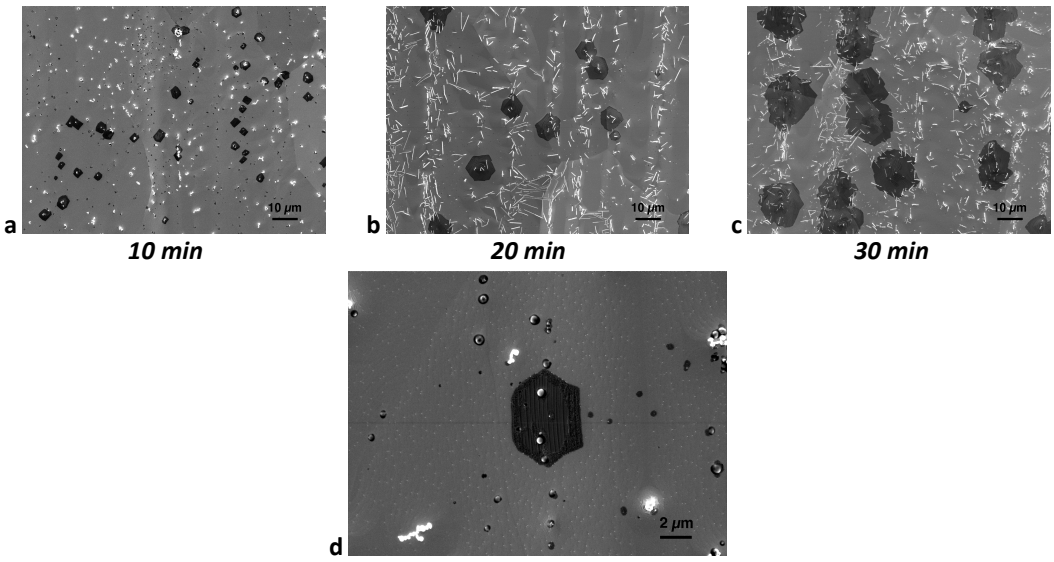


Figure 53: Hexagon-like LPCVD graphene domains on as-received 99.8 % Alfar Aesar Cu foil with a high concentration of surface contaminations

CH_4:H_2 flow rate ratio of 1:500 (ie. 1 sccm CH_4 and 500 sccm H_2) for synthesis times of (a) 10 minutes, (b) 20 minutes, (c) 30 minutes. (d) High resolution image of hexagonal domain synthesised after 10 minutes

5.3 Investigations into the influence of synthesis parameters on LPCVD graphene growth on as-received 99.999 % Alfa Aesar Cu foil

Concurrent to the investigations being conducted into the LPCVD growth of graphene on 99.8 % Alfa Aesar Cu foil, I also conducted investigations into the LPCVD growth of graphene on 99.999 % Alfa Aesar Cu foil. I selected this substrate as I hypothesised that impurities in the Cu foil may influence the growth of graphene, and thus a higher purity foil should therefore provide a cleaner substrate.

5.3.1 Influence of synthesis time and CH_4:H_2 flow rate ratio

I synthesised LPCVD graphene on 99.999 % Alfa Aesar Cu foils using an excess of H_2 owing to the results from synthesis on 99.8 % Alfa Aesar Cu foil. I conducted experiments to investigate the influence of synthesis time with 5 sccm CH_4 and 500 sccm H_2, equating to a CH_4:H_2 flow rate ratios of 1:100, Figure 54.

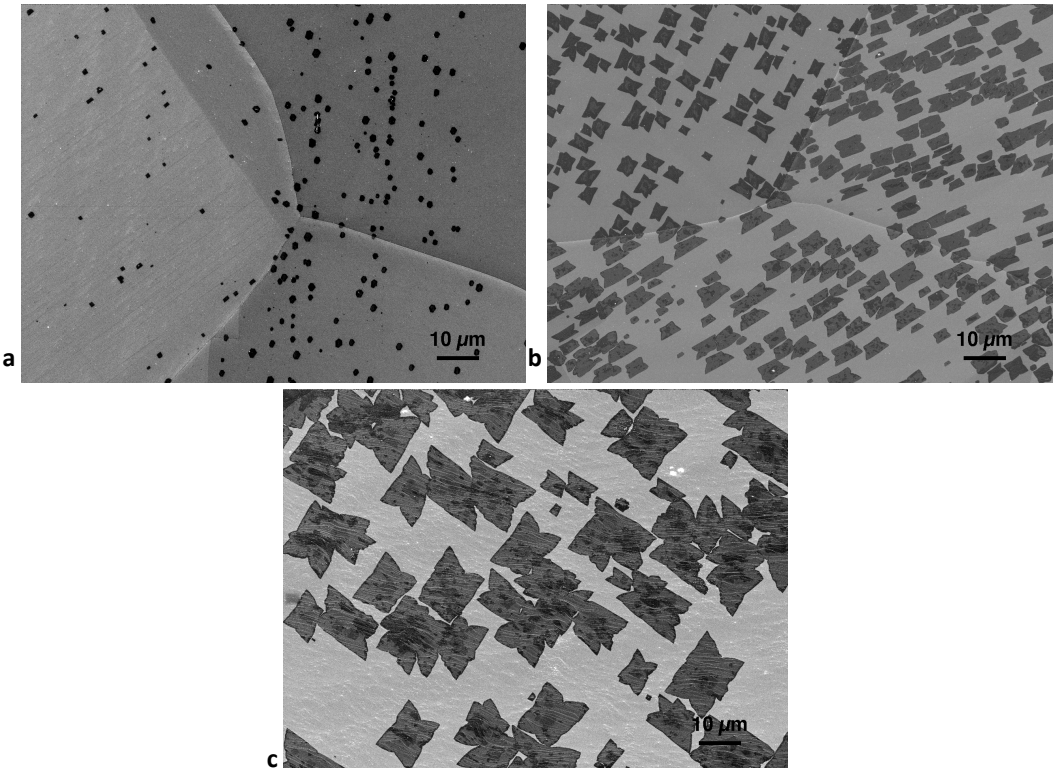


Figure 54: LPCVD growth of graphene domains on as-received 99.999 % Alfa Aesar Cu foil with CH_4:H_2 flow rate ratio of 1:100

5 sccm CH_4 and 500 sccm H_2 for synthesis time of (a) ½ minute, (b) 1 minute, (c) 5 minutes

SEM demonstrates that isolated graphene domains, ~1 µm in size, were synthesised after ½ minute synthesis time. Increasing the synthesis time to 1 minute resulted in ~5-8 µm graphene domains. After 5 minutes synthesis time these isolated domains were ~15-25 µm, and frequently merged together. This equates to a growth rate of ~5-8 µm min^{-1}. Comparing these observations with the growth under equivalent synthesis conditions (5 sccm CH_4, 500 sccm H_2, 1035˚C) on 99.8 % Alfa Aesar Cu foil, Figure 50, it is evident that the growth rates differ slightly between these two Cu foils, ~3 - 6 µm min^{-1} *versus* ~5 - 8 µm min^{-1}. More significantly, even when accounting for variations across the two surfaces, the nucleation density is considerably higher on the 99.999 % Alfa Aesar Cu foil.

Inspecting the graphene domains carefully, I observed that domains synthesised on the 99.999 % Alfa Aesar Cu foil appeared to changed shape and orientation on different Cu grains, notably visible in Figure 54b. This observation led to extensive investigations into the influence of the Cu crystallographic orientation on the growth of graphene that is presented in Chapter 7. The differences between the growth

observed on the two Cu foils raises the question- what influence does the Cu foil have on graphene growth? And furthermore, what is the ideal Cu foil for the synthesis of graphene? I recognised the importance of a thorough investigation into the influences that different Cu foils have on the growth of LPCVD graphene, and this is presented in Chapter 8.

While I did not conduct an extensive study into the synthesis of graphene at lower CH_4:H_2 flow rate ratios, initial experiments with a ratio of 1:500 using 1 sccm CH_4 and 500 sccm H_2 confirmed that the growth rate was significantly reduced, to ~1 µm min^{-1}, as demonstrated by growth for 10 minutes synthesis time, Figure 55.

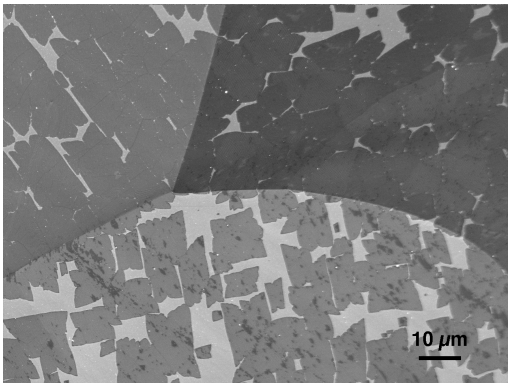


Figure 55: LPCVD growth of graphene domains on as-received 99.999 % Alfa Aesar Cu foil with CH_4:H_2 flow rate ratio of 1:500

5.4 Investigations into the influence of the side of the Cu foil

During the course of the LPCVD experiments I discovered that the morphology and growth rate of graphene domains was different on either side of the Cu foil, Figure 56.

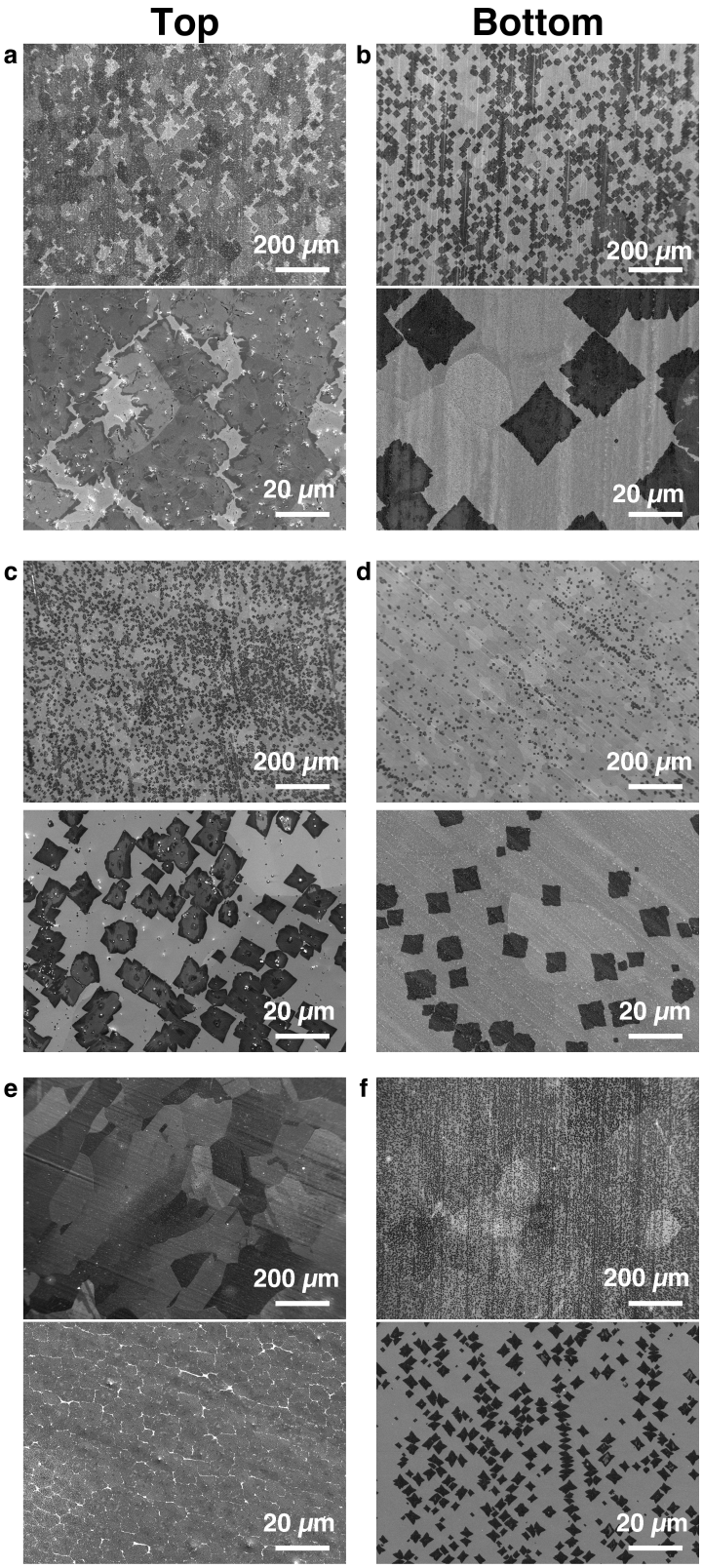


Figure 56: Variation of LPCVD growth of graphene domains on different sides of Cu foil. SEM images demonstrating different growth on the top (a, c and e) and bottom (b, d and f) surface of Cu foil. Synthesised under LPCVD with (a,b) 5 sccm CH_4 and 500 sccm H_2 on 99.8 % Alfa Aesar Cu foil, (c, d) 1 sccm CH_4 and 500 sccm H_2 on 99.8 % Alfa Aesar Cu foil, (e, f) 5 sccm CH_4 and 500 sccm H_2 on 99.999 % Alfa Aesar Cu foil

Graphene growth varied on the top and bottom surface on 99.8 % Alfa Aesar Cu foil with 1 sccm CH_4 and 500 H_2, Figure 56a and Figure 56b, and 5 sccm CH_4 and 500 sccm H_2, Figure 56c and Figure 56d. I also observed variations using 99.999 % Cu foil with 5 sccm CH_4 and 500 sccm H_2, Figure 56e and Figure 56f. In all cases the size of domains- and hence growth rate- and nucleation density was reduced on the bottom surface of the Cu foil. In addition, the shape of graphene domains was more uniform on the bottom surface, with well-defined edges. In comparison, domain edges on the top surface often appeared jagged.

In some cases the concentration of contamination particles appeared different on the two sides of the Cu foil, Figure 56a and Figure 56b. However, the growth of graphene domains varied on different sides of the Cu foil irrespective of whether the concentration of contamination particles varied or not, for instance on 99.999 % Alfa Aesar Cu foils. As such, the concentration of contamination particles is not believed to be responsible for the variations in growth between the top and bottom surface of the Cu foil. Instead, I hypothesised that this occurrence was due to the difference in reactant gas flow over the top and bottom surface of the Cu foil. As the flat Cu foil is supported by the curved surface of the quartz tube a restricted volume will be present below the foil, Figure 57.

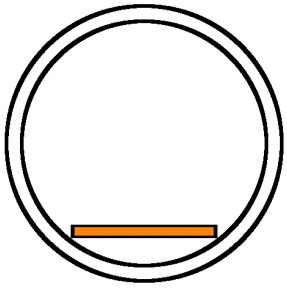


Figure 57: Diagram of restricted space below Cu foil

Scale cross-section of 10 mm wide flat Cu foil on curved surface of 25 mm diameter quartz tube

Variations in gas flow above and below the Cu foil, and through the restricted volume below the foil, will cause a lower gas speed below the foil. This produces a reduction in the growth rate of graphene domains, and increases the uniformity of domain edges. This phenomenon demonstrates the importance of the local reaction environment and gas flow over the metal substrate, and shows similarities with

improved growth in copper foil enclosures[205], and using a vapour-trapping method[208].

This observation has important implications, particularly for ensuring the consistency and reproducibility of investigations into LPCVD graphene growth. Researchers should always compare graphene growth from the same side of Cu foils, either the top or the bottom surface, to prevent erroneous conclusions. Furthermore, Cu foil substrates should always be cut to the same dimensions; variations in the substrate width will change the volume below the substrate, and consequently change graphene growth.

For consistency, throughout this thesis I have presented and compared images of LPCVD graphene growth from the bottom surface of a ~15 mm wide piece of Cu foil.

5.5 Investigations into the influence of the position within furnace

The growth of large-area graphene on Cu foils with uniform properties has been a long-standing goal. In 2010, Bae *et al*.[68] reported the growth of 30 inch diameter LPCVD graphene by rolling a large sheet of Cu foil into a tube within a furnace. The researchers claimed this geometry was beneficial to promote homogeneity by reducing radial variations in reactant gas flow rates and temperatures. I questioned the reproducibility of the claim, as a temperature distribution often exists along the length of a cylindrical tube furnace with a single heating zone. Furthermore, the variation in temperature may also influence the gas composition along the length of the furnace. Both these variations will impact the growth of graphene with position within the furnace. While Bae *et al.*[68] did not clarify whether their furnace had multiple heating zones, furnaces with single heating zones are used for graphene growth[120], and hence the influence of temperature gradient requires investigation.

To investigate this phenomenon I conducted an experiment using CH_3COOH treated 99.8 % Alfa Aesar Cu foil spanning the length of the LPCVD furnace, Figure 58. I conducted LPCVD growth of graphene using 5 sccm CH_4 and 500 sccm H_2 for 5 minutes at 1035 ˚C.

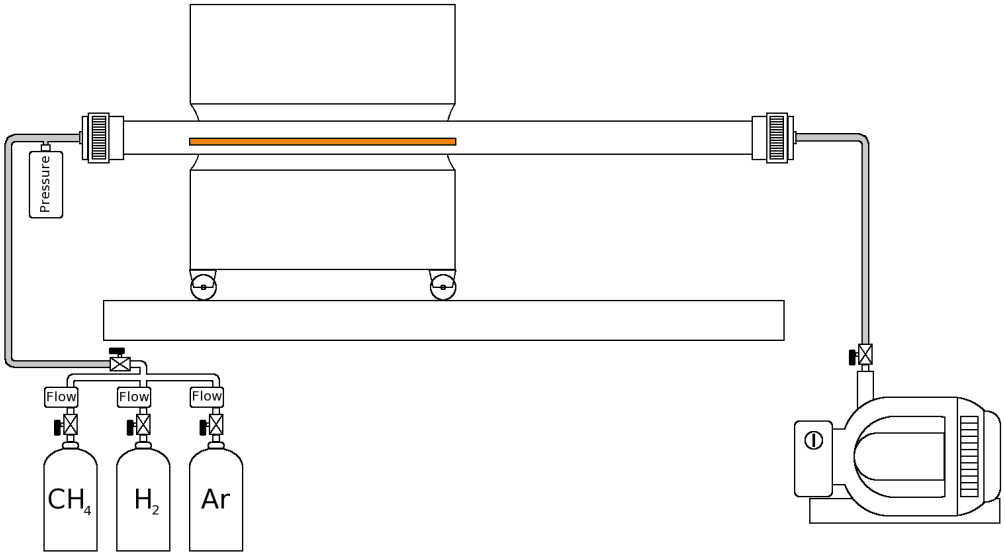


Figure 58: Diagram of LPCVD experiment with Cu foil spanning length of furnace

I measured the temperature distribution along the length of the LPCVD furnace using a K-type thermocouple probe in ambient pressure with no gas flow when the furnace controller's set point was 1035 ˚C, Figure 58.

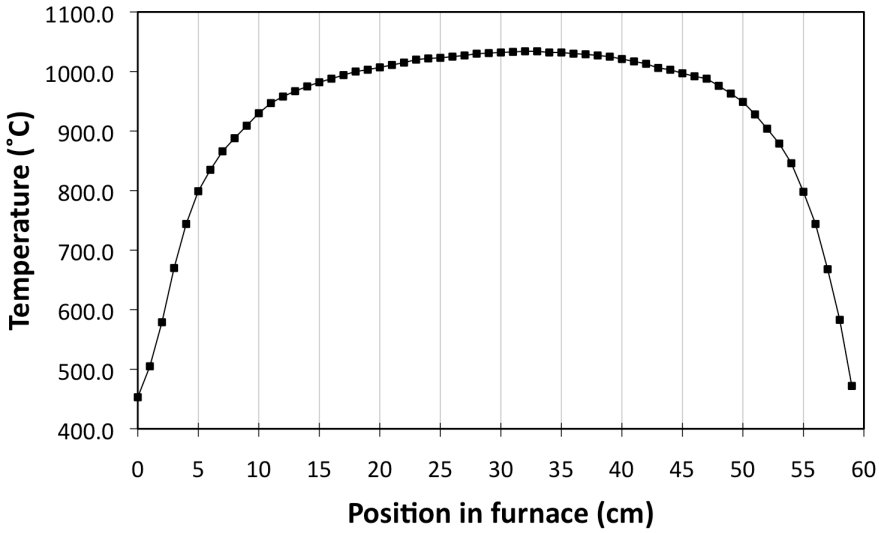


Figure 59: Temperature profile of LPCVD furnace at 1035 ˚C set point

Measured in ambient pressure with no gas flow using K-type thermocouple

The temperature varied across the length of the furnace; an isothermal zone of 1035 ± 5 ˚C exists in the centre between positions of 28 cm and 36 cm, and the temperature gradually decreases from this zone towards minima of ~450 ˚C at the two ends. To investigate the variation of graphene growth I conducted SEM on the Cu foil that was located at different positions in the furnace, Figure 60.

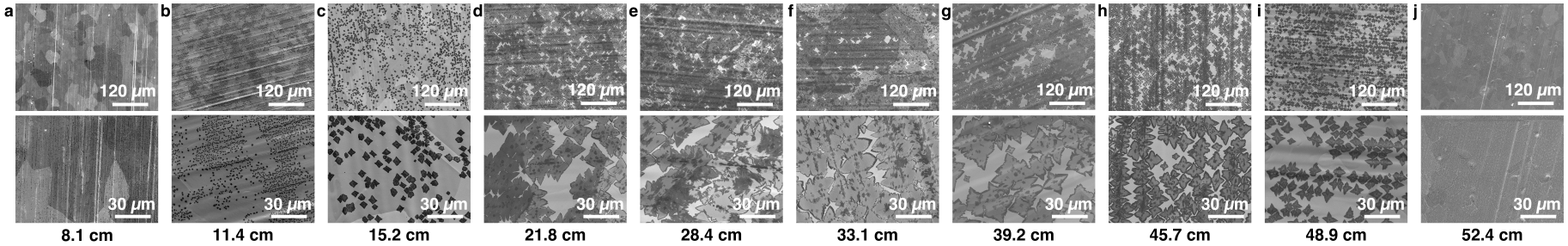


Figure 60: Variation of LPCVD graphene growth on Cu foil with position within furnace

SEM images taken along the length of strip of Cu foil, measured relative to the gas inlet

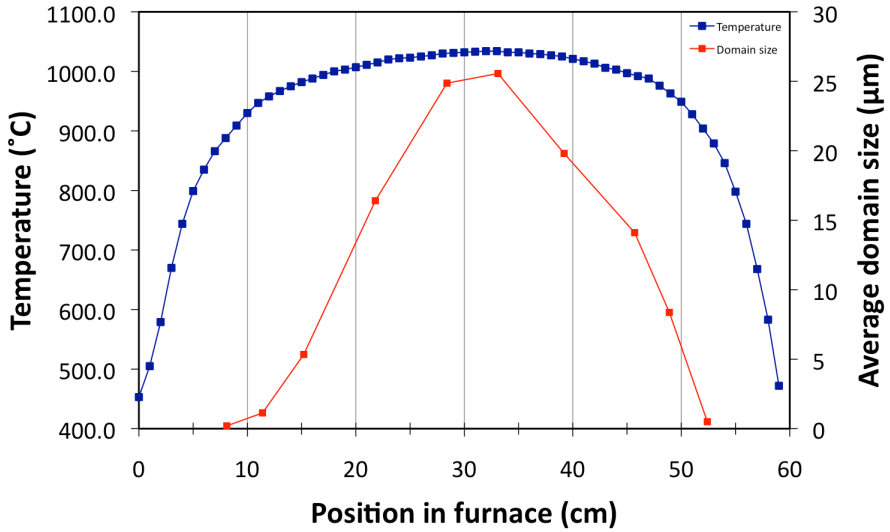


Figure 61: Variation of average size of LPCVD graphene domains with position within furnace

alongside reproduction of temperature profile from Figure 59

The size, shape and nucleation density of the graphene domains vary significantly along the length of the Cu foil strip. The coverage of graphene domains on the Cu foil increases from the gas inlet end of the furnace towards the central isothermal zone, and then progressively decreases towards the exhaust end. This trend corresponds with an equivalent increase in the size of the graphene domains, but with a decrease in the nucleation density.

To quantify this variation I measured the size of over 20 graphene domains at different locations and plotted the average domain size against the position in the furnace, Figure 61. Domain size varies from ~0.5 µm at positions up to 8 cm from both of the furnace ends, to ~25 µm in the central zone at a position of 30 cm inside the furnace. This variation can be primarily explained by the temperature distribution of the furnace presented in Figure 61; an increase in temperature causes the growth rate and size of graphene domains to increase and the nucleation density to decrease[168]. However, the variation in domain size is non-symmetrical about the centre-point of the furnace; the coverage is lower upstream of the centre-point compared to an equivalent distance downstream of the centre-point. For example, on average 5.3 µm domains are observed at 15.2 cm (upstream of the centre-point), whereas 14.1 µm domains are observed at 45.7 cm (equivalent to 13.3 cm from the downstream end of the furnace). This demonstrates that the temperature variation is not the only influential synthesis variable that changes along the length of the furnace. I hypothesise that this observation is due to variations in the concentration of decomposed reactant molecules. Downstream from the furnace's centre-point the reactant gas molecules will have passed through the maximum hot-zone of the furnace and therefore will have a residual influence of this region, with an increased probability of decomposition and formation of radicals. In comparison, upstream of the furnace's centre-point the percentage decomposition of reactant molecules will be dictated solely by the temperature at the particular location in the furnace. This observation compares very well with the variation in the growth of MWCNTs along the length of a similar cylindrical tube furnace[300].

This investigation demonstrates that the growth of LPCVD graphene can vary with the substrate position within the furnace. Variations in reaction conditions along the

length of the furnace, primarily due to changes in temperature which will also impact the percentage of decomposed reactant molecules, results in variable domain size and inconsistent, inhomogeneous graphene coverage as the distance increases from the central isothermal zone. This observation has important implications for the commercial production of reproducible, uniform large-area CVD graphene. If a cylindrical tube furnace is to be used then manufacturers will need to improve its homogeneity. The size of the isothermal zone that will produce high-quality graphene should be maximised, and simultaneously the size of the extremity regions that will produce poor-quality graphene should be reduced. These issues could be improved by using a furnace with multiple temperature control zones (e.g. a three-zone furnace), which will have a larger isothermal zone, or more generally by increasing the furnace dimensions. Alternatively, manufacturers may need to use an alternative furnace design, e.g. a box furnace, to increase the area with uniform conditions that will produce high-quality graphene.

5.6 Conclusions on low-pressure chemical vapour deposition of graphene on copper foils

My investigations into the LPCVD growth of graphene on copper foils demonstrate:

- Multiple sources of carbon contamination can affect LPCVD growth
- Modifying apparatus can effectively remove contamination sources in combination with annealing in high hydrogen flow rates,
- The CH_4:H_2 flow rate ratio and synthesis time influence graphene growth on 99.8 % Alfa Aesar Cu foil and 99.999 % Alfa Aesar Cu foil,
- The nucleation density and shape of LPCVD graphene domains can be influenced by the side of the Cu foil, with a lower density of well-defined domains on the bottom side attributed to variations in gas speed,
- The nucleation density and domain size vary with the position of the Cu foil within a single heating zone cylindrical furnace. The variation is asymmetric, with increased average domain size downstream of the centre point and temperature distribution, which is attributed to an increase in the percentage of decomposed reactant radicals downstream of the high temperature zone.

6 Atmospheric-pressure chemical vapour deposition of graphene on copper foils

This chapter outlines experiments into the APCVD growth of graphene on Cu foils. The investigations provide a complimentary study to those presented in Chapter 5 on the LPCVD synthesis, offering a more complete understanding of the CVD growth parameters. This short chapter stands alone and provides the groundwork for all my future APCVD investigations, including the studies into the influence of Cu crystallographic orientations on aligning hexagonal APCVD graphene domains, Chapter 7, the influence of Cu foils on APCVD graphene growth, Chapter 8, and APCVD growth on platinum foils, Chapter 9. Work currently being completed in Professor Nicole Grobert's Nanomaterials by Design research group using APCVD also relies on this investigation. While I completed the great majority of investigations presented in this chapter, Dr Antal Koos and Ms Jude Britton (Department of Materials, University of Oxford) provided some incidental assistance with APCVD synthesis and SEM imaging.

6.1 Benefits of APCVD

The investigations presented herein were conducted following the demonstration of APCVD as a viable method for the production of large-area[147, 150, 152, 167, 169] and isolated hexagonal domains[210, 211]. Prior to these studies, graphene growth had only been demonstrated under LPCVD conditions, and, of particular importance, studies had demonstrated that the LPCVD growth of graphene was improved by reducing the system pressure[168, 205]. These studies provided guidance and justification for undertaking the initial LPCVD investigations presented in Chapter 5. However, with the demonstration that APCVD of graphene was viable, I recognised the need for investigations into this procedure due to its benefits over LPCVD, namely:

(i) Simpler procedure, as gas evacuation, pump operation and ballast gas operation is not necessary,

(ii) Quicker procedure, as timely gas evacuation and pump to base pressure is not required,

(iii) Safer than LPCVD due to the absence of low pressure conditions which increase the explosion risk,

(iv) Easily scalable for future commercial production,

(v) Cheaper, due to absence of low-pressure conditions.

6.2 Construction of APCVD apparatus

An APCVD system was constructed by adapting a CVD system used for multi-walled CNT synthesis[295]. The system makes use of standard conical joints to connect the quartz tube with the gas panel, while an acetone bubbler is inserted downstream of the furnace to ensure no backflow of oxygen into the system, Figure 62.

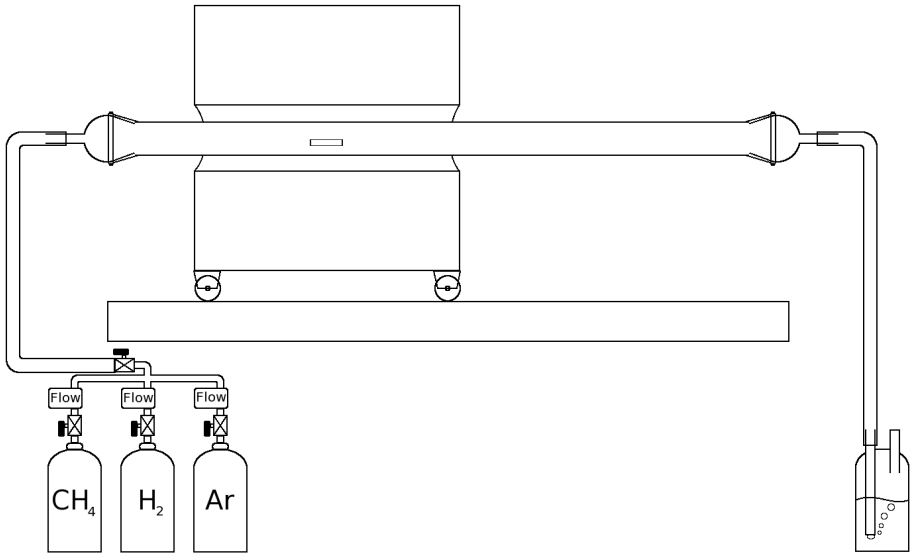


Figure 62: APCVD apparatus with conical joints and acetone bubbler

6.3 Investigations into the influence of synthesis parameters on APCVD graphene growth on 99.8% Alfa Aesar Cu foil

As for LPCVD investigations presented in Chapter 5, the synthesis parameters of reactant gas flow rate ratios, synthesis temperature and synthesis time dictate the growth of APCVD graphene. To quickly establish the appropriate parameters for research into APCVD growth of graphene I initially conducted experiments with parameters similar to those used for LPCVD experiments: 5 sccm CH_4 and

500 sccm H_2 at a synthesis temperature of 1035 ˚C, with pre-annealing for 30 minutes at 1035 ˚C under 500 sccm H_2. Owing to surface contaminations previously mentioned in Chapter 5.2, and as will be discussed in Chapter 8, the Cu foils were cleaned by ultrasonicating for 10 minutes in CH_3COOH and then dried with flowing N_2. While an initial experiment for 1 minute synthesis time resulted in no observable graphene growth, reducing the H_2 flow rate to 300 sccm and extending the synthesis time to 15 minutes produced ~2-3 µm hexagonal graphene domains, Figure 63a. This demonstrates that APCVD growth requires a lower hydrogen concentration than LPCVD growth to etch well-defined hexagonal shapes. As the synthesis time increased the size of hexagonal graphene domains correspondingly increased, to ~8 - 12 µm domains following 30 minutes growth, Figure 63b. Bilayer and few-layer regions are visible due to image contrast, indicating that a reduction in the CH_4:H_2 flow rate ratio is necessary to promote single-layer graphene on CH_3COOH cleaned 99.8 % Alfa Aesar Cu foil.

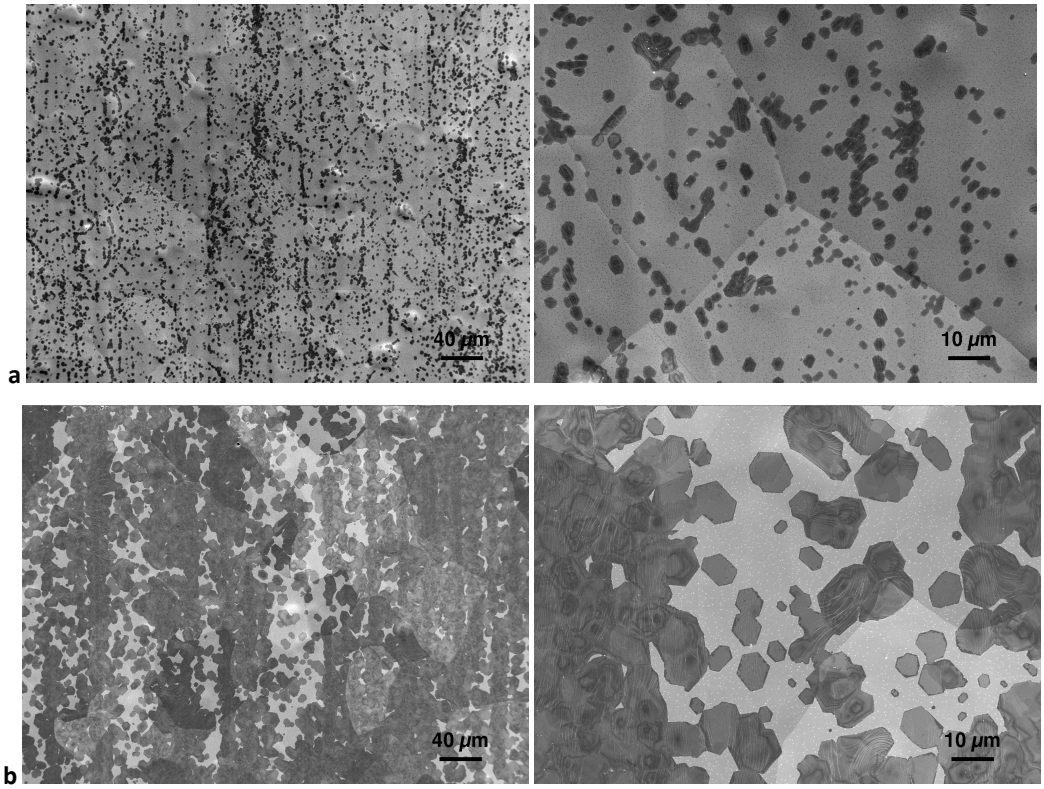


Figure 63: APCVD graphene domains on CH_3COOH cleaned 99.8 % Alfa Aesar Cu foil with CH_4:H_2 flow rate ratio of 5:300 (5 sccm CH_4 and 300 sccm H_2) for synthesis time of (a) 15 minutes and (b) 30 minutes

6.4 Investigations into the influence of synthesis parameters on APCVD graphene growth on 99.9% Goodfellow Cu foil

Owing to the presence of the surface contaminations on 99.8% Alfar Aesar Cu foil following the growth procedure, alternative Cu foil substrates were investigated for the APCVD growth of graphene. This chapter covers the investigations into the influence of APCVD synthesis parameters that was conducted on CH_3COOH cleaned 99.9% Goodfellow Cu foil, with the comparisons between different Cu foils and cleaning procedures discussed in Chapter 8.

6.4.1 Influence of synthesis time

I conducted experiments to investigate the influence of synthesis time on the growth of APCVD graphene on CH_3COOH cleaned 99.9 % Goodfellow Cu foil, with fixed CH_4:H_2 gas flow rate ratios of 5:300 and synthesis times of 15, 30 and 45 minutes, Figure 64.

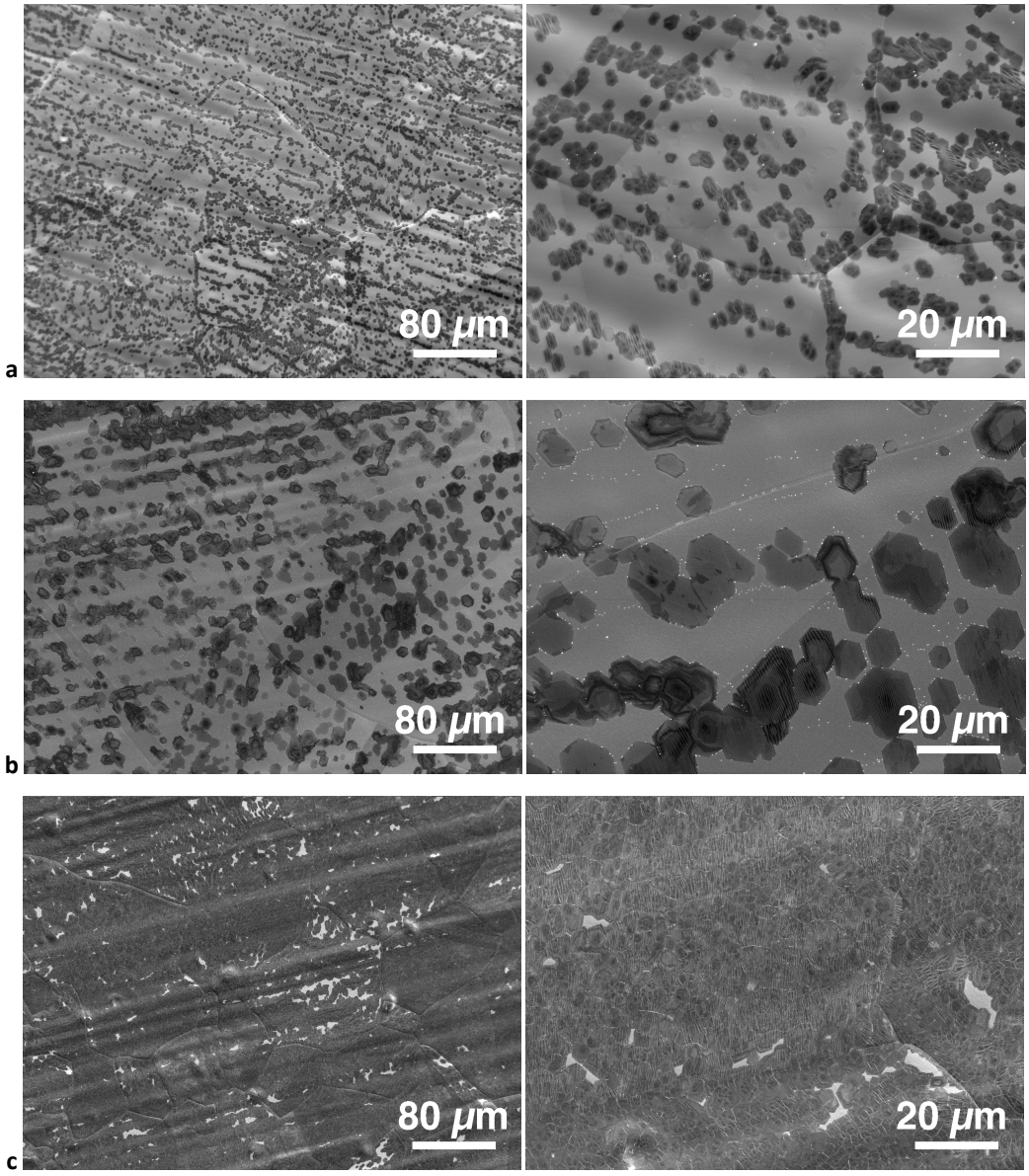


Figure 64: APCVD graphene domains on CH_3COOH cleaned 99.9 % Goodfellow Cu foil with varying synthesis time and CH_4:H_2 flow rate ratio of 5:300 for (a) 15 minutes, (b) 30 minutes, (c) 45 minutes

SEM imaging demonstrates as expected that the domain size and surface coverage increase as the synthesis time increases. For synthesis using 5 sccm CH_4 and 300 sccm H_2 domains of ~3 - 5 µm formed after 15 minutes, after 30 minutes domains increased to ~10 µm, and after 45 minutes the surface was almost entirely covered with merged domains. Bilayer and few-layer regions are identified in Figure 64b, showing similarities with the growth observed on CH_3COOH cleaned 99.8 % Alfa Aesar Cu foil in Chapter 6.3. This indicates that a reduction in the CH_4:H_2 flow rate ratio is necessary to promote single-layer graphene, discussed in Chapter 6.4.2.

6.4.2 Influence of CH_4:H_2 flow rate ratio

I investigated the APCVD synthesis on cleaned 99.9% Goodfellow Cu foil with variable CH_4:H_2 gas flow ratios between 2:300 and 5:300 and a constant excess H_2 flow rate of 300 sccm H_2 with the aim of preferentially growing large-areas of single-layer graphene. SEM demonstrated that isolated graphene domains were synthesised with hexagonal shapes, Figure 65.

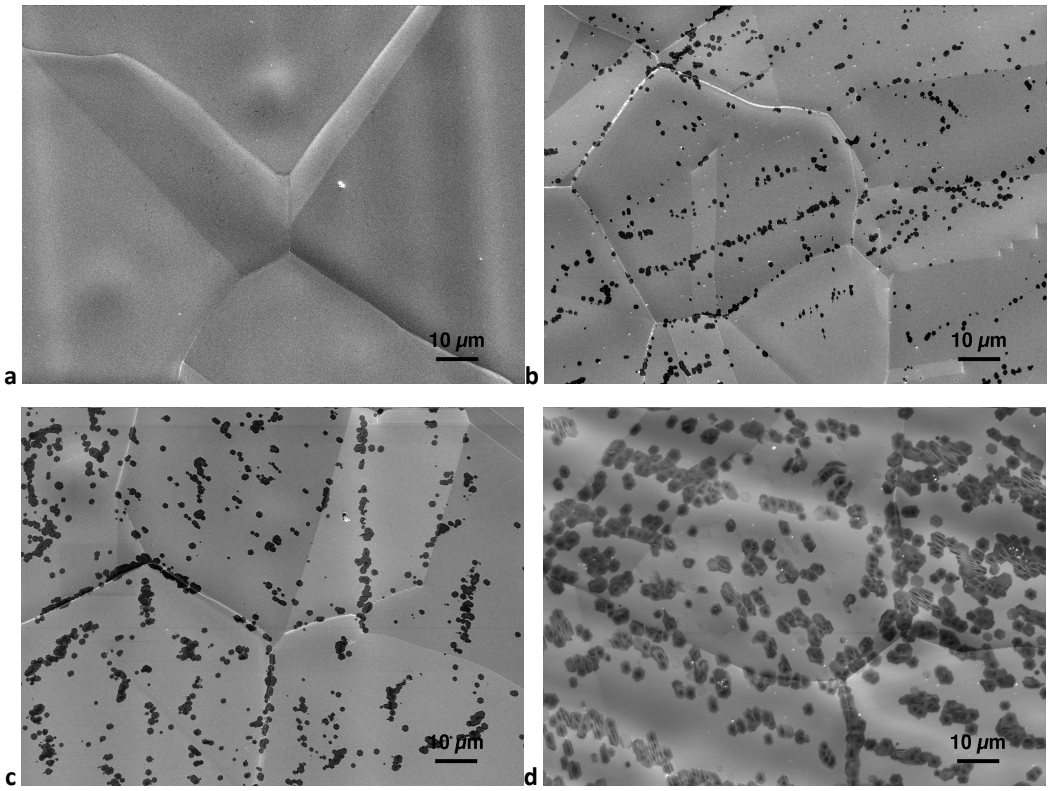


Figure 65: APCVD graphene domains on CH_3COOH cleaned 99.9 % Goodfellow Cu foil with varying CH_4:H_2 flow rate ratio for 30 minutes synthesis (15 minutes synthesis for (d)) with CH_4:H_2 flow rate ratio of (a) 2:300, (b) 2.5:300, (c) 2.8:300 and (d) 5:300 CH_4:H_2

Figure 65 demonstrates that the domain size, and hence growth rate, of the graphene domains increased as the CH_4:H_2 flow rate ratio increased from 2:300 to 5:300. While no growth is observed for a flow rate ratio of 2:300, ~0.8 - 1.0 µm domains are observed for 2.5:300, ~1.0 - 1.5 µm domains for 2.8:300, and ~3 - 5 µm domains for 5:300 (using a reduced synthesis time of 15 minutes). Variations in the thickness of the APCVD hexagonal domains are visible for synthesis using a flow rate ratio of 5:300, with very faint single-layer graphene domains visible beside few-layer and multilayered domains in Figure 65d. Viewing the growth at higher resolution,

Figure 66, this contrast variation is almost completely removed using a flow rate ratio of 2.5:300, Figure 66.

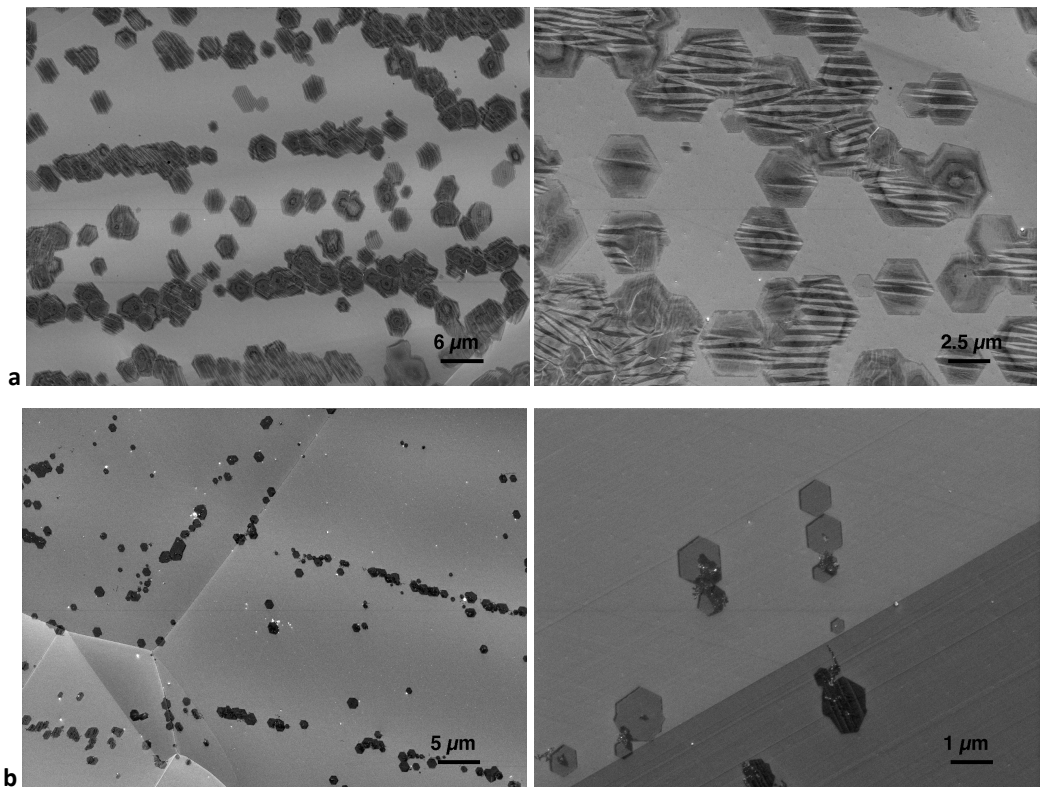


Figure 66: Higher magnification of APCVD graphene domains formed on CH_3COOH cleaned 99.9 % Goodfellow Cu foiil with varying CH_4:H_2 flow rate ratio of (a) 5:300 and (b) 2.5:300. Variations in thickness are visible due to contrast variations

This confirms that single-layer APCVD hexagonal graphene is promoted by careful control of the synthesis parameters. For our system, at 1035 ˚C using CH_3COOH cleaned 99.9 % Goodfellow Cu foil, I predicted to observe single-layer graphene by using a CH_4 flow rate between 2 and 2.5 sccm and a H_2 flow rate of 300 sccm. By extending the synthesis time beyond 30 minutes the hexagonal domains should also increase in size to form large-area coverage of the Cu foil. As such, I synthesised APCVD graphene using a 2.3:300 flow rate ratio for 60 minutes, Figure 67.

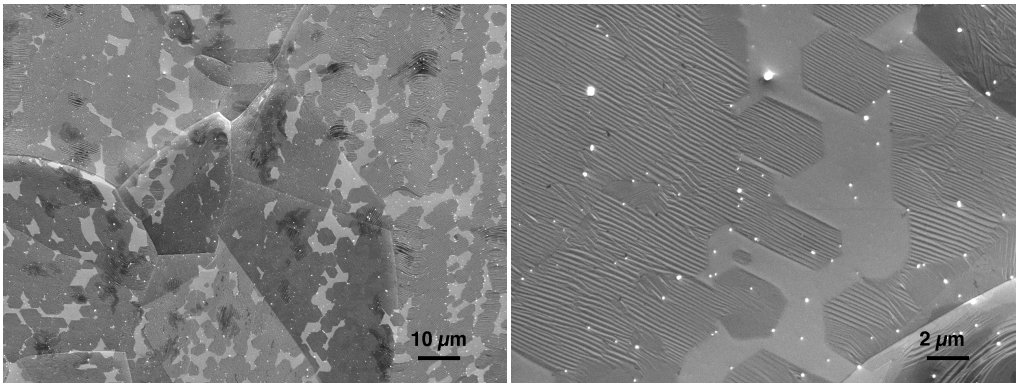


Figure 67: Predominately single-layer APCVD graphene domains formed on CH_3COOH cleaned 99.9 % Goodfellow Cu foil with CH_4:H_2 flow rate ratio of 2.3:300

Hexagonal APCVD graphene domains, ~5 µm in size and frequently merged together, covered the surface of the Cu foil. Based on the uniformity of the contrast of SEM images over tens of microns of the Cu surface these synthesis conditions produce primarily single-layer APCVD graphene. Nevertheless, some bilayer and few-layer regions are still present, indicating that more detailed investigations are necessary using conditions near to 2.3:300 flow rate ratio for production of entirely single-layer APCVD graphene.

The experiments in Chapter 6.4.1 and Chapter 6.4.2 define the synthesis parameters suitable for producing a range of types of graphene on CH_3COOH cleaned 99.9 % Goodfellow Cu foil: isolated few-layer hexagonal APCVD graphene domains, large areas of predominately single-layer graphene, and full coverage of multilayer graphene.

6.5 Pulsed APCVD graphene growth

While the investigations presented in Chapter 6.4 demonstrate that precisely tuning the CH_4:H_2 flow rate ratio is an effective method to preferentially synthesise single-layer graphene, I also investigated an alternative method to suppress multilayer growth demonstrated by Han *et al*.[301] by using a pulsed, cyclic injection of CH_4, termed "pulsed-CVD". I conducted pulsed-APCVD synthesis on CH_3COOH cleaned 99.9 % Goodfellow Cu foils at 1035 ˚C for 30 minutes total synthesis time by alternating the gas flow controller set points between 30 second injections of 3 sccm CH_3 and 300 sccm H_2, and 30 seconds of pure H_2 at 300 sccm, Figure 68a. The pulsed-APCVD growth can be compared with standard APCVD experiment of

equivalent synthesis time, namely 3 sccm CH_4 for 30 minutes, Figure 68b. Alternatively, this pulsed-APCVD procedure equates to a total flow of 45 cm^3 of CH_4 over the duration of the 30-minute experiment. An equivalent quantity of CH_4 is delivered during a standard APCVD experiment using 3 sccm CH_4 for 15 minutes, Figure 68c.

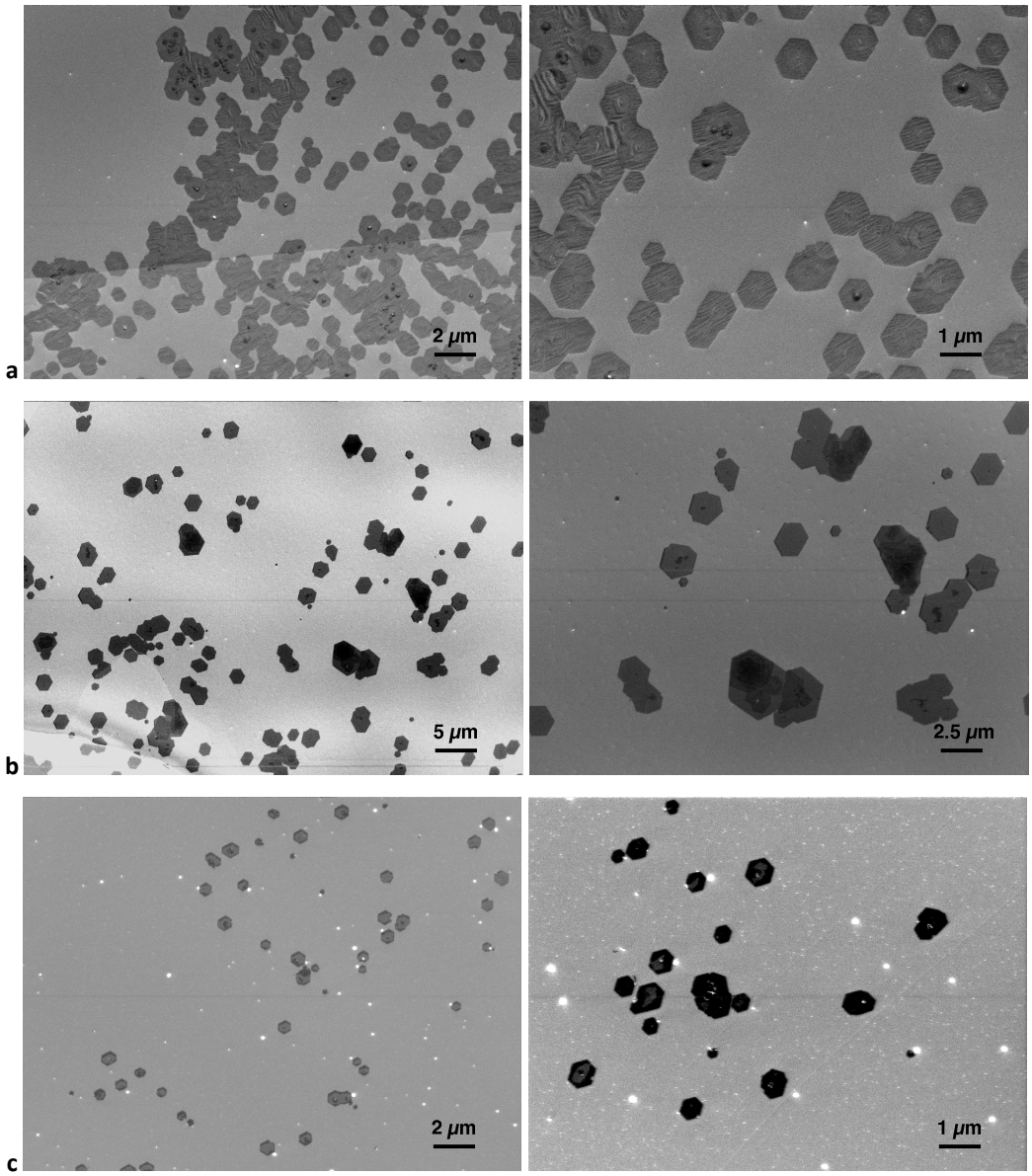


Figure 68: Pulsed-APCVD graphene domains formed on CH_3COOH cleaned 99.9 % Goodfellow Cu foil (a) pulsed-APCVD procedure for 30 minutes total synthesis time by alternating between 3 sccm CH_4 and 300 sccm H_2 for 30 seconds, and pure H_2 at 300 sccm for 30 seconds, (b) standard APCVD synthesis with 3 sccm CH_4 and 300 sccm H_2 for 30 minutes (c) standard APCVD synthesis with 3 sccm CH_4 and 300 sccm H_2 for 15 minutes. Low and high magnification images

The pulsed-APCVD synthesis procedure appears to reduce the size of multilayers. While small multilayers are still frequently visible at the nucleation point at the centre of pulsed-APCVD graphene domains, these regions are restricted to the very centre of the domains, <0.5 μm in size, Figure 68a. Extended bilayer and few-layer domains are never observed for the pulsed-APCVD growth. In comparison, bilayer and few-layer regions >2 μm in size form for the comparable APCVD synthesis for 30 minutes, Figure 68b. The single-layer pulsed-APCVD domains also have very uniform contrast, with no multilayer regions or amorphous carbon at the edge of the domains. These features are however observed for the standard APCVD using an equivalent volume of CH_4, Figure 68c.

By increasing the pulse frequency or reducing the duration of reactant gas flow in the pulsed-APCVD procedure the remaining multilayer regions at the centre of the domains can be completely eliminated[301]. I repeated the procedure using a reduced duration of CH_4 flow, 15 seconds, and increased duration of pure H_2 flow, 45 seconds, thereby maintaining the 1-minute pulse frequency. To maintain the total volume of reactant gas over the duration of the experiment at 45 cm^3 I extended the total synthesis time to 60 minutes. This experiment resulted in no growth of graphene domains, and so represents the lower boundary of suitable synthesis parameters for pulsed-APCVD in our system.

These initial investigations into pulsed-APCVD demonstrate that it is an effective method to reduce multilayer regions and preferentially grow large-area single-layer APCVD graphene. Further optimisation of the synthesis conditions within the parameter boundaries outlined here will provide a valuable alternative method to standard optimisation of flow rate ratios. Future experiments should investigate synthesis alternating between 3 sccm CH_4 and 300 sccm H_2 for $15 < t_{CH4+H2} < 30$ seconds with pure H_2 flow of 300 sccm for $30 < t_{H2} < 45$ seconds.

6.6 Conclusions on atmospheric-pressure chemical vapour deposition of graphene on copper foils

My investigations into APCVD growth of graphene on Cu foils demonstrate that:

- Hexagonal graphene domains are produced under APCVD using an excess of H_2
- APCVD growth requires a lower hydrogen concentration than LPCVD growth for production of isolated domains
- The CH_4:H_2 flow rate ratio and synthesis time influence the nucleation density, growth rate, and thickness of hexagonal APCVD graphene domains
- In our apparatus single-layer graphene can be promoted using a CH_4:H_2 flow rate ratio near to 2.3:300
- Pulsed-APCVD shows promise as an alternative method to reduce multilayer regions and promote single-layer graphene.

7 Influence of the crystallographic orientations of copper foil on the growth and properties of chemical vapour deposition graphene domains

This chapter outlines experiments investigating the influence of the crystallographic orientations of the Cu foil on the growth and properties of graphene domains. This work follows on from observations made during the analysis of LPCVD graphene growth in Chapter 5.3 where the shape and orientation of domains appeared to vary across Cu grain boundaries. The investigation demonstrates that Cu crystallographic orientations play an important role in controlling the growth and properties of LPCVD and APCVD graphene domains. Many collaborators assisted with the work presented in this chapter including Dr Antal Koos for LPCVD experiments and SEM imaging, Dr Ben Britton and Dr Angus Wilkinson (Department of Materials, University of Oxford) for EBSD training and initial EBSD characterisation, Dr Christina Lekka (Department of Materials Science and Engineering, University of Ioannina) for computational modelling, Dr Tim Batten and Dr Tong Zhang (Renishaw PLC) for two-dimensional Raman mapping, and Dr Lothar Houben and Professor Rafal Dunin-Borkowski (Ernst Ruska Centre for Microscopy and Spectroscopy with Electrons, Forschungszentrum Juelich GmbH) for high-resolution TEM.

Parts of this chapter have been published in:

Murdock, A.T., Koos, A., Britton, T.B., Houben, L., Batten, T., Zhang, T., Wilkinson, A.J., Dunin-Borkowski, R.E., Lekka, C.E., Grobert, N., Controlling the orientation, edge geometry, and thickness of chemical vapor deposition graphene, *ACS Nano*, 2013, 7, 1351-1359[1]

Parts of this chapter have been filed as a GB (EU) and US patent:

Grobert, N., Murdock, A.T., Koos, A.A., Producing two-dimensional nanomaterials (graphene) by chemical vapor deposition, used in e.g. display, comprises contacting substrate with flow of hydrogen and flow of precursor such that precursor forms material on surface of substrate, Patent number WO2013144640-A1[5]

7.1 Variation of the growth of graphene on Cu crystallographic orientations

Early on in my studies I hypothesised that Cu crystallographic orientations may be influential in controlling the growth of graphene domains. The Cu foil acts as a supportive substrate for the graphene network as it grows. However, the surface of Cu foil is non-uniform. Cu has a face-centred cubic crystal structure and the polycrystalline foil is composed of many grains, each with different crystallographic orientations that exhibit surfaces with unique atomic packing and structures such as terraces and lattice steps. I hypothesised that the graphene network may show varying affinity to the surface of different crystallographic orientations, and this may influence the growth of graphene domains by promoting domain nucleation, increased growth rates, or epitaxial alignment.

7.2 Influence of Cu crystallographic orientations on LPCVD graphene domains

During the analysis of LPCVD growth of graphene in Chapter 5.3 I observed that the shape and orientation of domains appeared to vary across Cu grain boundaries in some instances, notably visible in Figure 54. To investigate this further I synthesised isolated LPCVD graphene domains on 10 x 25 mm samples of as-received 99.999 % Alfa Aesar Cu foil following procedures outlined in Chapter 5.3, using a short synthesis time of 1 minute to avoid significant domain coalescence. I then analysed the shape, orientation, size, growth rate, thickness and edge geometry of the LPCVD graphene domains that grew on the bottom-side of the Cu foil and correlated this with the Cu crystallographic orientations as determined by EBSD analysis.

7.2.1 Influence on the shape and orientation

Distinct shapes and orientations of LPCVD graphene domains were identified on different regions of the substrate. Variations corresponded to different Cu grains, with transitions from one shape to the next occurring at the Cu grain boundaries, Figure 69.

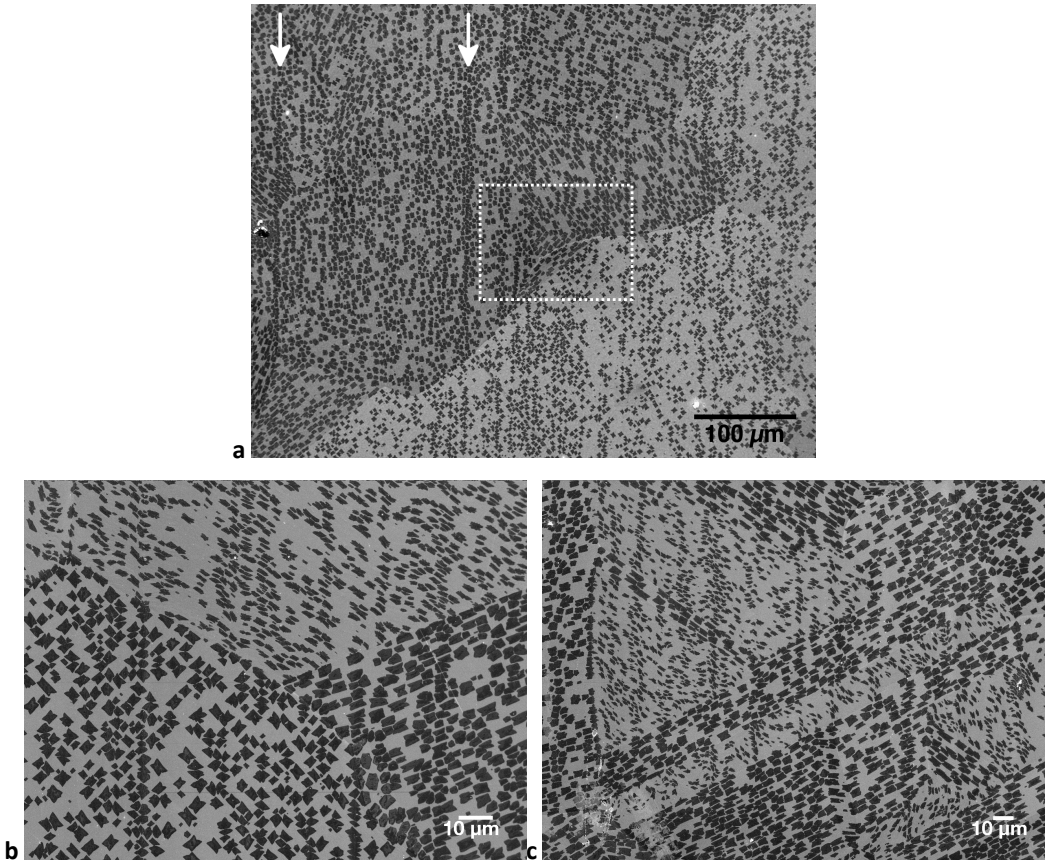


Figure 69: Variation of shape and orientation of LPCVD graphene domains over different Cu grains (a) Low-magnification image demonstrating large areas with isolated domains. Increased nucleation is visible along cold rolling striations, indicated by white arrows. White dashed box represents region analysed in Figure 70. (b) Three predominant Cu grains, and consequently three representative shapes of graphene domains with specific shapes and orientations. (c) A complex Cu surface with many grain boundaries. Nonetheless, graphene domains consistently change shape and orientation on different Cu grains. Reproduced from Murdock et al.[1]

I used OM, SEM and EBSD mapping to correlate the different LPCVD graphene domain shapes and their orientations with the crystallographic orientations of the respective Cu grains, Figure 70.

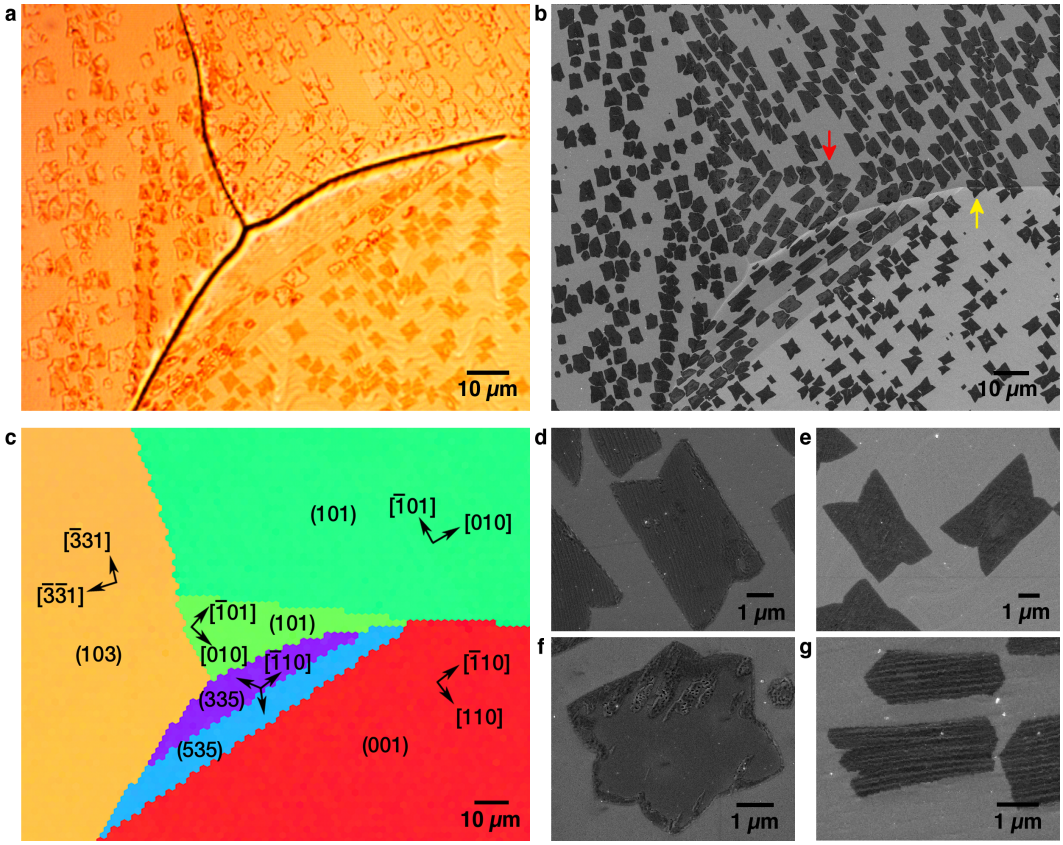


Figure 70: Shape and orientation dependence of LPCVD graphene domains on polycrystalline Cu foil. (a) Optical micrograph of graphene domains on Cu foil. A triple point and twin are at the centre of the image. Graphene domains formed across grain boundaries and surface terraces. (b) SEM image of the same region highlighting variations of LPCVD graphene domain shape and orientation on different Cu grains. A graphene domain spanning across two Cu orientations, Cu{001} and Cu{101}, and changing shape is indicated by the yellow arrow, while the red arrow indicates a domain changing edge orientation across two misoriented grains sharing the same surface normal, Cu{101}. (c) Surface normal-projected inverse pole figure EBSD map of the same region of polycrystalline Cu using the standard EBSD colour key (in Appendix). Miller indices list the closest low index crystallographic orientation of each grain while detailed maps with overlaid unit cubes are provided in the Appendix. Vectors indicate the in-plane orientation of unit cells. Unlabelled vectors on Cu(335) represent component of <101> within the tilted plane, [50-3] and [0-53]. (d)(e)(f)(g) SEM images of representative LPCVD graphene domain shapes grown on Cu{101}, Cu{001}, Cu{103} and orientations close to Cu{111}, e.g. Cu{769}, respectively. Reproduced from Murdock et al.[1]

I identified four predominant cases:

- *Four-lobed, parallel-sided domains* (Figure 70e) form on Cu(101) (green region in Figure 70c), orientated in one direction, *i.e.* [-101],
- *Four-lobed, parallel-sided domains* (Figure 70f) form on Cu(001) (red region in Figure 70c), orientated in two ~90˚ rotated directions with equal probability, *i.e.* near [110] and [-110],
- *Six-lobed, star-shaped domains* (Figure 70g) form on tilted and high-index Cu grains, *e.g.* Cu(103) (orange region in Figure 70c), with only minor alignment, *i.e.* [-331],
- *Hexagonal-edged elongated domains* (Figure 70h) form on orientations close to Cu(111), *e.g.* Cu(335) (purple region in Figure 70c) and Cu(535) (blue region in Figure 70c), orientated in one direction, *i.e.* [-110]. Hexagonal edges align to components of [10-1] and [0-11] within the plane of the tilted surface, *i.e.* [50-3] and [0-53] for Cu(335).

While the 4-lobed domains on Cu(101) and Cu(001) show similarities to those previously reported[14, 15], the parallel edges and alignment suggest that additional factors may be influencing domain formation. The edge orientation of the graphene domains on Cu(101) and Cu(001) was measured to quantify the degree of alignment, Figure 71.

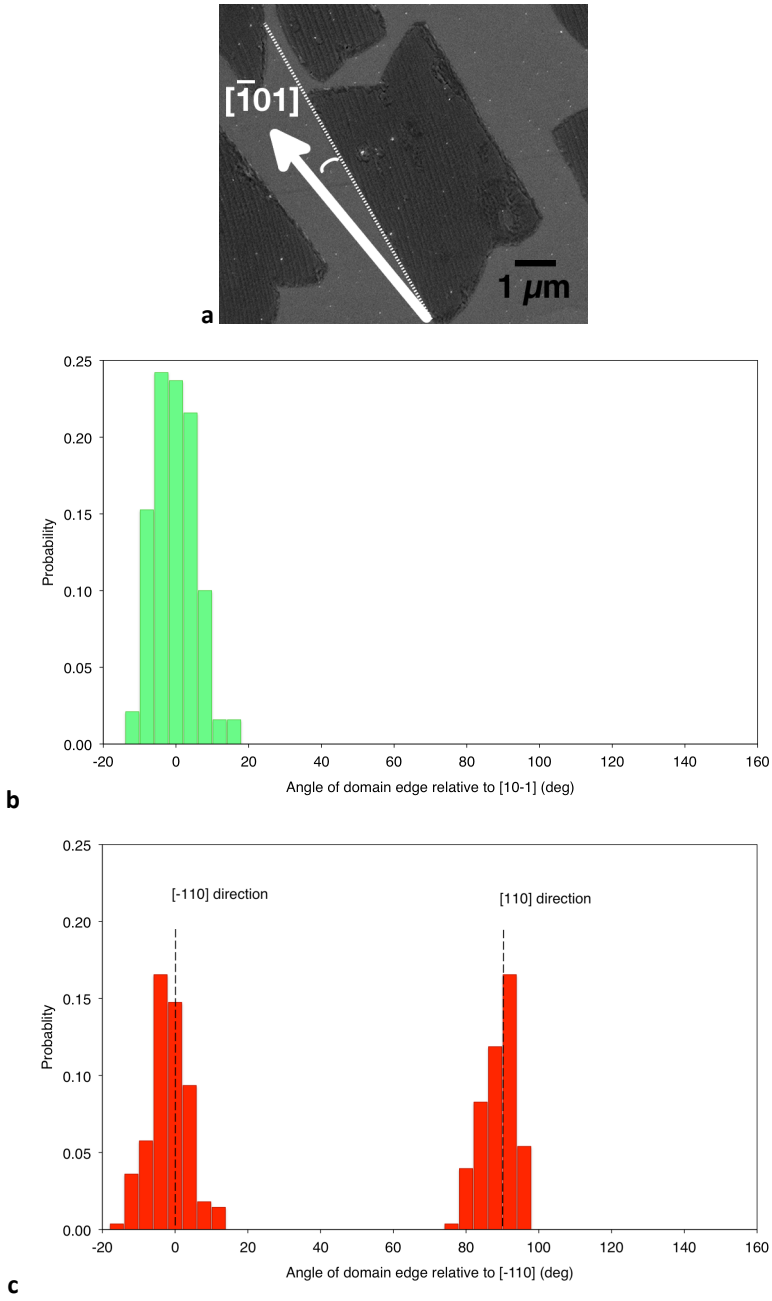


Figure 71: Distribution of the edge angle of graphene domains on Cu surfaces

(a) Diagram demonstrating method of measuring edge angle of domain relative to <101> direction determined by EBSD analysis. (b) The edge orientation was measured for over 150 graphene domains grown on Cu(101). The resulting distribution is centred 2˚ from the [-101] direction (standard deviation of 6˚). (c) The edge orientation was measured for over 300 domains on Cu(001). The resulting distribution is bimodal with 53 % of the measurements distributed around the [-110] direction and 47 % distributed around the [110] direction. The two modes are -4˚ misaligned (standard deviation 5˚) and 3˚ misaligned (standard deviation 4˚), respectively. Reproduced from Murdock et al.[1]

The angle of the domain edge was measured relative to the <101> direction of the underlying Cu grain as determined by EBSD analysis. The distribution of edge orientations for over 150 graphene domains on Cu(101) is centred 2˚ from the [-101] direction, with a standard deviation of 6˚. On Cu(001) the distribution of edge orientations for over 300 domains is bimodal with 53% of the measurements distributed around the [-110] direction and 47% distributed around the [110] direction. The two modes are -4˚ and 3˚ misaligned, with standard deviations of 5˚ and 4˚, respectively.

For orientations close to Cu(111) the presence of terraces and lattice steps appear to influence the domain growth. This causes elongation of the domains parallel to the step direction, *i.e.* [-110]. For example, Cu(335) and Cu(535) are tilted ~13˚ from Cu(111). As such, these grains are stepped surfaces, exhibiting terraces with (111) atomic packing and lattice steps running parallel to [-110][302]. Viewing Figure 70c, graphene domains on Cu(335) and Cu(535) are elongated parallel to [-110], corresponding to preferential growth along the terraces rather than over steps. However, the edges of these domains are hexagonally shaped and align to the direction of components of [10-1] and [0-11] within the (111) terraces on the stepped surface, namely [50-3] and [0-53]. As such, while terrace and lattice steps may promote elongated domains, a preference still exists for edges to orient parallel to the <110> direction. A larger grain was also investigated so that the influence of grain boundaries was reduced. Domains on Cu(769), tilted ~9˚ from (111), showed similar behaviour to domains on Cu(335)/Cu(535), with the elongated edge aligning to [1-10] and hexagonal edges to the component of <110> within the surface plane (see Appendix).

On tilted and high-index Cu grains, such as Cu(103), multiple factors influence the growth and domains show minor alignment. Owing to the absence of parallel edges, the six-lobe star-shaped domains on Cu(103) display only minor edge alignment with [-331]. Cu(103) is again a stepped surface, but in this case the surface terraces have (001) atomic packing and lattice steps run parallel to [010]. Consequently, a number of competing factors may influence domain growth on Cu(103): the preference for edge orientations parallel with [110] and [1-10] directions on the (001) terraces

(corresponding to [-331] and [-3-31] in the surface plane); preferential growth in the [010] direction parallel to steps; and growth dictated by the six-fold symmetrical graphene lattice. The observation of 6-lobe domains with minimal edge alignment illustrates that growth is dictated by a combination of these factors, with the graphene lattice perhaps being highly influential. This indicates that Cu(103), and other tilted and high-index Cu grains, provide less control of domain growth compared to other crystallographic orientations.

SEM and EBSD mapping also demonstrated that when LPCVD graphene domains crossed Cu grain boundaries their shape and orientation changed accordingly because of the different Cu crystallographic orientations. Transitions occurred for domain growth over two different Cu crystallographic orientations, and for growth over two misoriented grains sharing the same surface normal. For example of the first case, domains growing across Cu{001} and Cu{101}, highlighted by the yellow arrow in Figure 70c, changed both shape and direction. A similar occurrence with domains growing across Cu{001} and Cu{769} is presented in Figure 72a. In the second case, domains growing across two neighbouring Cu{101} grains with a relative in-plane misorientation of 68˚ align to the [-101] direction of each grain, highlighted by the red arrow in Figure 70c and imaged at higher magnification in Figure 72b.

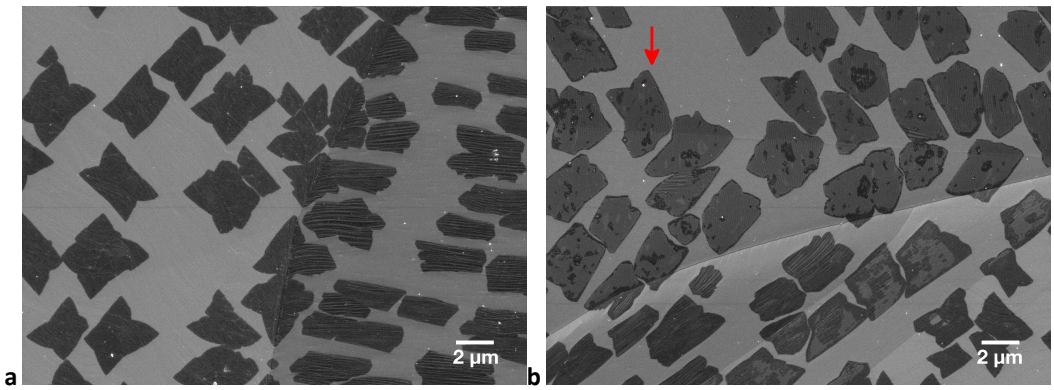


Figure 72: Change of shape and orientation of LPCVD graphene domains at Cu grain boundaries (a) Domains growing over Cu{001} (left side) and Cu{769} (right side) change from 4 lobed parallel-sided domains to hexagonal-edged elongated domains. (b) Region from Figure 70c with red arrow indicating domains spanning across two misorientated grains that are both Cu(101). Domains orientate to the [-101] direction of each underlying grain, and so change direction at the grain boundary. Reproduced from Murdock et al.[1]

The edge orientations of these LPCVD graphene domains are therefore directly related to a specific crystal direction of the Cu surface, and not solely to the crystallographic orientation. This type of graphene domain growth therefore appears to be epitaxial with preferential orientation along the Cu <101> direction.

7.2.2 Influence on the domain size and growth rate

The Cu crystallographic orientations also influence the size and growth rate of LPCVD graphene domains. This was evident in Figure 69b, with variations in the length and area of domains visible between different Cu grains. To quantify this observation I used SEM and EBSD to locate isolated domains on the primary Cu crystallographic orientations- Cu{111}, Cu{101} and Cu{001}- and then measured the distribution of the length and area of domains with *Image J* software, Figure 73.

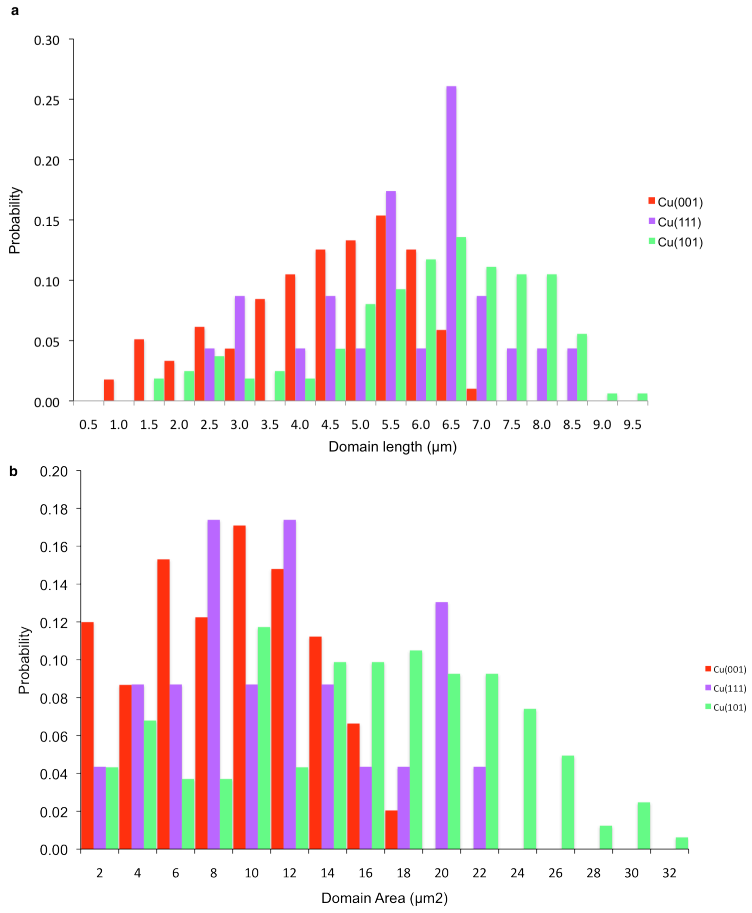


Figure 73: Influence of Cu crystallographic orientation on LPCVD graphene domain size and area (a) Distritution of maximum feret diameters of domains on different Cu crystallographic orientations. (b) Distribution of feret area of domains on different Cu crystallographic orientations. Determined using Image J analysis.

The analysis demonstrates that, at least under these synthesis conditions, the length and surface area of graphene domains are dependant on the Cu crystallographic orientations, such that Cu{101} > Cu{111} > Cu{001}. The growth rate of graphene domains is therefore also dependent on the Cu crystallographic orientation. This observation is in agreement with the observation by Wood *et al.*[232], who demonstrated that growth rate on Cu{111} is higher than Cu{001}. The discovery has significance potential to improve the efficiency of the industrial manufacturing of large-area LPCVD graphene; by using Cu foils with a higher percentage of Cu{101} the production costs could be reduced as a shorter synthesis time will be required owing to the increased growth rate.

7.2.3 Influence on the thickness

Spatially resolved Raman spectroscopy conducted on the same region as analysed in Figure 70 revealed that the quality and thickness of LPCVD graphene domains also varied with Cu crystallographic orientations, Figure 74.

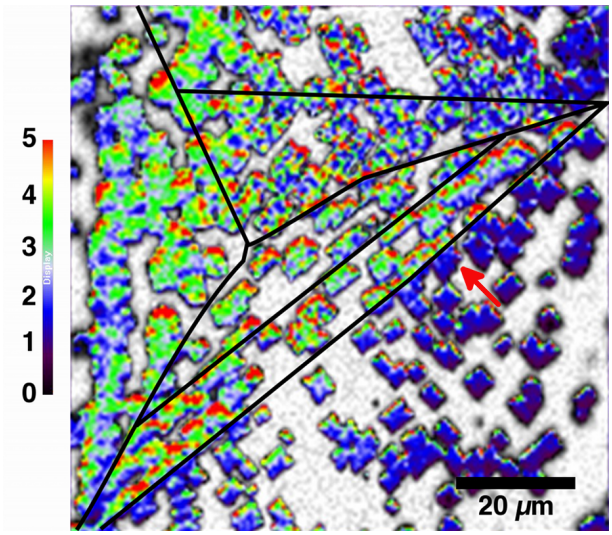


Figure 74: Spatially resolved Raman spectroscopy I_{2D}/I_G map of graphene on polycrystalline Cu foil 90 x 90 µm, showing variation of 2D and G peak intensity ratio, I_{2D}/I_G, for graphene domains on different Cu grains, corresponding to the Cu substrate area depicted in Figure 70. Black lines indicate Cu grain boundaries, while red arrow indicates graphene domain spanning a Cu grain boundary Reproduced from Murdock et al.[1]

Raman peak intensity ratios (I_{2D}/I_G), Figure 74, correlate with crystallographic orientations of the Cu substrate, Figure 70c. Since I_{2D}/I_G>2, single-layer graphene preferentially formed under these synthesis conditions on Cu{103} and orientations

close to Cu{111}, *i.e.* Cu{535} and Cu{335}. Bilayer graphene forms on Cu{001} since $1<I_{2D}/I_G<2$. On Cu{101} the ratio varies but is consistently $I_{2D}/I_G>1$, indicating that both single and bilayer graphene form. These observations agree with results by Wood *et al.*[33] indicating that single layer graphene forms on Cu{111} and multilayer graphene forms on Cu{001}. A change in I_{2D}/I_G is observed for graphene domains spanning across two Cu orientations, for example the domain spanning Cu{535} and Cu{001} indicated by red arrow in Figure 74. These domains show spectra representative of either single or bilayer graphene, dictated by the underlying Cu grain. The crystallographic orientation of the Cu substrate therefore strongly influences the type of LPCVD graphene that forms. I hypothesise that the thickness variations of LPCVD graphene domains on different Cu crystallographic orientations arise from differences in the interaction between the domains and the substrate surface. Nie *et al.*[34] have demonstrated that bilayer graphene can form from secondary layers growing underneath an initial domain. Computational modelling (presented in Chapter 7.5) indicates less affinity between the graphene adlayer and the Cu{001} surface compared to other Cu crystallographic orientations, which would increase the likelihood of diffusion of carbon species underneath domains on Cu{001} and the formation of bilayer graphene.

While the intensity of the D peak was inspected across the 90 x 90 μm region depicted in Figure 74 the peak was invariably absent (see Appendix for representative spectra). This indicates that the graphene domains are high quality with minimal defects. The absence of the D peak also suggests that the domains are single crystals, as misoriented graphene domain boundaries within a polycrystalline domain produce a detectable D peak[211].

High-resolution TEM imaging provided a complimentary method to investigate the influence of the Cu crystallographic orientation on the thickness of graphene domains. Graphene was transferred to lacey-carbon TEM grids by modifying the PMMA transfer procedure described in Chapter 2.4.3.1 (briefly, 20 mg/mL PMMA in chlorobenzene was drop-coated onto the graphene/Cu foil; Cu was dissolved in 0.2 g/mL $FeNO_3$; PMMA was dissolved in warm acetone; and TEM grids were heated to 180 ˚C in a vacuum oven for 60 minutes to reduce polymer residues). Domains

were identified as originating from Cu{001} owing to their location near other domains that were ~ 90˚ rotated (see Figure 76 in Chapter 7.2.4 for low-magnification image), and high-resolution imaging of the domain edge confirmed that bilayer graphene formed on Cu{001}, Figure 75. Single-layer graphene domains were also identified as originating from either Cu{101}, or an orientation close to Cu{111}, and high-resolution imaging and SAED demonstrated these as single-layer graphene, Figure 75b-e.

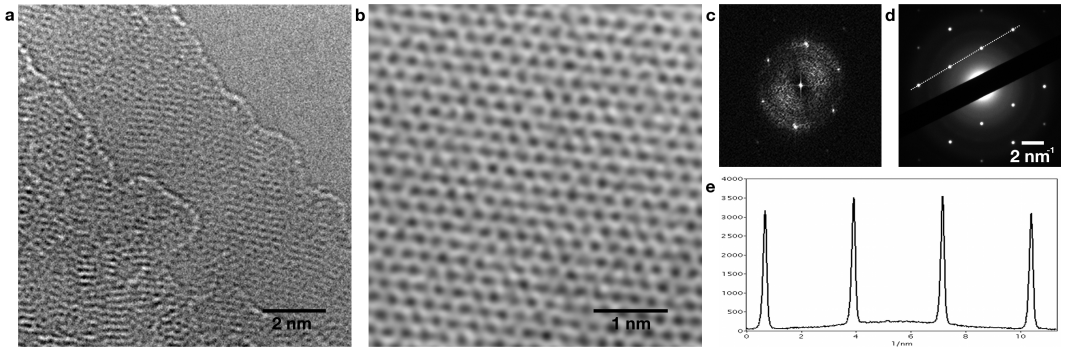


Figure 75: HRTEM and SAED analysis of thickness of graphene domains
(a) High-resolution TEM imaging of the domain originating from Cu{001} confirmed bilayer graphene, (b)(c)(d)(e) High-resolution TEM imaging, associated FFT, SAED pattern and associated line profile, respectively, for a different graphene domain originating from Cu{101} or an orientation close to Cu{111}, confirming domain as single-layer graphene. Reproduced from Murdock et al.[1]

7.2.4 Edge geometry of aligned LPCVD graphene domains

The edge geometries of the LPCVD graphene domains were investigated after transfer using TEM and SAED, Figure 76.

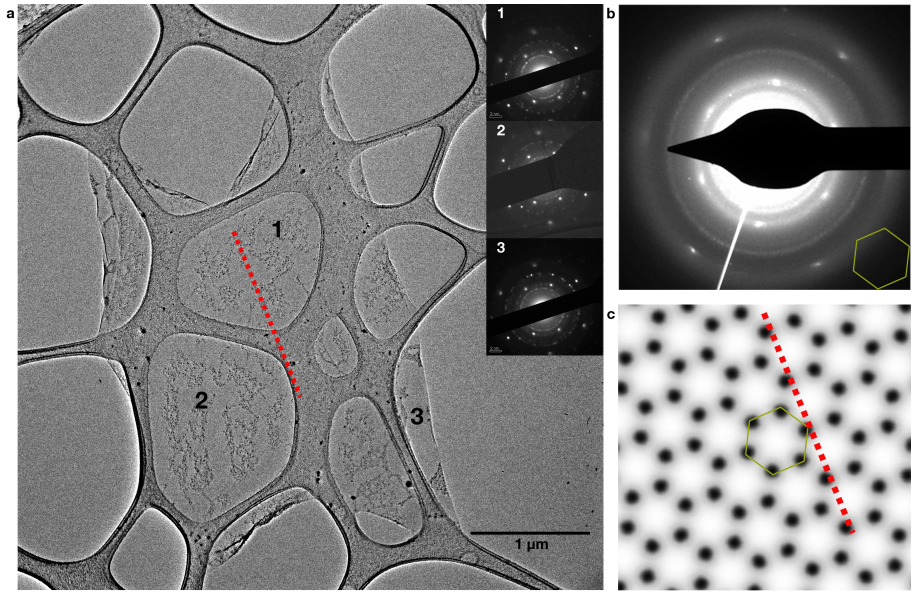


Figure 76: TEM and SAED analysis of graphene domain edge geometry

(a) Low magnification TEM image of a single domain identified as originating from Cu{001}. Irregular contrast over the domain is due to PMMA residues, (b) SAED over entire domain elucidates orientation of graphene lattice, (c) Orientation of graphene lattice from (b), indicating zigzag geometry of the long axis- the red dashed line in (a) and (c). Reproduced from Murdock et al.[1]

Domains showing the characteristic four-lobed, parallel side shape were identified as originating from Cu{001} owing to their location near other domains that were ~90˚ misoriented. While multi-lobed graphene domains may be composed of several single crystals[207, 217], SAED patterns taken from multiple locations across the domains did not rotate relative to each other, thereby demonstrating single crystal graphene, Figure 76a insets, taken from points 1, 2, 3. The orientation of the graphene lattice of the domains, and hence the edge geometry of the domains, were investigated by correlating TEM images, Figure 76a, with the orientation of selected area electron diffraction (SAED) patterns, Figure 76b. The orientation of the long axis of the graphene domains, highlighted by the red dashed line in Figure 76a, coincided with the zigzag edge of the graphene lattice that was orientated using the SAED pattern for all investigated, Figure 76c. Consequently, the two parallel edges of the LPCVD graphene domains show zigzag geometry.

7.2.5 Substrate-induced strain in LPCVD graphene domains

The effect of substrate-induced strain in graphene domains is also detected by spatially resolved Raman spectroscopy as the 2D and G peak positions vary with Cu crystallographic orientation, Figure 77.

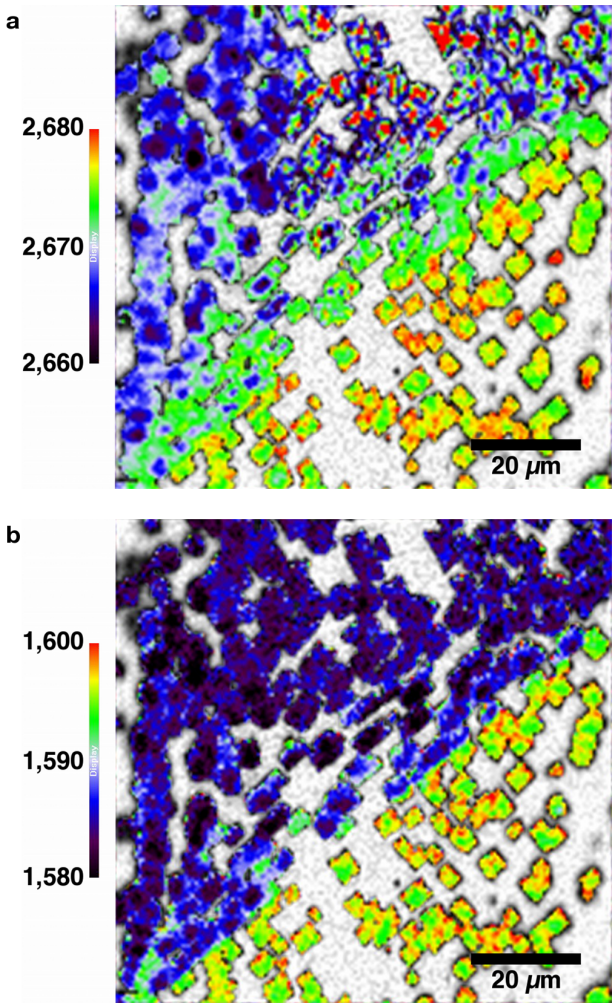


Figure 77: Spatially resolved Raman spectroscopy map of 2D and G peak position map of graphene on polycrystalline Cu foil ,90 x 90 µm, for corresponding to the Cu substrate area depicted in Figure 70, showing variation of (a) 2D peak position, (b) G peak position with Cu crystallographic orientation. Reproduced from Murdock et al.[1]

The positions of the 2D and G peaks can indicate the presence of substrate-induced electrical doping (charge transfer)[303-305] and strain in graphene domains. The G peak up-shifts for both electron and hole doping, while the 2D peak down-shifts for electron doping and up-shifts for hole doping[188, 256, 306]. In comparison, the 2D and G peaks down-shift for tensile strain[307, 308] and up-shift for compressive strain[309]. Both substrate-induced doping and strain may be present in graphene domains on Cu foil,

with influences dependent on the crystallographic orientation. Spatially resolved Raman spectroscopy maps of the 2D and G peak position, Figure 77a and Figure 77b respectively, demonstrate the variation of the peak positions with Cu crystallographic orientations, and should be viewed collectively and compared to Figure 70c. Traversing the maps from the bottom-right to the top-left, the 2D peak position systematically down-shifts across different crystallographic orientations ranging from ~2675 - 2680 cm^{-1} on Cu{001}, ~2670 - 2675 cm^{-1} on Cu{535} and ~2660 - 2665 cm^{-1} for Cu{103}. Meanwhile, the G peak position is observed to be somewhat higher on Cu{001}, between ~1595 - 1600 cm^{-1}. Intercalation of oxygen between domains and the substrate preferentially on Cu{001} may cause this anomaly as samples were stored in air[238]. Otherwise, a minor down-shift in G peak position is observed from the Cu{535} orientation at ~1588 cm^{-1} and the Cu{335}, Cu{103} and Cu{101} orientations at ~1580 - 1585 cm^{-1}. Tensile strain can explain the variations observed in the 2D and G peak position across different crystallographic orientations. Strain could be introduced into the graphene domains as Cu steps and hillocks accumulate underneath them during growth[207]. More generally, strain may originate because of the lattice mismatch between the graphene network and the Cu surface. Such influences will be dependent on the atomic spacing of the Cu surface and therefore crystallographic orientation as investigated by computational modelling Chapter 7.5.

To verify that tensile strain originates from interactions with the Cu substrate, graphene domains were transferred onto 300 nm SiO_2 coated Si substrate using the PMMA transfer outlined in Chapter 2.4.3.1 and Chapter 7.2.3, and Raman spectra were again recorded. The G and 2D peak were located at 1594 cm^{-1} and 2685 cm^{-1} respectively for transferred domains. This confirms that the peak positions down-shift due to interactions with the Cu substrate. The 2D position downshifts by a maximum of ~25 cm^{-1} across the different crystallographic orientations, corresponding to a maximum possible tensile strain of 0.18 %[308].

This observation of tensile strain is in contradiction to observations of compressive strain for graphene on Cu(111)[229, 310]. This difference may be due to variations between the synthesis procedures, or an added influence of substrate-induced

doping, which may vary between different Cu orientations, and could also be contributing to the observed shift in Raman peak positions.

A more detailed examination of a single graphene domain on Cu{001} is presented in Figure 78.

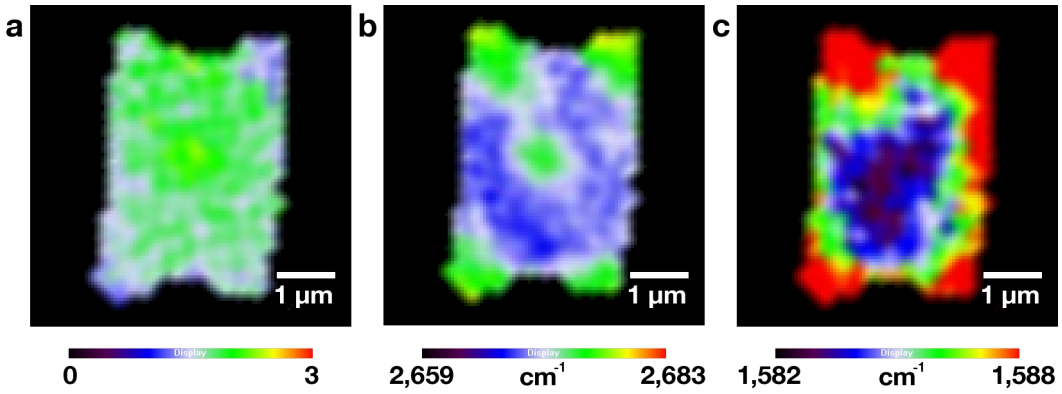


Figure 78: High resolution spatially resolved Raman spectroscopy of an individual graphene domain from Cu{001} representing (a) I_{2D}/I_G, (b) 2D position, and (c) G position

The I_{2D}/I_G ratio, Figure 78a, is unchanging across the domain indicating uniform bilayer graphene. The 2D and G peak positions, Figure 78b and Figure 78c respectively, increase at the tips of the four lobes of the domain, regions that correspond to the growth front of the graphene domain. An increase in the 2D peak position is also observed at the centre of the domain at the nucleation site. The shift in peak positions may originate from (i) increased oxygen intercalation, (ii) variations in the interaction between the domain and the substrate, or (iii) variations in the localized strain of the graphene domain at these regions. Even with high-resolution mapping the D peak was absent across the domain.

7.3 Influence of Cu crystallographic orientations on the orientation of APCVD graphene domains

Following the observation of the influence of Cu crystallographic orientations on the alignment of LPCVD graphene domains I recognised the importance of complementary investigations into the alignment of APCVD graphene domains. The edge geometry of hexagonal APCVD graphene domains has been shown to be zigzag geometry[211, 212]. The specific orientation of a hexagonal graphene domain on the Cu foil surface therefore directly indicates the orientation of the graphene lattice of the domain. Controlling the orientation of the domains would therefore control the graphene lattice, meaning that aligned domains would form low-angle domain boundaries with reduced disorder and defects, thereby improving the mechanical strength and electrical performance, Figure 79[276, 311-314].

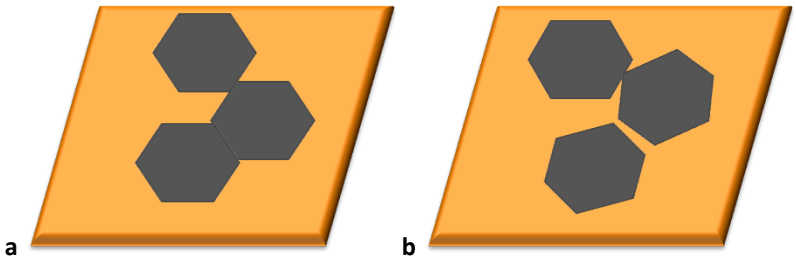


Figure 79: Schematic demonstrating variation in domain boundaries for (a) oriented domains, (b) randomly oriented domains

I conducted a range of APCVD experiments using different Cu foils to attempt to reproduce the influence of the Cu crystallographic orientations on the orientation of APCVD graphene domains, aiming to synthesise aligned hexagonal graphene domains.

7.3.1 Influence of crystallographic orientations of 99.999 % Alfa Aesar Cu foil

I synthesised characteristic hexagonal-shaped graphene domains via APCVD on 99.999 % Alfa Aesar Cu foils and conducted SEM and EBSD mapping to correlate the orientation of the domains with the Cu crystallographic orientations, Figure 80.

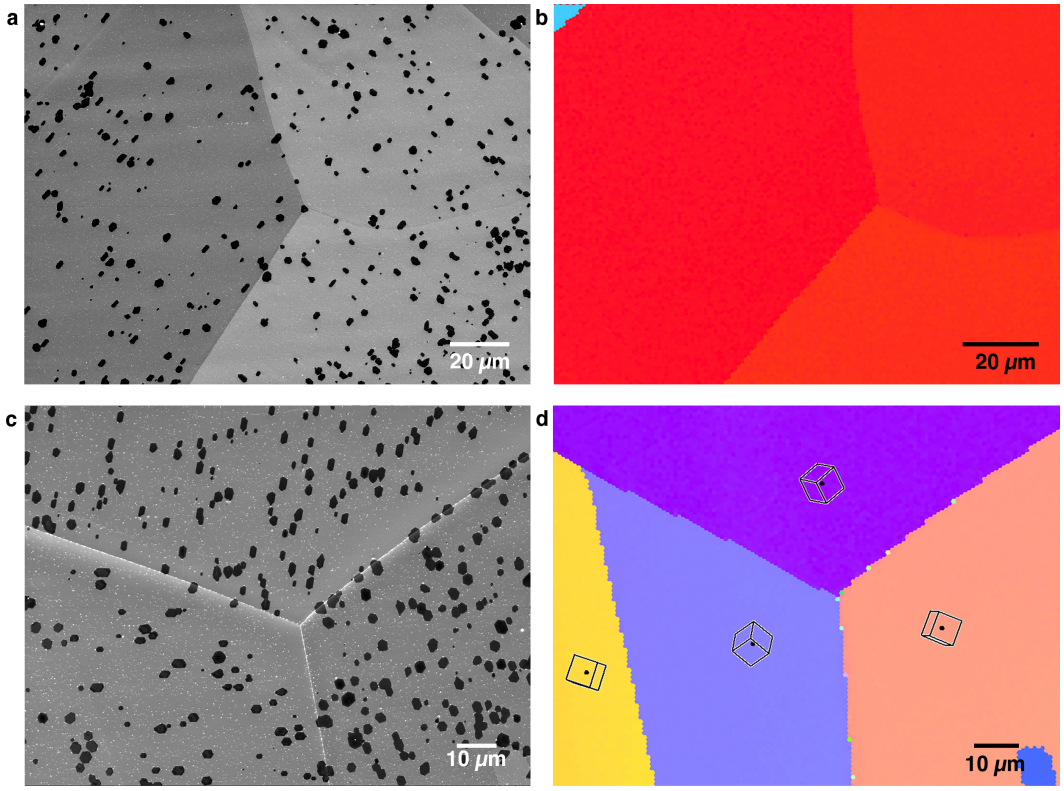
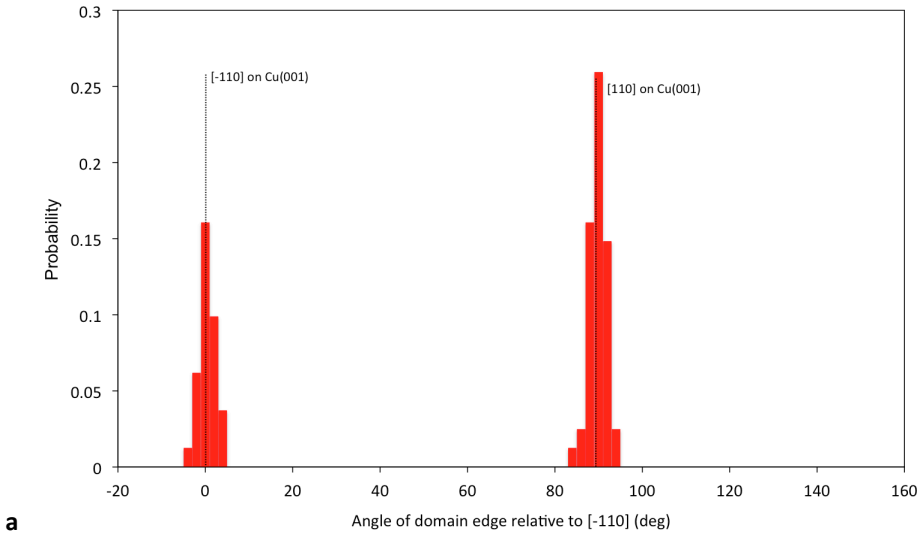
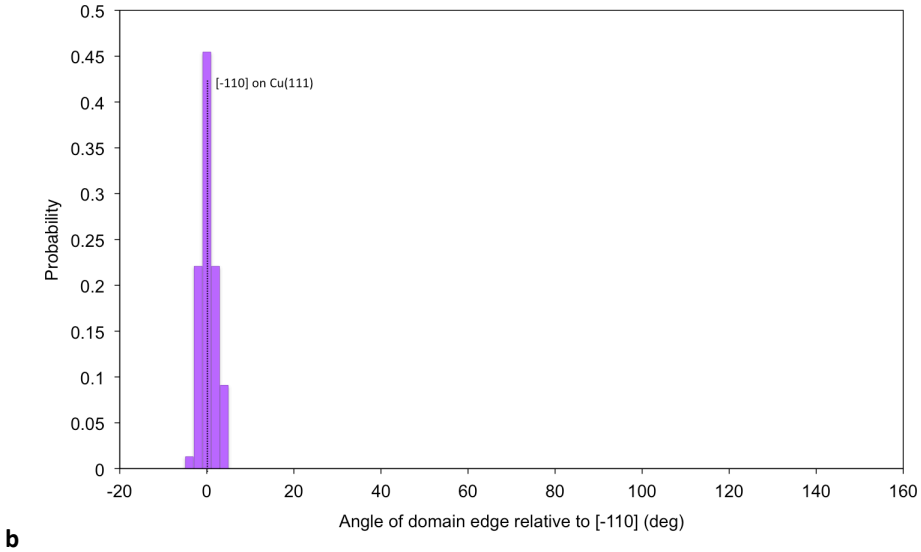


Figure 80: Variation of orientation of isolated hexagonal APCVD graphene domains on 99.999 % Alfa Aesar Cu foil (a)(c) SEM images demonstrating variation in orientation of hexagonal APCVD graphene domains on 99.999 % Cu foil. (b)(d) Associated EBSD maps with colours corresponding to the Cu crystal plane normals indexed and unit cubes demonstrating crystallographic orientations

The hexagonal domains orientated to two <101> directions, ~90˚ rotated, on grains close to Cu{001} (red region in Figure 80b) and to a single <101> direction on grains close to Cu{111} (purple and blue region in Figure 80d). Less alignment is observed on grains misoriented between Cu{001} and Cu{101} (orange and yellow regions in Figure 80). This is equivalent to my observations for the alignment of LPCVD graphene domains. It is noteworthy that domain alignment was not immediately discernable on Cu{001} compared to Cu{111}. This is due to the six-fold symmetrical hexagonal domains orientating to the two <101> directions on Cu{001} so at most only 30˚ separates the two possible orientations of the domains. To quantify the degree of alignment I measured the edge orientation relative to the <101> direction of the underlying Cu grain for over 50 graphene domains on Cu{001} and Cu{111}, Figure 81.



a



b

Figure 81: Distribution of edge angle of hexagonal APCVD graphene domains on 99.999 % Alfa Aesar Cu foil, measured relative to [-110] (a) on Cu{001}, (b) on a crystallographic orientation near Cu{111}

The distribution of edge orientations on Cu{001} is bimodal with 37% of measurements distributed around [-110] and 67% distributed around [110]. The means of the two modes are -0.5˚ and 1˚ misaligned from the ideal, respectively. Both show a standard deviation of 2%. On Cu{111} the measurements are centred -0.5˚ from the [-110] direction, with a standard deviation of 2˚.

7.3.2 Influence of crystallographic orientations of 99.8 % Alfa Aesar Cu foil

I also conducted investigations using 99.8 % Alfa Aesar Cu foil and again observed preferential alignment of the hexagonal APCVD graphene domains to the <101> directions, Figure 82.

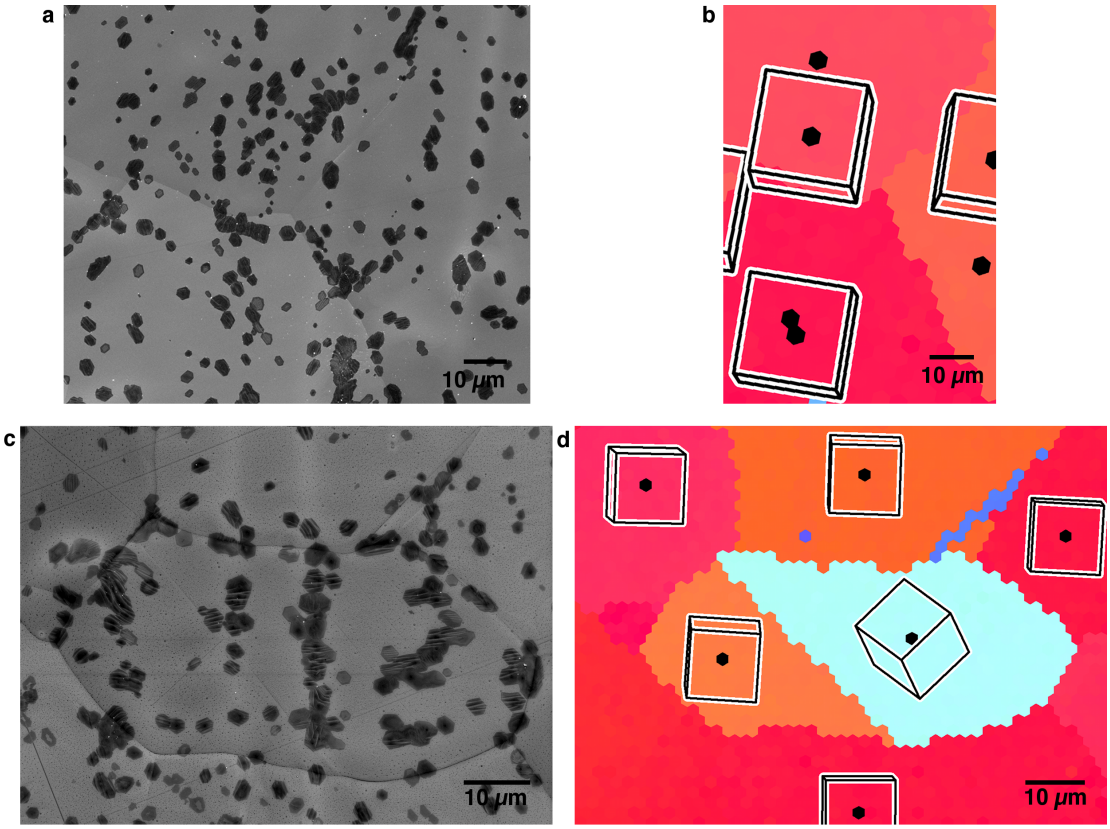


Figure 82: Variation of orientation of isolated hexagonal APCVD graphene domains on 99.8 % Alfa Aesar Cu foil (a)(c) SEM images demonstrating variation in orientation of hexagonal APCVD graphene domains on 99.8 % Alfa Aesar Cu foil. (b)(d) Associated EBSD map with colours corresponding to the Cu crystal plane normal indexed and unit cubes demonstrating crystallographic orientations

On 99.8 % Alfa Aesar Cu foil the graphene domains showed greater misalignment compared to the 99.999 % Alfa Aesar Cu foils. I hypothesise that the increased misalignment is due to greater topographical variations in the foil, as is confirmed in Chapter 8.1.1.1. The increased misalignment is visible as a broader distribution for the measurements of the edge angle of the graphene domains, Figure 83.

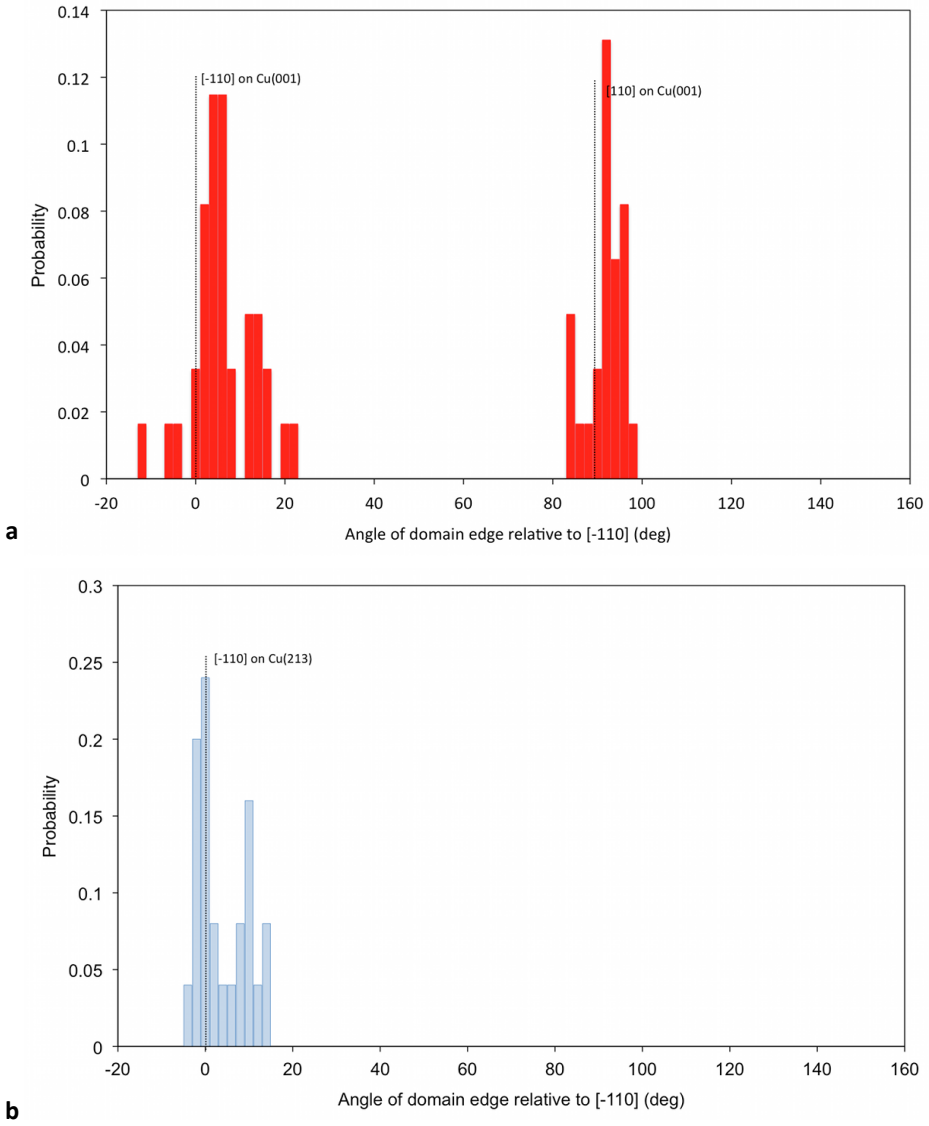


Figure 83: Distribution of the edge angle of hexagonal APCVD graphene domains grown on 99.8 % Alfa Aesar Cu foil, measured relative to [-110](a) On Cu{001}, (b) On a crystallographic orientation misaligned from Cu{111}

The domain edge orientation was measured for over 60 graphene domains on Cu{001} and showed a bimodal distribution aligning to the <101> directions. The means of the two modes were misaligned 4˚ and 1˚, with standard deviations of 7˚ and 4˚ respectively. On a grain with crystallographic orientation misaligned from Cu{111} the edge orientation of over 30 domains was measured and found to orient around the [-110] direction, with an average of 3˚ misalignment and a standard deviation of 6˚.

7.3.3 Influence of crystallographic orientation of 99.9 % Goodfellow Cu foil

As a final investigation I synthesised isolated domains on 99.9 % Goodfellow Cu foil. As in the previous cases with different substrates I again observed preferential alignment of the hexagonal APCVD graphene domains to the <101> directions, Figure 84, even on surfaces with many small Cu grains.

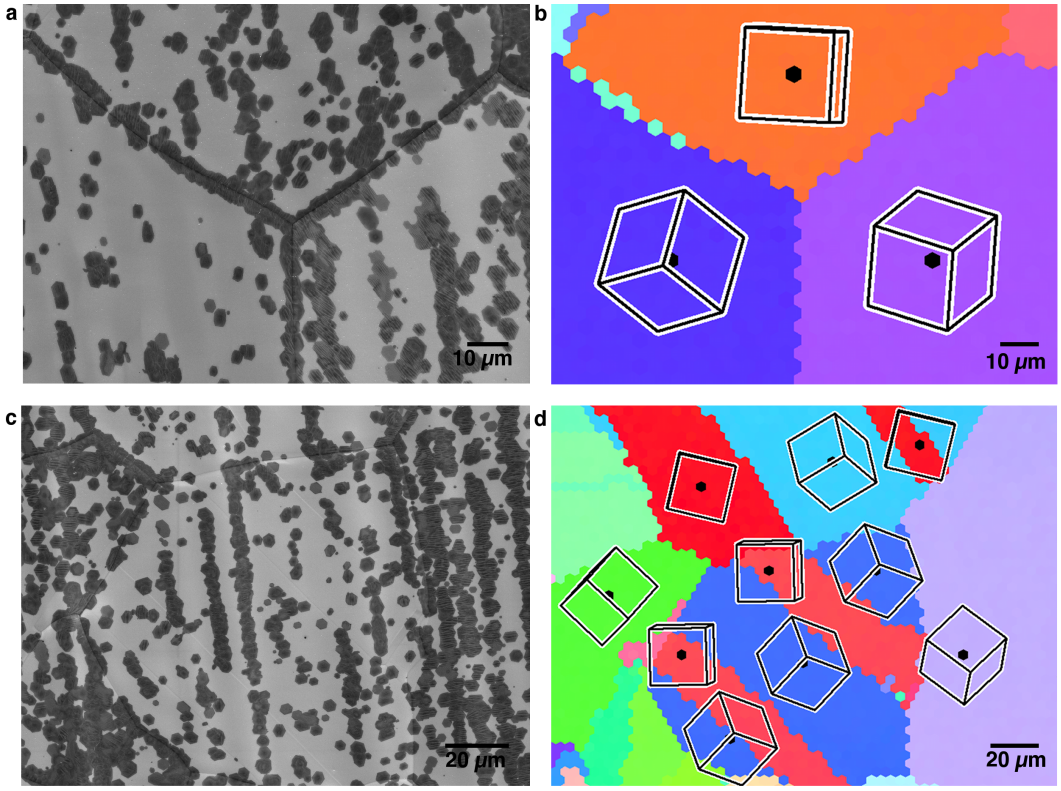


Figure 84: Variation of orientation of isolated hexagonal APCVD graphene domains on 99.9 % Goodfellow Cu foil (a)(c) SEM images demonstrating variation in edge alignment of hexagonal APCVD graphene domains on 99.9 % Goodfellow Cu foil. (b)(d) Associated EBSD maps with colours corresponding to the Cu crystal plane normals indexed and unit cubes demonstrating crystallographic orientations

Comparing the SEM images with EBSD crystallographic orientations, the hexagonal domains show significant alignment to <101> direction on grains close to Cu{111} (purple and blue regions in Figure 84) and Cu{101} (green region in Figure 84). The graphene domains align to two 90˚ rotated <101> directions on Cu{001} (red region in Figure 84) and on the grains misaligned from Cu{001} (pink and orange regions in Figure 84). The measured distribution of edge alignment of graphene domains on

99.9 % Goodfellow Cu foil, Figure 85, showed similar results to the previous investigations.

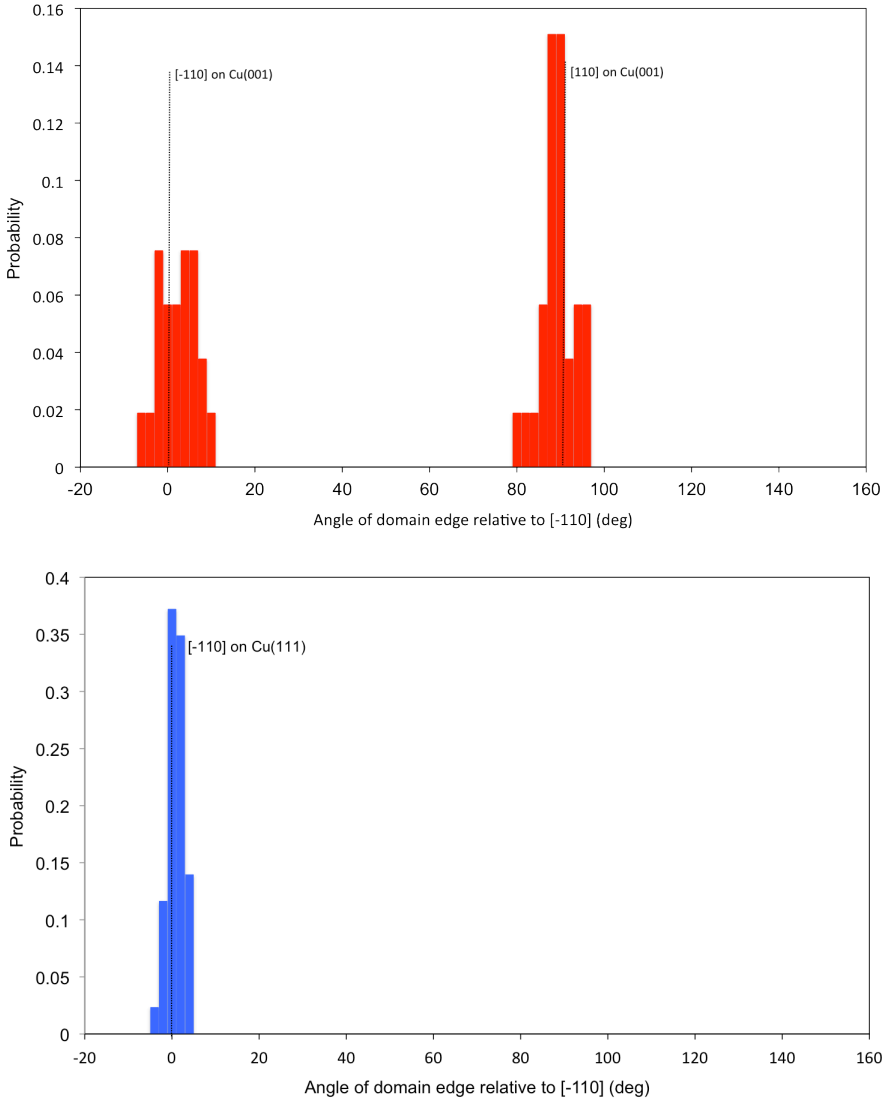


Figure 85: Distribution of the edge alignment of hexagonal APCVD graphene domains grown on 99.9% Goodfellow Cu foil, measured relative to [-110](a) On Cu(001), (b) On Cu(111)

The edge orientation was measured for over 50 graphene domains on Cu(001) and showed a bimodal distribution, with 43% of domains aligning around [-110] and 57% aligning around [110]. The means of the two modes were both misaligned 1.6˚ from the ideal, and had standard deviations of 4.3˚ and 3.9˚ respectively. On Cu(111) the domains aligned to the [-110] direction, with no misalignment from the ideal mean and a standard deviation of 1.7˚.

7.4 Variation of Cu crystallographic orientations with Cu foils

I conducted large-area EBSD mapping on the Cu foils to investigate the distribution of crystallographic orientations and grain sizes of the annealed Cu foils, Figure 86.

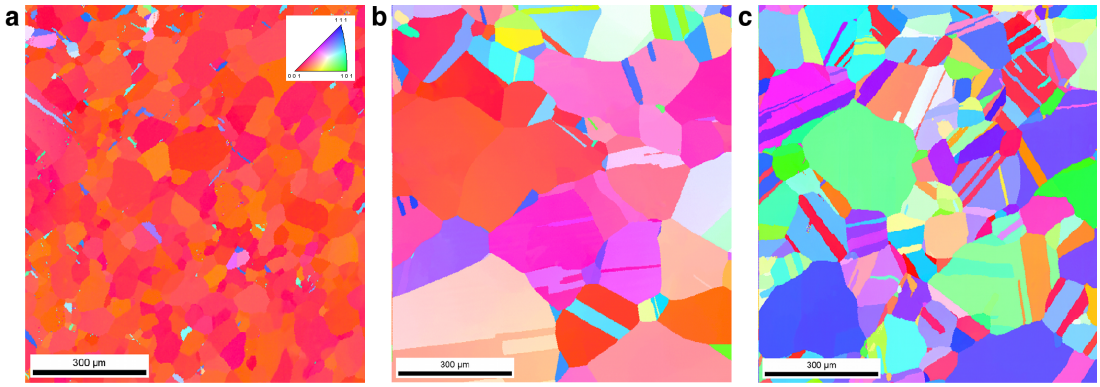


Figure 86: Large-area EBSD maps of crystallographic orientations of various Cu foils (a) 99.8 % Alfa Aesar, (b) 99.999 % Alfa Aesar, (c) 99.9 % Goodfellow.

The large-area EBSD mapping demonstrates that grain size and crystallographic orientations vary greatly between different Cu foils. The 99.8% coated Alfa Aesar is almost entirely composed of grains less than 100 µm in size with crystallographic orientations near to Cu{001}. Very few grains of Cu{111} or Cu{101} are visible. In comparison, many grains in excess of 300 µm with high-index orientations are visible on the higher purity 99.999 % Cu foil supplied by Alfa Aesar. When viewing the EBSD map from the 99.9 % Goodfellow Cu foil, the grains are between 100 - 200 µm in size, with Cu{101} and Cu{111} the dominant orientations. Detailed investigations into variations of crystallographic orientations for different Cu foils are presented in Chapter 8.1.1.3, Figure 104. These initial investigations demonstrate that while Cu foils may be sourced from the same supplier, or have the same purity, each foil possesses a distribution of grain sizes and crystal surfaces that are unique to the specific foil. This knowledge is important for understanding the differences between graphene synthesised on different Cu foils, and particularly, how the alignment of graphene domains will vary for different Cu foils. Due to the abundance of Cu{001} in the 99.8 % Alfa Aesar Cu foil, hexagonal domains synthesised on this surface will almost exclusively have edges aligning to two ~90˚ rotated <101> directions. This could explain why researchers who use 99.8 % Alfa Aesar Cu foil did not previously identify the alignment of domains via the Cu crystallographic orientation. In

comparison, distinctive edge alignment of hexagonal domains was easily identified on low purity Cu foils purchased from an alternative supplier, 99.9 % Goodfellow, due to the prevalence of large grains with orientations near Cu{111} and Cu{101}.

7.5 Computational modelling of graphene on primary Cu crystallographic orientations

As large-area graphene domains are commonly single crystalline, I hypothesised that a domain's final alignment may be dictated by the preferential orientation of nanoscale nucleating domains on the Cu surface. Computational modelling provides an opportunity to investigate this, corroborating the experimental observations and providing further insight. Such a model has since been theoretically evaluated by Zhang *et al.*[315]. This study shows the hexagonal graphene lattice has varying affinity for different crystallographic orientations of Cu. This suggests that a decisive factor during domain formation is the minimisation of the lattice mismatch between the graphene and the Cu. Electron hybridisation may also stabilise and promote domain growth.

The three low index orientations, Cu{101}, Cu{001} and Cu{111}, were modelled with three-dimensional side-on views presented in Figure 87a-c (different coloured spheres represent the second and third atomic layers). The atomic arrangement and symmetry of the surface varies from one crystallographic orientation to the next, Figure 87(d-f), and can be summarised as follows:

- Cu(101): two-fold symmetrical rectangular lattice with unit cell a = 3.615 Å and $a\sqrt{2}/2$ = 2.556 Å,
- Cu(001): four-fold symmetrical square lattice with unit cell $a\sqrt{2}/2$ = 2.556 Å,
- Cu(111): six-fold symmetrical hexagonal lattice with unit cell $a\sqrt{2}/2$ = 2.556 Å.

Cu(101) is the most open surface displaying the conspicuous channels that are known to promote deposition and surface diffusion in the [-101] direction[316].

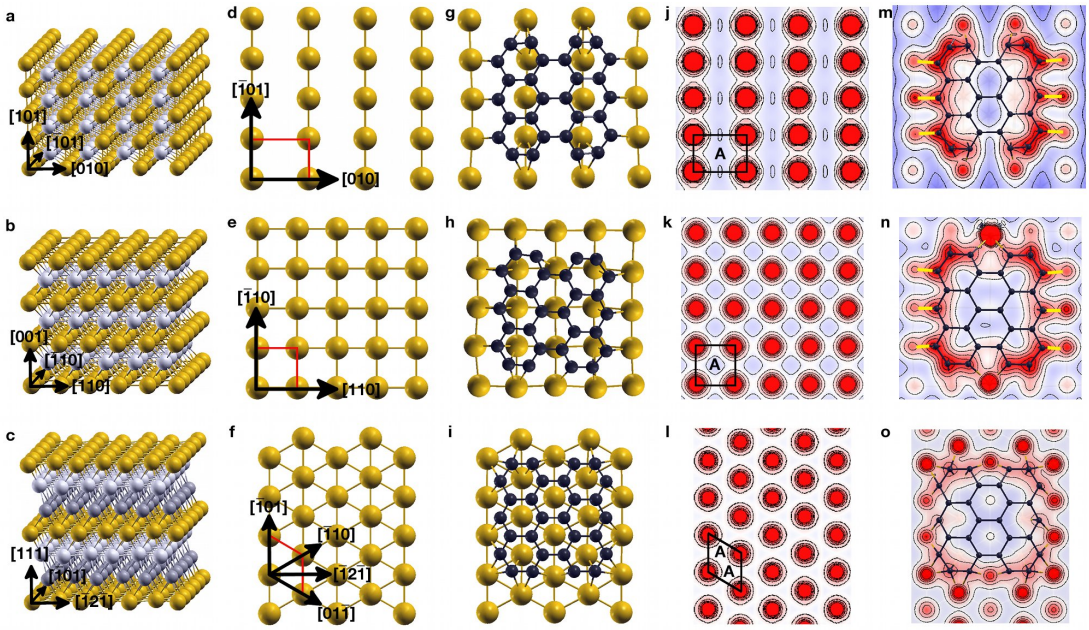


Figure 87: Computational modelling of graphene on primary Cu crystallographic orientations (a)(b)(c) Three-dimensional side-on view of the crystal structure of Cu(101), Cu(001) and Cu(111), respectively, with surface normal pointing upwards as indicated by vectors. (d)(e)(f) Top-down view of surface of Cu(101), Cu(001), and Cu(111), respectively, demonstrating varying lattice and symmetry. (g)(h)(i) Model graphene domain, C_{28}, on Cu(101), Cu(001) and Cu(111), respectively, demonstrating preferential zig-zag edge orientation with Cu <101> direction(s). (j)(k)(l) Total electron density plot of Cu{101}, Cu{001} and Cu{111}, respectively. Electron density increases from blue to red. Red circles correspond to the surface atoms (high electron density), while regions with depleted electron density are equivalent to available adatom sites (labelled A). (m)(n)(o) Total electron density contour plot for graphene cluster, C_{28}, on Cu(101), Cu(001) and Cu(111) respectively, projected at the interlayer plane between the substrate and C_{28}. Strong one-to-one hybridisation occurs along the Cu <101> direction between the electron orbitals of the zigzag edge atoms of C_{28} and Cu surface atoms on Cu(101) and Cu(001), indicated by yellow lines. Weaker one-to-two atom bonding between one C and two Cu atoms is observed on Cu(111). Reproduced from Murdock et al.[1]

A model graphene cluster (C_{28}), which included representative zigzag edges ($a_{cc}\sqrt{3}$ =2.46 Å) and armchair edges ($3a_{cc}$ =4.26 Å), was allowed to relax on each Cu surface so that the system energy was minimised, Figure 87g-i. Hexagons of C atoms preferentially located above Cu atoms. By comparing with a plot of the total electron density of each surface, Figure 87j-l (with increasing electron density represented by colour scale from blue to red), this arrangement corresponds with C atoms locating at the available adatom sites of low electron density (labelled A in Figure 87j-l). The zigzag edges of C_{28} preferentially oriented with the <101> direction of the Cu surface,

irrespective of Cu crystallographic orientation. Alternative orientations of C_{28} on anisotropic Cu{101} produced a lattice mismatch, Figure 88, causing a higher energy state. On Cu{001} the C_{28} cluster showed equivalent preference to align with zigzag edges parallel to [110] or [-110] due to the symmetrical lattice[239, 242, 243]. These results are in agreement with the experimentally observed alignment of graphene domains to one direction on Cu{111} and Cu{101}, and two ~90˚ rotated alignments on Cu{001}.

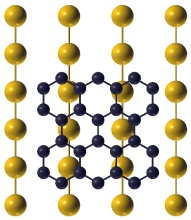


Figure 88: Graphene cluster C_{28} on Cu{101} oriented with armchair edge parallel to [-101] demonstrating lattice mismatch when compared to orientation of the zigzag edge parallel to [-101] as in Figure 87c.

The bonding of C_{28} with the Cu surface atoms provides further detail about the stability and growth of nanoscale domains. The characteristic dangling bonds of the zigzag edge of graphene[317], represented within the C_{28} cluster, form directional bonds with Cu surface atoms along the <101> direction(s) on Cu{101} and Cu{001}, Figure 87m and Figure 87n respectively. This stabilises the cluster on these surfaces On Cu{111} the zigzag edge atoms hybridise with two neighbouring Cu atoms while the outermost armchair edge atoms hybridise mainly amongst themselves, as reported for graphene armchair edges[317], Figure 87o. On all Cu surfaces the C_{28} cluster exhibits enhanced electron density at the corners that correspond with potential growth sites in the [-101] direction, and may explain the experimentally observed lobes in LPCVD domains.

The wavefunction at the Fermi level of C_{28} shows characteristic open 2p C orbitals along the zigzag edge[317], Figure 89a. For Cu(101), with $3d_{eg}$ orbitals of surface atoms pointing outwards, the wavefunction at the Fermi level demonstrates that the surface channels[316] exhibit electron depletion aligned along the [-101] direction Figure 89b. When C_{28} is placed on Cu{101} the zigzag edge atoms alternate between

hybridising with the surface and manifesting active sites, while armchair edge atoms instead hybridise amongst themselves, Figure 89c.

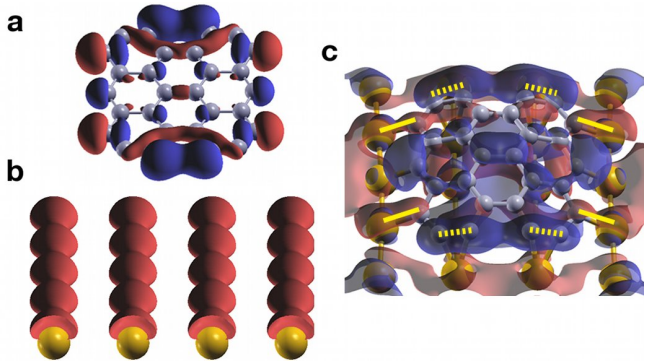


Figure 89: Wavefunction representation of graphene cluster on Cu{101}
(a) Wavefunction at the Fermi level for free-standing C_{28} graphene cluster, showing the 2p C orbitals along the zigzag edges. (b) Wavefunction at the Fermi level for Cu{101} surface layer. Lobes of the 3d electrons point outwards while characteristic channels show electron depletion. (c) Wavefunction at the Fermi level for C_{28} graphene cluster on Cu{101}. Blue and red regions correspond to the positive and negative values of the wavefunction, respectively. On the zigzag edge of C_{28} the red lobes of the 2p C orbitals hybridise with red lobes of the 3d Cu orbitals to forms directional bonds (solid yellow lines), while blue lobes represent active sites. On the armchair edge of C_{28} hybridisation occurs between neighbouring C atoms (dashed yellow lines). Reproduced from Murdock et al.[1]

The presence of the surface channel, emergence of 2p-3d hybridisation, and the relatively small lattice mismatch explain the experimentally observed stability and [-101] orientation of graphene domains on Cu(101). For channel-free surfaces, such as Cu{001} and Cu{111}, growth is likely to occur along the zigzag edge, in agreement with calculations for the favourable attachment of monomers to armchair edges[212]. Zigzag edges are therefore promoted on Cu{001} and Cu{111}.

7.6 Conclusions on the influence of Cu crystallographic orientation on the growth and properties of graphene domains

Our experiments demonstrate that epitaxial growth and edge alignment is observed for LPCVD and APCVD synthesis, using low purity and high purity Cu foil (99.8 % and 99.999 %), and for Cu foil sourced from two different suppliers (Alfa Aesar and Goodfellow). The crucial requirement for alignment of domain edges to one direction is the presence of Cu grains exhibiting crystallographic orientations of Cu{101} or Cu{111}. Under atmospheric-pressure conditions this results in

crystallographic orientation dependent alignment of hexagonal graphene domains, Figure 90.

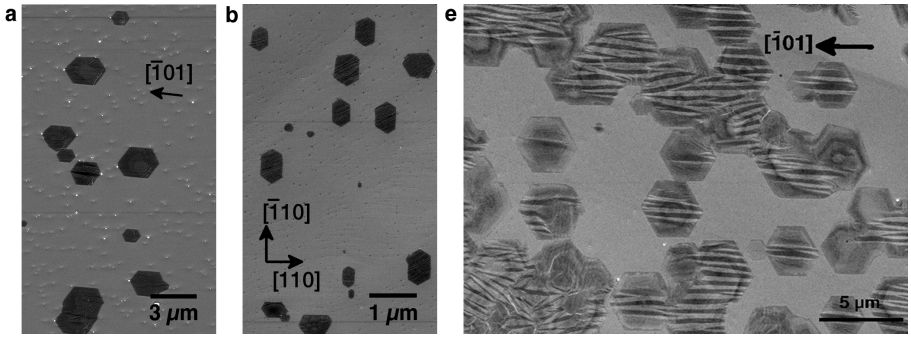


Figure 90: Orientation dependence of APCVD hexagonal graphene domains on polycrystalline Cu (a)(b) SEM images of APCVD hexagonal graphene domains grown on high purity (99.999 %) Alfa Aesar Cu foil, demonstrating alignment to one direction on Cu{111} and two directions on Cu{001}, respectively. (c) SEM image of APCVD hexagonal graphene domains grown on low purity (99.9 %) Goodfellow Cu foil, demonstrating alignment to one direction on Cu{101}.
Reproduced from Murdock et al.[1]

Our studies clarify why, to date, this phenomenon has been largely overlooked, particularly when using 99.8 % Alfa Aesar Cu foil. I therefore conclude that this observation of epitaxial growth is directly related to the crystallographic orientation of the Cu substrate, and is independent of the Cu purity and supplier. The discovery of substrate-controlled edge alignment of hexagonal graphene domains is an important advance towards the development of high-quality, large-area CVD graphene composed of perfectly orientated hexagonal domains that merge together with ideal, low-angle, defect-free domain boundaries.

8 Influence of the properties of copper foils on the growth of chemical vapour deposition graphene

This chapter outlines experiments investigating the influence of the Cu foil substrate on graphene growth. While the synthesis parameters of reactant gas concentration, reactant gas flow rate, synthesis temperature and synthesis time presented in Chapter 5 and Chapter 6 undoubtedly play an important role in dictating the growth of graphene via LPCVD and APCVD, early in my research project I hypothesised that the Cu foil's properties could also be an important factor. These investigations also follow from those presented in Chapter 7 with a natural question being how the distribution of crystallographic orientations varied between different Cu foils, and furthermore, whether any other properties of the Cu foil could influence graphene growth. While I completed the great majority of experiments presented in this chapter, Ms Jude Britton and Dr Antal Koos assisted with CVD experiments and SEM imaging, and Dr Hugh Bishop and Dr Alison Crossley (Oxford Materials Characterisation Services) conducted XPS and SIMS analysis.

Parts of this chapter have been prepared for publication:

Murdock, A.T., Britton, J., van Engers, C., Babenko, V., Lane, G., Bishop, H., Crossley, A., Koos, A.A., Grobert, N., Effect of metal contaminations and cleaning procedures on the CVD growth of graphene and hBN on copper foils, *2D materials*

8.1 Influence of the properties of copper foils on the growth of APCVD graphene

As a consequence of Li *et al*.[144]'s use of commercially available polycrystalline 99.8 % purity Cu foil (25 µm thick, as-received from the supplier, Alfa Aesar), many investigations, including my own, made use of this foil[42, 77, 144, 146, 152, 161, 216-221]. However, this substrate is by no means ideal, as demonstrated in Chapter 5.2 with the initial observation of surface contaminations. Given the Cu substrate provides a supporting surface for graphene growth and simultaneously catalytically assists the growth mechanism, investigations into the influence of the Cu foil's properties on

graphene growth are well-justified. In particular, I questioned whether expensive, high-purity Cu foils would show benefits compared to the relatively cheap 99.8 % Alfa Aesar Cu foil. To investigate this I sourced Cu foils with varying purity from two suppliers, Table 1.

Table 1: Details of Cu foils used for graphene growth

Purity (%)	*Brand*	*Descriptor*	*Thickness (µm)*	*Item number*
99.8	**Alfa Aesar**	**-**	**25**	**13382**
99.99+	**Alfa Aesar**	**-**	**127**	**00095**
99.999	**Alfa Aesar**	**Puratronic®**	**25**	**10950**
99.9999	**Alfa Aesar**	**Puratronic®**	**50**	**42972**
99.9	**Goodfellow**	**Annealed**	**25**	**375-907-90**

During the course of the investigation Alfa Aesar rebranded item 13382, and now supplies low purity Cu foil as summarised in Table 2.

Table 2: Details of rebranded Cu foils used for graphene growth

Purity (%)	*Brand*	*Descriptor*	*Thickness (µm)*	*Item number*
99.8	**Alfa Aesar**	**Coated**	**25**	**13382**
99.8	**Alfa Aesar**	**Uncoated, for graphene growth**	**25**	**46986**

Consequently, I used six Cu foils: the five foils listed in Table 1, with item number 13382- previously referred to as “99.8 % Alfa Aesar” in Chapter 5, Chapter 6 and Chapter 7- now referred to as “Coated 99.8 % Alfa Aesar”, and the additional item number 46365 from Table 2, referred to as “Uncoated 99.8 % Alfa Aesar”. The properties of the Cu foils were then investigated, Chapter 8.1.1, and this was compared with APCVD and LPCVD growth of graphene on each foil, Chapter 8.1.2 and Chapter 8.1.3.

8.1.1 Variations of copper foils due to purity and supplier

Differences will exist between different types of Cu foil due to natural variations within the raw material and the influence of processing by suppliers. Cu foils with different purities will more than likely have been processed in a different manner, and may originate from different origins. In a similar vein, Cu foils of similar purity but purchased from different suppliers may in fact show few similarities when compared by their physical and chemical properties.

The key properties I identified that may vary between different Cu foils include:

- Surface topography and roughness,
- Surface coatings and contaminations,
- Dissolved impurities,
- Crystallographic orientations, and
- Grain sizes.

I investigated these properties for the six Cu foils listed in Chapter 8.1 using SEM, OP, EBSD, XPS and SIMS. Prior to characterisation the Cu foils were annealed using the procedure outlined in Chapter 5 that was used before all LPCVD and APCVD growth: 30 minutes annealing at 1035 ˚C under 500 sccm H_2. By comparing the growth of graphene on each foil (conducted under identical conditions) with the respective foil's properties I demonstrate that subtle variations between Cu foils can influence the growth of graphene.

With respect to the uniformity of the Cu foils, and whether the characterisation of individual samples is representative, where possible measurements were repeated and compared for consistency, for instance, during SEM imaging and OP measurements. However, due to the nature and time restraints of some characterisation techniques, notably XPS, SIMS and EBSD, multiple reiterations of measurements were not possible. As such, while some variability no doubt exists across a foil, particularly with respect to surface coatings, due to the restrictions of the study and based on SEM imaging the uniformity of the foils has been assumed.

8.1.1.1 Surface topography and roughness of annealed copper foils via SEM and optical profilometry

The surface topography and roughness of the Cu foils, and the presence of contamination particles on this surface, may influence the growth of graphene. Increased surface roughness is known to increase the nucleation density of domains[121, 189, 225, 226]. Surface contamination particles can also promote nucleation and multilayer growth[219, 222, 227], or etching of domains[299].

SEM demonstrates that the surface topography and surface contamination particles varied for the six Cu foils after annealing, Figure 91.

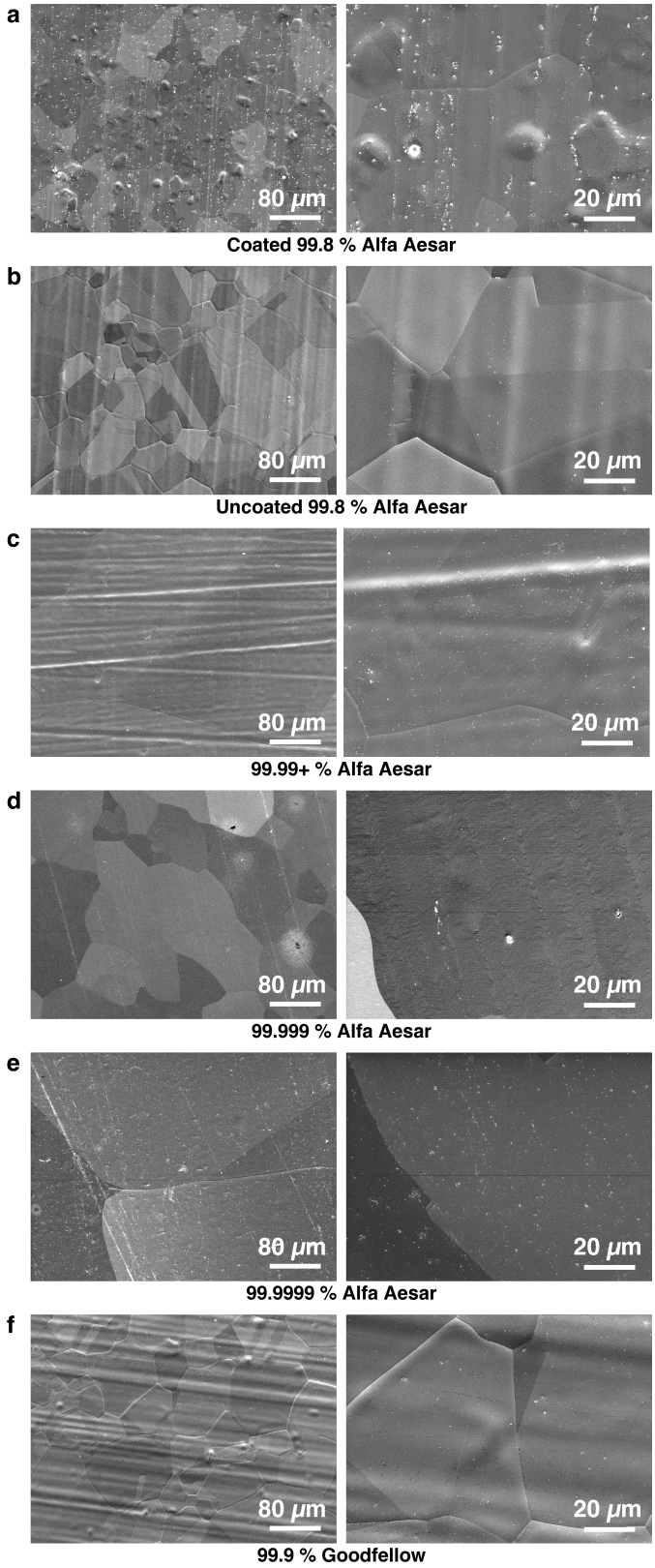


Figure 91: SEM images of various Cu foils annealed at 1035 ˚C for 30 minutes under 500 sccm H_2 (a) Coated 99.8 % Alfa Aesar, (b) Uncoated 99.8 % Alfa Aesar, (c) 99.99+ % Alfa Aesar, (d) 99.999 % Alfa Aesar, (e) 99.9999 % Alfa Aesar, (f) 99.9 % Goodfellow. Low and high magnification images

Parallel striations are visible on the Coated 99.8 % Alfa Aesar, Uncoated 99.8 % Alfa Aesar, 99.99+ % Alfa Aesar, and 99.9 % Goodfellow Cu foils, a residual effect of a cold-rolling stage in the manufacturing procedure (Figure 91a, b, c and f, respectively). These striations appear particularly visible on the 99.9 % Goodfellow Cu foil, Figure 91f, perhaps due to a variation in the process used by Goodfellow and Alfa Aesar. Striations are less pronounced on the higher purity foil of 99.999 % Alfa Aesar, and more-or-less absent on the 99.9999 % Alfa Aesar (Figure 91d and e, respectively). Otherwise, circular mounds are visible on the 99.8% coated Alfa Aesar Cu foil, Figure 91a. There is no clear correlation between the supplier-stated purity of the Cu foils and the amount of surface contamination particles. The highest density of particles is visible on the Coated 99.8 % Alfa Aesar Cu foil, Figure 91a, ranging in size from sub-500 nm (uniformly distributed at high density) to larger particles, 5 - 10 μm. In comparison, the Uncoated 99.8 % Alfa Aesar Cu foil, Figure 91b, shows only a sparse amount of sub-500 nm particles. A relatively uniform coverage of sub-micron particles is visible on all the other Cu foils. High-density contaminations covering circular regions 100 μm in diameter are also visible on the 99.999 % Alfa Aesar Cu foil, along with contaminations along the faint parallel striations, Figure 91c.

Optical profilometry of the annealed Cu foils provides a visualisation of the surface topography, Figure 92, and a quantitative measure of average surface roughness, S_a (calculated from five different measurements), Figure 93. Measurements were conducted within 48 hours of annealing, with the foils were stored in Ar atmosphere.

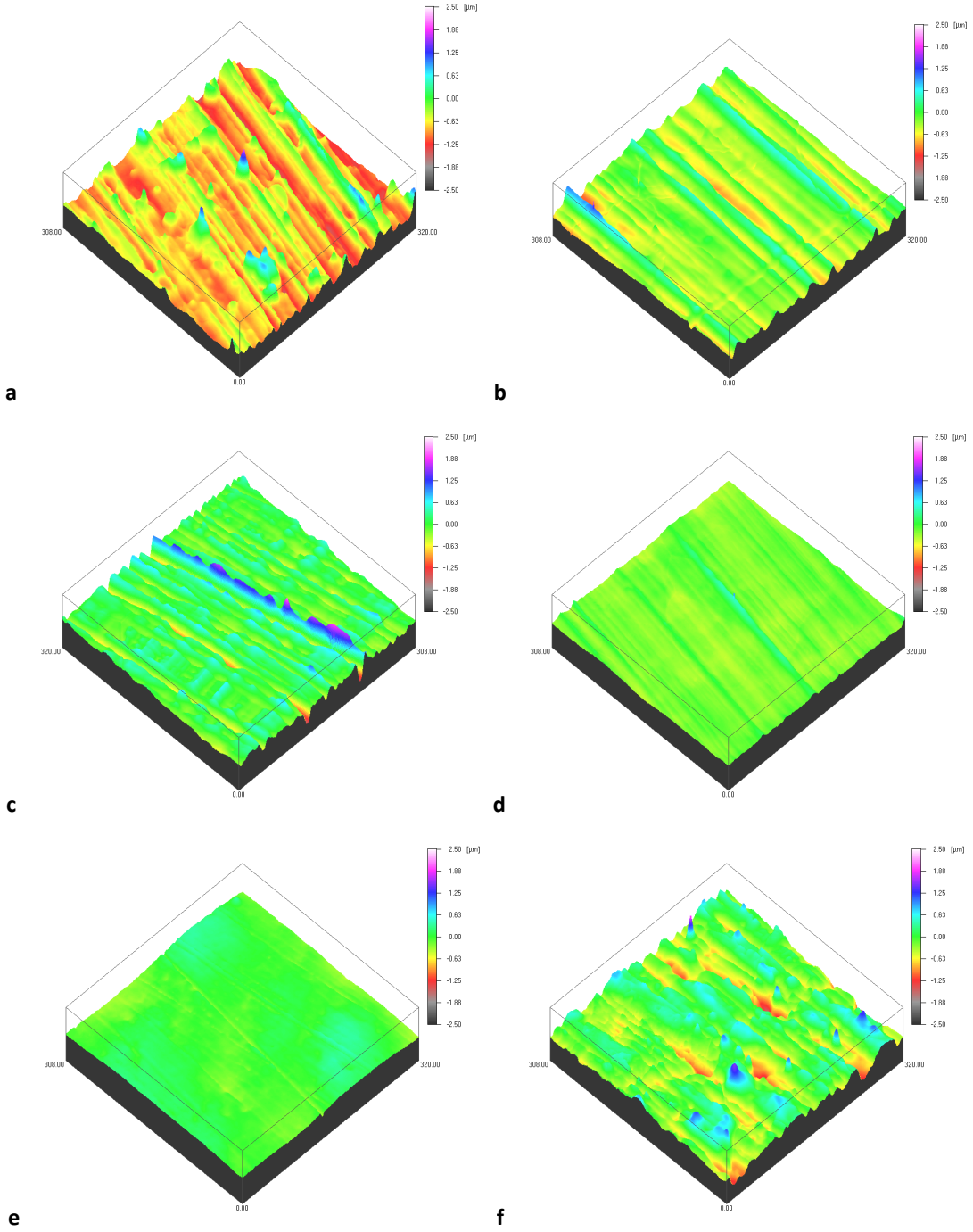


Figure 92: Optical profilometry 3D images of various Cu foils annealedat 1035 ˚C for 30 minutes under 500 sccm H_2 (a) Coated 99.8 % Alfa Aesar, (b) Uncoated 99.8 % Alfa Aesar, (c) 99.99+ % Alfa Aesar, (d) 99.999 % Alfa Aesar, (e) 99.9999 % Alfa Aesar, (f) 99.9 % Goodfellow. 308 x 320 µm, total z-range of 5 µm, with the mean height offset to Z= 0 µm

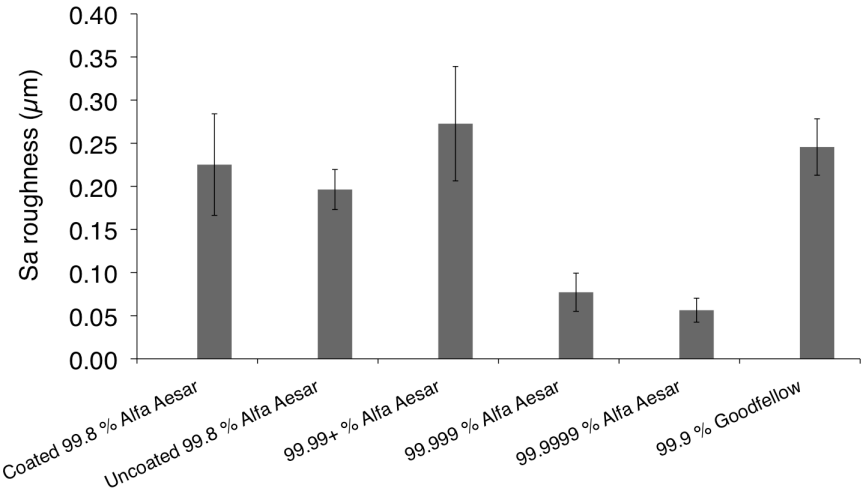


Figure 93: Optical profilometry measured mean surface roughness of various annealed Cu foils with error bars indicating 95% confidence interval

The surface topography and roughness differs between each annealed Cu foil, with grain boundaries, surface contamination particles, and residual striations from cold rolling visible. Cold rolling striations, identified by parallel ridges running across the substrate, are visible on the Coated 99.8 % Alfa Aesar, the Uncoated 99.8 % Alfa Aesar, the 99.99+ % Alfa Aesar and the 99.9 % Goodfellow Cu foil (Figure 92a, b, c and f, respectively). The striations, have the greatest influence on the topography of the 99.99+ % Alfa Aesar Cu foil, Figure 92c, making this the roughest surface with an average S_a of 0.27 µm. Bumps are on the surface of the Coated 99.8 % Alfa Aesar and the 99.9 % Goodfellow Cu foils, Figure 92a and f, resulting in a high S_a of 0.23 µm and 0.25 µm, respectively. In comparison, no bumps are visible on the Uncoated 99.8 % Alfa Aesar, Figure 92b, which has a lower average surface roughness of 0.20 µm. Comparing with SEM, Figure 91, these bumps are associated with topographical features and surface contaminations. The smoothest surfaces are the 99.999 % Alfa Aesar and 99.9999 % Alfa Aesar, Figure 92d and e, with an average S_a of 0.075 µm and 0.055 µm, respectively. Although grain boundaries did produce some topographical variations- indeed, they are present in each of the images in Figure 92, and can be visualised with an appropriate image contrast, Figure 94- their influence on the surface topography is insignificant in comparison to that of cold rolling striations and surface contaminations.

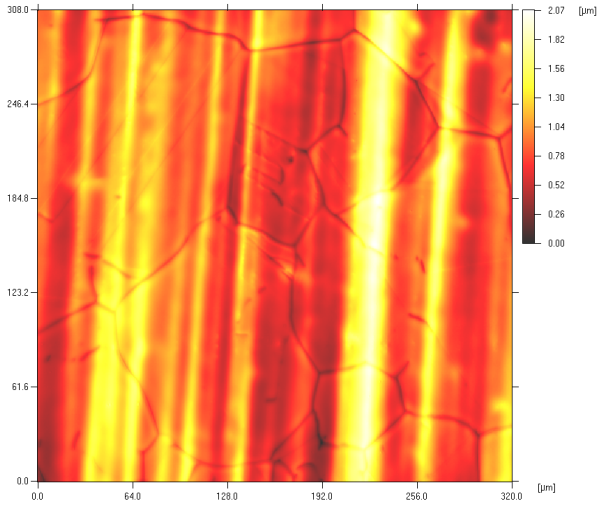


Figure 94: Optical profilometry 3D image of annealed Uncoated 99.8 % Alfa Aesar Cu foil with cold rolling striations and grain boundaries

8.1.1.2 Chemical composition and concentration of surface contaminations and dissolved impurities of as-received and annealed copper foils via XPS and SIMS

The contamination particles observed on the surface of the Cu foils in Chapter 8.1.1.1 may significantly influence the growth of graphene. Some chemical species can act as a catalyst to increase the nucleation density, growth rates of graphene, and promote multilayers[219, 222, 227], while others can inhibit the growth of graphene and increase etching[299, 318-320]. XPS and SIMS are powerful surface specific techniques for elemental analysis of surface contaminations, coatings and dissolved impurities.

XPS was conducted on the Cu foils (i) as-received from the supplier, (ii) following ion bombardment, and (iii) following annealing for 30 minutes at 1035 ˚C under 500 sccm H_2, Table 3 and see Appendix for raw spectra. Analysis of the as-received Cu foils investigated surface coatings from processing, Figure 95a. Carbon, oxygen and nitrogen were detected, but these may originate from adventitious contamination by absorbed species from the atmosphere. Phosphorous (4.9 atomic %), calcium (4.4 atomic %) and chromium (2.1 atomic %), either as the native species or an oxide, were detected on the Coated 99.8 % Alfa Aesar Cu foil. In comparison, no metallic species were detected on Uncoated 99.8 % Alfa Aesar Cu foil. Silicon was detected on the 99.999 % Alfa Aesar (2.7 atomic %) and the 99.9999 % Alfa Aesar

(1.6 atomic %), while low percentages (< 1 %) of chlorine, fluorine and sulphur were found on various foils.

Table 3: XPS analysis of elemental composition of various Cu foils as-received, following ~2 nm ion bombardment, and following annealing procedure

Cu foil	***Percentage Composition***										
	Cu	***C***	***O***	***N***	***Ca***	***P***	***Cr***	***Si***	***S***	***Cl***	***F***
Coated 99.8 % Alfa Aesar	4.6	32.3	51.7	-	4.4	4.9	2.1	-	-	-	-
Uncoated 99.8 % Alfa Aesar	4.7	71.4	23.9	-	-	-	-	-	-	-	-
99.99+ % Alfa Aesar	3.2	66.9	22.9	7.0	-	-	-	-	-	-	-
99.999 % Alfa Aesar	2.9	69.0	15.4	10.0	-	-	-	2.7	-	-	-
99.9999 % Alfa Aesar	2.7	67.7	14.4	12.7	-	-	-	1.6	-	0.4	0.6
99.9 % Goodfellow	1.3	85.9	12.4	-	-	-	-	-	0.4	-	-
~2 nm ion bombarded Coated 99.8 % Alfa Aesar	13.2	2.1	59.0	-	10.5	7.3	5.2	-	-	-	2.7
~5 nm ion bombarded Coated 99.8 % Alfa Aesar	93.1	1.6	3.4	-	-	-	1.9	-	-	-	-
~2 nm ion bombarded Uncoated 99.8 % Alfa Aesar	39.4	58.7	-	-	-	-	-	-	1.9	-	-
~2 nm ion bombarded 99.99+ % Alfa Aesar	81.4	13.8	4.8	-	-	-	-	-	-	-	-
~2 nm ion bombarded 99.999 % Alfa Aesar	72.4	25.9	1.6	-	-	-	-	-	-	-	-
~2 nm ion bombarded 99.9999 % Alfa Aesar	31.1	49.7	15.0	-	-	-	-	1.8	-	0.7	1.6
~2 nm ion bombarded 99.9 % Goodfellow	26.9	72.2	0.9	-	-	-	-	-	-	-	-
Annealed Coated 99.8 % Alfa Aesar*	32.6	27.7	39.8	-	-	-	-	-	-	-	-
Annealed Uncoated 99.8 % Alfa Aesar *	27.1	27.6	45.4	-	-	-	-	-	-	-	-
Annealed 99.99+ % Alfa Aesar	30.5	18.2	51.4	-	-	-	-	-	-	-	-
Annealed 99.999 % Alfa Aesar	40.0	23.6	36.4	-	-	-	-	-	-	-	-
Annealed 99.9999 % Alfa Aesar	32.4	17.4	50.3	-	-	-	-	-	-	-	-
Annealed 99.9 % Goodfellow	46.1	22.4	31.6	-	-	-	-	-	-	-	-

* Measured separately to other Cu foils

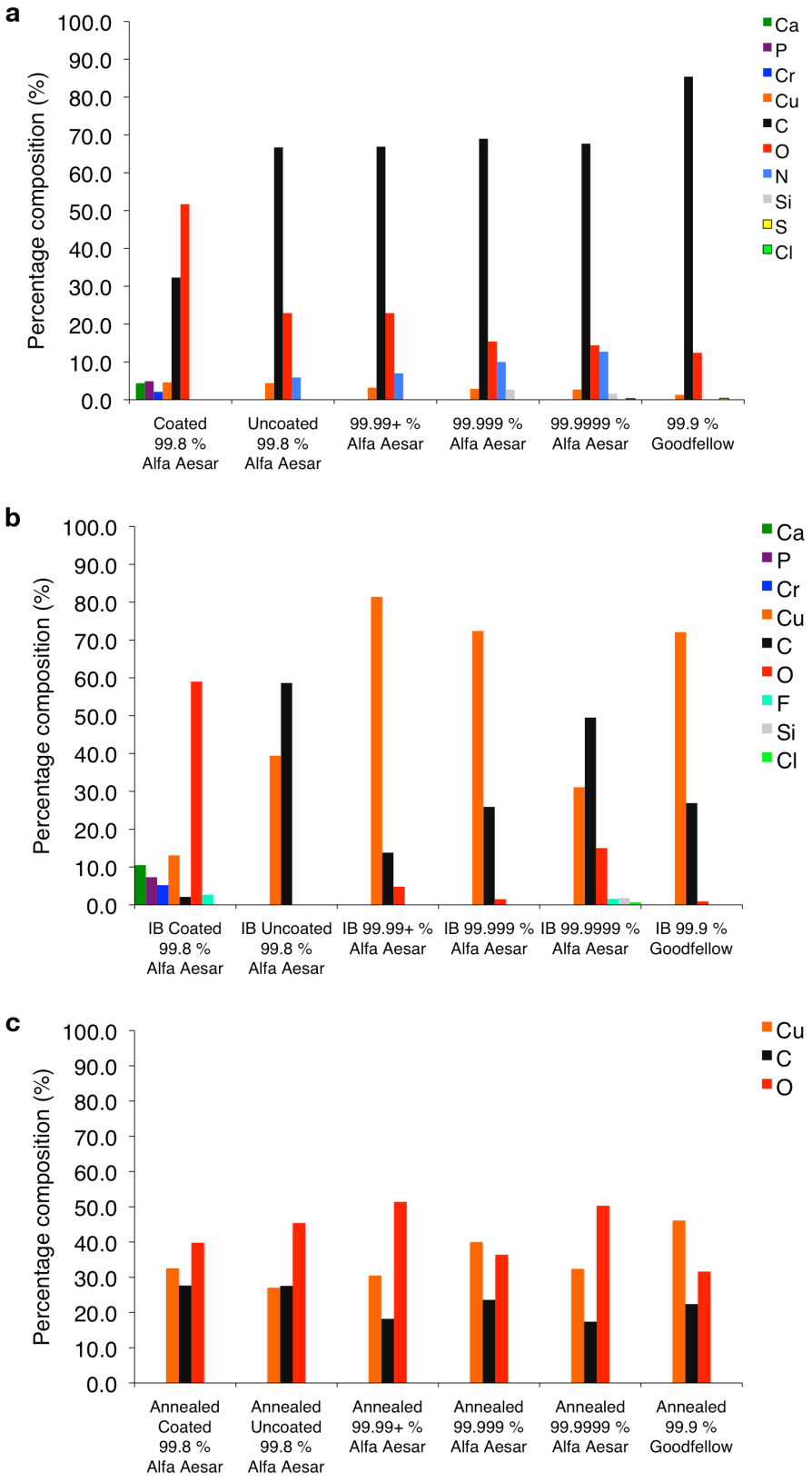


Figure 95: XPS analysis of elemental composition of various Cu foils

(a) as-received, (b) following ~2 nm argon ion bombardment (IB) in UHV, (c) following annealing at 1035 ˚C for 30 minutes under 500 sccm H_2

XPS depth profiling of the elemental composition of the unannealed Cu foils was possible by Ar ion bombardment to remove ~2 nm from the surface, Figure 95b. This investigated the thickness of surface coatings, and the concentration of dissolved impurities in the as-received foils. The percentage of carbon and oxygen reduced for all Cu foils following ion bombardment, indicating these elements are absorbed on the surface or present as a thin native oxide. Following ion bombardment, calcium, phosphorus and chromium were detected with increased signal intensity and percentage composition on the Coated 99.8 % Alfa Aesar Cu foil (10.5, 7.3, and 5.2 atomic %, respectively), while carbon was significantly reduced (2.1 atomic %). After a second ion bombardment, probing to a depth of ~5 nm, carbon and chromium were still present (1.6 and 1.9 atomic %, respectively), while calcium and phosphorus were no longer detected. Consequently the Coated 99.8 % Alfa Aesar Cu foil does indeed have a surface coating when received from the supplier. The coating is a thin layer, <2 nm, of carbon, calcium, phosphorus and chromium, with chromium and carbon persistence into the internal composition at least to ~ 5 nm depth. In comparison, no contaminants were detected on the Uncoated 99.8 % Alfa Aesar Cu, 99.99+ % Alfa Aesar and 99.9 % Goodfellow Cu foils at a depth of ~2 nm. These foils are relatively free of surface and bulk contaminants, within the ~0.2 atomic % detection limit of XPS, which supports the SEM observations from Figure 91. Ion bombardment removed the silicon from 99.999 % Alfa Aesar Cu foil, indicating this is a surface contamination from processing. The only other contaminations detected at ~2 nm depth were on the 99.9999 % Alfa Aesar Cu foil- silicon, chlorine and fluorine (1.6, 0.4 and 0.6 atomic %, respectively)- demonstrating a low concentration silicon surface contamination, as well as other impurities dissolved within the bulk foil.

Comparing XPS of the six Cu foils, the surface impurities did not vary with the supplier stated percentage purity as might have been expected. I conclude that the supplier state purity, which is indicative of the bulk composition, is not representative of the surface composition, and should not be used by researchers as an indicator for selecting a purer Cu foil.

XPS analysis after annealing indicates the surface impurities that may be present during graphene synthesis; surface coatings may etch or dissolve into the substrate

during annealing, while other dissolved impurities may segregate to the surface. The surface composition was limited to carbon and oxygen for all the annealed Cu foils, Figure 95c. No metallic impurities were detected within the detection limit of ~0.2 atomic %. However as SEM imaging from Figure 91 clearly demonstrates residual contamination particles on the surface I recognised that XPS is simply not sensitive enough to detect these species.

SIMS mapping of the annealed Cu foils investigated the spatial distribution of metallic contaminations at concentrations below the XPS detection limit, Figure 96 to Figure 100 (see Appendix for raw mass spectra). Atomic mass of 16u (O), 23u (Na), 24u (C2), 27u (Al), 35u and 37u (Cl), 39u (K), 40u (Ca), 63u and 65u (Cu), 69u and 71u (Ga) were detected. P and Cr could not be detected due to low sensitivity. SIMS was not initially conducted on the annealed 99.9999 % Alfa Aesar Cu foil, and this measurement could not be performed at a later date.

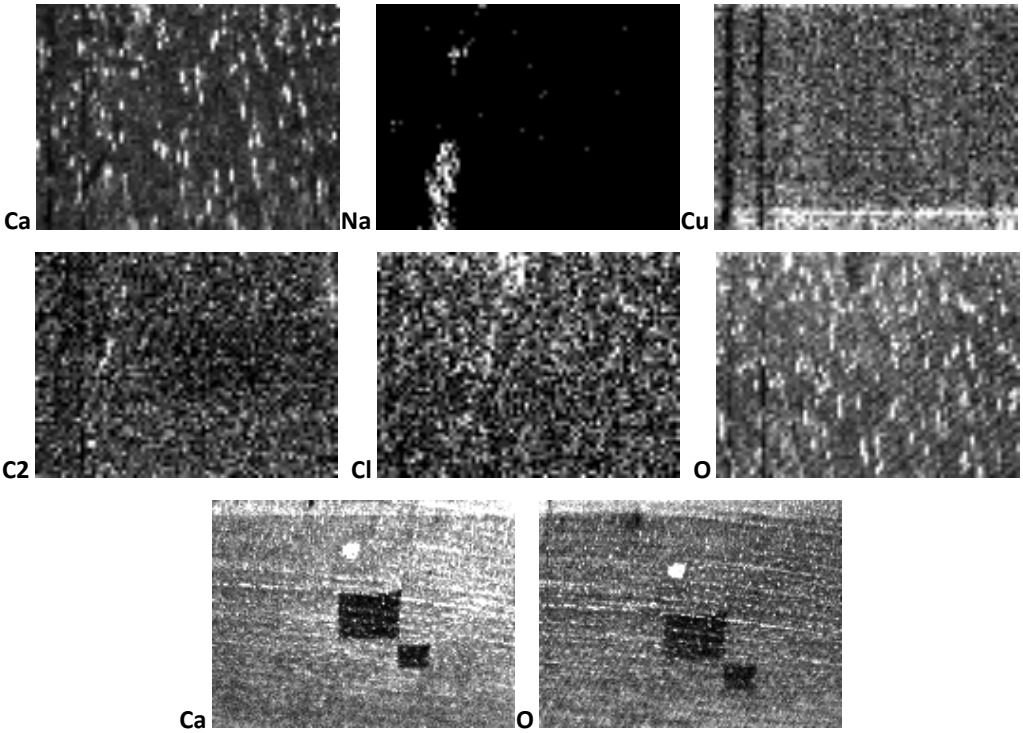


Figure 96: SIMS analysis of surface contamination on annealed Coated 99.8 % Alfa Aesar Cu foil
Positive ion images are shifted in the vertical direction with respect to the negative ion images.
300 µm field of view for top two rows, 750 µm for third row

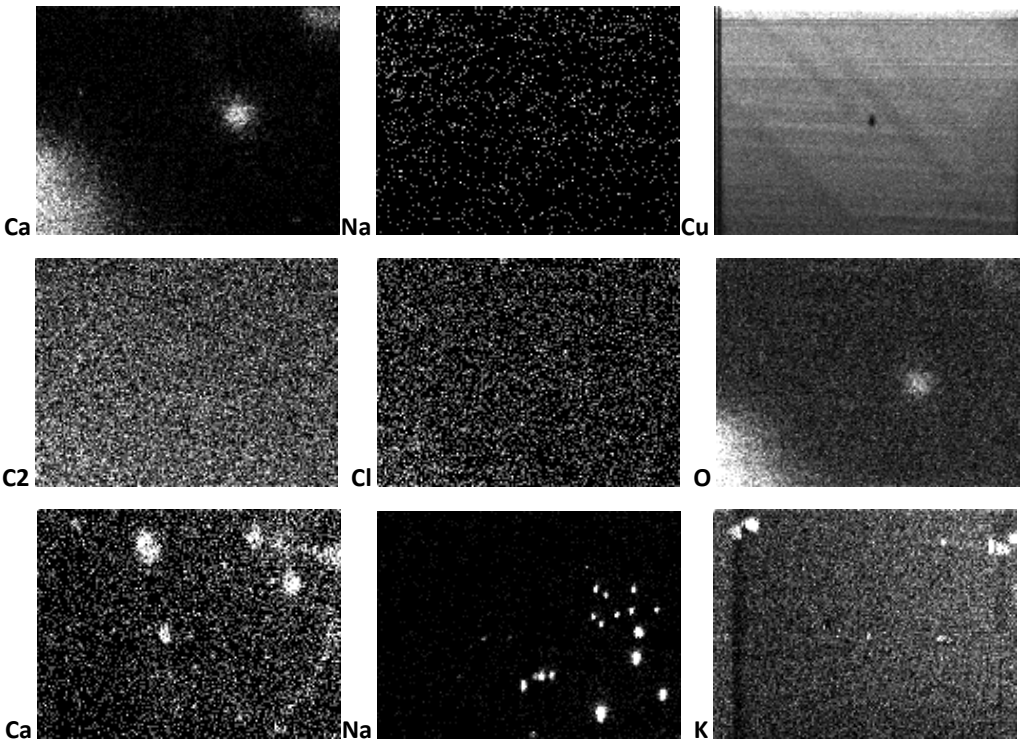


Figure 97: SIMS analysis of surface contamination on annealed Uncoated 99.8 % Alfa Aesar Cu foil
750 µm field of view for top two rows, 1500 µm for third row

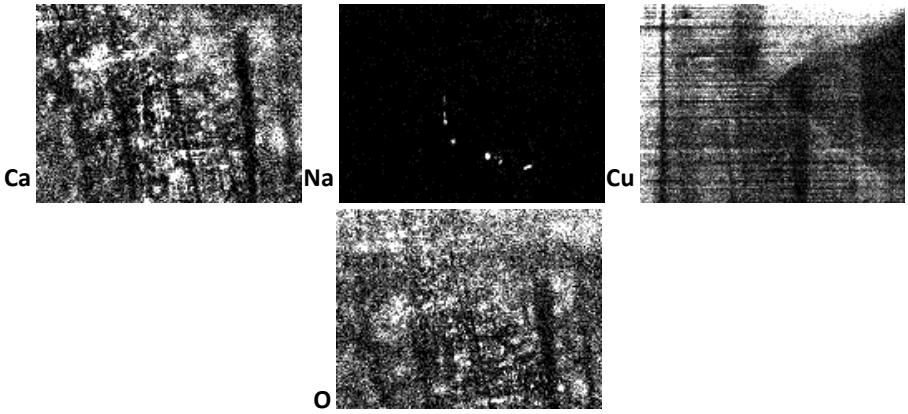


Figure 98: SIMS analysis of surface contamination on annealed 99.99+ % Alfa Aesar Cu foil

Positive ion images are shifted slightly in the vertical direction with respect to the negative ion images.

750 µm field of view

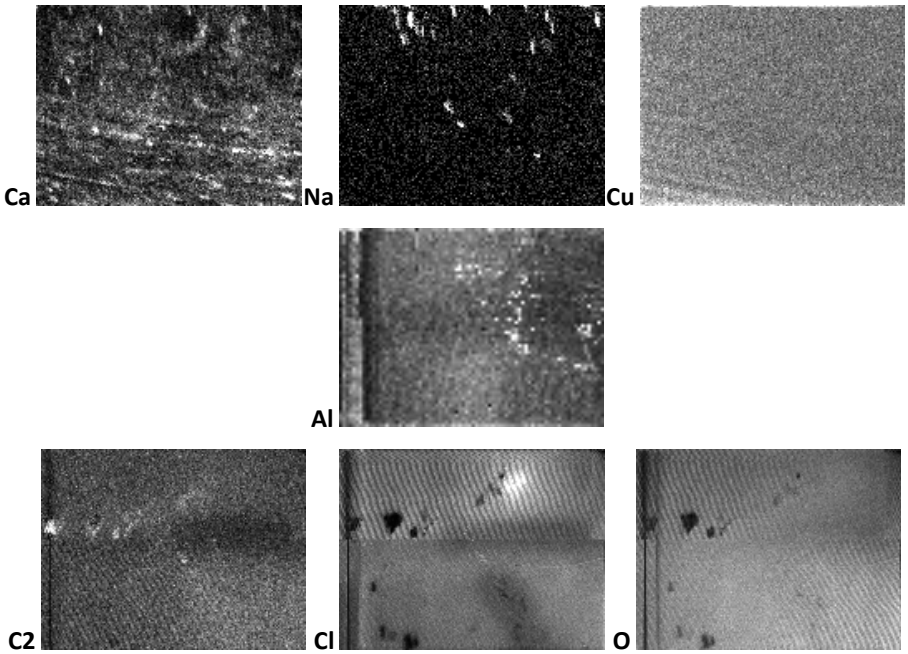


Figure 99: SIMS analysis of surface contamination on annealed 99.999 % Alfa Aesar Cu foil

300 µm field of view top two rows, 1500 µm field of view bottom row

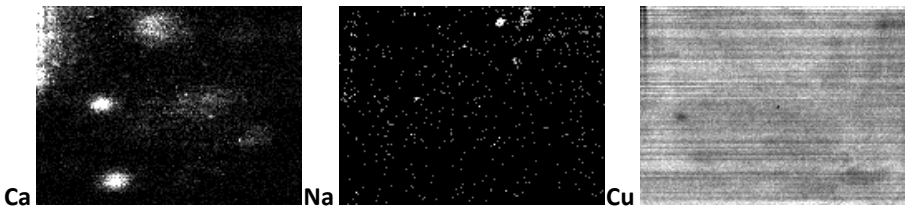


Figure 100: SIMS analysis of surface contamination on annealed 99.9 % Goodfellow Cu foil

300 µm field of view

SIMS detected:

- Calcium, sodium, carbon, chlorine and oxygen on annealed Coated 99.8 % Alfa Aesar, Figure 96,
- Calcium, sodium, carbon, oxygen and potassium on annealed Uncoated 99.8 % Alfa Aesar, Figure 97,
- Calcium, sodium and oxygen on annealed 99.99+ % Alfa Aesar, Figure 98,
- Calcium, sodium, carbon, aluminium, chlorine and oxygen on annealed 99.999 % Alfa Aesar, Figure 99,
- Calcium and sodium on annealed 99.9 % Goodfellow, Figure 100.

2D mapping of the characteristic signal intensity demonstrates the spatial distribution of the species varies between the Cu foils. For the annealed Coated 99.8 % Alfa Aesar Cu foil the calcium and oxygen signal are due to a very high-density uniform covering of particles on the surface. The spatial distribution of the calcium signal corresponds with the oxygen signal, indicating the calcium is present as calcium oxide, calcium hydroxide, or calcium carbonate. This corresponds to the particles observed via SEM in Figure 91. Sodium on the surface is localised to relatively large contaminant particles. In comparison, for the annealed Uncoated 99.8 % Alfa Aesar Cu foil the 2D mapping demonstrated that the calcium signal was sparsely distributed across the sample, but when present it was in high concentration as relatively large contaminant particles. Correlation between calcium and oxygen signals is again visible on this Cu foil, while sodium and potassium signals are localised to relatively large contaminant particles. For the annealed 99.99+ % Alfa Aesar Cu foil the calcium and corresponding oxygen signals appear to originate from particles as well as being diffusely distributed across the surface. Sodium is again present as isolated particles. Calcium distribution on the annealed 99.999 % Alfa Aesar Cu foil corresponds to relatively small particles across the surface. However, these particles are not uniformly distribution across the entire substrate, with regions of high density observed, which compares well with SEM observations of contaminations in circular patterns in Figure 91d. Finally, calcium signal on the annealed 99.9 % Goodfellow Cu foil shows similarities with the Uncoated 99.8 % Alfa Aesar, originating from a few relatively large contamination particles.

Elemental depth profiling of the surface through gallium ion bombardment and simultaneous SIMS analysis demonstrates the approximate depth of the metallic contamination species, Figure 101 and Figure 102. These depth profiling measurements should be viewed with some care, as the calculated depths may not be significant due to variations in sputtering rate with surface topographies, and variability in density and size of surface contamination particles across the surface of the Cu foil.

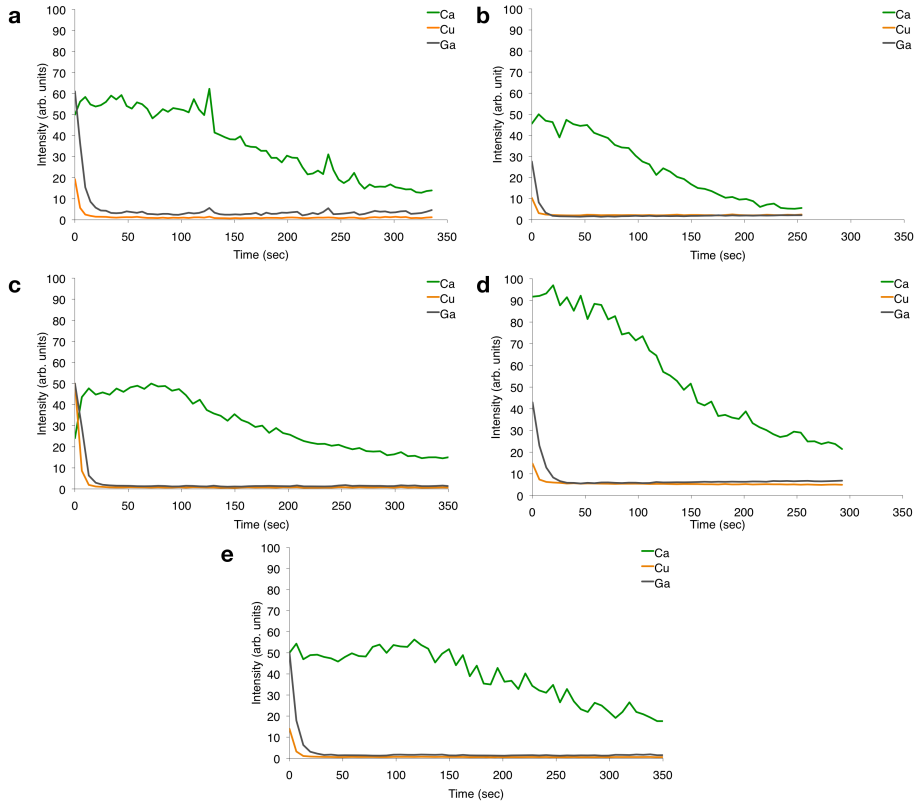


Figure 101: Depth profiling SIMS at high gallium ion bombardment rate demonstrating penetration of surface contaminations on various annealed Cu foils (a) Coated 99.8 % Alfa Aesar Cu foil, (b) Uncoated 99.8 % Alfa Aesar Cu foil, (c) 99.99+ % Alfa Aesar Cu foil, (d) 99.999 % Alfa Aesar Cu foil, (e) 99.9 % Goodfellow Cu foil. 75 µm raster

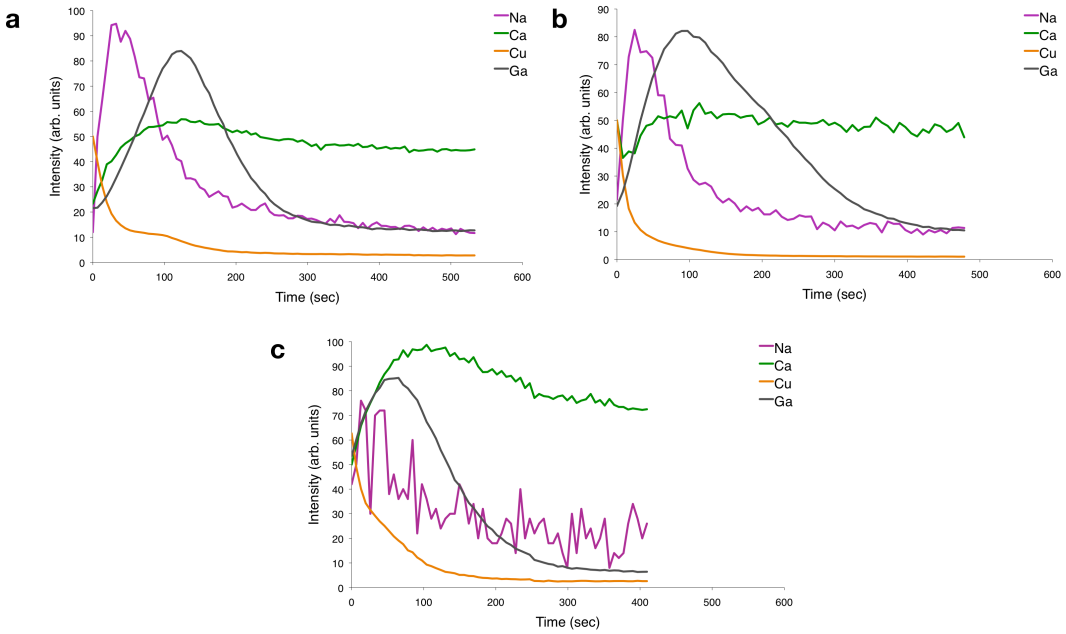


Figure 102: Depth profiling SIMS at low ion bombardment rate demonstrating surface contaminations on various annealed Cu foils (a) Coated 99.8 % Alfa Aesar Cu foil, (b) 99.999 % Alfa Aesar Cu foil, (c) 99.9 % Goodfellow Cu foil. 300 µm raster

The penetration depth of contaminants within the surface can be approximately calculated based on the time required for the signal intensity to reduce to a horizontal plateau that is representative of detector noise. The Ca signal reduced to a plateau after 200 - 350 seconds for all the foils investigated, correlating to a depth of ~20-35 nm. The greatest depth, ~ 35 nm, was observed on the Coated 99.8 % Alfa Aesar, the 99.99+ % Alfa Aesar, and the 99.9 % Goodfellow (Figure 101a, c, and e, respectively), while the shallowest depth, ~ 20 nm, was observed for the Uncoated 99.8 % Alfa Aesar (Figure 101b). The Na signal was also investigated for the Coated 99.8 % Alfa Aesar, 99.999 % Alfa Aesar, and 99.9 % Goodfellow Cu foils using a lower sputtering rate, Figure 102. The Na signal reduced to a plateau after 400, 300, and 200 seconds on the respective Cu foils, which is representative of a depth of ~4 nm, ~3 nm and ~2 nm.

From the SIMS analysis the Ca:Ga intensity ratio was calculated for each of the annealed Cu foils, Figure 103, to determine the relative concentration of Ca on each foil.

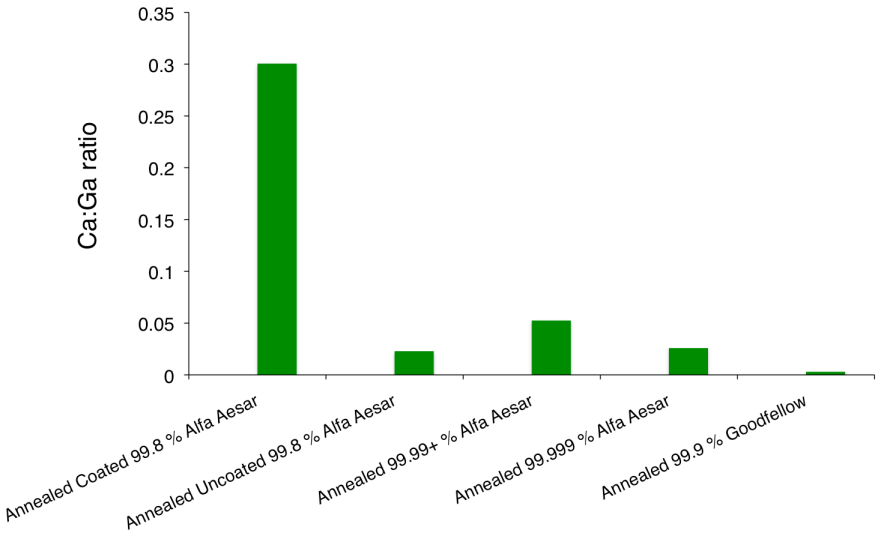


Figure 103: Variation of SIMS Ca:Ga ratio, and hence Ca concentration, for various annealed Cu foils

The Ca:Ga ratio, and hence Ca concentration, measured by SIMS is an order of magnitude higher for the Coated 99.8 % Alfa Aesar Cu foil (0.30) compared to the Uncoated 99.8 % Alfa Aesar (0.023). This demonstrates the influence of the surface coating applied by the supplier. The calcium concentration on the 99.99+ % Alfa Aesar (0.05) and 99.999 % Alfa Aesar (0.026) Cu foil is also an order of magnitude lower than the Coated 99.8 % Alfa Aesar Cu foil. Somewhat surprisingly, the Ca concentration on the 99.99+ % Alfa Aesar is double that measured for the Uncoated 99.8 % Alfa Aesar and the 99.999 % Alfa Aesar. The lowest Ca concentration was detected on the 99.9 % Goodfellow Cu foil (0.0030), nearly two orders of magnitude below the Coated 99.8 % Alfa Aesar.

8.1.1.3 Crystallographic orientations and grain sizes of annealed copper foils via EBSD

As described in Chapter 7, the crystallographic orientation of different grains of the Cu foils may significantly influence the shape, size, orientation, thickness, and growth rate CVD graphene. EBSD analysis already presented in Chapter 7.4 demonstrated that the Coated 99.8 % Alfa Aesar, 99.999 % Alfa Aesar and 99.9 % Goodfellow Cu foils are each composed of a unique distribution of crystallographic orientations: the foil's texture. I conducted large-area EBSD mapping on the remaining Cu foils to investigate the distribution of crystallographic orientations and grain sizes of the six annealed Cu foils, Figure 104.

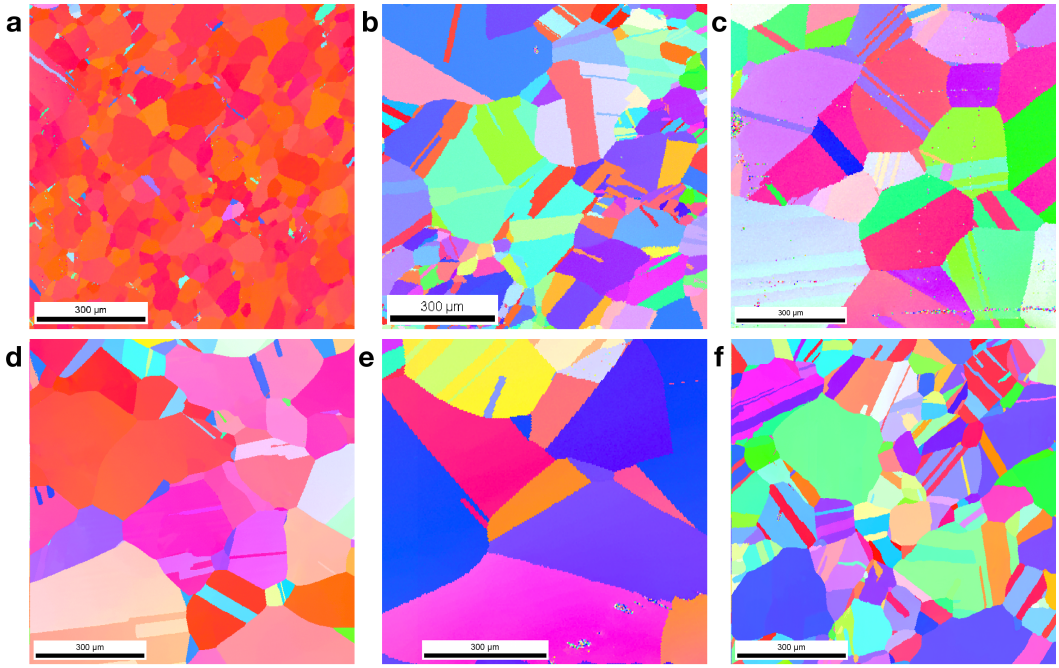


Figure 104: 900 x 900 µm EBSD maps of annealed Cu foils

(a) Coated 99.8 % Alfa Aesar Cu foil, (b) Uncoated 99.8 % Alfa Aesar Cu foil, (c) 99.99+ % Alfa Aesar Cu foil, (d) 99.999 % Alfa Aesar Cu foil, (e) 99.9999 % Alfa Aesar Cu foil, (f) 99.9 % Goodfellow Cu foil

The large-area EBSD mapping demonstrates that the grain size and crystallographic orientations vary greatly between the different annealed Cu foils:

- Coated 99.8 % Alfa Aesar is essentially composed entirely of crystallographic orientations near to Cu{001}. Its grains are relatively small, less than 100 µm;
- Uncoated 99.8 % Alfa Aesar is composed of crystallographic orientations near Cu{111} and Cu{101}. Cu{001} is rarely observed, but some grains misoriented from Cu{001} are visible. While some grains are up to 300 µm, there are many that are 100 µm or smaller;
- 99.99+ Alfa Aesar is composed of crystallographic orientations misoriented from Cu{001}, and near to Cu{101}. Its grains are uniformly large, often between 200 - 300 µm;
- 99.999 % Alfa Aesar is composed of crystallographic orientations near to and misoriented from Cu{001}. Its grains are uniformly large at 300 µm;
- 99.9999 % Alfa Aesar is composed of a significant proportion of crystallographic orientations near to Cu{111}. A second EBSD map of this foil (see Appendix) revealed crystallographic orientations near Cu{101} are also present. Its grains are the largest observed, frequently greater than 300 µm;

- 99.9 % Goodfellow is composed of crystallographic orientations near Cu{111} and Cu{101}. Grains are up to 300 μm are surrounded by many smaller grains less than 100 μm.

While there are similarities between the Uncoated 99.8 % Alfa Aesar and the 99.9 % Goodfellow Cu foils, Figure 104b and f, in general the six foils possess different textures and grain size distributions, which are unique properties of the specific Cu foil, and independent of purity or the foil's supplier. This is important for understanding the differences between graphene synthesised on different Cu foils, including any variations in the shape, alignment and growth rate of graphene domains that will arise due to the different Cu crystallographic orientations present within each foil. For instance, due to the abundance of Cu{001} in the Coated 99.8 % Alfa Aesar Cu foil, graphene domains will be aligned to two ~90˚ directions and have a lower growth rate. In comparison, due to the relatively low density of grain boundaries and high proportion of Cu{111} on the 99.9999 % Alfa Aesar, a higher growth rate of graphene domains would be expected on such grains for equivalent synthesis conditions. Variations in texture of Coated 99.8 % Alfa Aesar and 99.999 % Alfa Aesar Cu foils, Figure 104a and f, is likely to have contributed to the variations in growth on these two foils as described by Huang *et al*.[217], and the reduced carrier mobility for graphene grown on 99.8 % Alfa Aesar. Awareness of the foil's texture and grain size distribution is therefore important when comparing CVD graphene synthesised on different Cu foils, so that variations in growth are not attributed to an alternative property- for instance, foil purity- through erroneous conclusions.

8.1.1.4 Conclusions on variations of copper foils due to purity and supplier

At the outset of Chapter 8.1.1 I stated that a number of properties of Cu foils- the surface topography, roughness, surface coatings, dissolved impurities, crystallographic orientations and grain sizes- will vary between different types of foil due to natural variations of the raw material, and the influence of processing by suppliers. Using SEM, OP, EBSD, XPS and SIMS I investigated these properties for the six Cu foils listed in Chapter 8.1 which have increasing purity (99.8 %, 99.99+%, 99.999 %, 99.9999 %), were sourced from different suppliers (Alfa Aesar and Goodfellow) and may have a surface coating.

The analysis demonstrates that each of the Cu foils possess a unique combination of properties. Each foil is different from the next, and no consistent trend exists for a property changing systematically with an increase in the supplier-stated purity of the foil from 99.8 % to 99.9999 %. Differences were also observed between the two low purity Cu foils sourced from different suppliers. Some general observations include:

- Higher purity foils had a lower surface roughness (e.g. 99.999 % Alfa Aesar and 99.9999 % Alfa Aesar, both with $S_a < 0.06$ µm) compared to the lower purity foils. This was attributed to a higher frequency and magnitude of cold rolling striations and contamination particles on the lower purity substrates (e.g. Coated 99.8 % Alfa Aesar, 99.99+ % Alfa Aesar and 99.9 % Goodfellow, all with $S_a > 0.20$ µm)
- Surface contaminations were detected on all the as-received Cu foils. Annealing the foils at 1035˚C for 30 minutes in 500 sccm H_2 effectively reduced the concentration of surface contaminations below ~0.2 atomic %. However, sub-micron contamination particles are still present on all substrates. The remaining species below this concentration include calcium, sodium, potassium and aluminium, depending on the Cu foil. The annealed Uncoated 99.8 % Alfa Aesar and 99.9 % Goodfellow showed the lowest concentration of Ca contamination particles and a low density of visible contamination particles. A low concentration of Ca contamination particles was measured on the 99.999 % Alfa Aesar, however, contamination particles were visible which may be composed of aluminium.
- Crystallographic orientations and grain sizes varied significantly between foils. Often one primary crystallographic orientation (e.g. Cu{001}, Cu{101}, or Cu{111}) was dominant on the Cu foil, while another primary crystallographic orientation was entirely absent. 99.9999 % Alfa Aesar showed the largest grains (>300 µm) including a significant proportion of Cu{111}.
- A ~5 nm thick high density surface coating primarily composed of calcium and chromium was detected on the as-received Coated 99.8 % Alfa Aesar Cu foil. Annealing reduced this contamination, however calcium as calcium oxide or

calcium carbonate remained. The contamination concentration was orders of magnitude higher than that detected on all other Cu foils.

This investigation clearly demonstrates the importance of performing thorough characterisation of the Cu foil prior to graphene synthesis. Furthermore, the variability of properties between different Cu foils, and within samples of one Cu foil, demonstrates that researchers must ensure individual samples of Cu foil have consistent properties and are representative of the bulk foil. The confirmation of a surface coating on the Coated 99.8 % Alfa Aesar Cu foil explains many inconsistencies observed in Chapter 5. This also raises some concern about the use of this foil by a large proportion of the research community for many early publications on the growth of graphene, prior to the rebranding of the substrate by Alfa Aesar.

8.1.2 APCVD graphene growth on annealed Alfa Aesar copper foils with varying purity

I conducted APCVD graphene synthesis on the five Alfa Aesar annealed Cu foils of varying purity using identical synthesis parameters: a synthesis temperature of 1035 ˚C, synthesis time of 15 minutes, and reactant gas flow rates of 5 sccm CH_4 and 300 sccm H_2. By comparing the graphene growth from these equivalent experiments I hoped to investigate whether the supplier-stated purity of the Cu foils caused any obvious influence on the formation of the graphene domains. I investigated the graphene growth on each substrate using SEM, Figure 105.

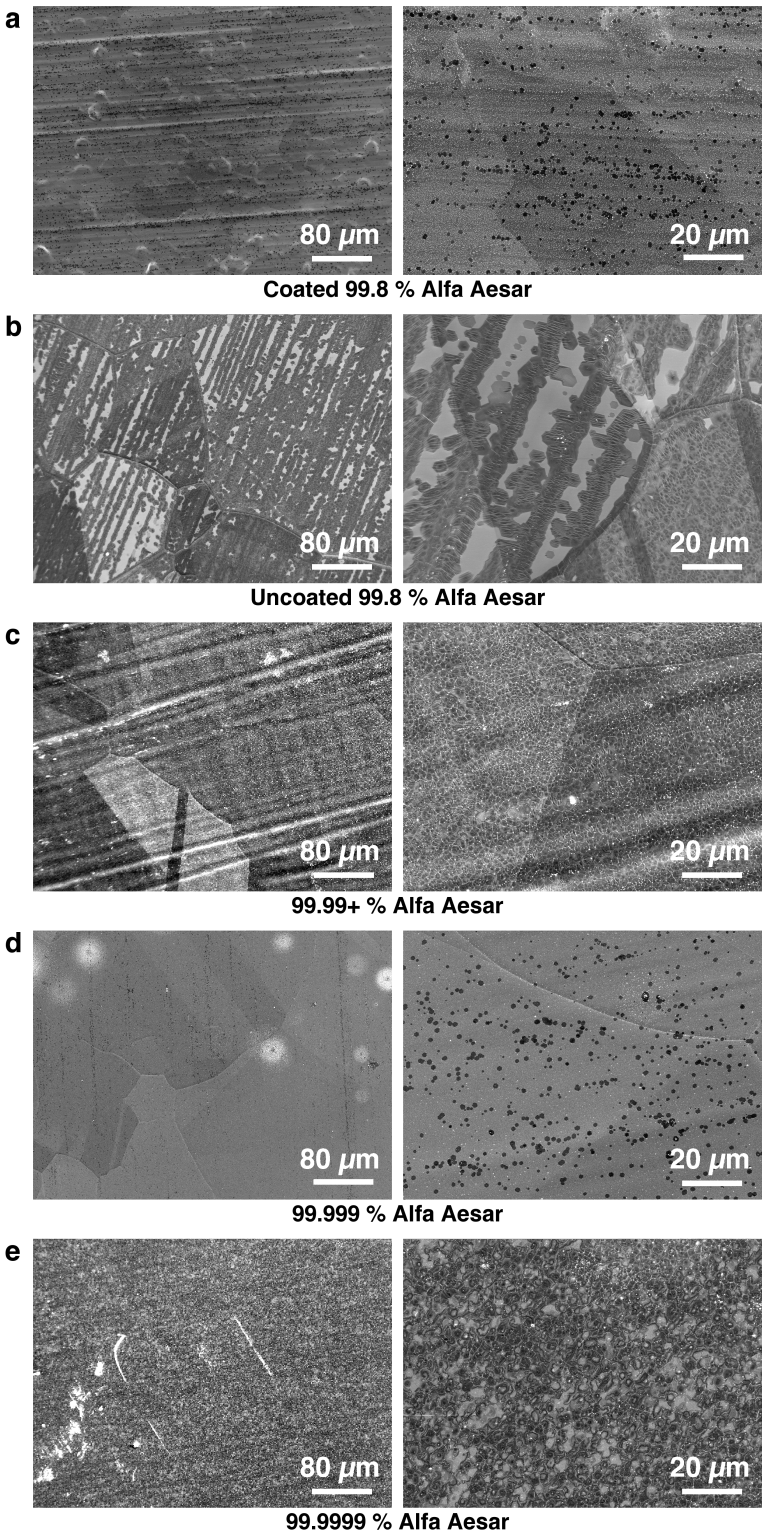


Figure 105: SEM images of APCVD graphene growth on Alfa Aesar Cu foils of varying purity following 15 minutes synthesis at 1035 ˚C with 5 sccm CH_4 and 300 sccm H_2 (a) Coated 99.8%, (b) Uncoated 99.8 %, (c) 99.99+ %, (d) 99.999 %, (e) 99.9999 %. Low and high magnification images

The SEM images demonstrate that the graphene growth differs significantly between the Cu foil substrates with varying purity, even though synthesis parameters were

the same. Individual graphene domains are observed on the Coated 99.8% Alfa Aesar and 99.999 % Alfa Aesar, ~1.5 µm and ~1 µm in size, respectively. In comparison, graphene completely covers the Cu surface for synthesis on 99.99+ % and 99.9999 % Cu foil. Domains on the Uncoated 99.8 % Alfa Aesar are frequently merged, with growth on some grains completely covering the surface. However, no clear trend is visible for the variation of graphene growth with increasing Cu foil purity from 99.8 % to 99.9999 %. I concluded that the growth rate and/or nucleation density is higher for the 99.99+ % and 99.9999 % Cu foils, and significantly lower for the Coated 99.8 % and 99.999 % Cu foils.

As the studies in Chapter 8.1.1 demonstrated, the crystallographic orientations, surface contaminations, surface topography and roughness vary significantly between these five Cu foils. The influence of each of these properties on the growth of graphene on the Cu foils will occur simultaneously, and cannot be assessed independently. As a consequence, conclusions about the cause of the variations of graphene growth on the Cu foils are difficult to make. One possible explanation for the reduced growth rate on the Coated 99.8 % Alfa Aesar and 99.999 % Alfa Aesar Cu foils is the high concentration of Cu{001} and misorientated grains on these foils, upon which graphene domains are known to have a reduced growth rate. However, given the graphene growth in Figure 105 is relatively uniform across each of the Cu foils, this may not be the only factor causing the observed difference in growth rate. While the surface roughness may be influential, no similarities in graphene growth exist for the smoother Cu foils- 99.999 % Alfa Aesar and 99.9999 % Alfa Aesar- or the rougher Cu foils- Coated 99.8 % Alfa Aesar, Uncoated 99.8 % Alfa Aesar and 99.99+ % Alfa Aesar. I therefore hypothesise that surface contaminations may be primarily responsible for a reduced growth rate and/or nucleation density on the Coated 99.8 % Alfa Aesar Cu foil, and to a lesser extent on the 99.999 % Alfa Aesar Cu foil. SEM imaging demonstrated contamination particles were in highest density on these two Cu foils after annealing, particularly the Coated 99.8 % Alfa Aesar. XPS measurements detected a significant surface contamination of calcium and chromium on the as-received Coated 99.8 % Alfa Aesar Cu foil, and silicon on the as-received 99.999 % Alfa Aesar Cu foil. SIMS measurements detected calcium on

the annealed Coated 99.8% Alfa Aesar Cu foil, and calcium and aluminium on the annealed 99.999 % Alfa Aesar Cu foil. These results suggest that the growth rate and/or nucleation density of graphene is reduced on Cu foils that have a higher concentration of metallic surface contaminations, particularly calcium. This discovery is in agreement with literature published in 1977 on the catalytic etching of graphite by calcium oxide particles[320]. Therefore, controlling and reducing the concentration of calcium and metallic surface contaminations is vital for reproducible production of CVD graphene.

8.1.3 APCVD graphene growth on annealed copper foils with similar purities from different suppliers

I conducted APCVD graphene synthesis on the Alfa Aesar and Goodfellow annealed Cu foils with 99.8 % / 99.9 % purity using identical synthesis parameters: a synthesis temperature of 1035 ˚C, synthesis time of 15 minutes, and reactant gas flow rates of 5 sccm CH_4 and 300 sccm H_2. By comparing the graphene growth from these equivalent experiments I aimed to investigate whether subtle variations between the Cu foils from different suppliers influenced the formation of the graphene domains. I investigated the graphene growth using SEM, Figure 106.

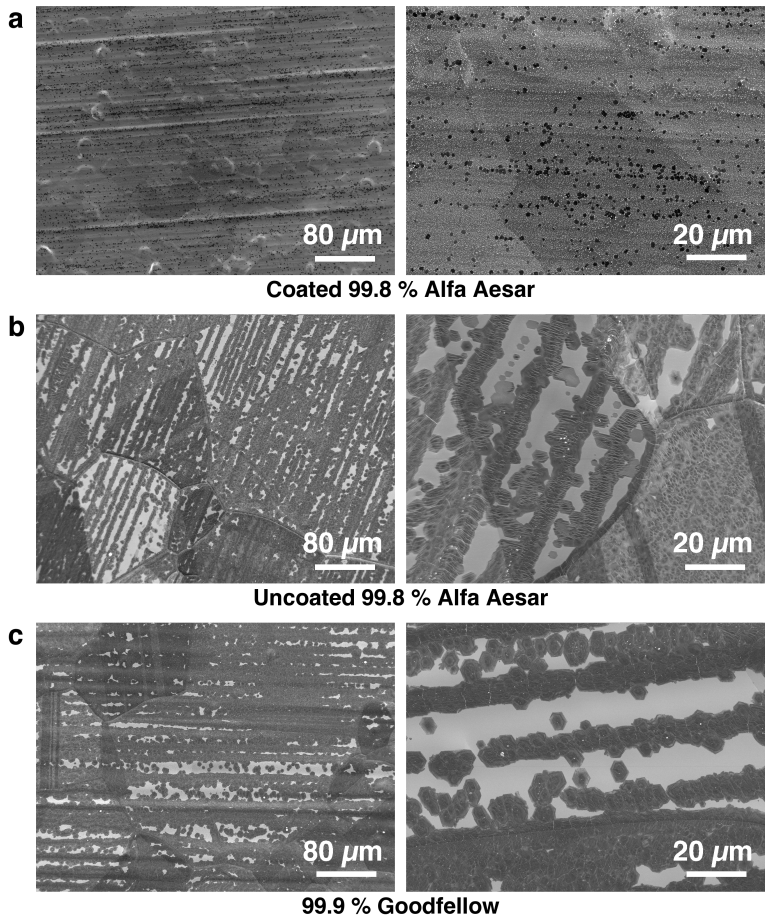


Figure 106: SEM images of APCVD graphene growth on low purity Cu foils from different suppliers following 15 minutes synthesis at 1035 ˚C with 5 sccm CH_4 and 300 sccm H_2 on (a) 99.8 % Alfa Aesar, and (b) 99.9 % Goodfellow Cu foils. Low and high magnification images presented

The SEM images demonstrate that the graphene growth varies significantly between the Cu foils. As discussed in Chapter 8.1.2, individual graphene domains ~1.5 µm in size are observed on the 99.8% Coated Alfa Aesar Cu foil. The nucleation densities and growth rates of graphene domains on the Uncoated 99.8 % Alfa Aesar Cu foil and the 99.9% Goodfellow Cu foil are higher, with domains ~5 µm and ~8 µm forming, respectively, that frequently merge together to cover large regions of the surfaces. These observations indicate that graphene growth can vary between Cu foils of equivalent purity even when the same synthesis conditions are used. This suggests that differences between the foils play a significant role in dictating the growth of graphene. The presence of metallic surface contaminants as confirmed by XPS and SIMS seems the likely cause for the reduced nucleation density and growth rate on the Coated 99.8 % Alfa Aesar. In comparison, metallic surface contaminants were not detected on either the Uncoated 99.8 % Alfa Aesar Cu foil or the 99.9 %

Goodfellow Cu foil by XPS, only low concentrations of Ca were detected by SIMS, and a higher nucleation density and growth rate was observed on these foils. Minor variations between the growth on the Uncoated 99.8 % Alfa Aesar and 99.9 % Goodfellow are observed, included more sparsely covered grains on the Uncoated 99.8 % Alfa Aesar and slightly larger domains on the 99.9 % Goodfellow. The reduced nucleation density may be due to subtle differences in the distribution of crystallographic orientations on these two foils, while the increased growth rate on the 99.9 % Goodfellow Cu foil could be explained by the very low concentration of Ca contaminations.

8.1.4 Conclusions on influence of properties and quality of coppers foils on APCVD graphene growth

The findings in Chapter 8.1.2 raise the question as to whether using a Cu foil with greater purity is advantageous and necessary for improving the growth of CVD graphene. My results indicate that graphene growth does vary significantly between the Cu foils of increasing purity, though no clear trend is observable. However, many properties of the foils also vary with increasing Cu foil purity, and these may also play an influential role in dictating graphene growth. Furthermore, the chemical composition measured from analysis of the Cu foils did not correlate with the supplier's stated purity. As such, the advantage of selecting a purer foil to reduce the concentration of surface contaminants cannot be guaranteed, and researchers shouldn't presume the concentration of surface contaminations would be reduced as the advertised purity of the supplied Cu foils increases. Instead, the type and concentration of surface contaminations for each type of Cu foil to be used for graphene growth should be independently investigated, and a foil should be selected as suitable for the researcher's needs.

The results from Chapter 8.1.3 suggest it is particularly important that researchers take care when attempting to replicate graphene growth experiments from published literature by using similar, but different, types of Cu foil; chemical equivalence and comparable properties cannot be presumed between different substrates simply because the purity stated by the supplier is equivalent. Instead,

systematic characterisation and chemical analysis should always be conducted on each Cu foil, as any differences between the Cu foils may cause spurious results.

Furthermore, if the concentration of contamination particles on the surface can be reduced in the laboratory- for instance, through chemical treatments as presented in Chapter 8.2- then a faster growth rate will be obtained and higher quality graphene may be achieved.

Finally, these studies demonstrate the need for exclusive systematic investigations into the influence of each of the properties of the Cu foil- the surface topography, roughness, chemical composition, and crystallographic orientations- on the growth of CVD graphene. For example, the impact of surface contaminations could be investigated systematically by ion implantation or drop coating with solutions of increasing concentration, while the influence of surface roughness could be investigated by controlled electrochemical polishing. By doing so the influence of these properties may be isolated and independently assessed, and the relevant property can then be optimised to improve and control production of CVD graphene in the future.

8.2 Influence of chemical treatment of copper foil on synthesis of graphene

The investigations presented in Chapter 8.1 demonstrate that the properties of the copper foils, in particular the concentration of surface contaminations, varied greatly from one substrate to the next as received from the supplier. As a consequence the growth of graphene differed between the Cu foils. A natural question then arises: can chemical treatment of the copper foil be used to remove surface contaminations, and so control and improve the quality of the graphene that forms? I conducted investigations into the influence of different chemical treatments on the quantity and type of impurities present on the copper foils, and then compared these findings with the variation in graphene growth between as-received and chemically treated annealed substrates. Through these investigations I conclude that chemical treatments can be used to remove contaminations from the surface of Cu foils, thereby reducing the nucleation density and increasing the growth rate of graphene domains.

8.2.1 Variation to copper foils by CH_3COOH cleaning

Levendorf *et al.*[148] first proposed that CH_3COOH could be used to remove copper oxide from the surface of Cu foils in 2009. By following a pre-annealing chemical treatment of Cu foils for 10 minutes in CH_3COOH at 35 ˚C the researchers claimed to *"eliminate the need for a lengthy anneal which can deteriorate the quality of the copper foil"*. Cleaning with CH_3COOH has also been replicated in a number of publications[212, 225, 231]. However, a thorough analysis of the influence of CH_3COOH cleaning on the surface topography and concentration of contaminations on Cu foils, and the associated growth of graphene on CH_3COOH cleaned foils, has not been reported. I modified Levendorf *et al.*[148]'s procedure by ultrasonicating the Cu foils in concentrated CH_3COOH for 10 minutes, followed by a 10 minute ultrasonication in deionised water to removal any residual CH_3COOH. The Cu foils were then immediately inserted into the APCVD furnace and annealed for 30 minutes under 500 sccm H_2. Using SEM, OM, XPS and SIMS I investigated the influence of CH_3COOH cleaning on the surface topography and chemical composition of the surface of the six Cu foils listed in Chapter 8.1.

8.2.1.1 Surface topography of CH_3COOH cleaned and annealed copper foils via SEM and optical profilometry

I conducted SEM to investigate the surface topography of the CH_3COOH cleaned and annealed Cu foils. By comparing each sample with the respective untreated annealed foil from Chapter 8.1.1.1 the influence of the chemical treatment can be deduced, with particular attention given to whether a change in surface contaminations is observed. Representative images of the CH_3COOH cleaned and annealed substrates alongside the untreated annealed substrates are presented in Figure 107.

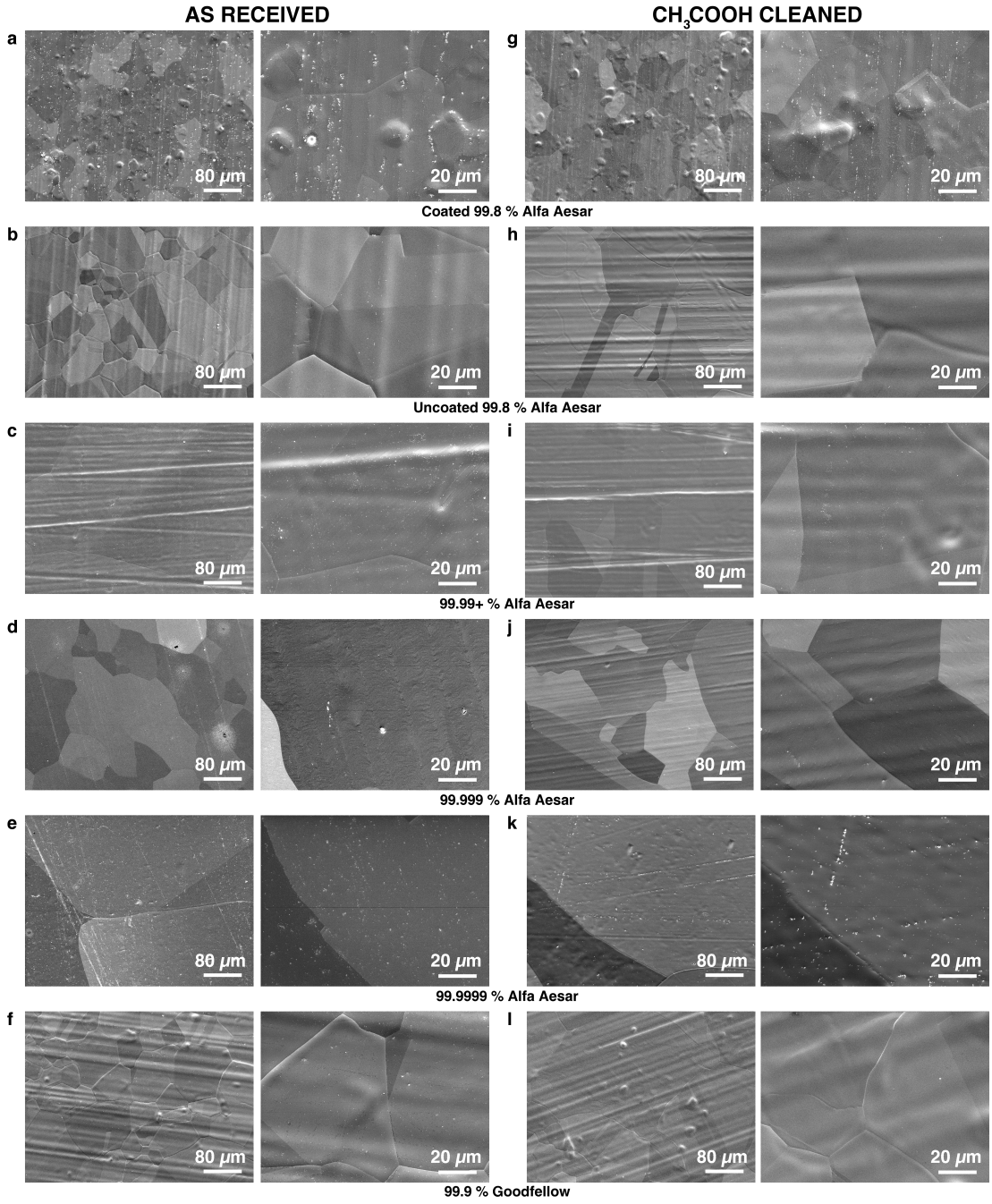


Figure 107: Comparison of SEM images of various annealed Cu foils with and without CH_3COOH cleaning (a)(b)(c)(d)(e)(f) without cleaning, (g)(h)(i)(j)(k)(l) with CH_3COOH cleaning. (a)(g) Coated 99.8 % Alfa Aesar, (b)(h) Uncoated 99.8 % Alfa Aesar, (c)(i) 99.99+ % Alfa Aesar, (d)(j) 99.999 % Alfa Aesar, (e)(k) 99.9999 % Alfa Aesar, (f)(l) 99.9 % Goodfellow. Low and high magnification images presented

The SEM imaging indicates that the CH_3COOH cleaning effectively reduced the surface contaminations on all the Cu foils. The cleaning appears least effective on the Coated 99.8 % Alfa Aesar Cu foil, as surface contamination particles are still visible on the CH_3COOH cleaned substrate. This is presumably due to the calcium surface coating that was confirmed through analysis presented in Chapter 8.1.1.2

being resistant to CH_3COOH etching, and also protecting the etching of the underlying copper oxide. Nonetheless, there is a minor reduction in the density and particle size of contaminants on the CH_3COOH cleaned substrate when compared to the untreated substrate. On all other substrates the CH_3COOH cleaning appears to have removed the great majority of contamination particles, leaving the Cu surface relatively clean. This observation suggests that a significant proportion of the surface contaminations visible after annealing the Cu foils must in fact be present on the surface prior to the annealing. Therefore, it seems likely that at least some of the contaminations originate from surface residues deposited in the manufacturing process, rather than impurities dissolved within the bulk foil. Due to this observation I hypothesised that alternative treatments that aggressively strip the surface of the Cu foils- such as cleaning in $FeNO_3$ or electropolishing- may also be helpful to produce a cleaner Cu substrate for graphene growth.

I conducted optical profilometry on the CH_3COOH cleaned and annealed Cu foils to investigate whether the cleaning procedure influenced the surface topography and roughness, Figure 108. By comparing each sample with the respective untreated annealed foil from Figure 92 the influence of the chemical treatment can be deduced. However, the cleaning treatment may simultaneously remove surface contaminations and etch copper oxides from the foil's surface, with opposing influences on the overall surface roughness.

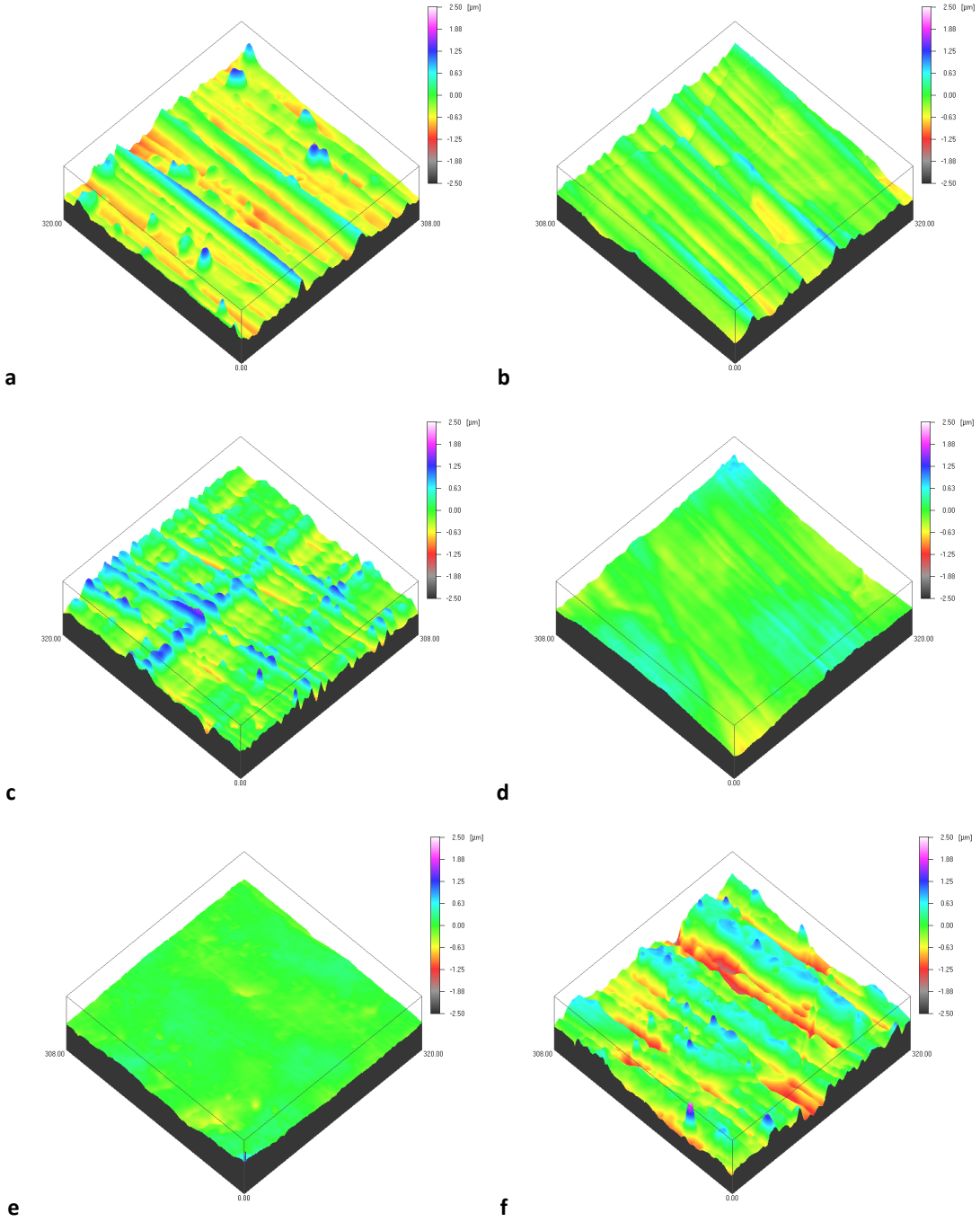


Figure 108: Optical profilometry 3D images of various CH_3COOH cleaned and annealed Cu foils (a) Coated 99.8 % Alfa Aesar, (b) Uncoated 99.8 % Alfa Aesar, (c) 99.99+ % Alfa Aesar, (d) 99.999 % Alfa Aesar, (e) 99.9999 % Alfa Aesar, (f) 99.9 % Goodfellow. 308 x 320 µm, total z-range of 5 µm, with the mean height offset to Z=0 µm

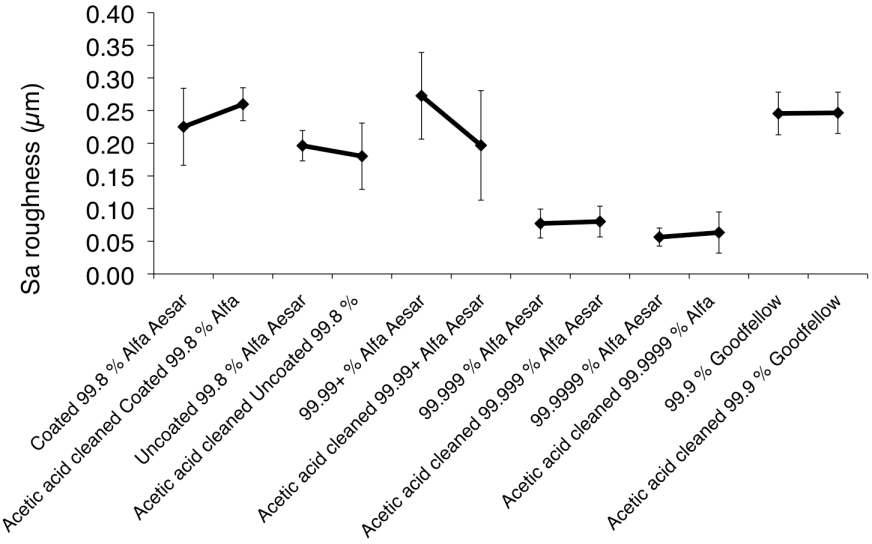


Figure 109: Comparison of mean surface roughness measured by optical profilometry of various Cu foils with and without CH_3COOH cleaning with error bars indicating 95% confidence interval

While the CH_3COOH cleaning resulted in some changes in the surface topography and roughness of some Cu foils, no consistent trend is observed for all the Cu foils. No significant change was detected for the surface roughness of the CH_3COOH cleaned and annealed 99.999 % Alfa Aesar, 99.9999 % Alfa Aesar and 99.9 % Goodfellow Cu foils, within the experimental variation observed across the foil. A reduction in surface roughness was detected for the CH_3COOH cleaned and annealed 99.99+ % Alfa Aesar Cu foils, while an increase in surface roughness was detected for the Coated 99.8 % Alfa Aesar Cu foil.

8.2.1.2 Chemical composition and concentration of surface impurities on CH_3COOH cleaned and annealed copper foils via XPS and SIMS

XPS analysis of the Cu foils following CH_3COOH cleaning and annealing provides an indication of the change in surface composition due to the cleaning procedure, Table 4.

Table 4: XPS analysis of elemental composition of untreated and CH_3COOH cleaned and annealed Cu foils

Cu foil	***Percentage composition***		
	Cu	***C***	***O***
Annealed Coated 99.8 % Alfa Aesar	32.6	27.7	39.7
CH_3COOH cleaned and annealed Coated 99.8 % Alfa Aesar	38.2	24.0	37.9
Annealed Uncoated 99.8 % Alfa Aesar	27.1	27.6	45.4
CH_3COOH cleaned and annealed Uncoated 99.8 % Alfa Aesar	34.1	27.0	38.9
Annealed 99.99+ % Alfa Aesar	30.5	18.2	51.4
CH_3COOH cleaned and annealed 99.99+ % Alfa Aesar	40.2	14.3	45.5
Annealed 99.999 % Alfa Aesar	40.0	23.6	36.4
CH_3COOH cleaned and annealed 99.999 % Alfa Aesar	46.0	22.2	31.9
Annealed 99.9999 % Alfa Aesar	32.4	17.4	50.3
CH_3COOH cleaned and annealed 99.9999 % Alfa Aesar	36.5	22.8	40.8
Annealed 99.9 % Goodfellow	46.1	22.4	31.6
CH_3COOH cleaned and annealed 99.9 % Goodfellow	54.0	18.2	27.9

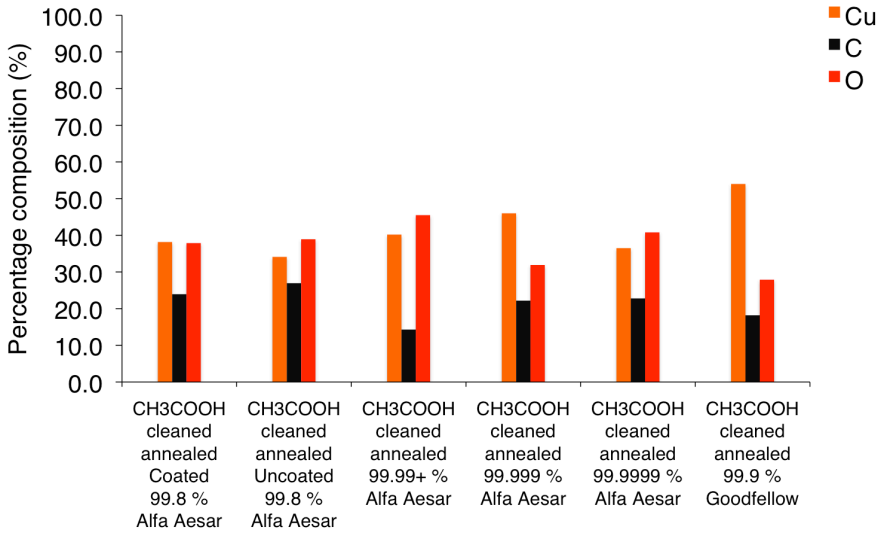


Figure 110: XPS analysis of elemental composition of Cu foils following CH_3COOH cleaning and annealing at 1035 ˚C for 30 minutes under 500 sccm H_2

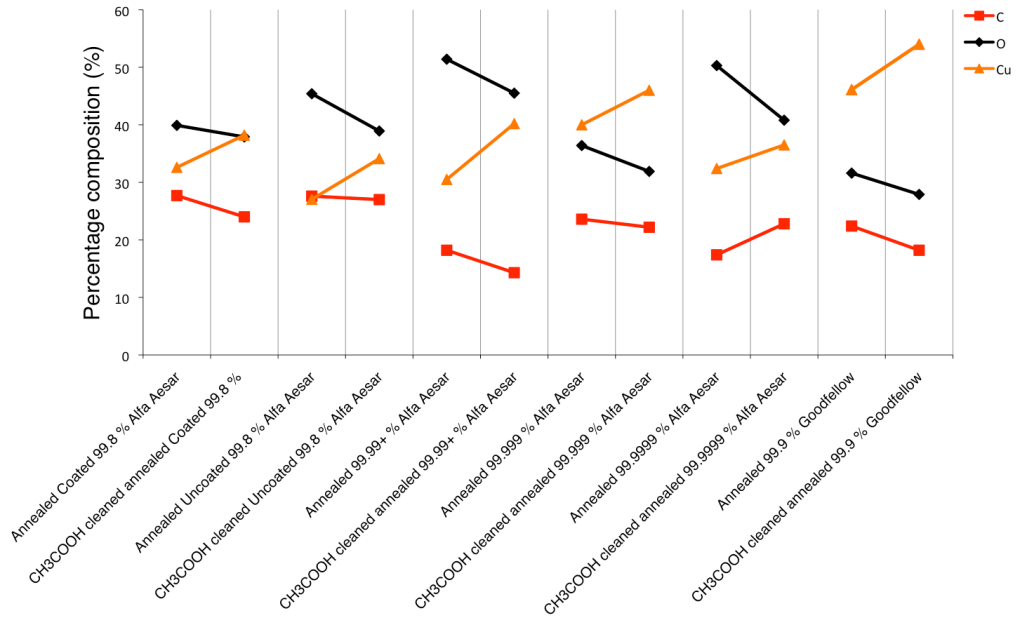


Figure 111: Comparison between XPS analysis of elemental composition of annealed Cu foils with and without CH_3COOH cleaning

XPS detected a change in the atomic percentage of Cu, C and O on the surface of the Cu foils after CH_3COOH cleaning. The XPS analysis indicated that the concentration of Cu increased and the concentration of O decreased for all the Cu foils due to the CH_3COOH cleaning, Figure 111 orange lines and black lines. A decrease in C concentration was also detected for all the Cu foils, except the 99.9999 % Alfa Aesar, Figure 111 red lines. This result indicates that, even after 30 minutes annealing in a reducing atmosphere at high temperatures, the influence of the CH_3COOH cleaning persists and is beneficial to reduce carbon contaminations and copper oxides from the surface. Any other surface contaminants present on the surface were below the XPS detection limit of ~0.2 atomic percent.

Qualitative SIMS analysis of the Cu foils following CH_3COOH cleaning provided information about the chemical composition with increased sensitivity. Surface contaminations were detected for each of the CH_3COOH cleaned Cu foils, Figure 112 to Figure 117, with similar species detected as on the untreated Cu foils in Chapter 8.1.1.2.

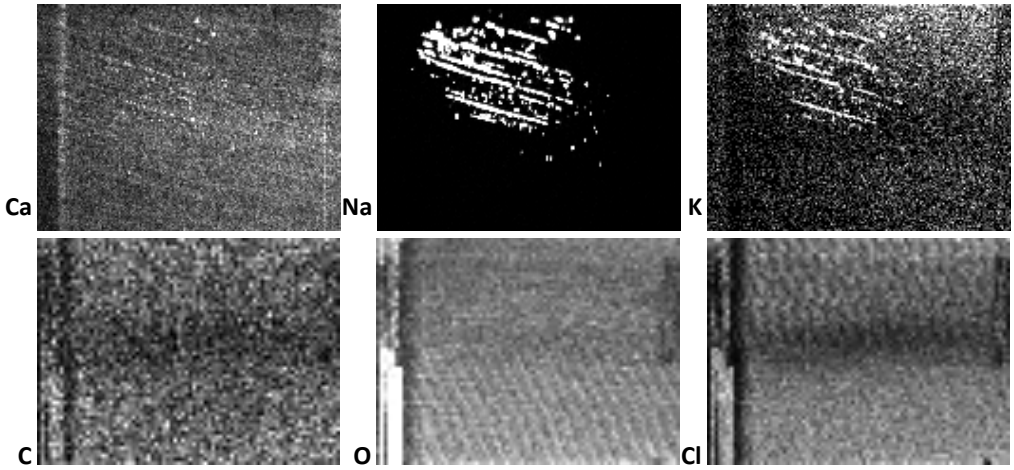


Figure 112: SIMS analysis of surface contamination on CH_3COOH cleaned and annealed Coated 99.8 % Alfa Aesar Cu foil. K map may include hydrocarbon contribution, O and Cl map include electronic interference effect. 1500 µm field of view. Top and bottom rows were obtained from different areas of sample

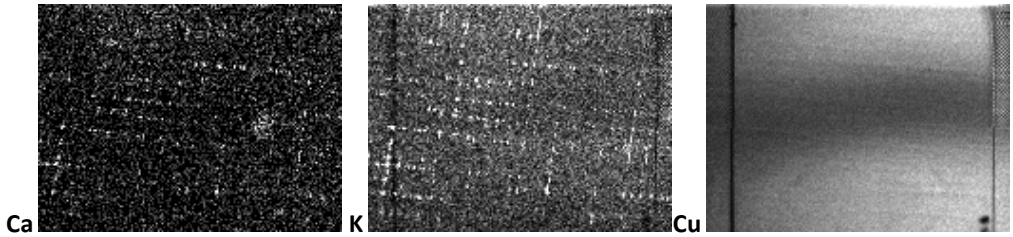


Figure 113: SIMS analysis of surface contamination on CH_3COOH cleaned and annealed Uncoated 99.8 % Alfa Aesar Cu foil. K map may include hydrocarbon contribution. 1500 µm field of view



Figure 114: SIMS analysis of surface contamination on CH_3COOH cleaned and annealed 99.99+ % Alfa Aesar Cu foil. Cu map includes electronic interference effect. 1500 µm field of view

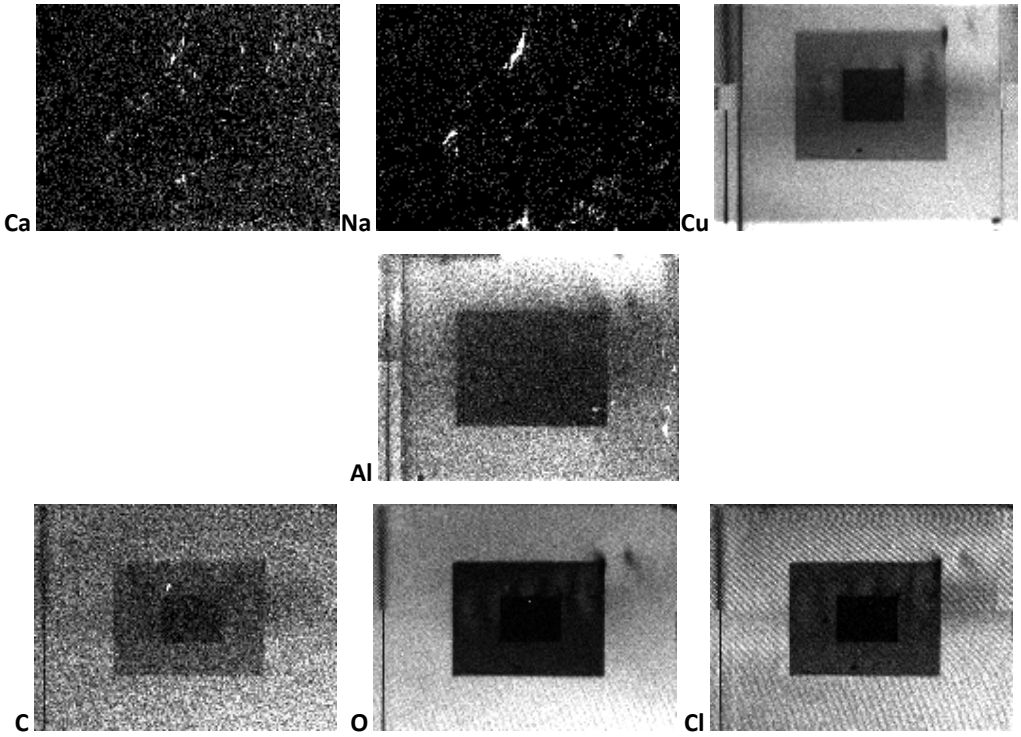


Figure 115: SIMS analysis of surface contamination on annealed 99.999 % Alfa Aesar Cu foil Darker rectangle is due to earlier exposure with smaller scan removing oxides. Ca and Na from separate region. 1500 µm field of view

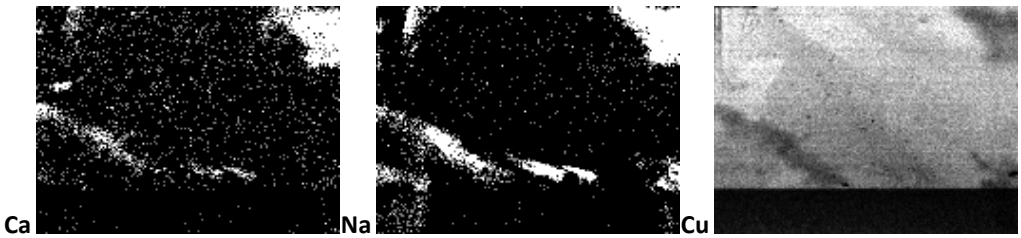


Figure 116: SIMS analysis of surface contamination on annealed 99.9999 % Alfa Aesar Cu foil 1500 µm field of view

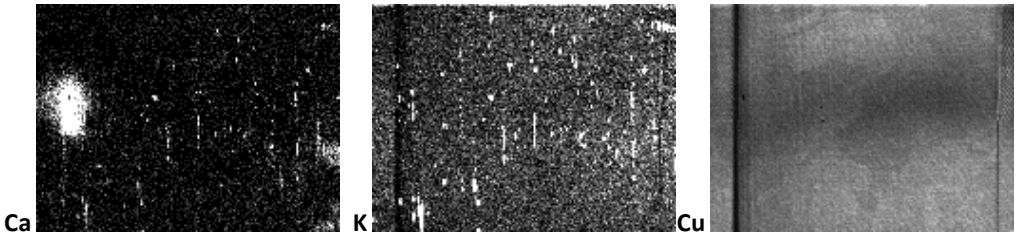


Figure 117: SIMS analysis of surface contamination on CH_3COOH cleaned and annealed 99.9 % Goodfellow Cu foil. K map may include hydrocarbon contribution. 1500 µm field of view

SIMS analysis detected a variety of elements on the CH_3COOH cleaned and annealed Cu foils including:

- Calcium, sodium, potassium (possibly with hydrocarbon contribution), carbon, chlorine and oxygen on CH_3COOH cleaned and annealed Coated 99.8 % Alfa Aesar, Figure 112,
- Calcium and potassium (possibly with hydrocarbon contribution), on CH_3COOH cleaned and annealed Uncoated 99.8 % Alfa Aesar, Figure 113,
- Calcium and sodium on CH_3COOH cleaned and annealed 99.99+ % Alfa Aesar, Figure 114,
- Calcium, sodium, carbon, chlorine, aluminium and oxygen on CH_3COOH cleaned and annealed 99.999 % Alfa Aesar, Figure 115,
- Calcium and sodium on CH_3COOH cleaned and annealed 99.9999 % Alfa Aesar, Figure 116,
- Calcium and potassium (possibly with hydrocarbon contribution) on CH_3COOH cleaned and annealed 99.9 % Goodfellow, Figure 117.

Comparing the SIMS analysis of the Cu foils with and without CH_3COOH cleaning, the same elemental contaminants were detected for each foil before and after the cleaning procedure. An exception is that potassium (possibly with some hydrocarbon contribution) was detected on the Coated 99.8 % Alfa Aesar, Uncoated 99.8 % Alfa Aesar, and 99.9 % Goodfellow Cu foils after CH_3COOH cleaning. Whether this is a new contamination from CH_3COOH cleaning, or a dissolved species within these low purity foils is unclear.

The Ca:Ga signal intensity ratio was measured for the CH_3COOH cleaned and annealed Cu foils to investigation the influence of CH_3COOH cleaning on the relative concentration of Ca contaminations, Figure 118.

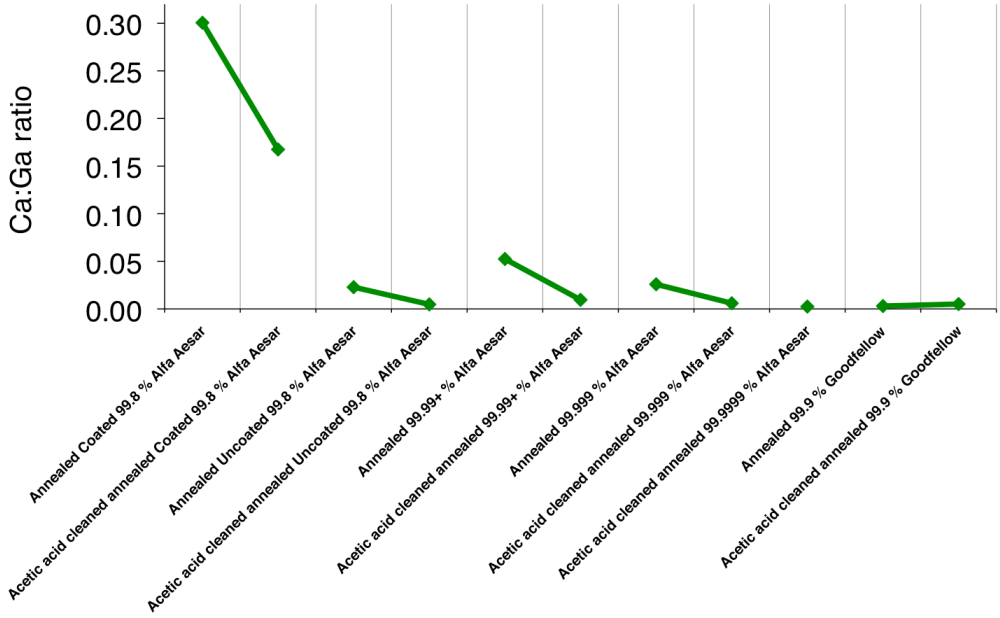


Figure 118: Comparison of SIMS Ca:Ga ratio, and hence Ca concentration, for various annealed Cu foils with and without CH_3COOH cleaning

The Ca:Ga ratio, and hence the Ca concentration, was reduced on the Cu foils cleaned with CH_3COOH. For the Coated 99.8 % Alfa Aesar Cu foil the CH_3COOH cleaning reduced the Ca concentration by ~57%, from a Ca:Ga ratio of 0.30 to 0.17. For the Uncoated 99.8 % Alfa Aesar, 99.99+ % Alfa Aesar, and 99.999 % Alfa Aesar the CH_3COOH cleaning reduced the Ca concentration by ~80% in each case (from 0.023 to 0.005, 0.052 to 0.010, and 0.026 to 0.006, respectively). The lowest detected Ca concentration was on the CH_3COOH cleaned and annealed 99.9999 % Alfa Aesar Cu foil, with a Ca:Ga ratio of 0.0025. The only exception to this trend was on the 99.9 % Goodfellow Cu foil, where the Ca:Ga ratio was measured as 0.003 before CH_3COOH cleaning, and 0.005 afterwards. This exception is due to the very low concentration of Ca initially on the 99.9 % Goodfellow Cu foil being at the limit of experimental uncertainty.

8.2.1.3 Conclusions on influence of CH_3COOH cleaning of copper foils

XPS and SIMS analyses of the chemical composition of the surface of the CH_3COOH cleaned and annealed Cu foils appears in agreement with the SEM images presented in Chapter 8.2.1.1 where CH_3COOH cleaning visibly reduced the density of surface contamination particles. Optical profilometry demonstrated that CH_3COOH cleaning can cause minor variations in the Cu foils surface roughness, however no clear trend

was observed for all the foils, and variations are within natural fluctuations. I therefore conclude that CH_3COOH cleaning and annealing is an effective method to reduce the concentration of carbon, oxygen and calcium contaminants from the surface of Cu foils prior to performing CVD of graphene. Notwithstanding, some contamination particles- with compositions that can include calcium, sodium, potassium, carbon, oxygen and chlorine- still remain on the surface of the Cu foils after CH_3COOH cleaning and annealing. The concentration of these contaminants varies between the Cu foils, however, there is no definitive correlation between the percentage purity stated by the supplier and the contaminant concentration. The CH_3COOH cleaned Coated 99.8 % Alfa Aesar Cu foil has a high density of contamination particles that corresponds with a high Ca concentration.

Based on the analysis by SEM, XPS and SIMS, I conclude that the CH_3COOH cleaned and annealed Uncoated 99.8 % Alfa Aesar, 99.9 % Goodfellow, and 99.9999 % Alfa Aesar Cu foils provide surfaces with the lowest Ca concentration and a low density of visible contamination particles. Of these foils, the CH_3COOH cleaned and annealed 99.9999 % Alfa Aesar Cu foil also has the lowest measured surface roughness.

Additionally, the discovery that CH_3COOH cleaning can reduce oxygen is an important discovery given the recent demonstration of the role of surface oxygen for decreasing nucleation density of graphene[321].

8.2.2 Variation of CVD graphene growth by CH_3COOH cleaning of copper foils

8.2.2.1 Variation to APCVD graphene growth by CH_3COOH cleaning of copper foils

I conducted APCVD graphene synthesis on the CH_3COOH cleaned Cu foils using identical synthesis parameters as presented in Chapter 8.1.2 for growth on untreated Cu foils: a synthesis temperature of 1035 ˚C, synthesis time of 15 minutes, and reactant gas flow rates of 5 sccm CH_4 and 300 sccm H_2. By comparing the graphene growth from these equivalent experiments I investigated whether the CH_3COOH cleaning of the Cu foils caused any obvious influence on the formation of the APCVD graphene domains. I aimed to correlate any variations in graphene growth with the physical and chemical analysis from Chapter 8.2.1. I investigated the APCVD graphene growth on each substrate using SEM, Figure 119.

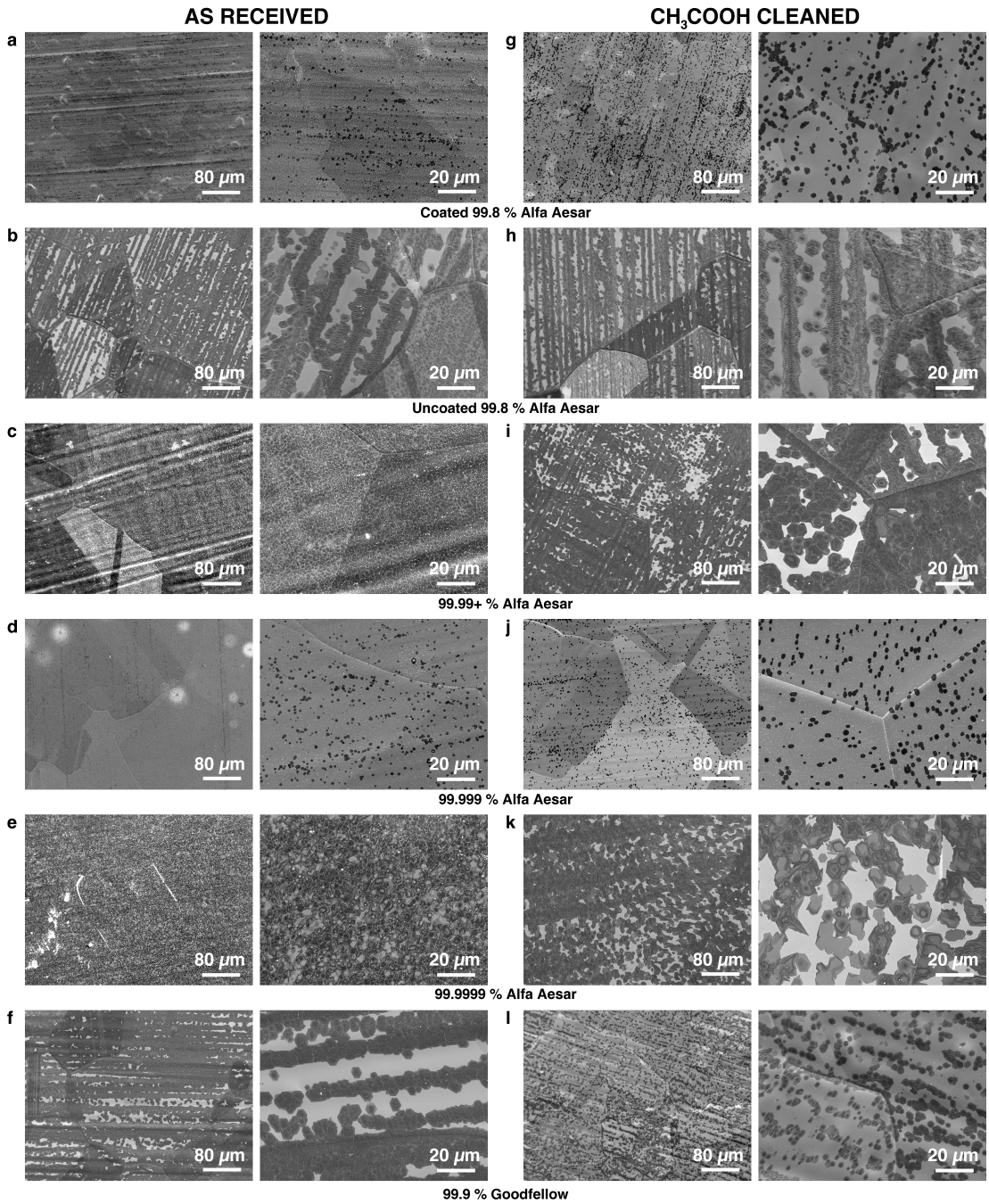


Figure 119: Comparison of SEM images of APCVD graphene growth on various Cu foils with and without CH_3COOH cleaning following 15 minutes synthesis at 1035 ˚C with 5 sccm CH_4 and 300 sccm H_2 (a)(b)(c)(d)(e)(f) without cleaning, (g)(h)(I))(j)(k)(l) with CH_3COOH cleaning. (a)(g) Coated 99.8 % Alfa Aesar, (b)(h) Uncoated 99.8 % Alfa Aesar, (c)(i) 99.99+ % Alfa Aesar, (d)(j) 99.999 % Alfa Aesar, (e)(k) 99.9999 % Alfa Aesar, (f)(l) 99.9 % Goodfellow. Low and high magnification images

The SEM images demonstrate that the CH_3COOH treatment of the Cu foils influenced the growth of APCVD graphene domains. Comparing the size and quantity of domains formed on treated and untreated Cu foils, fewer, larger domains form on

the CH_3COOH treated Cu foils (Figure 119g, h, I, j, k) for all but one of the substrates investigated (with the exception of the 99.9 % Goodfellow Cu foil, Figure 119l). This variation can be clearly observed on the Coated 99.8 % Alfa Aesar, and 99.999 % Alfa Aesar Cu foils as the domains are rarely merged together which means the size of individual, isolated domains can be measured. CH_3COOH cleaning causes the average domain size to increase from ~1.4 μm to ~2.5 μm, and the domain density to decrease from ~0.060 - 0.090 domains μm^{-2} to ~0.040 - 0.050 domains μm^{-2} on the Coated 99.8 % Alfa Aesar Cu foil (comparing Figure 119a and g). On the 99.999 % Alfa Aesar Cu foil the average domain size increases from ~1.4 μm to ~2.7 μm, and the average domain density decreases from ~0.045 - 0.055 domains μm^{-2} to ~0.023 - 0.030 domains μm^{-2} (comparing Figure 119d and j). The increase in domain size and decrease in density of domains can be inferred on the Uncoated 99.8 % Alfa Aesar, 99.99+ % Alfa Aesar, 99.9999 % Alfa Aesar Cu foils, where the graphene often completely covers the surface, due to contrast variations in the SEM images highlighting the domains boundaries (comparing Figure 119b and h, Figure 119c and i, and Figure 119e and k). However, growth on 99.9 % Goodfellow does not follow this trend, as a lower growth rate is observed (comparing Figure 119f and l). This may be understood given that the CH_3COOH cleaning did not significantly alter the properties of the 99.9 % Goodfellow Cu foil. Regardless, the observations on the five other Cu foils indicate that the nucleation density decreases and the growth rate increases on the CH_3COOH treated surfaces. Comparing this observation with the physical and chemical analysis of the CH_3COOH treated Cu foils presented in Chapter 8.2.1, I conclude that the concentration of surface contamination particles and/or surface oxides is an important factor in the growth of graphene domains on Cu foils. By cleaning the Cu foils with CH_3COOH the concentration of surface oxides, carbon contaminants, and metallic contaminants (notably Ca) is decreased, and this correlated with a decrease in the nucleation density, and increase in the growth rate, of graphene domains. It appears reasonable to hypothesise that this correlation may also indicate causation, which would provide information about the growth mechanism of graphene on Cu foils. Causation would indicate (i) the initial nucleation of a graphene domain is controlled or initiated by the presence of surface particles or surface oxides, (ii) the growth of graphene domains on the Cu surface is

reduced through the presence of surface particles or surface oxides, presumably through a mechanism that either inhibits catalysis or promotes etching. I conclude that further studies to systematically control, vary, and reduce the concentration of surface particles or surface oxides on Cu foils are important to optimise the nucleation density and growth rate of APCVD graphene domains.

8.2.2.2 Variation to LPCVD graphene growth by CH_3COOH cleaning of copper foils

I also conducted a minor investigation into LPCVD graphene synthesis on the CH_3COOH cleaned Coated 99.8% Alfa Aesar and 99.999 % Alfa Aesar Cu foils using identical synthesis parameters as presented in Chapter 5.2 for growth on the untreated foils: a synthesis temperature of 1035 ˚C, synthesis time of 5 minutes, and reactant gas flow rates of 5 sccm CH_4 and 500 sccm H_2. By comparing the graphene growth from these equivalent experiments I investigated whether the CH_3COOH cleaning of the Cu foils caused any obvious influence on the formation of the LPCVD graphene domains, and if so to correlate this with the conclusions made for APCVD growth in Chapter 8.2.2.1.

SEM images on CH_3COOH treated and untreated Coated 99.8 % Alfa Aesar Cu foil and 99.999 % Alfa Aesar Cu foil demonstrated that growth of graphene domains was influenced by cleaning of the substrate, Figure 120.

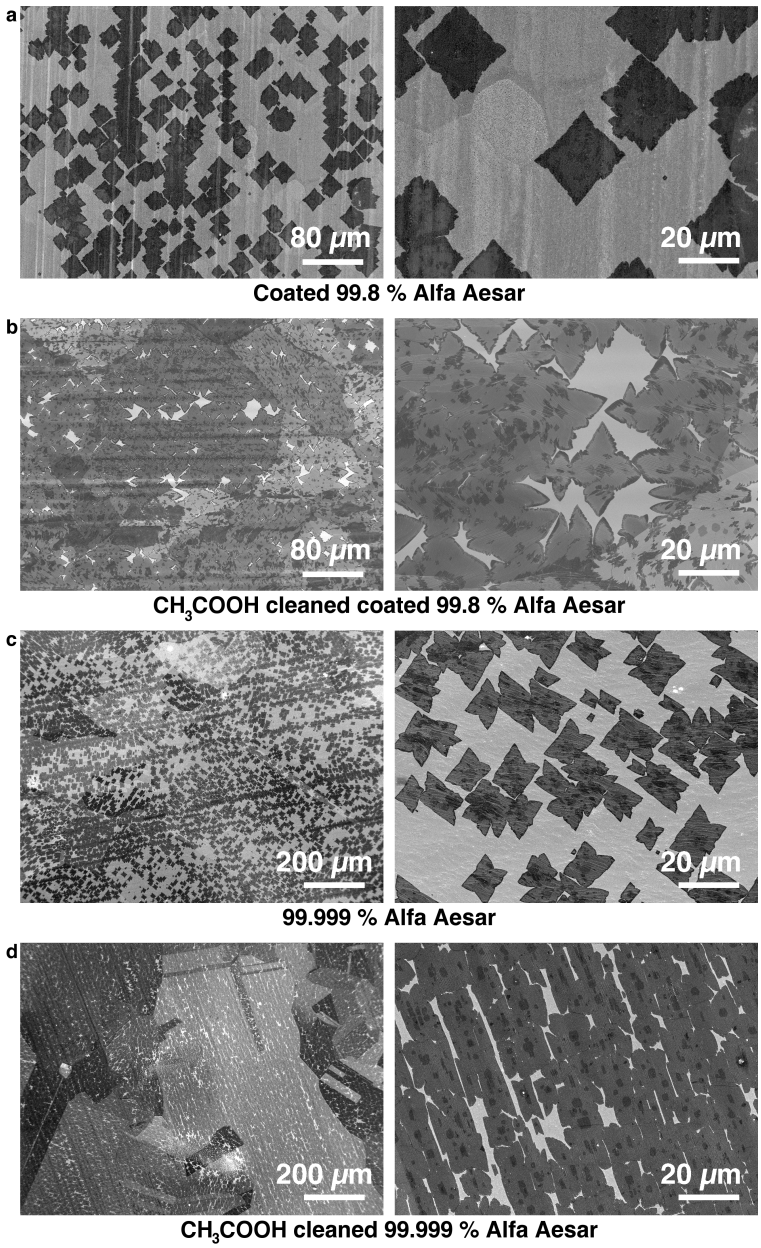


Figure 120: LPCVD graphene growth on various Cu foils with and without CH_3COOH cleaning following 5 minutes synthesis at 1035 ˚C with 5 sccm CH_4 and 500 sccm H_2 (a) Coated 99.8 % Alfa Aesar, (b) CH_3COOH cleaned Coated 99.8 % Alfa Aesar, (c) 99.999 % Alfa Aesar, (d) CH_3COOH cleaned 99.999 % Alfa Aesar

A higher nucleation density is observed on the CH_3COOH cleaned Cu foils (Figure 120 b and d) compared to the uncleaned foils (Figure 120a and c) for both the Coated 99.8 % Alfa Aesar Cu foil and the 99.999 % Alfa Aesar Cu foil. For the Coated 99.8 % Alfa Aesar Cu foil, CH_3COOH cleaning causes the domains to become well-defined shapes, often with dendritic features branching of the sides of the major lobe of each domain (comparing Figure 120a and b). The concentration of contamination

particles on the surface of the graphene domains is also reduced on the CH_3COOH cleaned Coated 99.8 % Alfa Aesar Cu foil, Figure 120b. These observations, in combination with the chemical analysis of the CH_3COOH cleaned Cu foils presented in Chapter 8.2.1.2, indicate that by reducing the concentration of surface contamination particles the probability of LPCVD graphene nucleation increased. As a consequence, this result suggests that while surface contaminations may be beneficial in promoting graphene nucleation, an excess of particles may also restrict the formation of graphene domains through an etching mechanism. The variation in domains from square to dendritic shapes with CH_3COOH cleaning of the Coated 99.8 % Cu foil is perhaps indicative of the type of etching that the surface contatmination particles produce when in an excess concentration.

8.2.2.3 Conclusions on influence of CH_3COOH cleaning of copper foils on APCVD and LPCVD graphene growth

These investigations demonstrate that CH_3COOH cleaning is an effective method of reducing the concentration of carbon, oxygen and calcium contaminations on Cu foils. CVD graphene growth was influenced as a consequence of this cleaning treatment. APCVD growth on CH_3COOH cleaned Cu foils had a reduced nucleation density and an increased growth rate. In comparison, LPCVD growth on CH_3COOH cleaned Cu foils had an increased nucleation density and resulted in graphene domains becoming well-defined dendritic shapes. This difference may be indicative of fundamental differences between the reaction mechanisms of APCVD and LPCVD graphene growth. I conclude that CH_3COOH cleaning is a useful technique for controlling and improving the growth of CVD graphene on Cu foils.

8.2.3 Alternative cleaning treatments

During my research I also conducted some minor investigations into alternative methods of cleaning the surface of the Cu foils. I selected methods that would aggressively strip the surface of the Cu foils, aiming to remove a maximum amount of contaminations that remained from the manufacturing process. By following this treatment with subsequent annealing of the substrate I hoped to produce a clean and smooth surface for graphene growth. While the influence of the cleaning

treatments on the properties of the Cu foils was left as future work to be completed, comparison of APCVD and LPCVD graphene growth on treated and untreated Cu foils indicates that using aggressive treatments can be beneficial.

8.2.3.1 Variation to APCVD graphene growth by $FeNO_3$ cleaning of copper foil

I cleaned Coated 99.8 % Alfa Aesar Cu foils for 10 minutes in 1 M $FeNO_3$. This was followed by a rinse in deionised H_2O, 10 minutes cleaning in concentrated CH_3COOH, and a final deionised H_2O rinse and blow dry by flowing N_2.

I conducted APCVD growth of graphene on the $FeNO_3$ treated Cu foil at 1035 ˚C using 5 sccm CH_4, 300 sccm H_2 for 15 minutes. This is presented beside equivalent growth on untreated and CH_3COOH cleaned Cu foils in Figure 121.

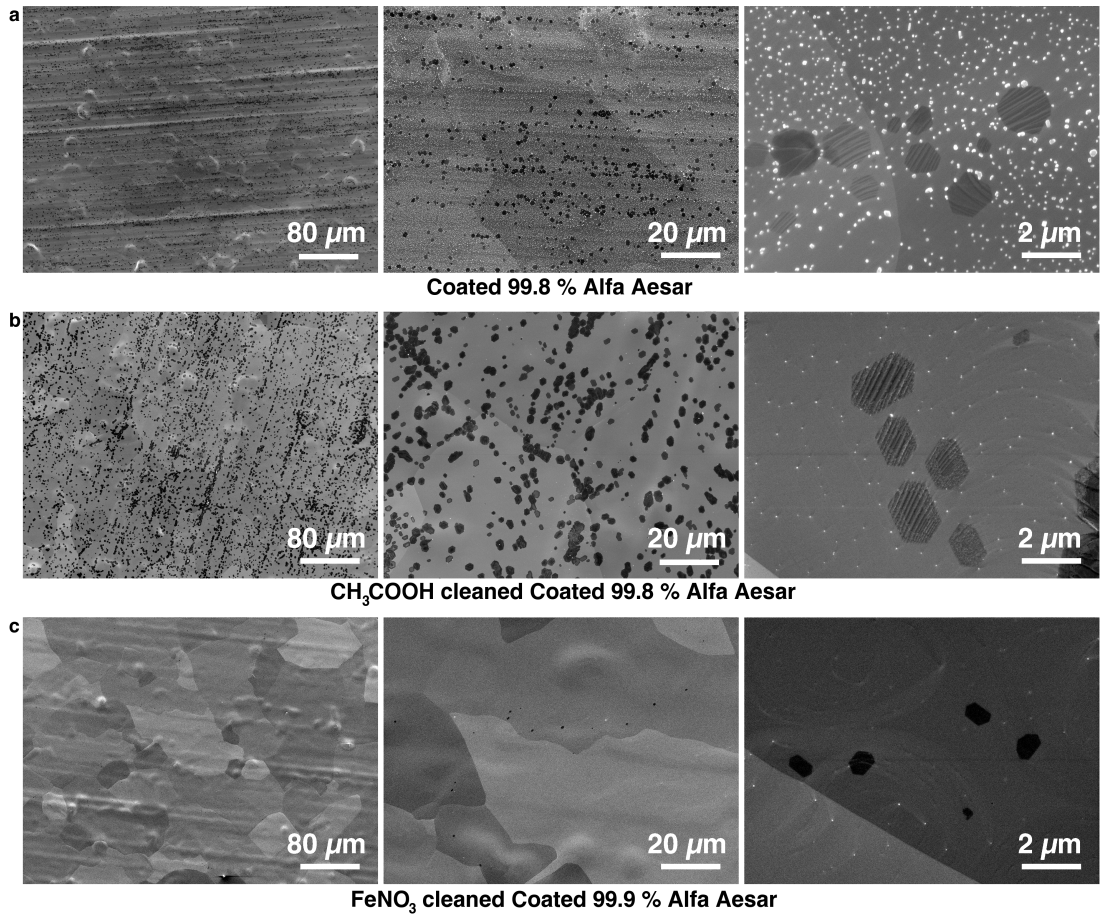


Figure 121: Comparison of APCVD graphene growth on Coated 99.8 % Alfa Aesar Cu foil with CH_3COOH and $FeNO_3$ cleaning following 5 minutes synthesis at 1035 ˚C with 5 sccm CH_4 and 500 sccm H_2 on (a) untreated Cu foil, (b) CH_3COOH cleaned Cu foil, (c) $FeNO_3$ cleaned Cu foil

APCVD growth was conducted simultaneously on the $FeNO_3$ cleaned Cu foil and the CH_3COOH cleaned Cu foil. As a consequence, any variations between the domains

are purely due to differences in the surfaces due to the two cleaning procedures and resulting Cu surface. The $FeNO_3$ treatment significantly reduced the nucleation density of APCVD graphene domains, from ~0.060 - 0.090 domains µm $^{-2}$ to ~0.0018 domains μm^{-2}, while the average domain size decreased from ~1.4 µm to ~0.8 µm (comparing Figure 121a and c). The nucleation density was not uniform across the substrate, with many regions having a much lower density, or appearing completely free of graphene domains.

8.2.3.2 Variation to LPCVD graphene growth by $FeNO_3$ cleaning of copper foil

I also conducted LPCVD growth of graphene on the $FeNO_3$ treated Cu foil at 1035 ˚C using 5 sccm CH_4 and 500 sccm H_2 for 6 minutes, Figure 122.

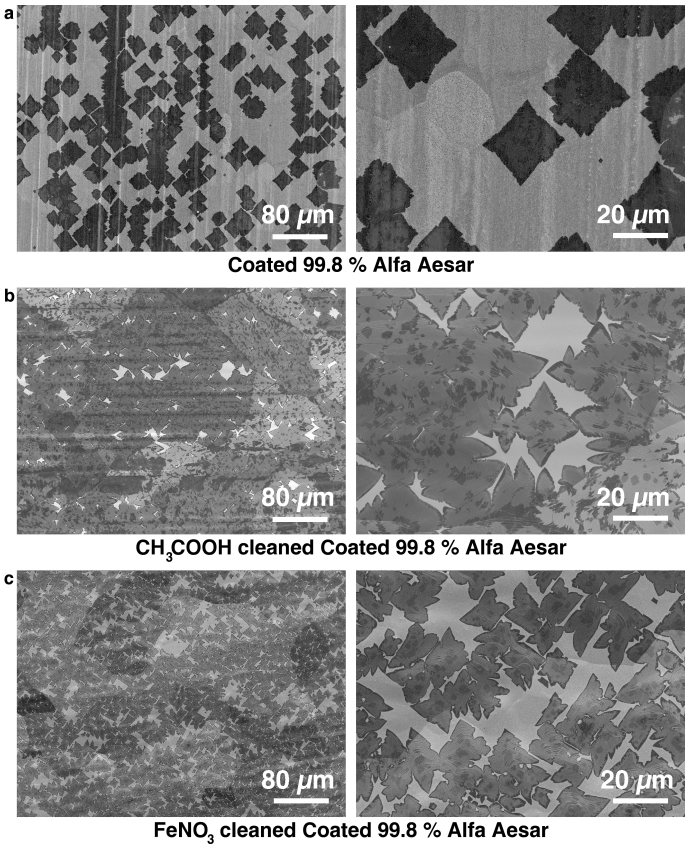


Figure 122: Comparison of LPCVD graphene growth on Coated 99.8% Alfa Aesar Cu foil with CH_3COOH and $FeNO_3$ cleaning at 1035 ˚C with 5 sccm CH_4 and 500 sccm H_2 on (a) Untreated Cu foil, (b) CH_3COOH cleaned Cu foil, (c) $FeNO_3$ cleaned Cu foil. (a)(b) 5 minutes synthesis time, (c) 6 minutes synthesis time

An increase in nucleation density is visible on the $FeNO_3$ cleaned Coated 99.8 % Alfa Aesar Cu foil when compared to the untreated foil (comparing Figure 122a and c). As occurred with CH_3COOH cleaning, the domains on the $FeNO_3$ cleaned Cu foil show

dendritic growth and have a significant reduction in the concentration of surface contamination particles, Figure 122c. However, the surface coverage and growth rate of LPCVD graphene domains is reduced for the $FeNO_3$ cleaned Coated 99.8 % Cu foil when compared with the foil cleaned by CH_3COOH. This is notable by comparing Figure 122b and Figure 122c- even though the latter demonstrates growth from a synthesis time of 6 minutes, rather than 5 minutes- and was also confirmed by comparing with growth on CH_3COOH cleaned Cu foil for 6 minutes which resulted in full coverage of graphene across the surface.

8.2.3.3 Variation to LPCVD graphene growth by electrochemical polishing of copper foils in $K_2S_2O_8$

99.999 % Alfa Aesar Cu foils were cleaned via electropolishing for 60 minutes in an electrolytic cell following a procedure similar to that outlined by Wang *et al*.[198] for the electrochemical delaminating transfer of PMMA-coated graphene. 0.05 M $K_2S_2O_8$ was used as the aqueous electrolyte, a glassy carbon rod was used as the anode, and the Cu foil was used as a cathode with -5 V applied voltage. This caused simultaneous reactions at the Cu foil cathode; H_2O was reduced to produce H_2 bubbles, while Cu was etched by $S_2O_8^{-2}$ to form Cu^{2+}. The Cu foil was then rinsed in deionised water, annealed for 30 minutes at 1035 ˚C under 500 sccm H_2, and LPCVD growth of graphene was conducted at 1035 ˚C with 5 sccm CH_4 and 500 sccm H_2 for 5 minutes. The experiment was also conducted with an additional 10 minute CH_3COOH ultrasonic treatment of the Cu foil prior to the electropolishing. SEM imaging demonstrated that graphene growth varied significantly between the Cu foils with different cleaning, Figure 123.

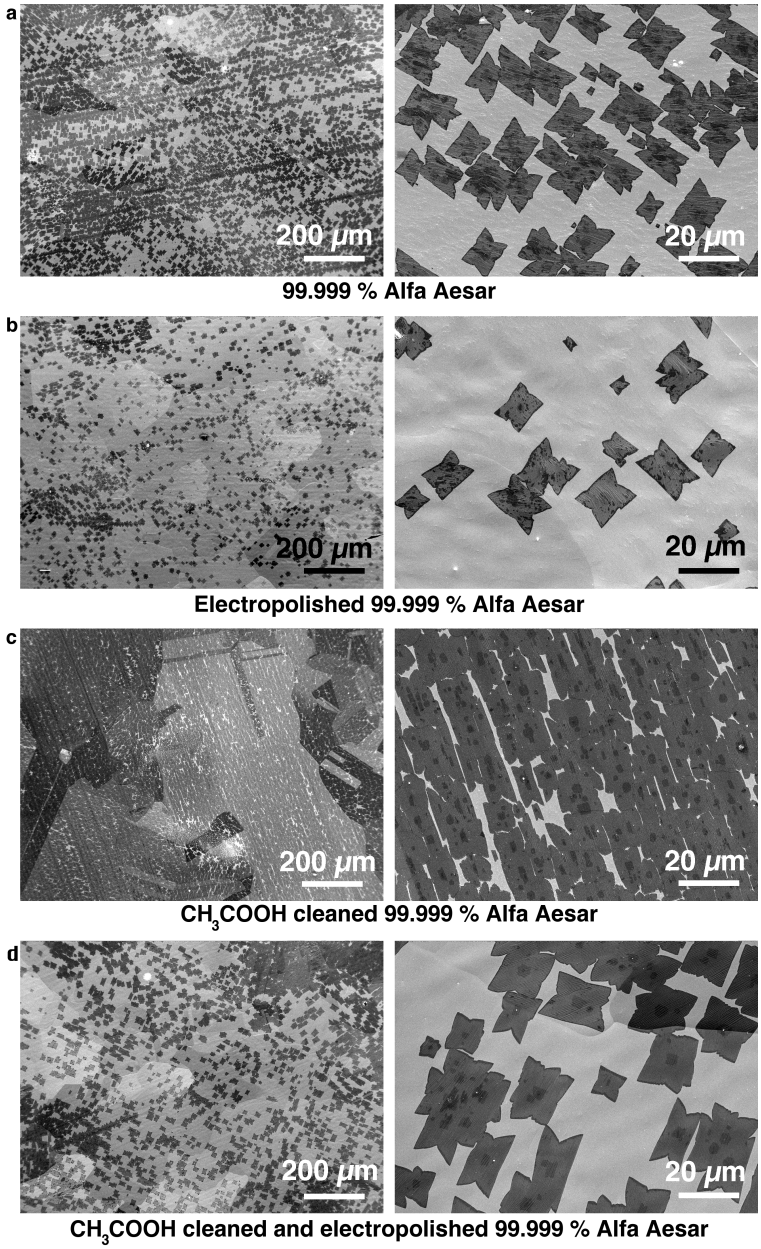


Figure 123: Comparison of LPCVD graphene growth on 99.999 % Alfa Aesar Cu foil with CH_3COOH cleaning and electropolishing following 5 minutes synthesis at 1035 ˚C with 5 sccm CH_4 and 500 sccm H_2 on (a) untreated Cu foil, (b) Electropolished Cu foil, (d) CH_3COOH cleaned Cu foil, (d) CH_3COOH cleaned and electropolished Cu foil

The nucleation density of graphene domains decreased on the electropolished 99.999 % Alfa Aesar Cu foil, from ~0.065 domains μm^{-2} to ~0.00107 domains μm^{-2} (comparing Figure 123a and b). However, the nucleation density was not homogenous across the electropolished Cu foil, Figure 123b. Regions can still be identified with a locally high nucleation density, notably near surface contamination particles. This is further evidence that suggests the contamination particles aid the

nucleation of the graphene domains. In comparison, the nucleation density increased on CH_3COOH treated Cu foil, Figure 123c, as previously demonstrated in Chapter 8.2.2.2. The nucleation density on the CH_3COOH treated and electropolished Cu foil varies significantly, Figure 123d, with some regions showing a locally low density similar to the electropolished Cu foil, and other regions showing locally high density similar to the CH_3COOH treated Cu foil. The growth rate of domains appears relatively uniform across all the Cu foils. These observations indicate that electropolishing can be used to reduce the nucleation density of graphene domains on Cu foils, however, further improvements to the treatment are necessary to improve the uniformity of growth across the Cu foil. Further investigations into the influence of parameters for the electropolishing- for instance, the applied voltage, time, electrolyte concentration, and geometry of the cell- may be beneficial to optimise this treatment.

8.2.3.4 Conclusions on alternative cleaning treatments

My investigations demonstrate $FeNO_3$ and electropolishing show promise as alternative cleaning treatments. Cleaning 99.8 % Alfa Aesar Cu foil with $FeNO_3$ significantly reduced the nucleation density and average domain size of APCVD graphene domains, but increased the nucleation density of LPCVD graphene domains. Electropolishing of 99.999 % Alfa Aesar Cu foil was also demonstrated to reduce the nucleation density, however, this influence was inhomogenous across the substrate.

9 Atmospheric-pressure chemical vapour deposition of graphene on platinum foils

This chapter outlines experiments investigating the APCVD synthesis of graphene on Pt foil substrates. The investigations provide a complimentary study to the research on Cu foils presented in Chapter 5, Chapter 6, Chapter 7 and Chapter 8, and, to some extent, these investigations represent the culmination of my research into the production of large-area graphene. The experiments were conducted in partnership with Mr Vitaliy Babenko (Department of Materials, University of Oxford), who at the time was a Summer Student within Professor Nicole Grobert's Nanomaterials by Design research group. Vitaliy conducted the great majority of APCVD synthesis procedures, while I conducted all the SEM and EDX analysis. With mutual discussion I directed the progress of the research into APCVD growth on Pt foils as presented herein. Owing to the success of these investigations research is continuing into the synthesis of large-area graphene on Pt foil within the Nanomaterials by Design group. Dr Antal Koos also provided some incidental assistance with SEM and discussion in the later stages of the investigations.

Parts of this chapter have been prepared for publication:

Murdock, A.T., Babenko, V., Britton, J., Koos, A.A., Grobert, N., Influence of the synthesis parameters on the growth of polycrystalline chemical vapour deposition graphene domains on Pt foils, *Nanoscale*

Babenko, V., Murdock, A.T., Koos, A.A., Britton, J., Crossley, A., Holdway, P., Moffat, J., Alexander-Webber, J., Huang, N., Nicholas, R., Grobert, N., Rapid, epitaxy-free graphene synthesis on silicidated polycrystalline platinum, *Nature Materials*

9.1 Investigations into the influence of synthesis parameters on APCVD graphene growth on 99.99+ % Goodfellow Pt foil

APCVD growth of graphene on commercial, polycrystalline Pt foils was first demonstrated in 2011 by T. Gao *et al.*[175]. In early 2012 L. Gao *et al.*[176] produced millimetre-size single-crystal hexagonal graphene domains. Prior to these studies, graphene growth on Pt was limited to single crystal substrates such as Pt(111) under UHV conditions[117, 173, 174]. With the discovery that APCVD of graphene was viable on relatively cheap polycrystalline Pt foils (compared to single crystal substrates) I recognised the need for investigations into this procedure due to the benefits of using Pt foils over Cu, namely:

(i) Ease of producing high quality large-area graphene sheets, as very large domains (100 µm - 1mm) form for equivalent reaction conditions when using Pt,

(ii) Quicker and cheaper procedure, as a higher growth rate is achieved on Pt,

(iii) Cheaper procedure, as Pt foil is reusable by adopting the non-destructive electrochemical bubbling transfer of graphene[176].

In this study APCVD graphene was grown on 10 x 10 mm samples of 25 µm thick, 99.99+ % Pt foils (Goodfellow, item number: 820-253-11), as-received from the supplier without pre-treatment, using the APCVD setup described in Chapter 6.2. Initial experimental conditions of 5 sccm CH_4 and 500 sccm H_2 at 1045 ˚C were selected based on the results from Chapter 6 for APCVD on Cu foils, with adjustment of a higher H_2 flow rate (500 sccm rather than 300 sccm) and shorter synthesis time (5 minutes rather than 15 minutes) given the increased catalytic nature of Pt compared to Cu. Together with experiments conducted for 10 minutes and 30 minutes the variation of graphene growth with synthesis time can be observed, Figure 124.

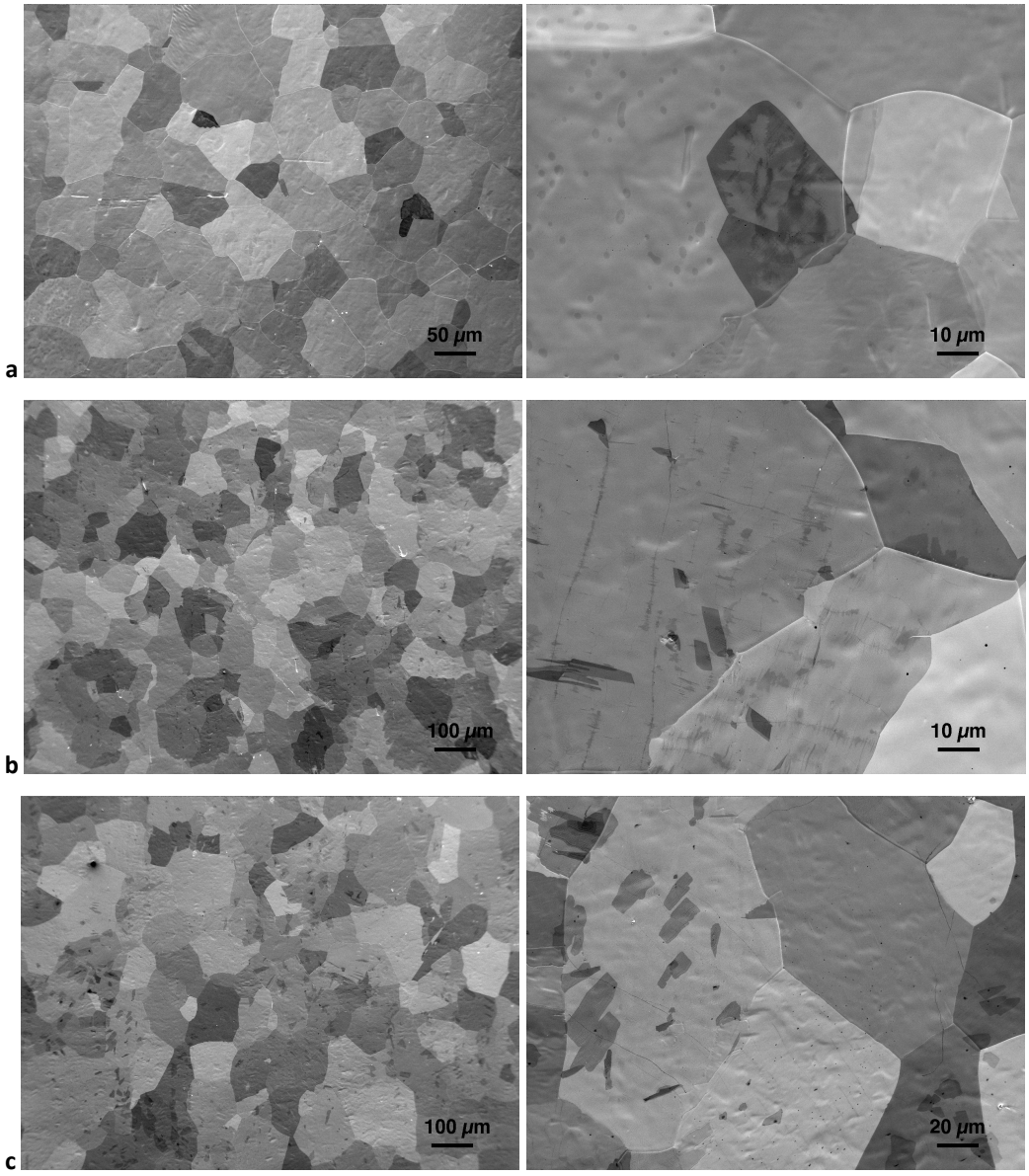


Figure 124: APCVD graphene growth on 99.99+ % Goodfellow Pt foil at 1045˚C with 5 sccm CH_4 and 500 sccm H_2 for synthesis time of (a) 5 minutes, (b) 10 minutes, and (c) 30 minutes

The domains formed after 5 minutes synthesis time appear to be single-layer, however, after 10 minutes synthesis time many bilayer and few-layer regions can be observed. The size and density of these multilayers increase for 30 minutes synthesis time. The shape of the multilayers appeared similar to those reported previously[175, 176].

The APCVD growth of graphene on Pt foils shows some notable variations to growth on Cu foils with equivalent reaction conditions. The domains on Pt foil have no distinct shape or orientation in comparison to the aligned hexagonal domains observed on Cu foil. Furthermore, as predicted, on Pt the growth rate is significantly

higher than for equivalent reactant gas flow rate ratios used with Cu. Comparing Figure 124 with Figure 64 from Chapter 6.4, a growth rate of ~10 - 25 µm min^{-1} is observed on Pt foil (with 500 sccm H_2), two orders of magnitude higher than the rate of ~0.15 - 0.40 µm min^{-1} observed on Cu foil (with 300 sccm H_2). Given this result, it is somewhat unexpected that the density of nucleation sites is significantly lower on Pt compared to Cu. This observation may be indicative of a fundamental difference in the growth mechanism and energy barrier for nucleation of graphene domains on the two metals. Another possible explanation is that the concentration of surface contaminants is lower on Pt foil. Indeed, the Pt foil appeared incredibly clean and devoid of contamination particles following annealing pre-treatment, Figure 125.

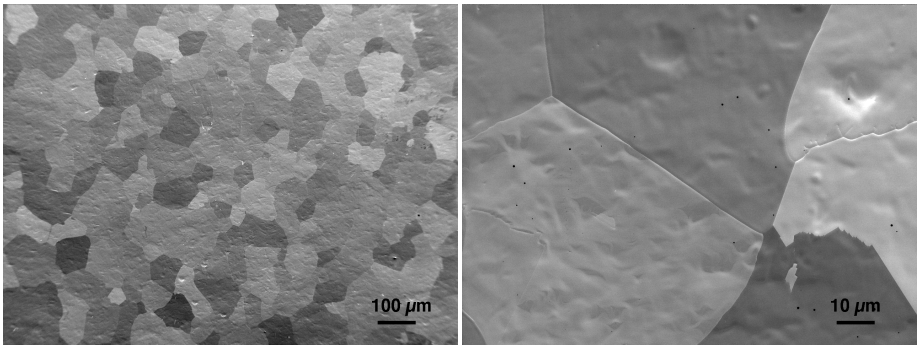


Figure 125: 99.99+ % Goodfellow Pt foil annealed at 1045 ˚C for 30 minutes

This observation warranted the need for investigations into the nature of nucleation sites on the Pt foils, discussed further in Chapter 9.2.

9.1.1 Influence of CH_4:H_2 flow rate ratio

The influence of the reactant gas flow rate ratio on the growth of graphene on Pt foils was investigated by systematically varying either the CH_4 or H_2 flow rate while keeping other parameters constant. The aim of this investigation was to (i) increase the size of individual domains, (ii) reduce the density of nucleation sites, and (iii) reduce the quantity of bilayer and few-layer regions across the domain, thereby promoting synthesis of large-area single-layer hexagonal graphene domains across the entire Pt foil. Representative SEM images are presented in Figure 126 for a series of experiments with varying CH_4 flow rate (with constant 500 sccm H_2) and Figure 127 for varying H_2 flow rate (with constant 4 sccm CH_4).

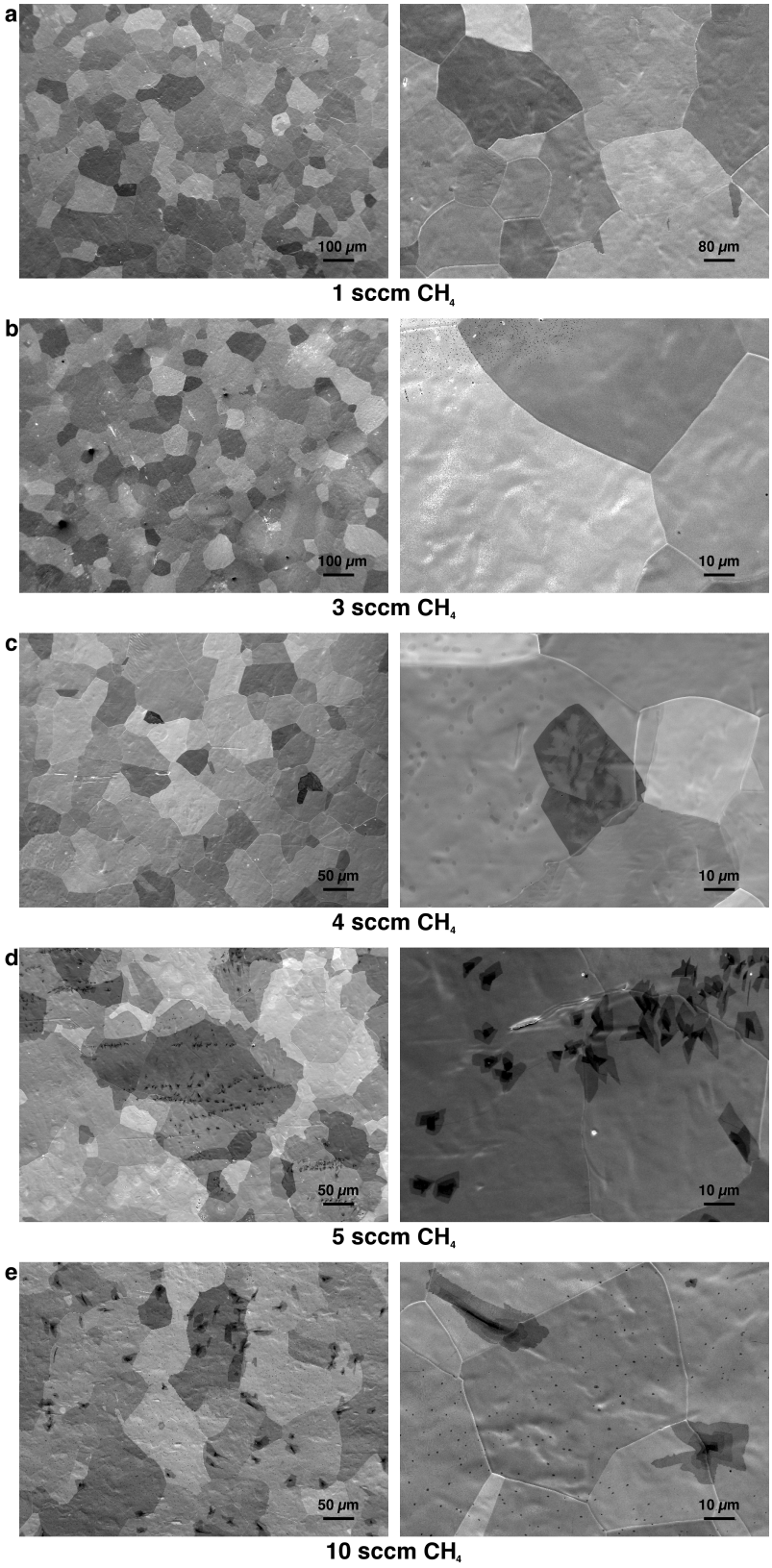


Figure 126: APCVD graphene growth at 1045˚C on Pt foil with 500 sccm H_2 and varying CH_4 flow rate (a) 1 sccm CH_4, (b) 3 sccm CH_4, (c) 4 sccm CH_4, (d) 5 sccm CH_4, (e) 10 sccm CH_4. (a) and (b) are for 30 minutes synthesis time and show no growth, (c)(d)(e) are for 5 minutes synthesis time

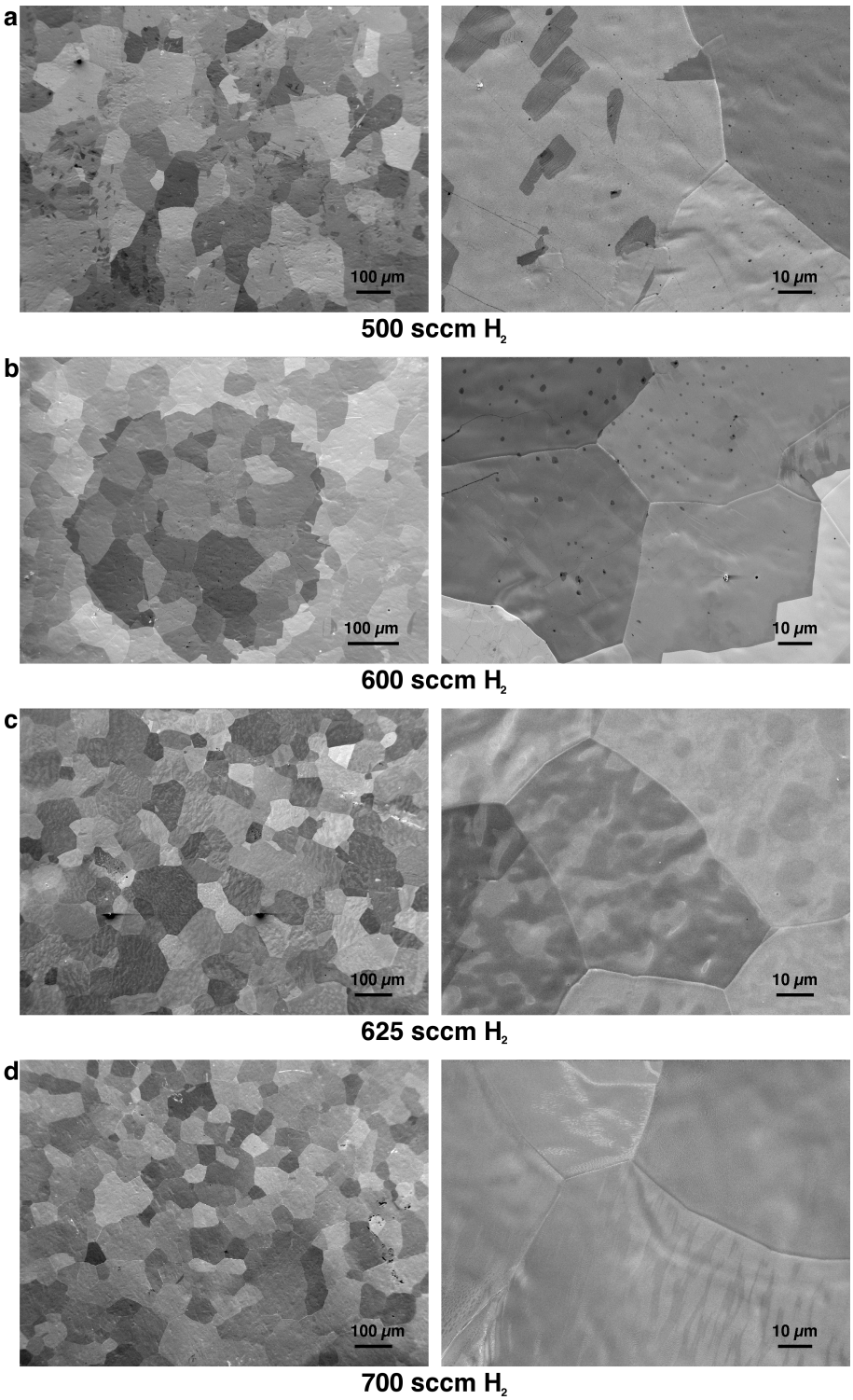


Figure 127: APCVD graphene growth on Pt foil at 1045˚C with 4 sccm CH_4 and varying H_2 flow rate (a) 500 sccm H_2, (b) 600 sccm H_2, (c) 625 sccm H_2, (d) 700 sccm H_2. (a)(b)(c) 30 minutes synthesis time, (d) 120 minutes synthesis time. (c) and (d) show no growth

The two series of experiments demonstrate that the CH_4 and H_2 flow rates influence the density of nucleation sites, the density of bilayer and few-layer regions, and the growth rate and size of the graphene domains. As the CH_4 flow rate is increased from 1 sccm to 4 sccm with constant H_2 flow rate of 500 sccm the growth transitioned from initially being altogether absent, Figure 126a and Figure 126b, to producing relatively small ~30 µm individual single-layer domains, Figure 126c. As CH_4 flow rate was increased further to 5 sccm, relatively large ~200 µm individual domains formed with a high density of bilayer and few-layer regions across the domain, Figure 126d. Ultimately, with 10 sccm CH_4 full coverage of the Pt foil occurs with relatively large ~30 µm bilayer and few-layer regions, Figure 126e.

As the H_2 flow rate is increased from 500 sccm to 700 sccm, with constant CH_4 flow rate of 4 sccm, an opposite trend is observed. Full coverage with ~20 µm bilayer and few-layer regions is observed for 500 sccm H_2, Figure 127a. This growth transitions to very large ~500 µm individual domains with some ~2 µm bilayer and few-layer regions as the hydrogen flow rate increases to 600 sccm H_2, Figure 127b. Eventually, as the H_2 flow rate increases to 625 sccm the growth is restricted completely, Figure 127c, which prevails for growth with 700 sccm H_2 even with extended synthesis time of 120 minutes, Figure 127d.

These observations demonstrate there are regions of the synthesis parameters space in which optimum single-layer growth can be promoted. From these trends this is with $3 < CH_4 < 4$ sccm and 500 sccm H_2 for a synthesis time greater than 30 minutes, and 4 sccm CH_4 with $600 < H_2 < 625$ sccm for a synthesis time greater than 30 minutes. This is equivalent to a CH_4:H_2 flow rate ratio of 1:125 - 1:166 and 1:150 - 1:156, respectively.

Two notable situations occurred during this investigation. Domains with a clear hexagonal shape were observed on a few rare occasions following growth with 4 sccm CH_4 and 500 sccm H_2 for 5 minutes synthesis time, Figure 128. These domains always formed within a single grain of the Pt foil, never across grain boundaries.

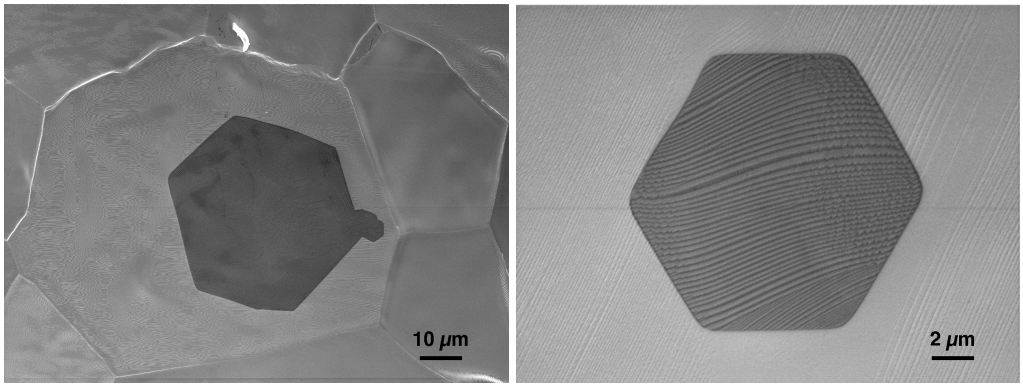


Figure 128: Hexagonal single-layer APCVD graphene domains on Pt foil following 5 minutes synthesis at 1045 ˚C with 4 sccm CH_4 and 500 sccm H_2

A second observation was that the density, shape, and orientation of the bilayer and few-layer regions sometimes varied with different grains of the Pt foil, Figure 129.

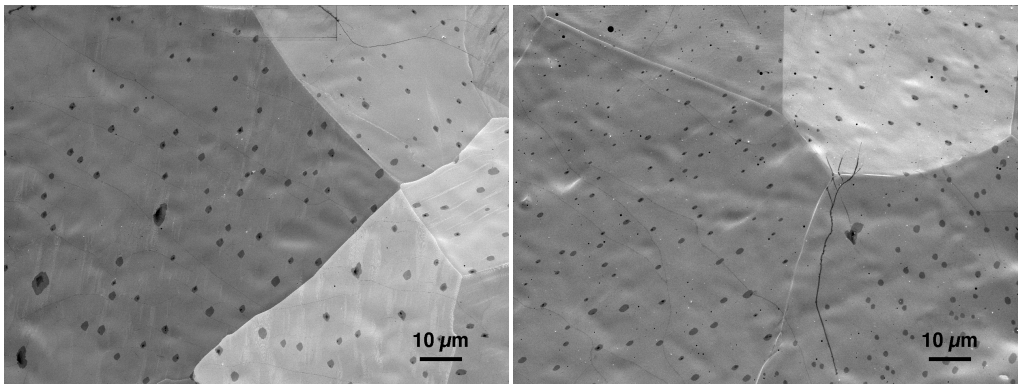


Figure 129: Bilayer and few-layer regions with the shape and orientation varying over grains of Pt foil

While by no means conclusive, these two observations suggest that the grain boundaries and crystallographic orientations of the Pt foil impact to some extent on the crystallinity and orientation of the graphene domains.

During this experimentation I also observed strange surface features and damage on the edge of the Pt foil when the H_2 flow rate was greater than 600 sccm, Figure 130.

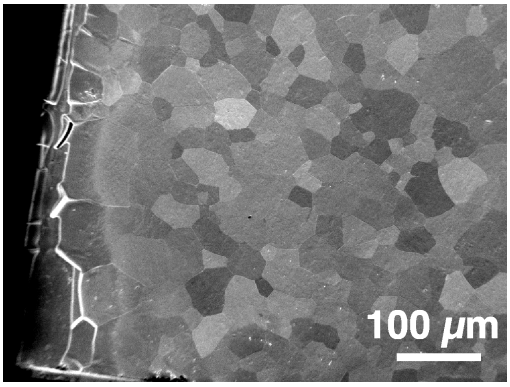


Figure 130: Damage to edge of Pt foil due to reaction with quartz tube

The quartz tube appeared to melt to the Pt foil after some experiments, and in a few cases the quartz visibly coated the surface. This led us to modify the experimental setup so that a protective support was placed between the Pt foil and the quartz tube.

Experiments were conducted using a 1 cm^2 ceramic plate as the protective support, within the range of optimum parameters determined for support-free growth, ie. 3 sccm < CH_4 < 5 sccm and 500 sccm < H_2 < 700 sccm, Figure 131, Figure 132 and Figure 133. This investigation aimed to better define the boundaries of the parameter space for optimum growth and, particularly, to produce hexagonal graphene domains.

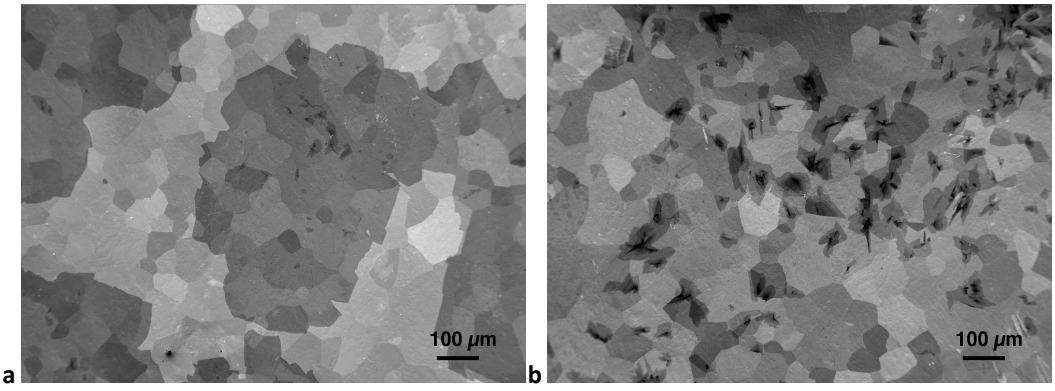


Figure 131: APCVD graphene growth at 1045˚C on ceramic-plate-supported Pt foil with 500 sccm H_2 and varying CH_4 flow rate for 30 minutes with (a) 4 sccm CH_4, CH_4:H_2 flow rate ratio of 1:125 (b) 5 sccm CH_4, CH_4:H_2 flow rate ratio of 1:100

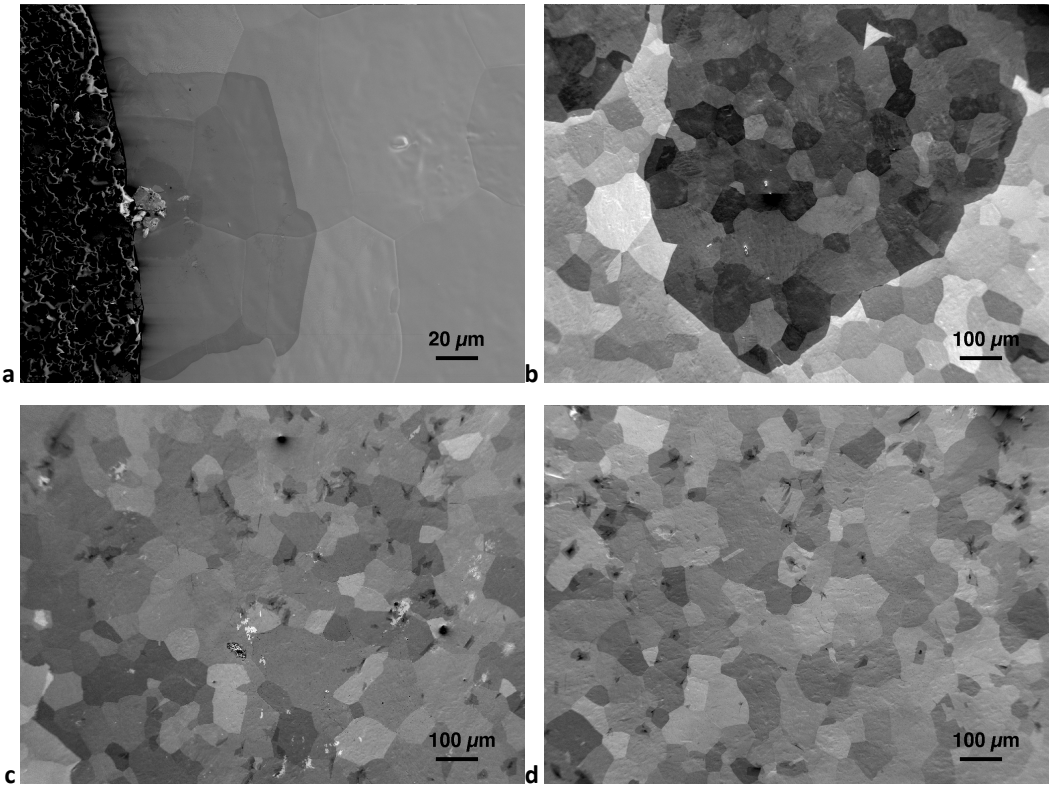


Figure 132: APCVD graphene growth at 1045˚C on ceramic-plate-supported Pt foil with 600 sccm H_2 and varying CH_4 flow rate for 30 minutes (a) 4 sccm CH_4, CH_4:H_2 flow rate ratio 1:150, (b) 4.5 sccm CH_4, CH_4:H_2 flow rate ratio 1:133, (c) 5 sccm CH_4, CH_4:H_2 flow rate ratio 1:120, (d) 6 sccm CH_4, CH_4:H_2 flow rate ratio 1:100

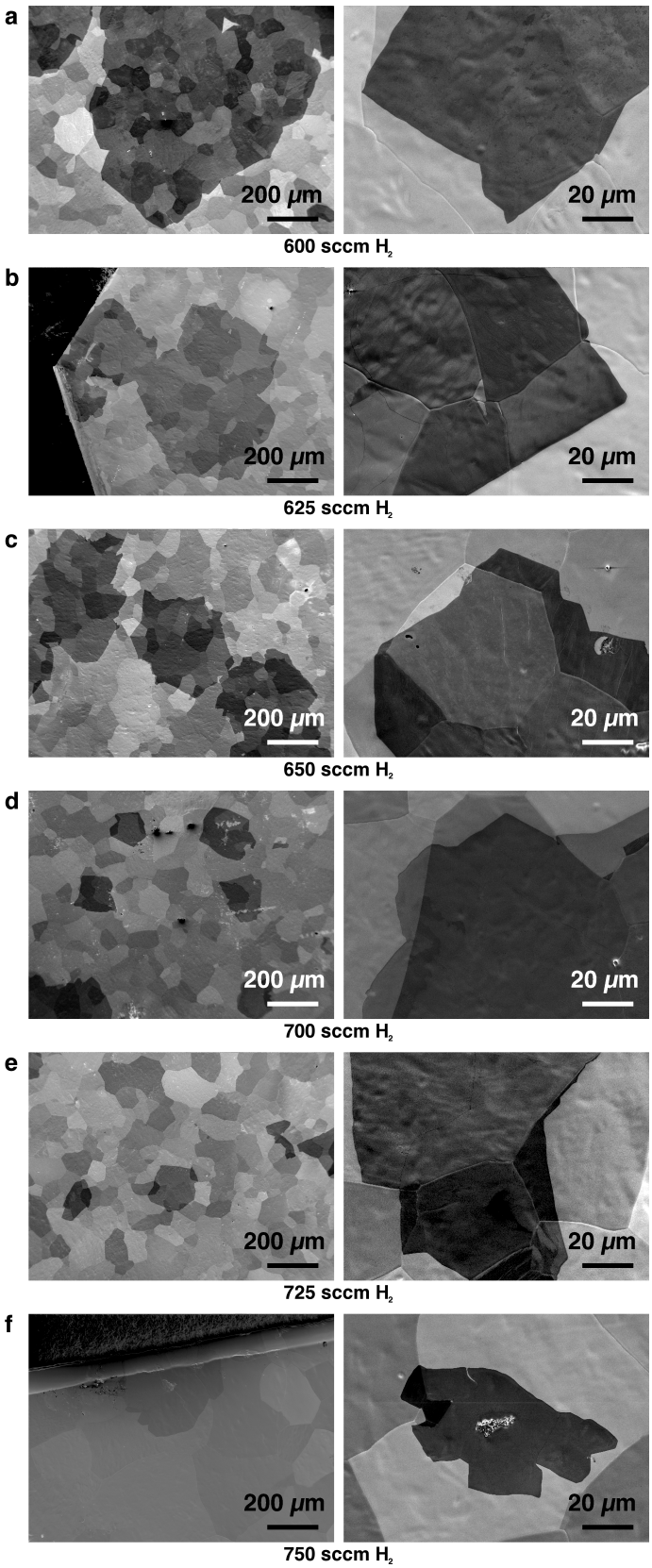


Figure 133: APCVD graphene growth at 1045˚C on ceramic-plate-supported Pt foil with 4.5 sccm CH_4 and varying H_2 flow rate for 30 minutes (a) 600 sccm H_2, CH_4:H_2 flow rate ratio 1:133, (b) 625 sccm H_2, 1:139 (c) 650 sccm H_2, 1:144, (d) 700 sccm H_2, 1:155, (e) 725 sccm H_2, 1:161, (f) 750 sccm H_2, 1:166, (g) 775 sccm H_2, 1:172

The investigation using the protective ceramic plate produced similar results to support-free growth. Synthesis with a CH_4 flow rate greater than 5 sccm and H_2 flow rate less than 600 sccm in Figure 132 produced full coverage with many few-layer regions. In Figure 133, with 4.5 sccm CH_4 and higher H_2 flow rate of 600 sccm < H_2 < 650 sccm, the production of few-layer areas was reduced so that single layer domains grew from individual nucleation sites up to 500 µm in size. These domains were always irregular shapes, and so they are polycrystalline (as per Figure 14c[176]). Further increase in H_2 flow rate, 650 sccm < H_2 < 750 sccm caused a reduction in the size of domains and the density of nucleation sites on the surface, however the shape always remained irregular rather than becoming hexagonal. When H_2 was increased further, 750 sccm < H_2 < 775 sccm, the nucleation sites were limited to the edges of the Pt foil and contamination particles on the surface, and eventually solely to contamination particles on the surface. By 800 sccm H_2 the graphene growth was restricted entirely.

The results from the investigation into the influence of CH_4 and H_2 flow rates with and without the protective ceramic plate appear to contradict previous reports by L. Gao *et al.*[176] that single-crystal hexagonal domains are promoted by controlling the flow rates of reactant gases and systematically increasing the hydrogen concentration. I observed that a systematic increase in the hydrogen concentration (i) reduce the production of bilayer and few-layer regions, (ii) restricts the size the graphene domains, (iii) restricts the nucleation density of graphene domains. However, hexagonal domains could not be promoted by increasing the hydrogen flow rate.

This observation led to the following question: why could L. Gao *et al.*[176] synthesise hexagonal graphene domains on Pt foils whereas my experiments produced irregular domains? It was hypothesised that the observed reaction between the Pt foil and the quartz tube may provide the explanation, through the formation of a silicon or platinum silicide surface layer that may be influential for the growth of hexagonal domains. This hypothesis was supported by the observation that domains that nucleated near the edge of the Pt foil- where quartz contaminations were present- often appeared hexagonal, Figure 134.

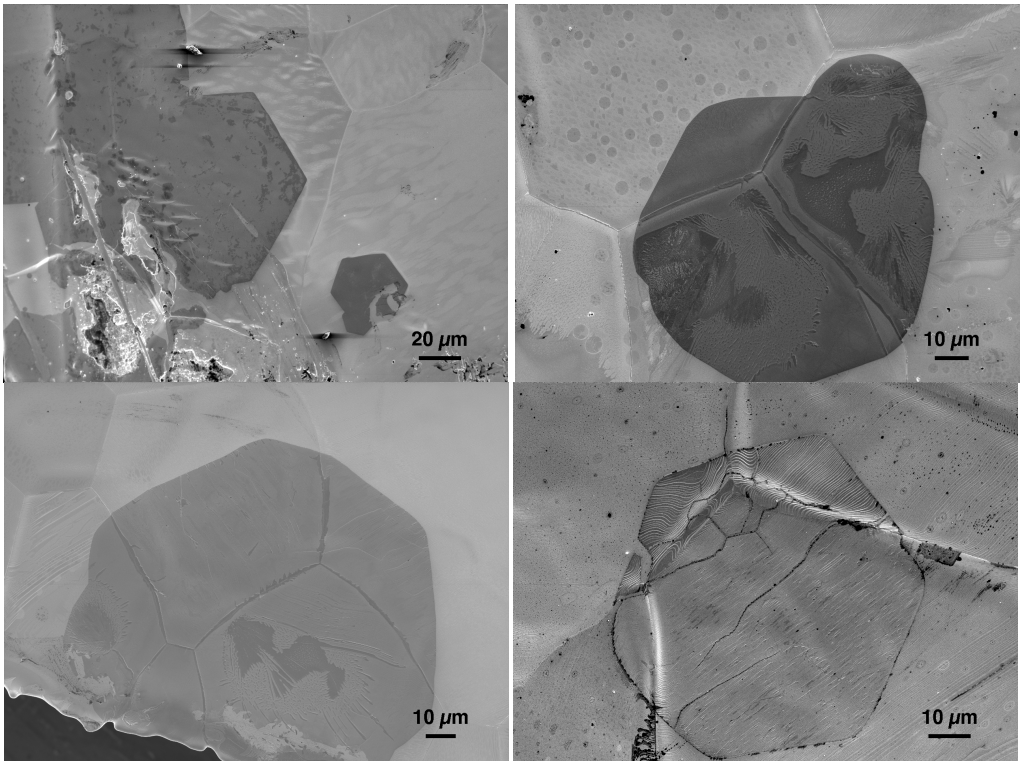


Figure 134: Hexagonal-like domains formed near the edges of unsupported Pt foils

The Pt surface does not appear uniformly clean due to the reaction with the quartz tube, and the formation of a silicon, silicon oxide, or platinum silicide surface layer. Furthermore, this surface appears similar to surfaces presented by L. Gao *et al.*[176], reproduced in Figure 14b. As such, a silicon or platinum silicide surface layer may have been present on the Pt foil used by L. Gao *et al.*[176], and this layer can promote the growth of hexagonal graphene domains. Vitaly Babenko has investigated this hypothesis further by successfully and reproducibly synthesising large-area single-crystal hexagonal graphene domains on silicidated Pt foils[322].

9.1.2 Influence of synthesis temperature

I hypothesised that increasing the synthesis temperature would increase the domain size and growth rate, and decrease the nucleation density of graphene on Pt foils, in a similar manner to that observed on Cu foils[168]. The influence of synthesis temperature was investigated while keeping reactant gas flow rates constant at 4 sccm CH_4 and 500 sccm H_2 for 5 minutes, Figure 135.

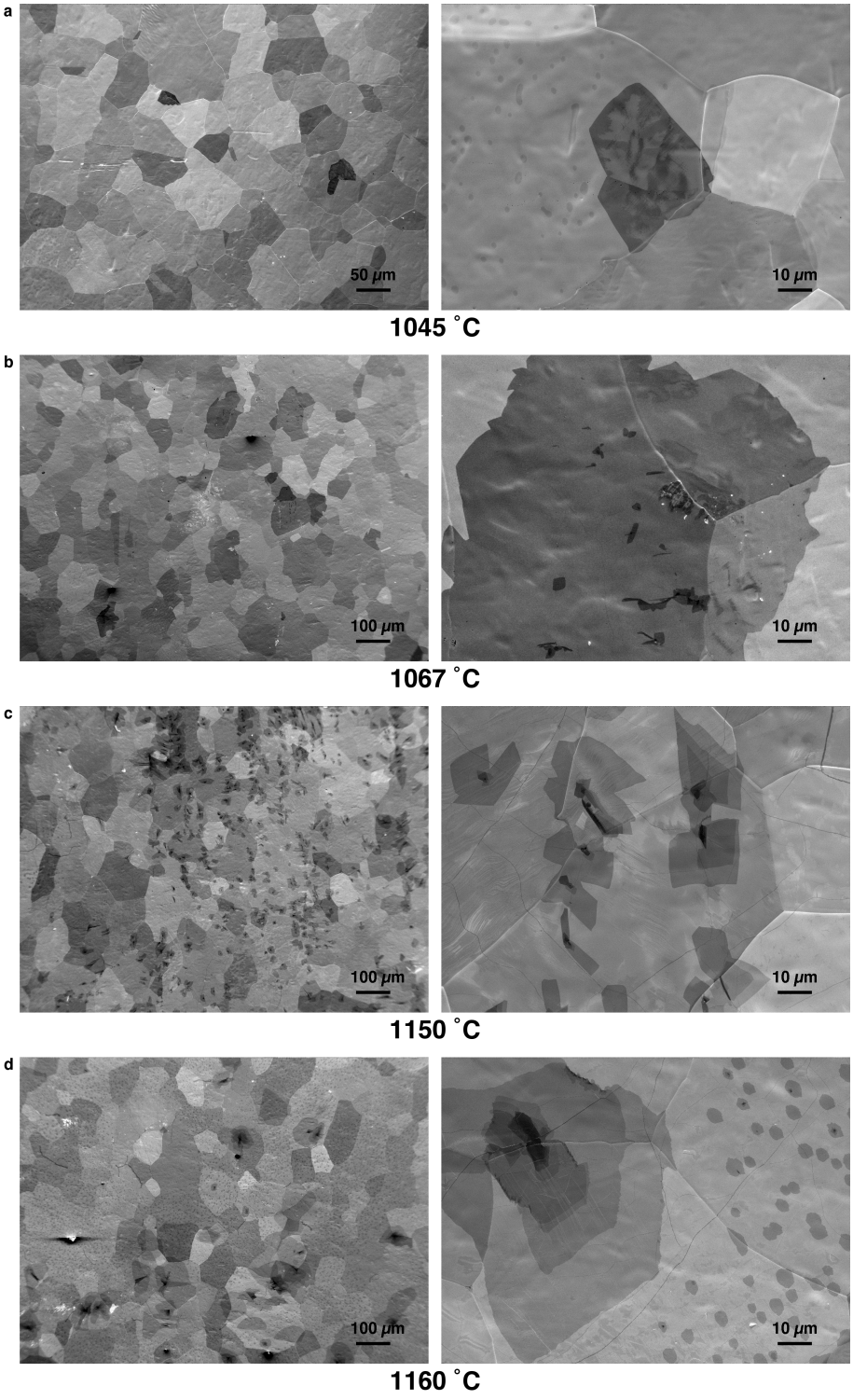


Figure 135: APCVD graphene growth on Pt foil with 4 sccm CH_4 and 500 sccm H_2 at varying synthesis temperature for 5 minutes (a) 1045 ˚C, (b) 1067 ˚C, (c) 1150 ˚C, (d) 1160 ˚C

The increase in synthesis temperature caused an increase in the growth rate and size of domains, from ~30 - 40 µm and ~7 - 8 µm min^{-1} at 1045 ˚C to ~115 - 160 µm and ~20 - 40 µm min^{-1} at 1067 ˚C. This change occurred simultaneously with an increase in the size and quantity of bilayer and few-layer regions. As such for growth at higher temperatures of 1150˚C and 1160˚C the graphene completely covered the Pt foil, with very large few-layer regions up to ~30 µm and ~90 µm respectively.

In order to reduce the quantity of bilayer and few-layer regions experiments were conducted at 1150 ˚C with varying CH_4 flow rate for 5 minutes, Figure 136.

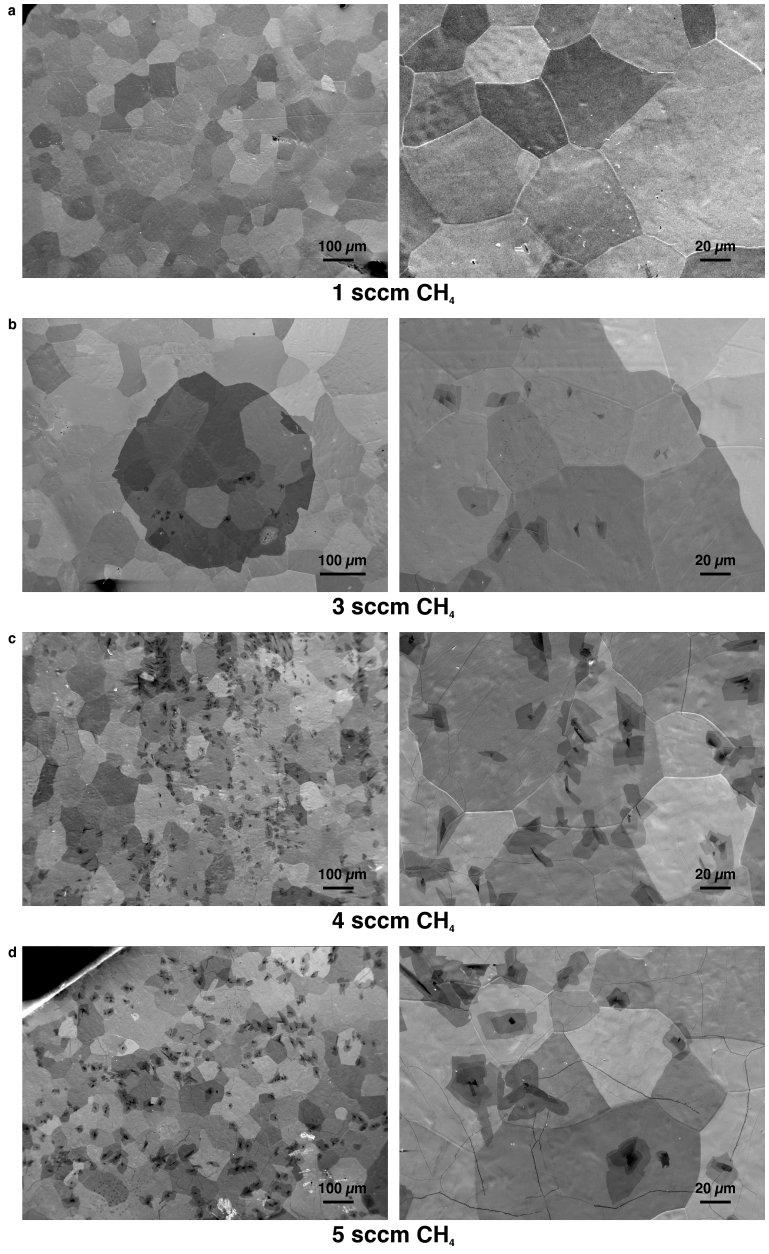


Figure 136: APCVD graphene growth on Pt foil at 1150 ˚C with 500 sccm H_2 and varying CH_4

By reducing the CH_4 flow rate to 3 sccm at 1150 ˚C the synthesis resulted in very large domains of ~0.5 mm diameter with few bilayer regions at a growth rate of ~100 μm/min. Synthesis at higher temperatures is more efficient than at lower temperatures as equivalent growth can be achieved while using a reduced CH_4 flow rate, for instance, 3 sccm CH_4 at 1150 ˚C compared to 4.5 sccm CH_4 at 1045 ˚C. Optimum conditions at 1150 ˚C for producing full coverage single-layer graphene composed of large domains should be 1 sccm < CH_4 < 3 sccm with 500 sccm H_2. This indicates the importance of optimising the reactant flow rates at the particular synthesis temperature used, while also ensuring the stability and uniformity of synthesis temperature of the synthesis apparatus for reproducible production of high-quality graphene on Pt foils.

9.2 Investigations into nucleation sites of APCVD graphene domains on Pt foil

9.2.1 Influence of surface topography on location of nucleation sites

I devised an experiment to investigate whether the surface topography of the Pt foil played an important role in dictating the location of nucleation sites of graphene domains. By synthesising graphene multiple times on the same sample of Pt foil, using a non-destructive cleaning stage in between reiterations, I aimed to investigate whether domains ever nucleated at the same location. I conducted the primary APCVD growth of graphene on a sample of Pt foil at 1050 ˚C with 4.5 sccm CH_4 and 650 sccm H_2 for 30 minutes to produce isolated single-layer domains across the surface and then conducted SEM to locate the initial domains, Figure 137a. The Pt foil was then cleaned using the bubbling transfer described by L. Gao *et al.*[176], reannealed, and the synthesis procedure was repeated for secondary growth, Figure 137b.

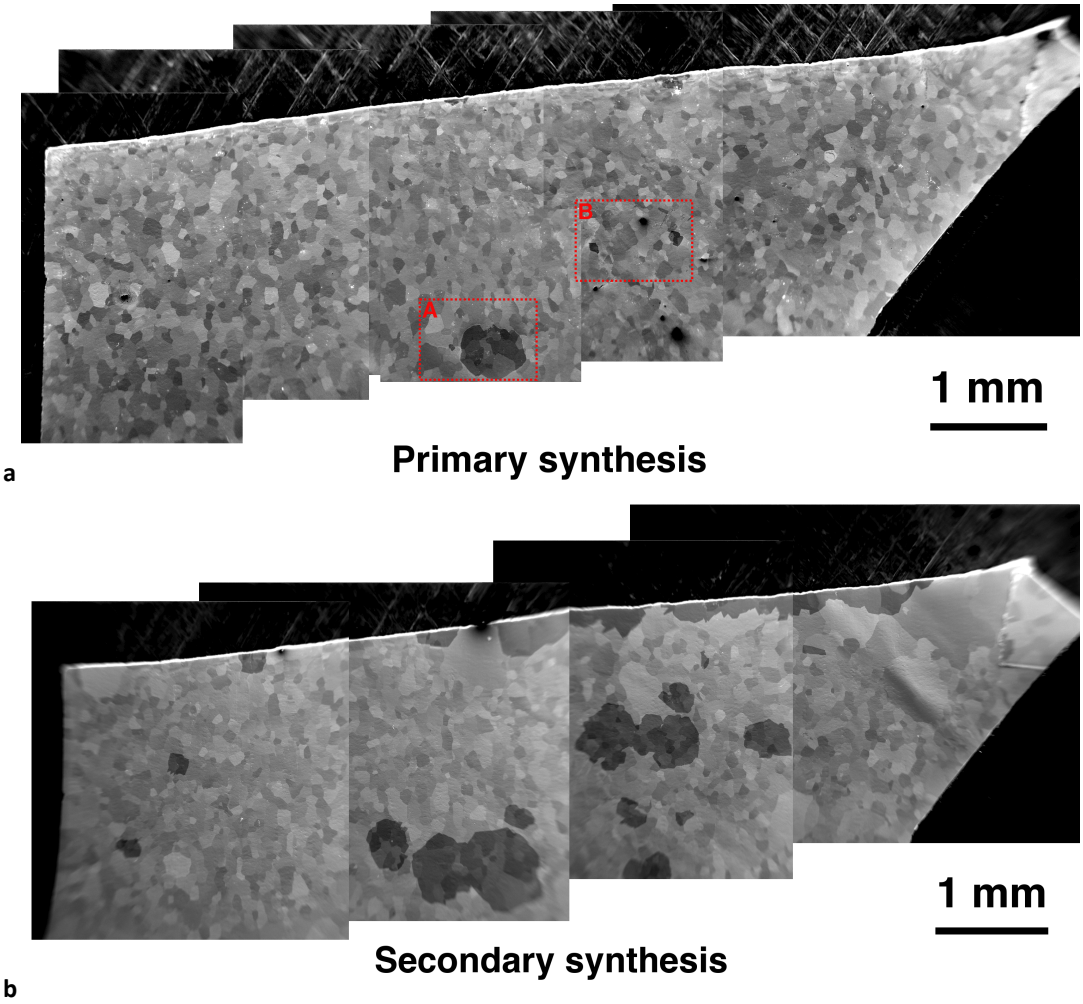


Figure 137: Low magnification SEM composite images of APCVD graphene growth on Pt foil after primary and secondary synthesis at 1050 ˚C with 4.5 sccm CH_4 and 650 sccm H_2 (a) 30 minutes primary synthesis time, (b) 30 minutes secondary synthesis time. Red dashed boxes labelled A and B represent regions imaged at higher magnification in Figure 137

By comparing the low magnification SEM images of the surface after the primary synthesis with the surface after the secondary synthesis it appears that graphene domains often nucleated at different locations when using the Pt foil a second time. However, the surface of the Pt foil also appears to have changed after the second synthesis stage; large merged Pt grains can be identified on the top right of the foil after the secondary synthesis, Figure 137b, which were not present after the primary synthesis, and in other regions grains appear distorted when comparing the surface from the secondary synthesis with the primary synthesis. This grain growth occurs during the relatively long synthesis time and annealing time- 30 minutes each- and the variations may therefore influence where the graphene nucleates. Nonetheless,

I compared higher resolution images of the areas of the Pt foil where larger graphene domains formed after both the primary and secondary synthesis (highlighted by red dashed boxes in Figure 137), aiming to determine whether growth ever occurred from the same nucleation site, Figure 138.

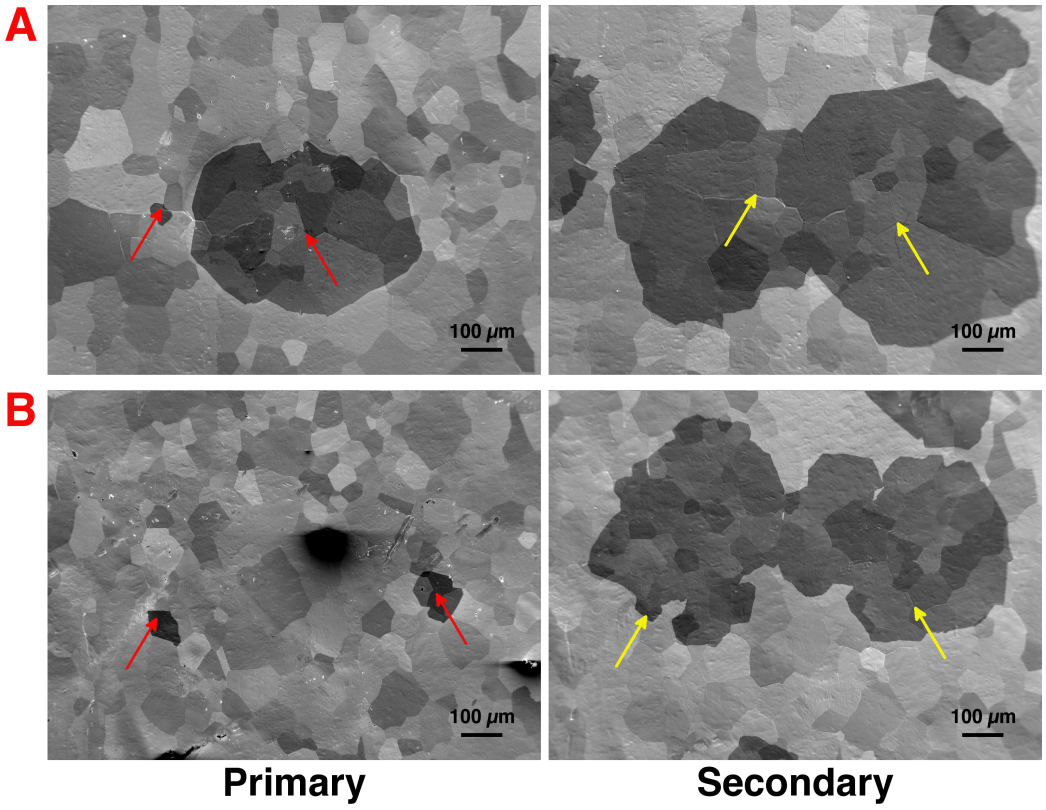


Figure 138: APCVD graphene growth following primary and secondary synthesis on the same region of Pt foil. Upper images show region A and lower images show region B as highlighted by red dashed boxes in Figure 137a. Left images show surface after primary synthesis, right images show surface after secondary synthesis. Red arrows highlight approximate location of the nucleation sites of the graphene domains from the primary synthesis, by selecting grain boundaries at the centre of each domain. Yellow arrows indicate the equivalent location on the surface after secondary synthesis

While there does not appear to be a definitive correspondence between the location of the nucleation sites of the primary and secondary experiments, at least on these occasions a domain appears to have formed from the same nucleation site, or within near proximity. The locations appears to be devoid of surface contamination particles, suggesting that the surface of the Pt foil plays a crucial role in dictating the location of the nucleation sites. As such, I suggest that further investigations should be conducted into the importance of the surface topography in controlling the location of nucleation sites of graphene domains. In particular, repeating this

experiment using conditions suitable for a shorter synthesis time and annealing time (e.g. 5 minutes) would be beneficial to reduce the grain growth observed between the two syntheses, and therefore conclusively determine whether particular surface features repeatedly act as nucleation sites for graphene domains.

9.2.2 Influence of contamination particles on location of nucleation sites

During the course of the investigations I often observed through SEM imaging that contamination particles were present at the centre of the graphene domains. Particles can also be observed in Gao *et al.*[176]'s publication, reproduced in Figure 14c. This suggests that these particles might in fact assist with the nucleation of graphene domains. To investigate the extent that contamination particles controlled the nucleation I screened all the visible graphene domains. I conducted SEM across the entire 1 x 1 cm^2 sample of Pt foil used for APCVD growth of graphene presented in Figure 137a (synthesis conditions of 1050 ˚C, 4.5 sccm CH_4, 650 sccm H_2 for 30 minute), locating and imaging each graphene domain in turn. This investigation, Figure 139 and Figure 140, demonstrates that out of the 21 domains identified, large contamination particles of ~5 - 10 µm in size were present on six occasions.

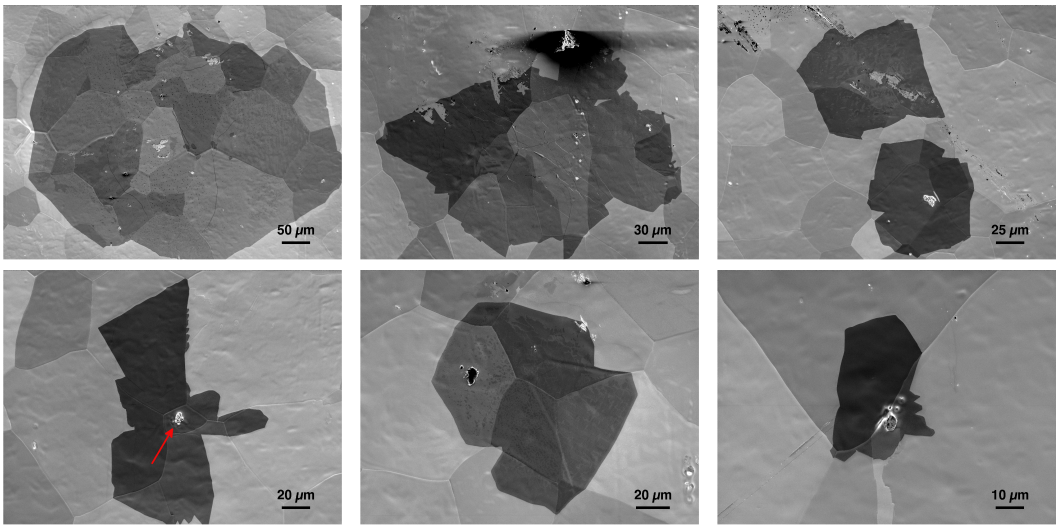


Figure 139: APCVD graphene domains formed on 1 x 1 cm^2 Pt foil with contamination particles Red arrow highlights one example contamination particle.

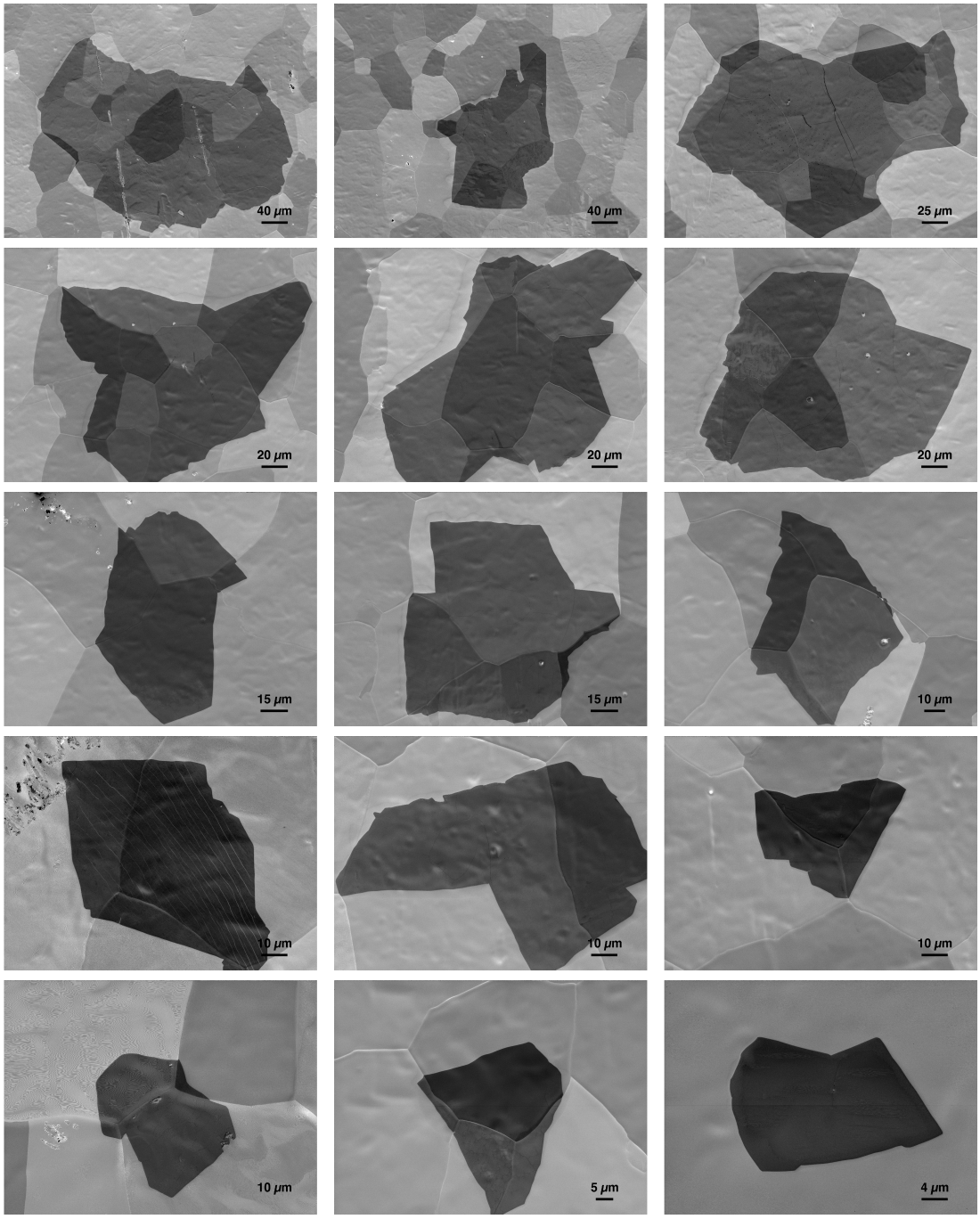


Figure 140: APCVD graphene domains formed on 1 x 1 cm^2 Pt foil without significant contamination particles

This suggests that while nucleation is not solely limited to the location of contamination particles, their presence may be an important factor that could be useful for controlling the location of graphene domains.

To investigate the chemical composition of the contamination particles I conducted EDX on a number of samples after SEM imaging, Figure 141 and Figure 142.

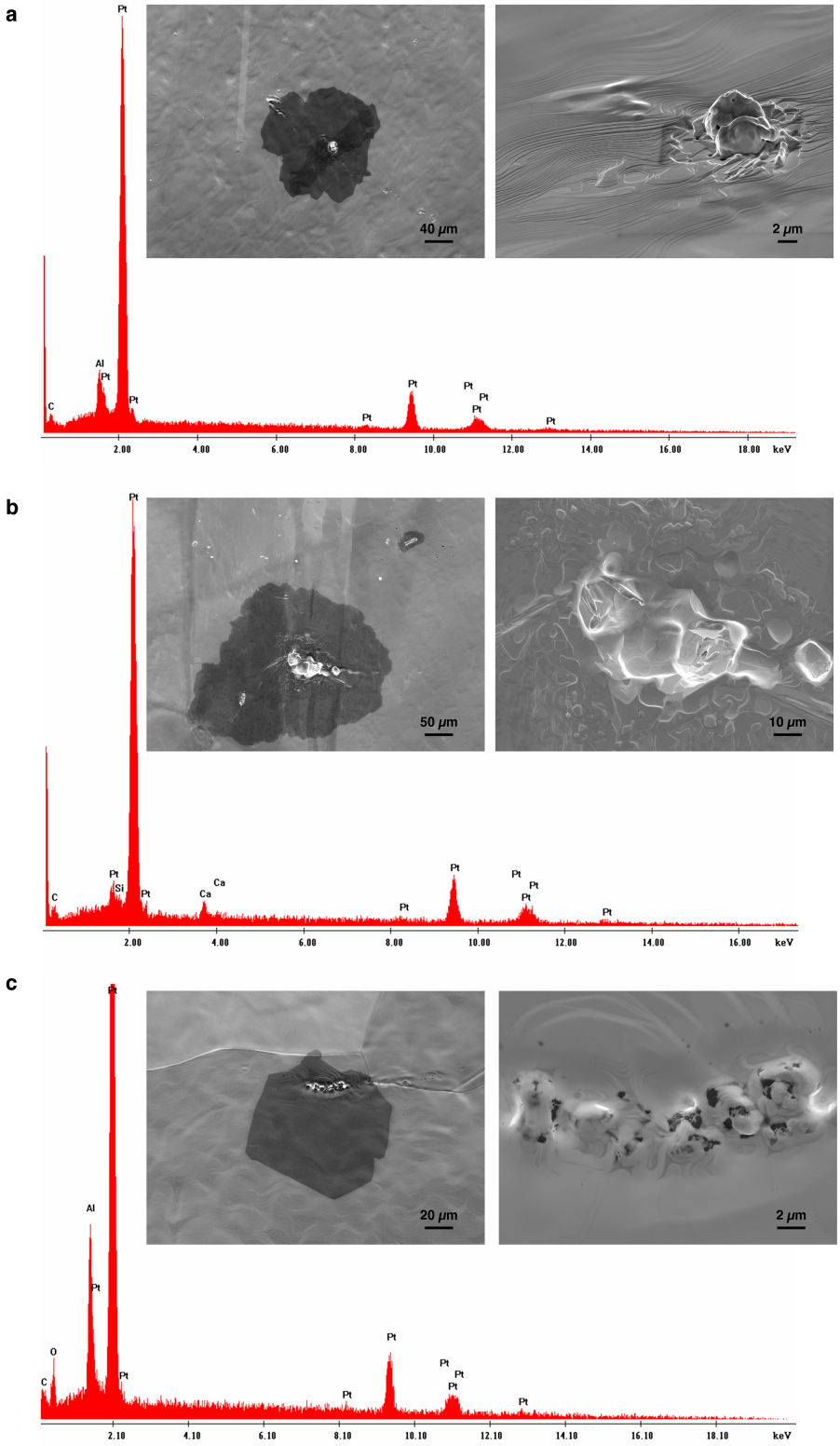


Figure 141: EDX spectrum and SEM images of contamination particles on APCVD graphene domains grown on Pt foil. Metallic contaminations detected including (a) Al, (b) Si and Ca, (c) Al and O

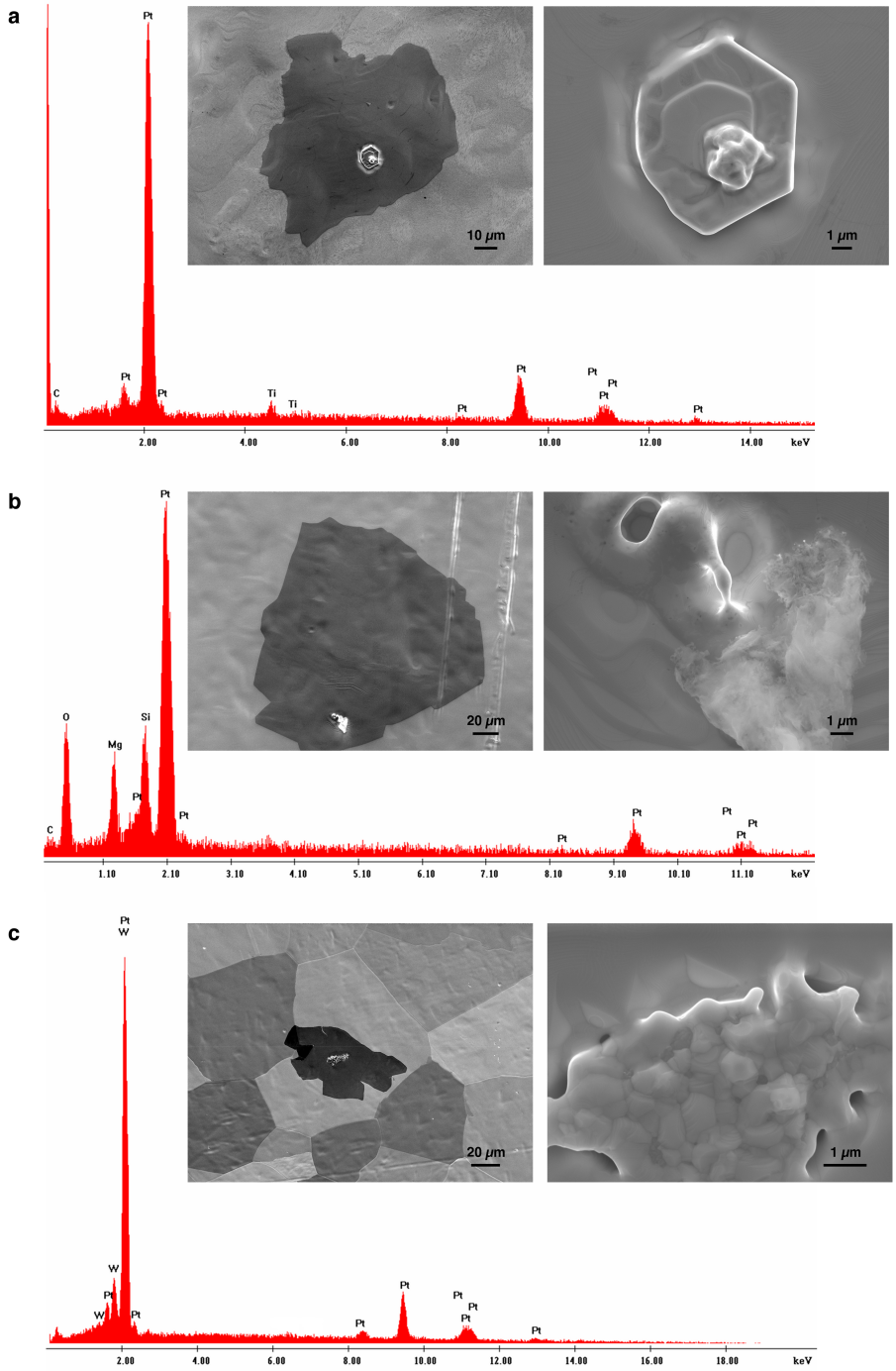


Figure 142: EDX spectrum and SEM images of contamination particles on APCVD graphene domains grown on Pt foil.Metallic contaminations detected including (a) Ti, (b) Mg, Si and O, (c) W and Fe

EDX on the contamination particles detected many different metallic species: aluminium, silicon, calcium, titanium, magnesium and tungsten. This suggests that graphene nucleation is promoted due to the irregular surface provided by the contamination particle, rather than through a chemical catalytic process of a particular metal. These particles presumably originate from low-percentage

dissolved impurities from within the foil, or from residues after the manufacturing process. As such, this experiment indicates that the purity and cleanliness of Pt foils should be investigated and carefully controlled to improve the growth of graphene.

9.3 Conclusions on atmospheric-pressure chemical vapour deposition of graphene on platinum foils

My investigations into the APCVD growth of graphene on Pt foils demonstrate:

- The CH_4:H_2 flow rate ratios, synthesis time, and synthesis temperature influence the nucleation density, density of bilayer and few-layer regions, and the growth rate of APCVD graphene domains on 99.99+ % Goodfellow Pt foils,
- Optimised conditions lead to production of ~0.5 mm single-layer graphene domains with reduced nucleation density, increased growth rate of ~100 μm/min, and improved efficiency (reduced CH_4:H_2 flow rate ratio) by synthesis at 1150 ˚C, a higher temperature than previously reported,
- Large-area, hexagonal, single-crystal graphene domains do not form on pristine Pt foil even with optimised CH_4:H_2 flow rate ratios, explained by the observation of a reaction between the Pt foil and quartz tube that has led to the investigation of APCVD growth of graphene on silicidated platinum substrates,
- The surface topography can influence the location of nucleation sites of APCVD graphene domains on Pt foil,
- Metallic contamination particles, of composed of various elements, can influence the location of nucleation sites of APCVD graphene domains on Pt foil.

10 Chemical vapour deposition of heteroatom-doped graphene on copper foils

This chapter outlines investigations focussed on producing and characterising heteroatom-doped CVD graphene. The primary aims were to produce nitrogen-doped graphene, to investigate the influence of the synthesis parameters on the dopant concentration and growth, and to obtain unprecedented atomic-resolution STEM imaging and chemical analysis of the nitrogen-doped graphene. Complementary investigations also aimed to produce boron-doped graphene from liquid precursors. These studies were motivated by the wide-range of applications for large-areas of heteroatom-doped graphene (outlined in Chapter 2.3) being limited by insufficient growth studies. Sections of the work in this chapter were completed in collaboration with a number of internal and external researchers. Dr Antal Koos and I jointly conducted experiments into the influence of synthesis parameters on the growth of heteroatom-doped graphene. Dr Antal Koos conducted STM and CITS with Dr Peter Nemes-Inzce and Professor Laszlo Biro (Institute for Technical Physics and Materials Science, Hungary); Dr Rebecca Nicholls, Dr Jonathan Yates and part II student Joshua Tsang (Department of Materials, University of Oxford) conducted computational DFT modelling of nitrogen-doped graphene; Dr Timothy Pennycook (SuperSTEM) conducted STEM and EELS characterisation of nitrogen-doped graphene samples; and Dr Andrew Pollard, Dr Deb Roy, Steve Spencer and Dr Alex Shard (National Physical Laboratory) conducted XPS analysis.

Parts of this chapter have been published in:

Nicholls, R.J., Murdock, A.T., Tsang, J., Britton, J., Pennycook, T.J., Koos, A.A., Nellist, P.D., Grobert, N., Yates, J.R., Probing the bonding in nitrogen-doped graphene using electron energy loss spectroscopy, *ACS Nano*, 2013, 7, 7145-7150[3]

Koos, A.A., Murdock, A.T., Nemes-Incze, P., Nicholls, R.J., Pollard, A.J., Spencer, S.J., Shard, A.G., Roy, D., Biro, L.P., Grobert, N. Effects of temperature and ammonia flow rate on the chemical vapour deposition growth of nitrogen-doped graphene, *Physical chemistry chemical physics*, 2014, DOI:10.1039/C4CP02132K[2]

10.1 CVD of nitrogen-doped graphene on copper foils

10.1.1 Design and construction of low-pressure CVD apparatus for doping of graphene using gaseous precursors

The low-pressure CVD system presented in Chapter 5.1 was modified to provide the functionality for producing nitrogen-doped graphene by in-situ doping through the addition of gaseous ammonia to the reactant gas mixture. I adapted the system by introducing an additional line to the gas manifold so that 99.98 % NH_3 could be introduced at flow rates between 0.1 and 10 sccm, Figure 143. Due to the potential for degradation of components of the system by corrosive reaction with ammonia a number of additional modifications were made for improved safety: ammonia-resistant o-rings made of Buna-N were used in the Swagelok Ultra-Torr fittings, and an argon purge line was added so the system could be cleaned after experiments.

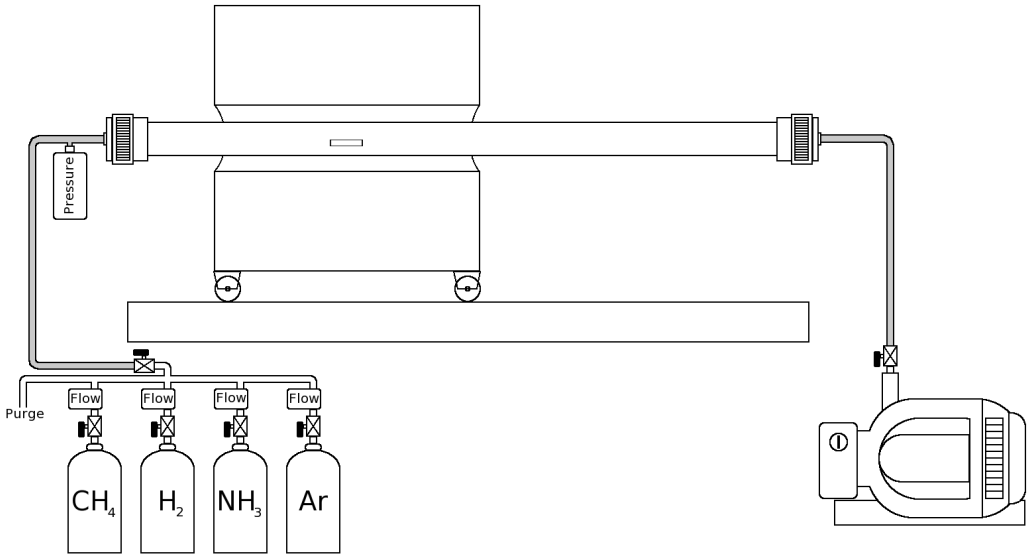


Figure 143: LPCVD apparatus for synthesis of nitrogen-doped graphene using NH_3 with modifications of NH_3 line, purge line, and ammonia-resistant Buna-N o-rings

10.1.2 Investigations into the influence of synthesis parameters on LPCVD nitrogen-doped graphene growth on 99.999 % Alfa Aesar Cu foil

The aim of this investigation was to determine the influence of the synthesis parameters on the production of LPCVD nitrogen-doped graphene, and as a result produce high-quality, large-area sheets with maximum doping levels. As discussed in

Chapter 2.4.3.4, before 2011 nitrogen-doped CVD graphene was commonly produced by the addition of NH_3 to the reaction chamber following graphene synthesis. However, the amount of nitrogen doping should depend on the probability for incorporation of nitrogen atoms into the graphene lattice. I hypothesised the amount of nitrogen doping could be increased by:

(i) Simultaneously growing and doping graphene (*in situ* doping) using CVD, rather than treating graphene in NH_3 gas after production,

(ii) Increasing the concentration or flow rate ratio of ammonia in the reactant mixture,

(iii) Decreasing the synthesis temperature given the increased incorporation of nitrogen dopants in the graphitic network of N-MWCNTs when synthesised at lower temperatures[295, 323].

I hypothesised that the type and distribution of nitrogen dopants in the graphene lattice would improve by *in situ* doping, with uniform substitutional incorporation more likely, rather than preference for doping at edges and defect sites.

While optimising these synthesis conditions may increase the amount of nitrogen-doping, the parameters also influence the growth of high-quality pristine graphene and so presumably have a similar effect on nitrogen-doped graphene; lower synthesis temperature results in smaller domain size and reduced quality graphene[168, 189] while excess N is known to inhibit the growth mechanism of graphitic structures[295, 323]. Consequently, while using a lower synthesis temperature and/or higher concentration of NH_3 may increase the percentage of dopants incorporated into the graphene lattice, this would be detrimental for the production of high-quality nitrogen-doped graphene. My experiments into the influence of synthesis parameters on the LPCVD growth of nitrogen-doped graphene on 99.999 % Alfa Aesar Cu foil therefore aimed to determine optimum conditions that achieve a compromise between the amount of nitrogen doping and the growth of high-quality doped graphene.

Initial experiments were conducted using synthesis parameters that produced isolated domains of high quality LPCVD graphene as outlined in Chapter 5.2, 5 sccm CH_4 and 500 sccm H_2 at 1035 ˚C for 5 minutes, with the addition of ammonia at the

minimum flow rate and concentration in the reactant gas mixture, 0.1 sccm NH_3. The synthesis conditions were then systematically varied from these initial parameters. A short synthesis time was used so that experiments were stopped before the Cu surface was fully covered with graphene, and SEM was used to investigate each parameter's influence on the size and shape of isolated graphene domains.

10.1.2.1 Influence of NH_3 flow rate and synthesis temperature on dopant concentration

I confirmed the LPCVD graphene synthesised with NH_3 was nitrogen-doped using Raman spectroscopy, Figure 144. As outlined in Chapter 4.4.1, shifts in peak positions and intensities indicate n-type doping due to the influence of nitrogen dopants. I compared the position of the G and 2D peaks for graphene synthesised using NH_3 with peak positions from pristine graphene that was synthesised under equivalent conditions of 5 sccm CH_4 and 500 sccm H_2 at 1000 ˚C for 5 minutes. For the pristine graphene the G peak was detected at 1583 cm^{-1} and the 2D peak at 2685 cm^{-1}, Figure 144 black line. The G peak position increased and the 2D peak position decreased for graphene synthesised with NH_3, thereby confirming nitrogen doping, Figure 144 coloured lines.

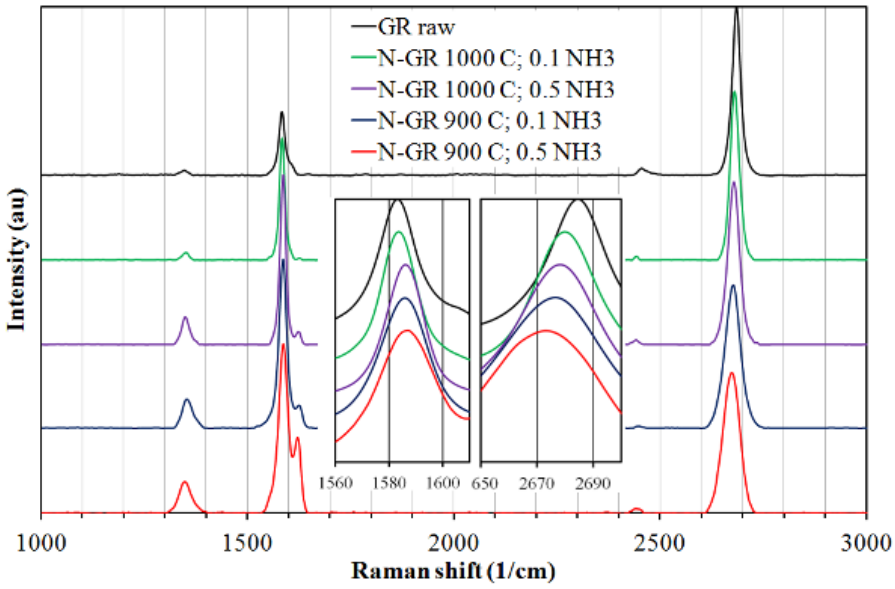


Figure 144: Raman spectra of nitrogen-doped and raw graphene domains on Cu foil. A decrease in the 2D/G intensity ratio, increase in the D and D' peak intensity, and shift in the position of the G and 2D peaks (inset) demonstrates the incorporation of nitrogen dopants. Greater shift is observed for lower synthesis temperatures and higher NH_3 flow rates.

Once nitrogen doping was confirmed, I used Raman spectroscopy to investigate the quality and relative dopant concentration of nitrogen-doped graphene synthesised with different NH_3 flow rates, 0.1 and 0.5 sccm, and at different synthesis temperatures, 900 and 1000 ˚C. Although a quantitative estimate of dopant concentration is possible through the shift of peak positions, this can be misleading due to different influences of different dopant configurations[268]. Instead, the relative amount of doping between samples can be inferred by the magnitude of different peak shifts. The intensity of the D and D' peaks also provides some quantitative indication of dopant concentration.

Our experiments demonstrate that increasing the NH_3 flow rate from 0.1 sccm to 0.5 sccm results in an increase in the G peak, and a decrease in the 2D peak, suggesting an increase in nitrogen-doping (Figure 144, comparing purple line with green line, and red line with blue line). For instance, when comparing nitrogen-doped graphene produced at 1000 ˚C using 0.1 sccm NH_3 with samples synthesised using 0.5 sccm NH_3, the latter specimen had the 2D peak position downshifted by ~2 cm^{-1} and the G peak position upshifted by ~2 cm^{-1} (Figure 144, purple line and green line, respectively). I therefore conclude that a higher dopant concentration was achieved by increasing the ammonia flow rate. This observation follows predictions from standard reasoning- a higher concentration of dopant reactants yields a higher concentration of doped products- and is in agreement with previous studies[24, 57].

Further studies demonstrate that decreasing the synthesis temperature from 1000 ˚C to 900 ˚C also results in an increase in the G peak position, and a decrease in the 2D peak position. For instance, for nitrogen-doped graphene produced with 0.1 sccm NH_3, comparing samples synthesised at 1000 ˚C and 900 ˚C, the average 2D peak position downshifted (by ~4 cm^{-1}) and the average G peak position upshifted (by ~2 cm^{-1}, Figure 144, green line and blue line, respectively). A similar trend occurs for samples synthesised with higher NH_3 flow rate (Figure 144, comparing purple line with red line). I therefore conclude that reducing the synthesis temperature resulted in an increase in the dopant concentration. This is believed to be the first demonstration of the importance of synthesis temperature on the dopant

concentration of nitrogen-doped graphene, and is in agreement with previous studies on the influence of synthesis temperature on the nitrogen doping of carbon nanotubes[295, 323].

An increase in the D peak and D' peak intensities is concurrently observed for increasing nitrogen doping. For instance, for synthesis at 1000 ˚C, an increase in D and D' peak intensity is observed between samples synthesised with 0.1 sccm NH_3 and 0.5 sccm NH_3 (Figure 144, green and purple line, respectively). This trend continues for samples synthesised at 900 ˚C, comparing samples synthesised with 0.1 sccm NH_3 and 0.5 sccm NH_3 (Figure 144, blue and red line, respectively). Increased disorder in the graphene lattice due to nitrogen doping also results in a decrease in the 2D peak intensity. This is due to the fact that increased disorder in the lattice decreases the probability of two-phonon scattering required to generate the 2D peak[324].

Some insight into the relative influence of the synthesis temperature and NH_3 flow rate on dopant concentration is possible by further analysis of the magnitude of Raman peak shifts. The magnitude of the shift of Raman peak positions was greater for samples synthesised at lower temperatures compared to samples synthesised with higher ammonia flow rates. For instance, the two samples synthesised at 900 ˚C (with 0.1 sccm NH_3 and 0.5 NH_3) have 2D peaks shifted ~8 cm^{-1} and ~11 cm^{-1}, and G peaks shifted ~3 cm^{-1} and ~4 cm^{-1}, respectively, whereas the two samples synthesised at 1000 ˚C (again with 0.1 NH_3 and 0.5 sccm NH_3) have less shift of the Raman peaks (2D peaks shifted only ~4 cm^{-1} and ~5 cm^{-1}, and G peaks shifted only ~1 cm^{-1} and ~3 cm^{-1}, respectively). The synthesis temperature therefore has a greater influence on the peak shift- and hence nitrogen dopant concentration- than the NH_3 flow rate, as might be expected. In other words, under these synthesis conditions, reducing the synthesis temperature by 100 ˚C results in a greater increase in nitrogen doping than a five times increase in the NH_3 flow rate. I therefore conclude that the synthesis temperature appears to be an overriding parameter for controlling the concentration of nitrogen-doped graphene. This observation has important implications if manufacturers are to maximise the concentration of nitrogen-doped graphene while reducing production costs.

Based on the Raman spectroscopy the nitrogen content of the graphene domains produced at lower temperatures and higher NH_3 flow rate are expected to have the highest nitrogen concentration. Therefore, nitrogen-doped graphene synthesised at 900 °C with 0.5 sccm NH_3 was analysed by XPS to determine the maximum dopant concentration, Figure 145. Samples were exposed to air prior to XPS analysis.

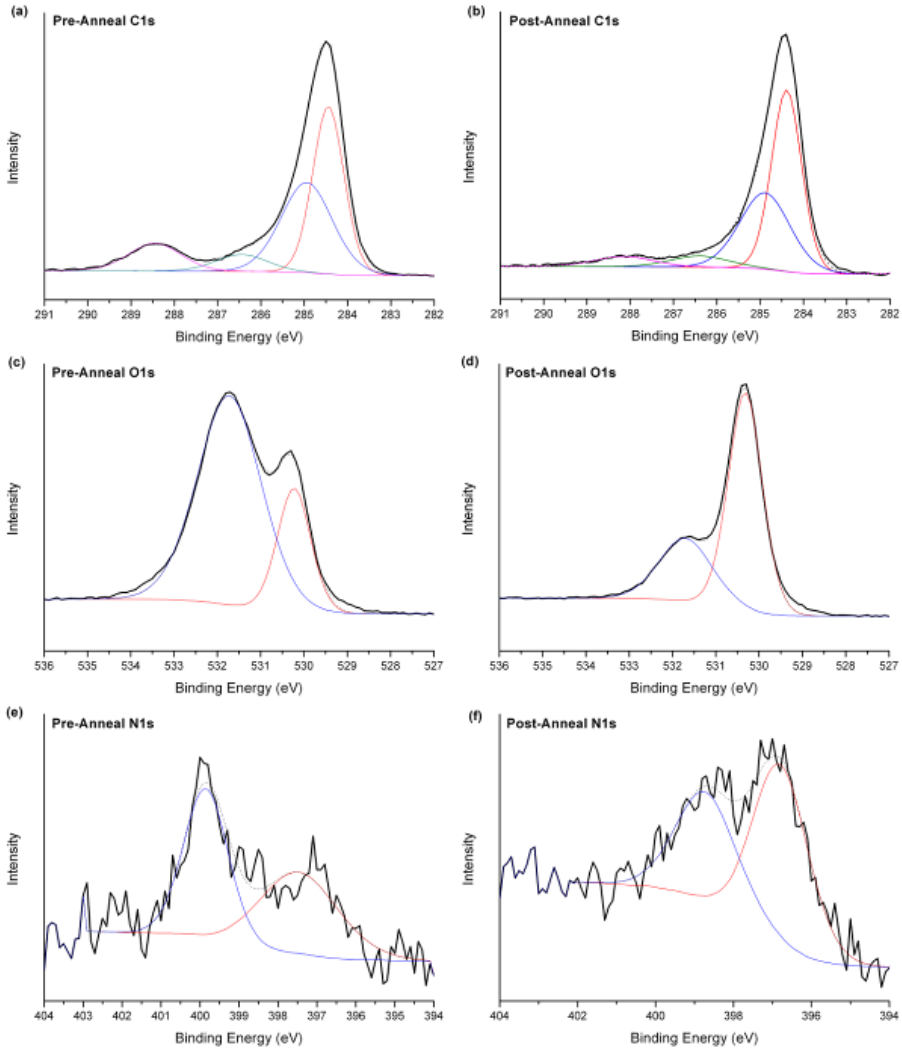


Figure 145: XPS analysis of nitrogen-doped graphene synthesised at 900 ˚C with 0.5 sccm NH_3. Spectra obtained from Cu substrate (a)(c)(e) before annealing, (b)(d)(f) after annealing at 300 ˚C for 30 min in UHV. (a)(b) C 1s, (c, d) O 1s, (e, f) N 1s peak-fitted spectra

Measurements were performed both before and after annealing at 300 ˚C in UHV to remove surface absorbed contaminants. XPS detected the presence of C, O, and N on the graphene, with the peak position and shape indicating the bonding in the samples. The C 1s peak showed two components at ~284.4 eV and ~285.0 eV, representative of graphite-like sp^2-hybridised carbon- typical for graphene- and

hydrocarbon species, respectively, Figure 145a. Acid ester and alcohol groups were also detected as peak components at ~288.3 eV and ~286.4 eV[325]. Oxygen was detected as oxygen-bound carbon species and copper hydroxide[326] at ~531.7 eV, and copper oxide at ~530.3 eV, Figure 145c. Nitrogen was detected as carbon-bound nitrogen between 398.7 - 399.8 eV, and copper nitride species between 396.8 - 397.5 eV, Figure 145e. These two peaks show low signal intensity, however they reliably represent N content in the nitrogen-doped graphene. Following annealing there was a reduction in the intensity of peaks due to acid esters, alcohols, and hydrocarbons in the C 1s spectra, Figure 145b, and a reduction in oxygen-bonded carbon peaks, Figure 145d. These peaks are associated with absorbed contaminants from storing the nitrogen-doped graphene under ambient conditions. The nitrogen content due to C-N bonding was essentially unchanged by annealing, Figure 145f. Although not associated with the nitrogen-doped graphene, the proportion of copper nitride present in the sample after annealing increases, and owing to the increase in background above the peak position this species appears to be present at some depth within the surface.

To determine the nitrogen content of the graphene the post-anneal peak areas of the C 1s component associated with graphene can be compared with the N 1s peak component, associated with carbon-bound nitrogen, using appropriate scaling factors. This XPS measurement suggests that the maximum nitrogen content of the nitrogen-doped graphene is ~2.1 % overall. This figure represents the overall nitrogen content, including both species associated with nitrogen-doped graphene and those associated with remaining contaminations after the annealing procedure. XPS analysis of pristine, undoped graphene that was synthesised under equivalent conditions determined the nitrogen content due to adventitious contamination to be ~0.8 %. I therefore conclude that the nitrogen content due to maximum doping was ~1.3 %.

10.1.2.2 Influence of NH_3 flow rate and synthesis temperature on growth rate and surface coverage

I investigated the influence of the NH_3 flow rate ratio and synthesis temperature on the growth rate and surface coverage of nitrogen-doped graphene using SEM. These

experiments demonstrate that decreasing the synthesis temperature and increasing the NH_3 flow rate reduces the growth rate of nitrogen-doped graphene. With respect to the influence of temperature, the average nitrogen-doped graphene domain size was ~7.9 µm at 1000 °C, ~2.7 µm at 950 ˚C, and only ~1.7 µm at 900 °C when synthesised using 5 sccm CH_4, 0.1 sccm NH_3 and 500 sccm H_2 for 5 minutes, Figure 146. This equates to a growth rate of 1.58 µm min^{-1} at 1000 °C, which decreased nearly three times to 0.54 µm min^{-1} at 950 °C, and further decreased to 0.34 µm min^{-1} at 900 °C, Figure 146d. The influence of synthesis temperature on the growth rate of nitrogen-doped graphene therefore follows a similar trend to previous studies investigating the influence of synthesis temperature on the growth rate pristine graphene[168].

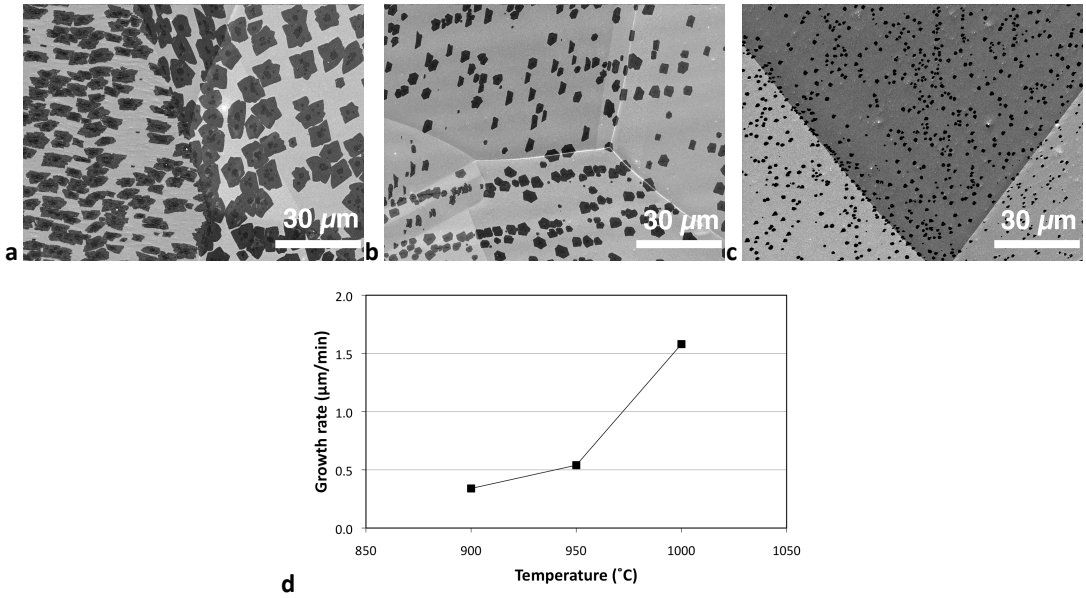


Figure 146: LPCVD nitrogen-doped graphene growth with 5 sccm CH_4, 500 sccm H_2 and 0.1 sccm NH_3, varying synthesis temperature for 5 minutes at (a) 1000 ˚C, (b) 950 ˚C, (c) 900 ˚C. (d) Plot demonstrating variation of growth rate with synthesis temperature of nitrogen-doped graphene

Increasing the NH_3 flow rate also decreased the growth rate, and as a consequence it was necessary to increase the duration of experiments and/or decrease the hydrogen flow rate so that domains were of an appreciable size for SEM imaging. The change in synthesis time and/or hydrogen flow rate helped to grow larger graphene domains without influencing their quality, and still provides the opportunity for comparing the growth rate between experiments with different NH_3 flow. For example, at 1000 °C using 5 sccm CH_4, 0.5 sccm NH_3 and 500 sccm H_2 for

10 minutes resulted in average domain size of 13.4 µm at a growth rate of 1.34 µm min^{-1}, Figure 147b. Comparing this growth with that using 0.1 sccm NH_3, Figure 147a, a five times increase of NH_3 flow rate decreased the average growth rate by approximately 15%, from 1.58 µm min^{-1} to 1.34 µm min^{-1}. At lower temperatures, 950 ˚C and 900 °C, a similar increase in ammonia concentration decreased the average growth rate approximately 25%, Figure 147c, d.

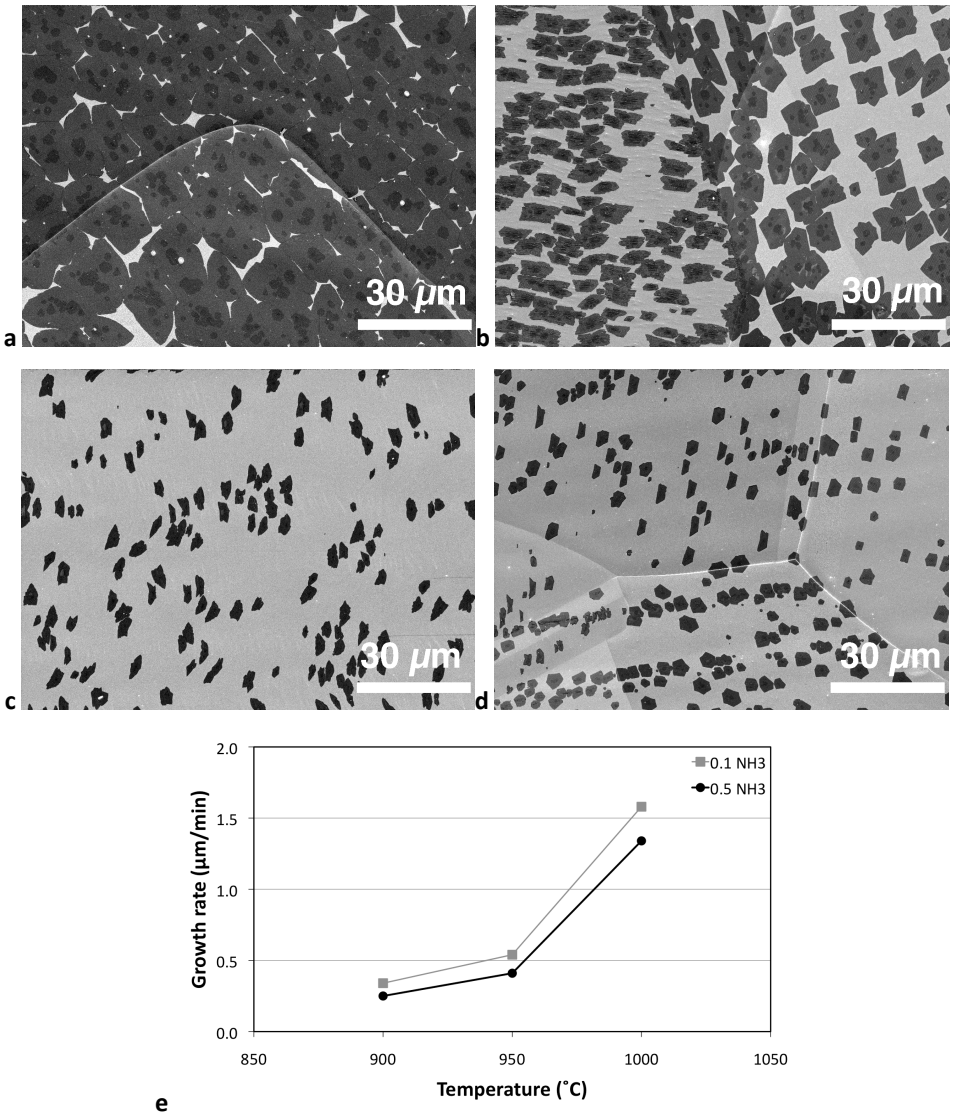


Figure 147: LPCVD nitrogen-doped graphene growth with 5 sccm CH_4 and 500 sccm H_2, varying NH_3 (a) 1000 ˚C with 0.5 sccm NH_3 for 10 minutes, (b) 1000 ˚C with 0.1 sccm NH_3 for 5 minutes, (c) 950 ˚C with 0.5 sccm NH_3 for 10 minutes, (d) 950 ˚C with 0.1 sccm NH_3 for 5 minutes. (e) Influence of synthesis temperature and NH_3 flow rate on the average growth rate of nitrogen-doped graphene

Collectively, I conclude that a decrease in synthesis temperature and increase of ammonia concentration caused a significant decrease in the growth rate of

nitrogen-doped graphene. A 100 °C reduction in synthesis temperature and five times increase in NH_3 flow rate resulted in approximately six times decrease in growth rate.

The temperature and ammonia concentration also influenced the graphene nucleation density and the maximum achievable surface coverage. Full coverage (or nearly full coverage) was observed when using high temperatures and high ammonia concentrations- for instance, 0.5 sccm NH_3 and 500 sccm H_2 at 1000 °C for 10 minutes, Figure 147a- or low temperatures and low ammonia concentrations, for instance, 0.1 sccm NH_3 at 900 ˚C. However, only incomplete surface coverage of the copper substrate was observed at low temperatures, 900 ˚C, and high ammonia concentrations, 0.5 sccm NH_3. Even for experiments with reduced H_2 flow rate (to minimise etching of domains) and longer synthesis time of 30 minutes the size of the graphene domains did not increase significantly, Figure 148a. Incomplete maximum surface coverage is achieved under such conditions, with further extension of the synthesis time to 60 minutes merely causing damage to the nitrogen-doped graphene, Figure 148b.

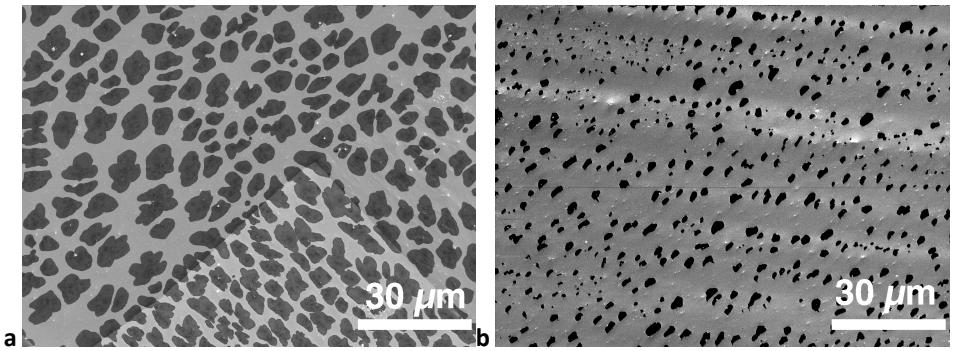


Figure 148: Damaged LPCVD nitrogen-doped graphene growth at 900 ˚C with 0.5 sccm NH_3 5 sccm CH_4 and 100 sccm H_2 for (a) 30 minutes, (b) 60 minutes

This damage is likely due to NH_3 reacting corrosively with the catalytic copper surface[182], inhibiting the growth of domains and also etching domain edges. Consequently, the right balance between the experimental parameters is necessary to control the surface coverage and growth rate of nitrogen-doped graphene. These findings have important implications for optimising the sample quality while minimising the production time and associated costs of manufacturing nitrogen-doped graphene if it is to find commercial application in the future.

10.1.3 Investigations into the bonding of dopants in nitrogen-doped graphene

STM and STEM were used to investigate how the nitrogen atoms are incorporated into the nitrogen-doped graphene lattice. Samples of nitrogen-doped graphene were imaged in air by STM while remaining on the Cu substrate to exclude the potential introduction of surface contaminations and polymer residues from a transfer procedure. Samples were exposed to air prior to imaging, while surface absorbed contaminations were removed by the STM tip through repeated scanning. Low magnification STM imaging demonstrates that dopant atoms can be identified at many different sites across the sample surface[86], Figure 149a, highlighted by arrows. Several larger defects are likely due to clusters of nitrogen atoms, circled in Figure 149a. Through atomic resolution imaging dopant atoms were observed to predominately show substitutional bonding, Figure 149b and c, highlighted by triangles. These images correspondence with DFT simulations reported by Lambin *et al.*[327] and so these features are confirmed as nitrogen dopants. The rotation between different features, highlighted by triangles in Figure 149b, indicates that the substitutional nitrogen dopant atoms can be incorporated in different sublattices of the few-layer nitrogen-doped graphene. Some defects resembling the DFT simulations of the pyridinic configuration[47] were also observed, Figure 149d.

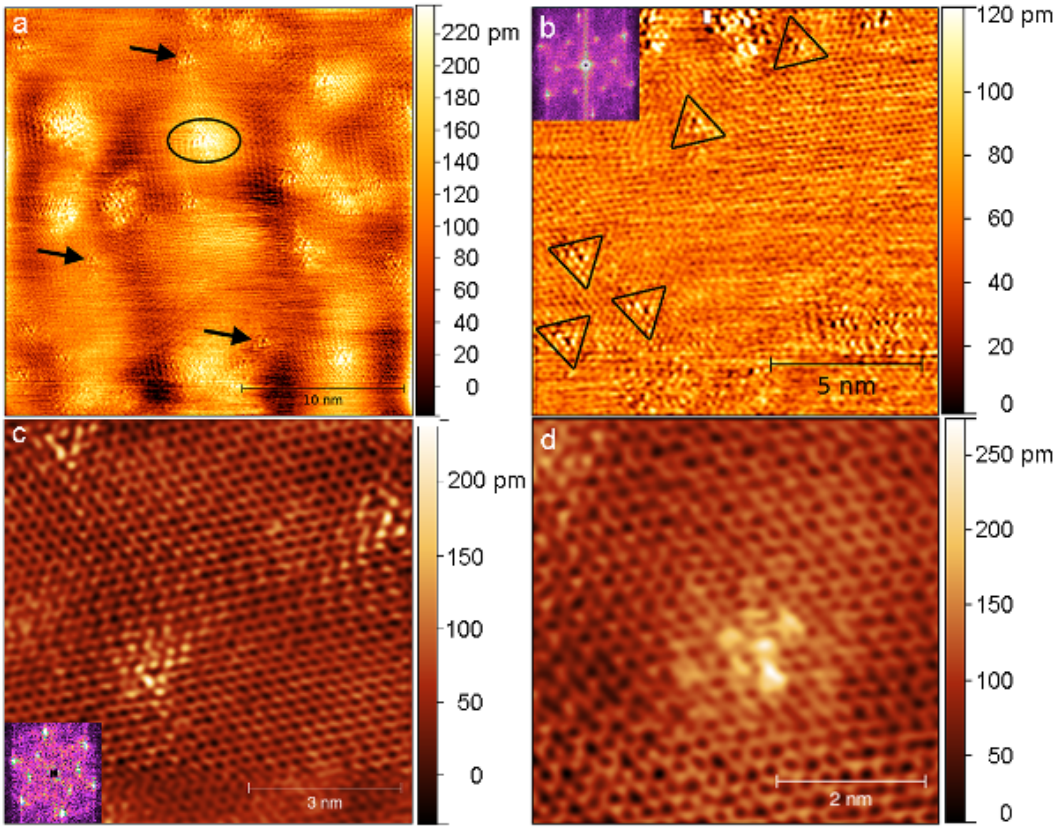


Figure 149: STM of LPCVD nitrogen-doped graphene on Cu foil

(a) Lower resolution STM image of nitrogen-doped graphene showing dopant atoms[327] (arrows) and larger defects likely containing multiple dopant atoms (circled), (b) Higher resolution STM image revealing typical patterns around individual substitutional nitrogen atoms oriented differently on different sublattices as highlighted by triangles. The inset presents the FFT of the STM image: the outer hexagon corresponds to the atomic lattice of graphene, the inner hexagon arises from the intervalley scattering induced by nitrogen dopants, (c) Additional examples of nitrogen atoms, (d) A defect resembling the pyridinic configuration[47]

Fast Fourier transforms (FFT) of Figure 149b and c (inset) demonstrate two sets of hexagonal spot patterns. The outer hexagon corresponds to the graphene lattice, while the inner hexagon arises from the nitrogen dopant atoms inducing strong intervalley scattering[86, 328]. The FFT therefore also confirms the features marked by triangles as nitrogen dopants. Furthermore, these strong intervalley peaks are caused by electron scattering processes between two non-equivalent Dirac cones[329], therefore the FFT demonstrates that the nitrogen dopants have an influence on the electronic structure of nitrogen-doped graphene, discussed further in Chapter 10.1.4. This observation is in agreement with the increase in intervalley scattering

for nitrogen-doped graphene detected by Raman spectroscopy through the increase in the D and D' peak intensities, Figure 144.

Aberration-corrected MAADF-STEM was also used as a complementary characterisation technique to investigate how the nitrogen atoms were incorporated in the graphene lattice. Low magnification MAADF STEM imaging demonstrated that the samples were predominately composed of few-layer graphene, Figure 150. Significant portions of the sample were also covered by amorphous carbon surface contaminants, but whether this originated from the synthesis procedure, transfer procedure, or exposure to the atmosphere is unclear. The contamination was often mobile on the graphene surface and attracted by the focussed electron beam. This resulted in beam deposition that made high-resolution imaging particularly difficult. Nonetheless, ~20 nm^2 single-layer graphene regions could frequently be identified, Figure 150d.

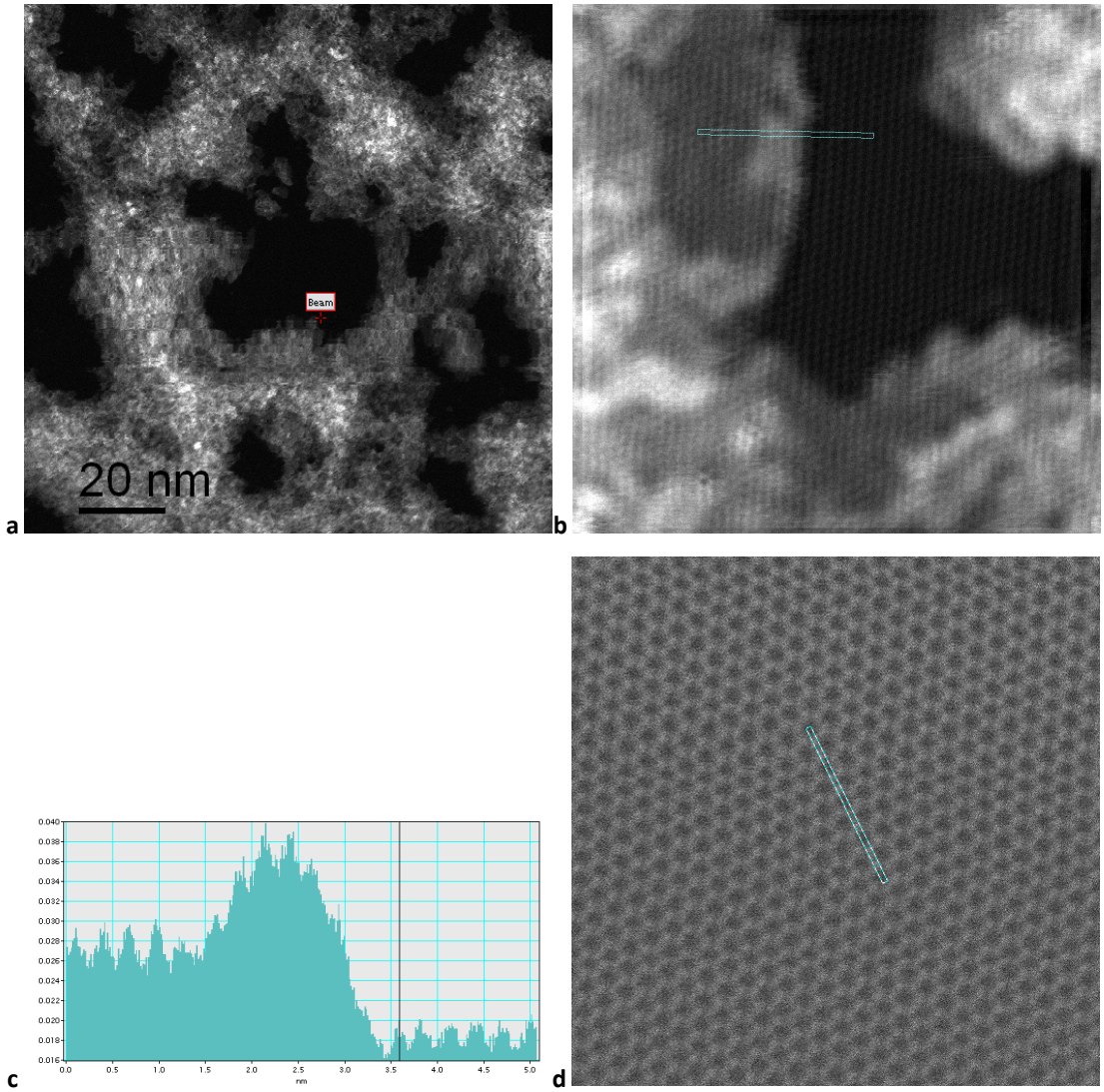


Figure 150: MAADF-STEM of LPCVD nitrogen-doped graphene

(a) Low-magnification image demonstrating contrast variations due to multi-layer regions and amorphous surface contaminations, (b) ~20 nm^2 region of single-layer graphene showing uniform dark contrast, while bilayer and few-layers surround this region (c) Line profile indicating bilayer and single-layer nitrogen-doped graphene (left and right side of profile, respectively), (d) Single-layer nitrogen-doped graphene that appears to be defect and dopant free

These regions provided the opportunity to directly locate individual heteroatomic dopant atoms in the graphene network due to the contrast intensity variations between individual atoms, Figure 151.

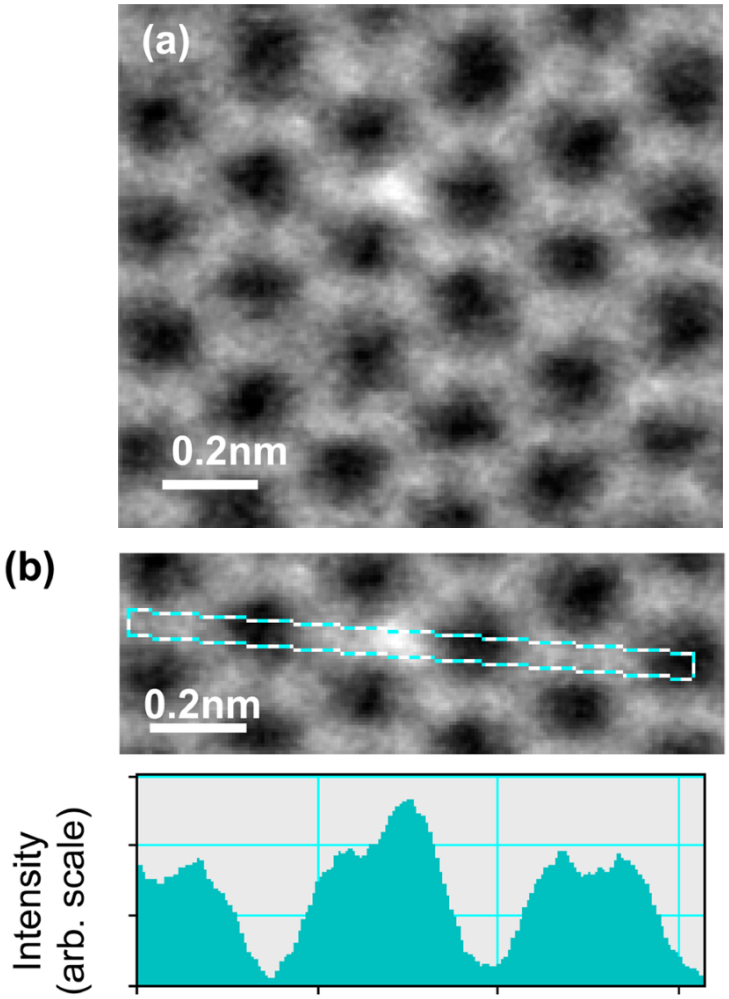


Figure 151: High-resolution MAADF-STEM of nitrogen dopant in single-layer LPCVD nitrogen-doped graphene (a) MAADF-STEM image of nitrogen dopant (bright atom) in single-layer nitrogen-doped graphene. Image was processed using a filter similar to Krivanek et al.[288], but is also visible in raw image (see Appendix), (b) Intensity profile demonstrates increased contrast intensity from the nitrogen dopant. Reproduced from Nicholls et al.[3]

Dopants were identified as nitrogen atoms owing to a 1.3:1 ratio difference in the measured intensity compared to the carbon atoms of graphene, Figure 151b, in agreement with theoretically predictions and experimental work by Krivanek *et al.*[288]. Line intensity profiles using imaging software assisted with detecting this intensity variation, as the difference is barely perceivable by the naked eye during live imaging. The bonding of the nitrogen atoms in Figure 151a can be directly interpreted from the images as substitutional; no alternative configurations were

observed during the investigations. This is believed to be the first experimental observation of individual nitrogen dopant atoms within nitrogen-doped graphene.

10.1.4 Investigations into the electronic structure of nitrogen-doped graphene

CITS and EELS was conducted to investigate the effect of individual nitrogen dopants on the electronic structure of nitrogen-doped graphene. Substitutional nitrogen-dopants detected by atomic-resolution STM imaging, Figure 152a, correspond with localised high intensity current variations in the CITS map, Figure 152b. Diffuse maximum in the CITS image are due to defects containing more than one nitrogen atom, as observed in STM. The CITS map demonstrates that the electronic structure of the nitrogen-doped graphene was strongly modified, but this modification was only present within a few lattice spacings of the nitrogen atoms. A representative CITS spectra measured above a nitrogen atom, marked N in Figure 152a and Figure 152b, is presented in Figure 152c.

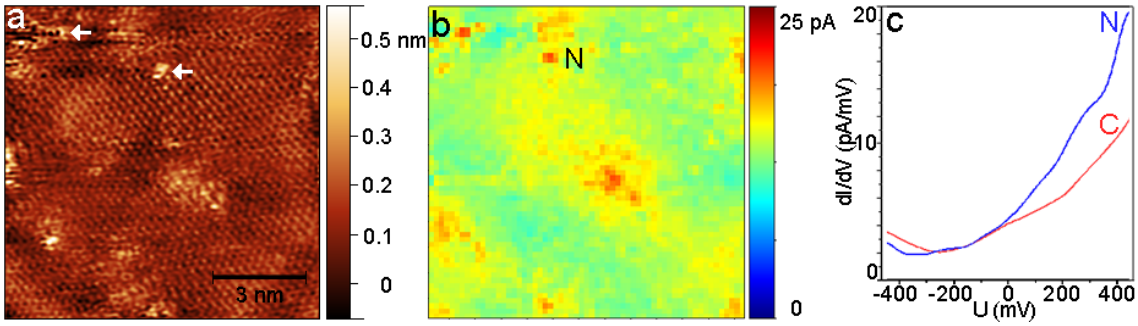


Figure 152: STM and CITS of LPCVD nitrogen-doped graphene on Cu foil

(a) High-resolution STM image of nitrogen-doped graphene demonstrating nitrogen dopants, highlighted by white arrows, (b) Corresponding CITS map at 335 mV of nitrogen-doped graphene. A minor translational shift exists between the STM and CITS map, (c) dI/dV spectra recorded above a nitrogen atom (blue line, obtained above label N in the CITS map), and a carbon atom (red line)

The minimum of the dI/dV curve is -300 meV, which is in agreement with values reported in the literature[86]. This spectra also demonstrates that the local density of states above the Fermi level around the nitrogen atom increased dI/dV at positive voltages, as is expected from DFT calculations[327]. The CITS measurements indicate that while nitrogen-doping does influence the electronic structure of graphene, the influence is localised around ~1-2 nm from dopant atoms. As such, at these doping levels the CITS suggests there may not be a significant influence on the electrical

properties over large-areas of nitrogen-doped graphene. This result requires further investigation to determine whether this will have negative implications for the integration of nitrogen-doped graphene in future applications.

Experimental EELS was also conducted simultaneously with MAADF-STEM to investigate the influence of nitrogen-dopants on the electronic structure of nitrogen-doped graphene. While EELS analysis of the nitrogen K-edge is possible[330], for nitrogen-doped graphene this measurement is experimentally challenging owing to the small cross section of the nitrogen K-edge, and difficulties in resolving the fine structure. Instead, the effect of the nitrogen dopant on the neighbouring carbon atoms was investigated- with the three nearest neighbours having a higher cross section- and a variation in the carbon K-edge EELS fine structure was measured. Localised EELS spectra were obtained from the nearest-neighbour carbon atoms surrounding the nitrogen dopant by repeatedly scanning a defined region that encompassed the dopant atom, Figure 153a. Owing to sample drift it was necessary to manually shift the scan box so that it remained centred on the nitrogen dopant, using the MAADF-STEM image as guidance. A representative EELS spectrum from the region surrounding a nitrogen dopant is presented in Figure 155b, alongside an EELS spectrum recorded from a region of pristine graphene for comparison.

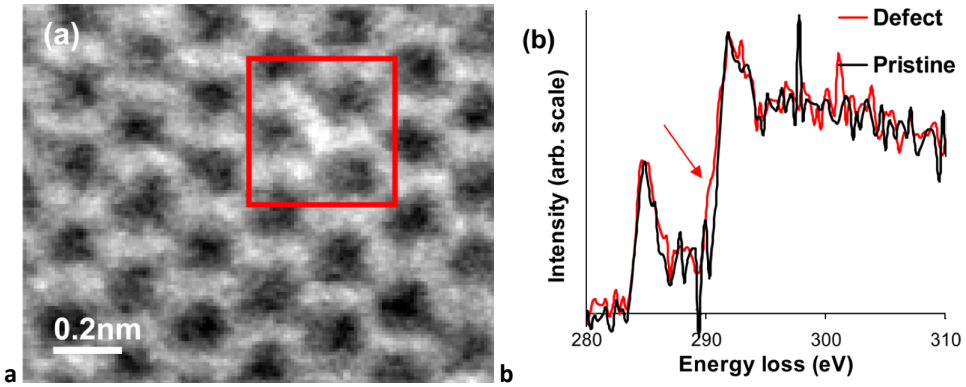


Figure 153: MAADF-STEM and EELS of LPCVD nitrogen-doped graphene

(a) Processed MAADF STEM image of nitrogen-doped graphene demonstrating scanning region for EELS analysis (red square) surrounding nitrogen atom, (b) Carbon K-edge obtained from scanning region surrounding nitrogen atom (red line, labelled defect) and from a region of pristine graphene (black line, labelled pristine). Peaks in the spectra at ~297 and 302 eV are artefacts, likely due to bad pixels on the CCD camera. Reproduced from Nicholls et al.[3]

A subtle variation in the carbon K-edge is visible for the localised EELS spectrum obtained from the region surrounding the nitrogen dopant, resulting in an additional feature at ~290 eV, highlighted by an arrow in Figure 153b. This variation was reproducible in spectra taken from three different nitrogen dopants (see Appendix). The peaks at ~297 eV and ~302 eV are not real features of the EELS spectra, and are likely due to bad pixels in the CCD.

Computational EELS simulations were conducted to investigate the theoretical influence of a nitrogen dopant on the electronic structure of the neighbouring carbon atoms in doped graphene. A representative graphene system containing substitutional nitrogen dopants was investigated, Figure 154a. This dopant caused no notable distortion of the geometry of the graphene lattice. The simulated EELS spectrum for pristine single-layer graphene shows two peaks at ~1 eV and ~8 eV above the onset of the C K-edge, which are recognised as the π* peak and the σ* peak, pink line in Figure 154b, labelled graphene. For single nitrogen atom substitutionally doped graphene, the simulated EELS spectra vary for each of the three symmetrically unique C atoms close to the N atom, labelled C1, C2 and C3 in Figure 154a. A notable peak, located ~4.5 eV above the π* peak, can be identified in the spectra for the C1 atom that directly bonds to the N dopant, navy line in Figure 154b, labelled C1. In contrast, the spectrum for C2 and C3 appear similar that of pristine graphene, blue and red line in Figure 154b, labelled C2 and C3, respectively.

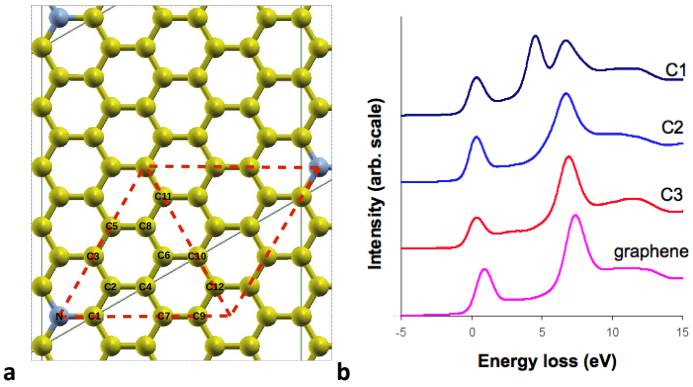


Figure 154: Computational EELS simulation of nitrogen-doped graphene

(a) Graphene model system containing a substitutional nitrogen atom. Symmetrically unique carbon atoms are labelled based on their distance from the nitrogen dopant atom. Solid grey lines mark the unit cell, while dashed red lines provide a guide. Reproduced from Nicholls et al.[3]

The experimentally measured EELS spectrum, Figure 153b, includes contributions from the carbon atoms within the scanning region, highlighted by red box in Figure 153a. To compare the simulated EELS spectra with the experimental EELS data, the simulated spectra of C1, C2 and C3 were combined in a ratio of 3:6:2 as a direct analogue for the contributions from nearest-neighbour carbon atoms within the experimental scan box. This combined spectra, Figure 155 (orange line), still exhibits a small feature at ~ 5 eV above the π* peak and shows great similarity to the experimental EELS spectrum from the region surrounding the N dopant, Figure 155 red line. The additional feature in the experimental EELS spectrum is therefore indicative of the influence of the nitrogen-dopant on the electronic structure of the neighbouring carbon atoms in graphene.

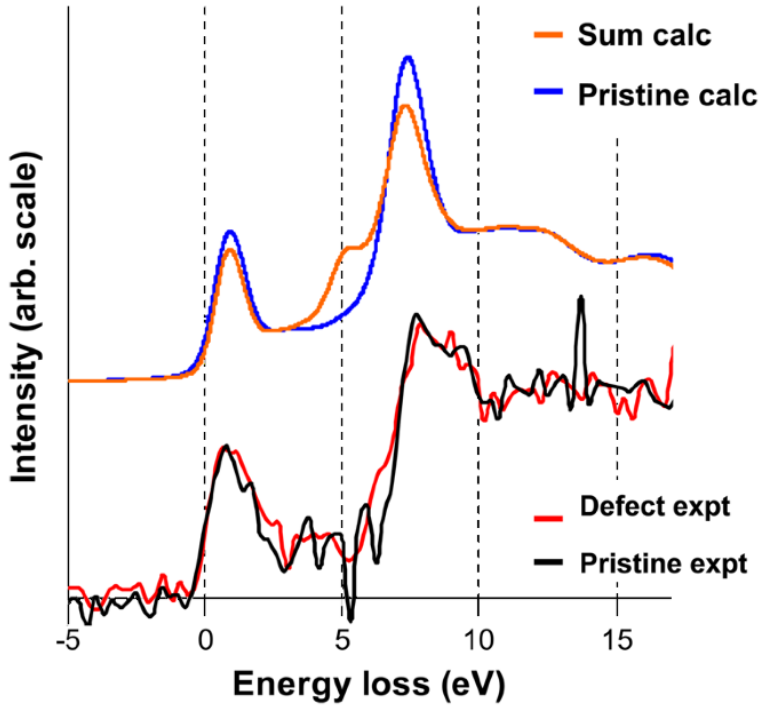


Figure 155: Comparison between experimental and simulated EELS spectra from pristine and nitrogen-doped graphene. Reproduced from Nicholls et al.[3]

10.2 CVD of boron-doped graphene on copper foils

10.2.1 Design and construction of low-pressure CVD apparatus for heteroatom doping of graphene using liquid precursors

Further modifications were made to the low-pressure CVD setup presented in Chapter 10.1.1 to provide the functionality for using liquid precursors. While some gases are suitable for heteroatomic doping of graphene, for instance, NH_3 for nitrogen doping, the range of gaseous reactants is limited in comparison to liquid reactants. Gaseous BF_3 or diborane was considered as a reactant for synthesising boron-doped graphene, but I decided against this route owing their high toxicity and spontaneous ignition. Instead, by adapting the system to use liquid precursors the scope for synthesising a variety of heteroatom-doped graphenes was increased by making a wider range of reactants accessible, while maintaining laboratory safety. Of course, the modified system is not limited to doping experiments, as pure graphene can also be produced using liquid precursors[157, 189].

I adapted the LPCVD apparatus by introducing an additional Swagelok ultra-Torr connection so that a 25 mL vial could be connected into the system, Figure 156. Evaporation of the liquid reactant inside the vial occurs favourably under the low-pressure conditions with the flow rate controlled using a needle-valve.

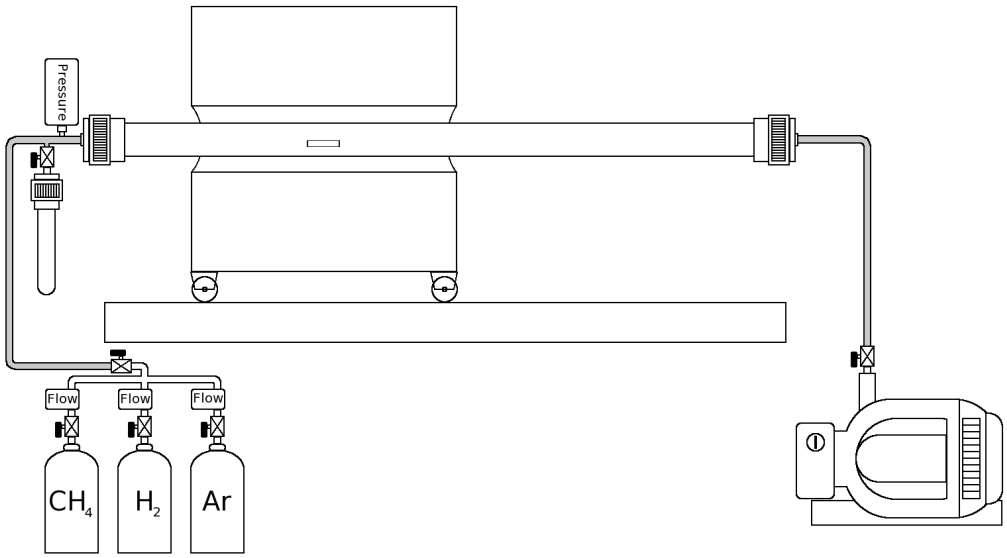


Figure 156: LPCVD apparatus for heteroatom doping using liquid precursors with Swagelok Ultra-Torr connected vial with needle-valve flow control

10.2.2 Initial experiments into synthesis of boron-doped graphene

To synthesis boron-doped graphene I selected triethylborane as a suitable boron-containing organic reactant. Based on experiments synthesising boron-doped MWCNTs, a maximum dopant concentration of only a few atomic percentage was expected to be stable for boron-doped graphene[323]. As such, the triethylborane was diluted as a 1M solution in hexane.

Initially the synthesis of pristine LPCVD graphene using hexane as the liquid precursor was investigated. This experiment was necessary so that graphene synthesised using diluted triethylborane could be compared and accurately interpreted. 99.999 % Alfa Aesar Cu foil was used as the substrate following 10 minutes ultrasonic cleaning in acetic acid. The foil was annealed at 1035 ˚C under 100 sccm H_2 for 30 minutes at a pressure of 1.27 Torr. The H_2 flow rate was increased to 1000 sccm and the tap to the liquid hexane was then opened to the minimum needle-valve setting for 1 minute for LPCVD synthesis from the liquid precursor. During the synthesis time the pressure increased to 5.11 Torr. The tap to the liquid precursor was then closed and the substrate was quickly shifted from the hot zone to cool under flowing H_2.

The procedure was repeated with the aim of synthesising boron-doped graphene by replacing the hexane with a solution of 1M triethylborane in hexane. SEM of these two experiments demonstrates the growth of isolated graphene domains from liquid hexane precursor, Figure 157a, and full coverage of graphene from 1M triethylborane in hexane. The doping procedure was repeated with an increase in H_2 to 1500 sccm, and subsequently observed isolated domains on the Cu foil,

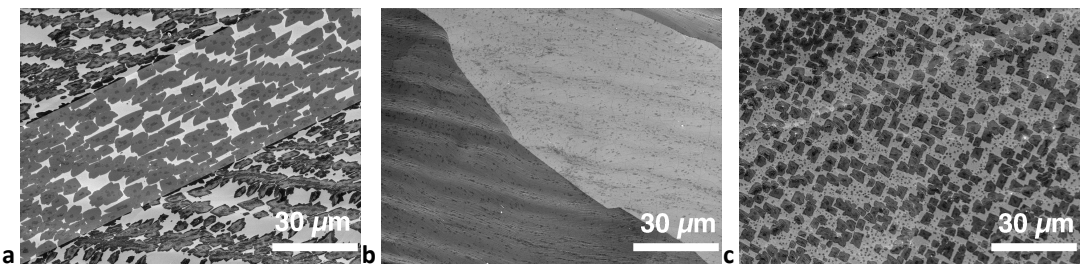


Figure 157: LPCVD pure and boron-doped graphene synthesised on 99.999 % Alfa Aesar Cu foil using liquid precursors at 1035 ˚C with (a) hexane and 1000 sccm H_2, (b) 1M triethylborane in hexane with 1000 sccm H_2. (c) 1M triethylborane in hexane with 1500 sccm H_2

I conducted Raman spectroscopy on the samples synthesised with pure hexane and with 1M triethylborane in hexane, aiming to observe peak shifts and intensity variations representative of boron-doping, Figure 158.

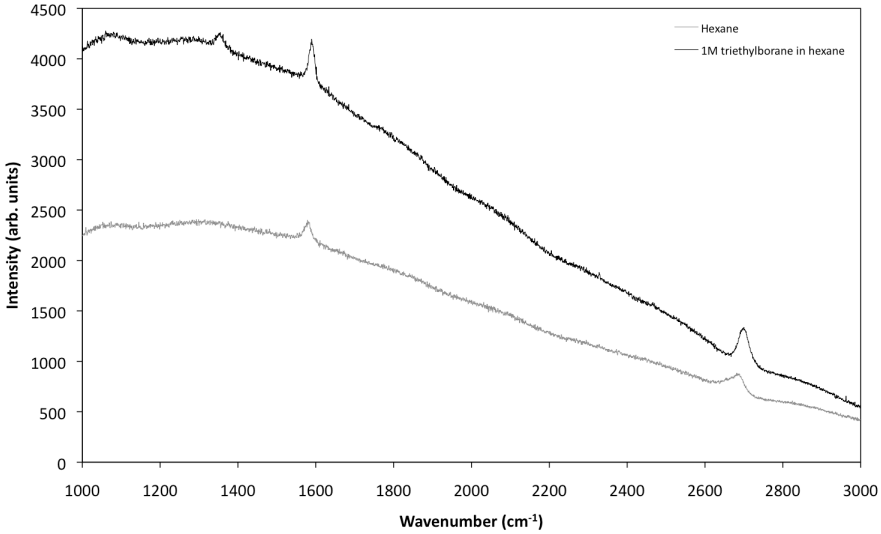


Figure 158: Raman spectra of LPCVD pure and boron-doped graphene synthesised using liquid precursors of hexane and 1M triethylborane in hexane

The G and 2D peaks are observed at 1576 cm^{-1} and 2682 cm^{-1} for graphene synthesised using liquid hexane. While some variation occurred between specimens, the G and 2D peak positions were observed to increase for specimens synthesised using 1M triethylborane in hexane, to 1589 cm^{-1} and 2700 cm^{-1}, respectively. This equates to an upshift of 13 cm^{-1} and 18 cm^{-1}, respectively. This upshift in both G and 2D peak is representative of p-type doping, which is expected due to the introduction of boron dopants into the graphene. A D peak is also detected in the Raman spectra of graphene synthesised using 1M triethylborane in hexane, which indicates disorder in the graphene lattice, presumably due to boron doping. This analysis appears a promising initial confirmation that synthesis of boron-doped graphene is possible through the use of a liquid precursor, 1M triethylborane in hexane. Further characterisation is undoubtedly required to conclusively prove boron doping, and alongside investigations into the influence of synthesis conditions on the dopant concentration and electronic properties this topic appears to be a fruitful area for future research.

10.3 Conclusions on heteroatom-doped graphene

My investigations into the LPCVD growth of heteroatom-doped graphene demonstrate:

- The dopant concentration of LPCVD nitrogen-doped graphene synthesised *in-situ* with NH_3 and CH_4 is increased at lower synthesis temperatures and higher NH_3:CH_4 flow rate ratios, up to 1.3 % as demonstrated by XPS analysis,
- The growth rate of nitrogen-doped graphene decreases at lower synthesis temperatures and higher NH_3 concentrations, and complete surface coverage of LPCVD nitrogen-doped graphene on Cu foil is restricted at high NH_3 flow rate ratios, which is attributed to corrosive damage of the surface,
- *In-situ* doping with NH_3 and CH_4 primarily leads to substitutional dopants, as demonstrated by high-resolution STM. These dopants modify the electronic structure of nitrogen-doped graphene, but only within a few lattice spacing, as demonstrated by CITS,
- Direct visualisation, elemental confirmation, and electronic characterisation of nitrogen-doped graphene for the first time using aberration-corrected MAADF-STEM, EELS and complementary computational simulations,
- Boron-doped graphene can be synthesised by LPCVD growth using liquid precursor of 1 M triethylborane in hexane.

11 Conclusions

11.1 Conclusions on the contributions and impact of research project

My research contributes to the wider scientific community- expanding the body of scientific knowledge on the CVD growth of graphene on metals- and to my immediate research community of Professor Nicole Grobert's Nanomaterials by Design research group.

Firstly, with respect to the major contributions to the scientific community at large, my DPhil research yielded a wide range of empirical conclusions that support theoretical postulates and models. Initially, dealing with each in turn for ease of discussion, the major contributions are as follows:

Influence of Cu crystallographic orientations on growth of graphene

In Chapter 7 I demonstrated the influence of Cu crystallographic orientations on the orientation of LPCVD and APCVD graphene domains, and on the shape, thickness, and edge geometry of LPCVD graphene domains; that macroscopic edges preferentially align parallel to Cu<101> direction(s), corresponding to one direction on Cu{111} and Cu{101}, and two ~90˚ rotated directions on Cu{001}; and by DFT modelling that such preferential alignment for nanoscale graphene domains on Cu{111}, Cu{101} and Cu{001} minimises the system energy by C atoms locating at available adatom sites of low electron density, with directional bonds between the graphene zigzag edge and the Cu substrate.

Graphene growth on Cu is dictated by kinetics, with different growth mechanisms occurring for LPCVD and APCVD condition[167, 331, 332]. My results for LPCVD growth are in agreement with previous LPCVD studies where domains exhibit lobed and dendritic shapes, which are representative of a diffusion-limited growth mechanism where growth is controlled by the flux of active C species. As such, diffusion-limited growth is promoted along energetically favourable graphene edges/growth fronts and often manifests 6-fold symmetrical lobed domains due to higher growth rates along specific directions of the graphene lattice. My investigations indicate that, at

least under the experimental conditions used here, the Cu foil also influences the direction of the fast growth front(s) for diffusion-limited growth, whereby the growth is preferential along specific Cu crystallographic orientations. I postulate that this variation arises from (i) increased diffusion of active species along specific directions of Cu crystallographic orientations, for example, the <101> direction on Cu(101) (due to the observed channels on this surface) and (ii) increased probability for attachment of active species to the armchair edges of graphene domains (supported by DFT modelling which showed unbonded electrons at the armchair edges representing preferential growth sites). My results for APCVD growth are also in agreement with previous studies where APCVD domains exhibit hexagonal shapes, which are representative of an edge-attachment-limited growth mechanism where growth is controlled by a high energy barrier for successful attachment of active C species onto the domain edge[331]. This growth follows the theory of Wulff construction that predicts formation of distinct domain shapes under equilibrium conditions[333]. As the energy barrier is lower for attachment of active C species to armchair edges than zigzag edges[331, 333] and by having excess hydrogen in the system to etched unstable edge geometries[209], the resulting hexagonal shapes possess zigzag edges[211]. However, my investigations indicate that the crystallographic orientations of Cu foil influence the orientation of these hexagonal domains. To explain this observation, I propose a growth model whereby the orientation of macroscale APCVD graphene domains is dictated by the preferential orientation of nanoscale domains during the early stages of the nucleation and growth due to (i) minimisation of system energy caused by a lattice mismatch between the graphene and the Cu substrate, (ii) stabilising bonds forming between zigzag edges and the Cu substrate. Once domains grow sufficiently large the energy required for rotation of the domain is too large to overcome, and consequently domains maintain the preferential orientation that is adopted from their inception.

Influence of properties of Cu foils on growth of graphene

In Chapter 8 I demonstrated that the properties of Cu foils- including the topography, surface roughness, crystallographic orientations, and chemical composition- vary greatly between different commercially-available Cu foils and this influences the growth of CVD graphene on different Cu foils; that the commonly used 'Coated' 99.8 % Alfa Aesar Cu foil does indeed have a surface coating composed of calcium, chromium and phosphorus; that CH_3COOH cleaning before annealing treatment reduces the concentration of calcium oxide contamination particles, carbon and oxygen on the surface of Cu foils; and that CH_3COOH cleaning of Cu foils reduces the nucleation density and increases the growth rate of APCVD graphene domains, which is attributed to the reduction in contamination particles.

My experiments demonstrate that the presence of metal nanoparticles on the Cu surface, specifically calcium oxide nanoparticles, have a detrimental influence on the growth of graphene by uncontrollably influencing the nucleation and growth rate of domains. Based on my experimental results, I propose that metal contamination particles act as sites where nucleation can preferentially occur, either due to a lowering of the barrier energy for nucleation or through an increase in the concentration of active carbon species by improved CH_4 dissociation. These nanoparticles therefore increase the nucleation density. Additionally, I postulate that CaO nanoparticles can catalytically oxidise graphene to form calcium carbide, as demonstrated by Cairns et al[320], and via a reaction proposed by Tagawa et al[334]:

$CaO + C \rightarrow CaO.C$ (interdiffusion state) $\rightarrow Ca + CO$

$Ca + 2C \rightarrow CaC_2$

For an overall reaction of:

$CaO + 3C \rightarrow CaC_2 + CO$

This reaction will etch the graphene, resulting in a decreased growth rate as observed. As a consequence, cleaning of the Cu foils with CH_3COOH (which effectively reduced the concentration of CaO) resulted in an increase in the growth rate and a decrease in the nucleation density of graphene domains.

Rapid growth of large-area single-layer polycrystalline graphene on Pt

In Chapter 9 I optimised production of ~0.5 mm single-layer polycrystalline graphene domains on Pt foils with reduced nucleation density, increased growth rate of ~100 μm/min and more efficient growth by synthesis at 1150 ˚C, a higher temperature than previously reported; I demonstrated that large-area, hexagonal, single-crystal graphene domains do not form on pristine Pt foil even with optimised CH_4:H_2 flow rate ratios.

Although my experiments invariantly did not form single-crystal hexagonal graphene domains as predicted by the work of Gao et al[176], my results support previous studies showing many random orientations of graphene on the Pt surface[173, 236, 335-337]. My investigations suggest a reaction between the Pt foil and the quartz tube may explain the results demonstrated by Gao et al[176], and this observation has led to the investigation of APCVD growth of hexagonal graphene domains on silicidated platinum[322]. I propose that polycrystalline graphene domains form on the Pt foils (rather than single-crystal domains) due to (i) the lattice mismatch between the graphene and Pt surface, and (ii) the weak interaction between outer 5d electron orbitals of the Pt surface and the π electrons of graphene[336]. While these aspects indicate only minor influence of the Pt substrate on graphene growth, based on my observation of some correlation between Pt grain boundaries and the vertices of polycrystalline domains, I postulate that surface features (e.g. steps and kinks, which occur in higher concentration at grain boundaries and regions of surface roughness) may actually provide the crucial disruption to the graphene growth front to trigger the growth of polycrystalline domains on Pt. Graphene growth on Pt is faster downhill than uphill[173], therefore growth over surface features may result in increased lattice inconsistency and energetically unfavourable strain at the downhill growth front[335] which is released or minimised by realignment of the lattice to form polycrystalline domain. Such occurrence has been observed when graphene on Cu formed mosaic structures due to crossing of steps[207, 243].

Influence of synthesis temperature and ammonia on growth of nitrogen-doped graphene, and high-resolution imaging and analysis of single dopants

In Chapter 10 I demonstrated the influence of the synthesis temperature and ammonia flow rate on the dopant concentration of nitrogen-doped graphene, with increased nitrogen-doping at lower temperatures and higher NH_3 flow rate ratios, up to 1.3 %, but with an associated decrease in growth rate. Additionally, the direct visualisation, elemental confirmation, and electronic characterisation of single nitrogen dopants in nitrogen-doped graphene was achieved using aberration-corrected MAADF-STEM, EELS and complementary computational simulations.

While the mechanism of incorporation of nitrogen atoms into the graphene lattice is still not fully understood[183, 338], the process must occur either (i) at the growth front of the graphene domain through a reaction with NH_3 (or addition of a nitrogen-containing active species[338]), or (ii) through direct attack of NH_3 to defects in the graphene lattice. Given that nitrogen-doped graphene can be synthesised by post-growth annealing of pristine graphene in NH_3[88, 182, 183], the second proposed growth mechanism must occur, at least to some extent. Additionally, it is well known that the defect concentration of CVD graphene (synthesised using CH_4) increases at lower synthesis temperatures[189]. As such, and comparing to my experimental conclusions, I postulate a growth mechanism where the incorporation of N in nitrogen-doped graphene is increased at lower synthesis temperatures due to a reaction between NH_3 and defects (e.g. vacancies) in the graphene lattice, which are at a higher concentration at lower synthesis temperatures. Such a proposal is supported by calculations by Lv et al[183] demonstrating nitrogen atoms could stablise structure defects in nitrogen-doped graphene. A secondary factor which may influence the concentration of nitrogen-doping is a concurrent and opposing reaction which may occur between NH_3 and Cu if any residual O or H_2O is present in the system (or if CuO is present). The rate of any reaction will increase with the synthesis temperature, thereby consuming N from the system and poisoning the Cu catalyst. This postulate is supported by my observation of a decreased growth rate with increased ammonia flow rate, and additionally, the inability to form a complete layer of graphene over the Cu foil at higher NH_3 concentrations.

To summarise the empirical and theoretical conclusions from the individual chapters I propose a growth model for pristine and nitrogen-doped graphene on transition metal substrates with low solubility (namely Cu and Pt). I hypothesis that graphene growth proceeds as follows:

(i) Dissociative chemisorption of CH_4 on the metal surface to form active carbon species. The rate of formation depends on the synthesis pressure, synthesis temperature, CH_4:H_2 flow rate ratios, the type of metal substrate and its crystallographic orientations, and the concentration of metal contamination particles.

(ii) Diffusion of active carbon species on the surface of the metal substrate. The rate of diffusion depends on the synthesis pressure and the type of metal substrate and its crystallographic orientations.

(iii) Formation of stable graphene nuclei when the concentration of active species is sufficient to overcome energy of formation. Lower energy barriers occur at surface features (step edges and kinks) and contamination particles on the metal surface, which act as the nucleation sites (demonstrated in Chapter 8 for Cu, and Chapter 10 for Pt).

(iv) Minimisation of system energy by reducing the lattice mismatch between the nanoscale graphene domain and metal substrate. If the interaction between the substrate and graphene is sufficient than the graphene domain will preferentially align with orientation dictated by the substrate's crystallographic orientation to form stabilising bonds between the zigzag edge and the metal substrate (demonstrated in Chapter 7 for Cu). For weakly interacting substrates the lattice mismatch will be more stable for larger domains (by the formation of wrinkles, for example) but can also be reduced by the formation of polycrystalline domains, which may be triggered by substrate features (demonstrated in Chapter 10 for Pt). The interaction between the substrate and graphene will be depend on the type of metal and its crystallographic orientation, the system pressure, and the concentration of species that can passivate graphene edges (H, O, or metal contaminations).

(v) Attachment of active C species to the edge of the graphene domain so that growth proceeds. The growth mechanism can be diffusion-limited (LPCVD, demonstrated in Chapter 5) or edge-attachment limited (APCVD, demonstrated in Chapter 6) which dictates the shape of the graphene domain. The rate and type of growth depends on the synthesis pressure, CH_4:H_2 flow rate ratio, synthesis temperature, the type of metal substrate and its crystallographic orientations (which can influence diffusion-limited growth by promoting diffusion along specific directions for LPCVD, demonstrated in Chapter 7), the presence of graphene-edge-passivating species (H, O and metal contaminations, demonstrated in Chapter 8), and the concentration of etchant species (H, and calcium oxide nanoparticles as demonstrated in Chapter 8)

(vi) If present, reaction between NH_3 and defects in the graphene lattice. The rate of inclusion depends on the concentration of NH_3, the defect concentration (influenced by synthesis temperature, amongst other factors), and the type of metal substrate (demonstrated in Chapter 10).

(vii) Continued growth of individual graphene domains until they merge together to form a polycrystalline graphene sheet covering the surface of the metal substrate.

With this summary, the implications of these major contributions for future research on CVD growth of graphene on metals, and more generally for the advancement of scientific knowledge for manufacturing large-area graphene, can be considered. In general, the contributions can be considered collectively as a group of discoveries that will assist with (i) improving the control and efficiency of production, and (ii) controlling the properties of CVD growth of large-area CVD graphene. For instance, by optimising synthesis conditions, controlling substrate surface contaminations, and raising synthesis temperatures on metals with increased catalytic ability, my research demonstrates many new routes for quicker, more efficient production of graphene. Similarly, by controlling the Cu crystallographic orientations and lowering synthesis temperatures to increase dopant concentrations, my research provides new routes towards controlling and tailoring the properties of CVD graphene.

The noteworthy discovery of the influence of Cu crystallographic orientations on the orientation of graphene domains is an essential advancement for controlling and predefining constituent graphene domains and domain boundaries, and opens a new avenue towards the controlled alignment of individual graphene domains for high-quality large-area polycrystalline graphene. This discovery has therefore been a valuable contribution as the scientific community readdresses the understanding of the epitaxial (or semi-epitaxial) growth of graphene on metals. The potential for future large-area manufacturing of CVD graphene to exploit specific Cu crystallographic orientations to tailor graphene's mechanical and electrical properties was recognised and provided the impetus for the filing of a GB and US patent surrounding this discovery.

More generally, the variability of Cu foil's properties, lack of correlation of properties with supplier-stated purity, and confirmation of a surface coating on the commonly used 99.8 % Alfa Aesar Cu foil demonstrates a need for researchers to adopt improved characterisation and quality assurance of substrates in the future. The importance of the substrate's properties in dictating CVD growth of graphene also suggests that targeted control of these properties, for instance, reducing the concentration of surface chemical contaminations or surface roughness, will be beneficial for improving graphene growth.

Complementary research using Pt foil that showed an increased graphene growth rate and capability of higher synthesis temperatures may have implications for efficient and rapid manufacturing of large-area CVD graphene. The observation of a reaction between Pt foils and the quartz tubes, and associated discovery that hexagonal graphene domains did not form even with optimised synthesis parameters, was the direct motivation for conducting APCVD growth on silicidated platinum foils which has yielded promising production of graphene[322]. This has opened an entire new class of eutectic substrates for growth of CVD graphene.

The discovery of the influence of synthesis temperature and NH_3 concentration on dopant concentration, and opposing impact on growth rate, will have important implications if nitrogen-doped graphene is to find commercial application. Using these samples the first direct visualisation of nitrogen dopants in nitrogen-doped

graphene by aberration-corrected STEM using contrast variations was demonstrated, with simultaneous probing of electronic structure by EELS of neighbouring C atoms was demonstrated. This establishes a new method of elemental and electronic analysis that may have far reaching implications for future materials research.

Additionally, minor contributions from my DPhil research include demonstrating that:

- The cleanliness of LPCVD apparatus and annealing in a high hydrogen flow are important to ensure Cu foils are free of carbon contaminations prior to growth of graphene. Potential carbon contamination origins include back-flow of oil mist from rotary-vane vacuum pumps, adsorbates on nylon gas lines, residues on quartz tubes from previous experiments, and dissolved or surface adsorbed species from the Cu foil,
- The nucleation density and shape of LPCVD graphene domains can vary on different sides of the Cu foil, with a lower density of well-defined domains on the bottom side attributed to variations in gas speed above and below the foil,
- The nucleation density and domain size vary significantly with the position of the Cu foil within a single heating zone cylindrical furnace. The variation is asymmetric, with increased average domain size downstream of the centre point and temperature distribution, which is attributed to an increase in the percentage of decomposed reactant radicals downstream of the high temperature zone shift,
- APCVD growth of graphene has a reduced growth rate and increased nucleation density compared to LPCVD for growth under equivalent synthesis conditions and experimental setup to produce hexagonal graphene domains,
- Pulsed APCVD promotes single-layer graphene,
- The commonly used 99.8 % Alfa Aesar Cu foil is primarily composed of Cu{001}, upon which two preferential orientations exist, which may explain why preferential domain orientation has been overlooked on this foil,

- Raman spectroscopy varies for LPCVD graphene domains on different Cu crystallographic orientations due to variations in thickness and substrate-induced stress on different Cu grains. Bilayer LPCVD graphene is suggested to form on Cu{001}, and single-layer LPCVD graphene on Cu{111} and Cu{101},
- The concentration of surface contaminations does not correlate with the supplier-stated purity for five Alfa Aesar Cu foils which have bulk purity varying from 99.8 % to 99.9999 %,
- Cleaning Cu foils with CH_3COOH increases the nucleation density and yields more-uniform, dendritic LPCVD graphene domains,
- Cleaning Cu foils with $FeNO_3$ reduces the nucleation density of APCVD and LPCVD graphene domains,
- Electropolishing Cu foils reduces the nucleation density of APCVD and LPCVD graphene domains
- Surface topography and surface contamination particles can influence the location of nucleation sites of APCVD graphene domains on Pt foil,
- Complete surface coverage of LPCVD nitrogen-doped graphene on Cu foil is restricted at high NH_3 flow rate ratios, which is attributed to corrosive damage of the surface,
- Synthesis temperature strongly influences the concentration of nitrogen-doped graphene, with a decrease from 1000 ˚C to 900 ˚C increasing the dopant concentration more than a 5x increase in NH_3 concentration, from 0.1 sccm to 0.5 sccm,
- Individual nitrogen dopant atoms influence the electronic structure of neighbouring carbon atoms.
- Boron-doped graphene can be synthesised using 1 M triethylborane in hexane.

These minor contributions provide many new insights to a broad range of topics surrounding CVD growth of graphene on metals. In some instances the contributions expand the scientific understanding of the importance of different experimental setups, synthesis conditions, or the substrate's properties (for instance, the variation

of graphene growth with the position of the Cu foil within the furnace, or that the supplier-stated bulk purity is not representative of the surface purity of Cu foils). Other contributions consist of a new, or expanded theory (for instance, the orientation of large-scale domains being dictated by the preferential orientation of nanoscale domains). The impact of some contributions will largely depend on future research to expand upon an initial positive finding (for instance, the influence of contamination particles in dictating nucleation sites on Pt foil, the use of $FeNO_3$ cleaning of Cu foils, or the growth of boron-doped graphene using triethylborane in hexane). While all these contributions have been classified as 'minor', in fact their full significance may be realised as time goes by and research continues to progress.

Shifting attention to the benefits my research contribution provides to my immediate research group, while maybe not necessarily as novel to the scientific community at large, nonetheless had a significant impact. My work on designing, assembling and testing LPCVD and APCVD apparatus capable of gaseous and liquid precursors for production of pure and doped graphene has spawned an entire new body of investigations within the Nanomaterials by Design research group. Research using these apparatus now encompasses graphene, two-dimensional chalcogenides, and hexagonal boron nitride, and is being conducted by three DPhil students and two Part II students. My determination of synthesis parameters and experimental setups for the growth of graphene by LPCVD and APCVD has provided the initial conditions for all future production of graphene within the group. A number of collaborations which I helped establish have also continued including with Renishaw PLC, Department of Physics at University of Oxford, Department of Materials Science and Engineering at University of Ioannina, Ernst Ruska Centre for Microscopy and Spectroscopy with Electrons at Juelich, and the National Physical Laboratory

11.2 Outlook and future work

There are a number of areas that would yield interesting discoveries and valuable insight through further investigations in the future. While some proposed future work aims to clarify a postulated theory or current research question, in other cases future work is proposed for establishment as an entirely new area for detailed investigations due to potential of promising initial results.

11.2.1 Influence of Cu crystallographic orientations on geometry of domain boundaries, and the electrical and mechanical properties of graphene

Based on the findings in Chapter 7 on the influence of the Cu crystallographic orientations on the orientation of hexagonal APCVD graphene domains, I expect that Cu crystallographic orientations will also influence the nature of graphene domain boundaries, and hence the electrical and mechanical properties of large-area graphene. HRTEM analysis of APCVD graphene domain boundaries grown on different Cu crystallographic orientations would confirm my proposed growth model whereby that the orientation of nanoscale graphene domains can be controlled by the substrate. Electrical and mechanical characterisation of merged APCVD graphene domains would provide valuable insight into this hypothesis and verify my proposal that specific Cu crystallographic orientations can be used to improve the properties of polycrystalline graphene sheets. As a consequence I have already started investigations into the growth of large-areas of aligned hexagonal APCVD graphene on Cu single crystals, namely Cu(111), Cu(101) and Cu(001). Electrical characterisation through fabrication of FETS, and mechanical characterisation through AFM nanoindentation is planned, and will be correlated with the orientation of domains and nucleation density. This future work therefore aims to directly relate the properties of large-area CVD graphene with the synthesis conditions and Cu crystallographic orientations.

11.2.2 Controlling the Cu substrate's properties aiming for CVD growth on an optimised Cu substrate

Given the influence of the substrate's properties on growth of CVD graphene, demonstrated in Chapter 7 and Chapter 8, effort should be directed towards controlling the substrate's properties, with the aim of producing an ideal, optimised Cu substrate. This may be possible by (i) direct synthesis of the substrate, (ii) further purification or treatment of commercially available Cu foils, or (iii) use of single-crystal substrates. Based on the findings in Chapter 8.2.2.3, I suggest that efforts should be directed to improving the properties of 99.9999 % Alfa Aesar Cu foil, which already demonstrates a low concentration of surface contaminations and low surface roughness. The promising initial demonstration in Chapter 8.2.3 that electropolishing and $FeNO_3$ cleaning can reduce the nucleation density could also receive further attention.

11.2.3 Confirming the nature and influence of metal contamination particles

My experiments demonstrate that CH_3COOH cleaning reduced the concentration of metal contamination particles, specifically CaO, and this resulted in a decrease in the nucleation density and an increase in the growth rate of APCVD graphene domains. I postulated this occurred because metal nanoparticles play a dual role by (i) acting as sites for preferential nucleation, and (ii) etching graphene domains through a reaction that yields CO and CaC_2. By depositing controlled and varying quantities of CaO nanoparticles on an ideal Cu foil (for instance, the relatively clean 99.9999 %) their influence on the graphene nucleation density could be systematically studied to validate the particles as nucleation centres. Investigations aimed at detecting CaC_2/CO, either through in-situ XPS or mass spectrometry, would also be beneficial to confirm my proposed reaction for how the particles influence graphene growth. As the concentration of these species may be at the detection limit of both XPS and mass spectrometry the results would need careful interpretation.

11.2.4 Influence of surface features and contamination particles on growth and nucleation of graphene on Pt foils

Future studies to investigate the nucleation and growth of polycrystalline graphene domains on Pt foils would be useful to clarify my proposed growth model on this weakly interacting substrate. I postulated that surface features, including step edges and kinks, may play a crucial role in triggering the formation of polycrystalline domains. These aspects could be investigated further by conducting in-situ STM and LEEM analysis of graphene growth on Pt. As such measurements require specialised equipment, by alternative investigations into the growth on different Pt foils and adopting polishing and cleaning treatments the influence of these surface features could be inferred. Additionally, the nature of nucleation sites on Pt is still not known in detail, however, the low density of nucleation sites suggests these sites correspond with specific surface features or contamination particles. Initial investigations presented in Chapter 9.2 demonstrated that the location of nucleation sites of APCVD graphene domains corresponded with metallic contamination particles and specific locations on the Pt surface. Additional studies investigating the influence of the surface topography and contamination particles would be beneficial to demonstrate to what extent the location of nucleation sites can be controlled. Furthermore, given the influence of the Cu substrate's properties on graphene growth, future investigations are suggested into the influence of the Pt foil's properties on graphene growth. EBSD analysis of Pt crystallographic orientations and correlation with polycrystalline APCVD graphene domains is suggested as an interesting initial experiment, while analysis of the chemical purity of the foils, and cleaning treatments, may be beneficial to reduce and control the graphene nucleation sites.

11.2.5 APCVD growth on silicidated platinum and eutectic substrates

As discussed in Chapter 9.1.1, and in contrast to work by L. Gao *et al.*[176], large-area, single-crystal hexagonal APCVD graphene domains did not form on pristine Pt foil even with optimised and systematically varied CH_4:H_2 flow rate ratios. Additionally, the observation of a reaction between quartz and Pt that promotes hexagonal

domains suggests that a silicon or platinum silicide surface layer may be advantageous for growth of large-area single-crystal hexagonal graphene. I proposed that analysis to confirm the chemical composition of this surface was a priority and that subsequently the controlled production of thin silicon or platinum silicide surface layers on Pt foils was a future research priority that was anticipated to yield groundbreaking results. Indeed, Mr Vitaly Babenko has investigated this hypothesis further by successfully and reproducibly synthesising few-millimetre single-crystal hexagonal graphene domains on silicidated Pt foils[322]. High temperature synthesis on silicidated Pt produces a similar increase in growth rate as demonstrated in Chapter 9.1.2, yielding one of the highest recorded growth rates. This work opens the possibility of an entirely new class of eutectic substrates for CVD of graphene.

11.2.6 Influence of synthesis conditions on the nitrogen-containing active species, the dopant bonding configuration, and electronic properties of nitrogen-doped graphene

My experiments demonstrated that the synthesis temperature influences the dopant concentration of nitrogen-doped graphene. I postulated that incorporation of N in nitrogen-doped graphene relies on a reaction between NH_3 and defects in the graphene lattice, which increase in concentration at lower synthesis temperatures for CVD growth using CH_4. To clarify this claim, growth could be conducted with cyclic addition of NH_3 (*ie.* 1 minute with CH_4 and NH_3, 1 minute with pure CH_4, repeated). If doping arises due to a reaction between NH_3 and defects than the doping will be uniform across the domain, whereas if doping occurs by a reaction at the domain edge than the dopant concentration would vary with the growth front of a domain. Two-dimensional Raman mapping of the D peak could be used to investigation the spatial variation of doping in these samples. Alternatively, investigations into influence of the defect concentration on the dopant concentration could clarify this growth mechanism. Kidambi et al[189] have demonstrated that CVD growth using C_6H_6 produces similar quality graphene between 900 ˚C and 1000 ˚C (and therefore similar defect concentrations). Based on my proposed growth model, and in contrast to my observations using CH_4, I predict that nitrogen-doped graphene synthesised using C_6H_6 would decrease in dopant

concentration at lower synthesis temperatures, as the defect concentration will be constant but reaction rates will decrease with temperature. Additionally, future studies into the influence of synthesis conditions on the bonding configuration and electronic properties of nitrogen-doped graphene would be beneficial. XPS analysis of nitrogen-doped graphene grown at various synthesis temperatures and with various precursors could be compared with electronic properties determined by fabrication of FETs to elucidate the optimum conditions for controlled doping with preference for specific dopant configurations. Studies into the growth of nitrogen-doped graphene on Pt foils also have merit to exclude the potential for a reaction between NH_3 and the Cu substrate.

11.2.7 Boron-doped graphene and LPCVD growth using liquid precursors

The promising initial demonstration in Chapter 10.2 that boron-doped graphene can be synthesised using 1 M triethylborane in hexane is an ideal situation for further investigations and establishment as a few area of research. Firstly, I suggest that XPS analysis should be conducted to confirm that boron is indeed acting as the dopant. Following this, systematic investigations into the influence of the synthesis conditions would assist with increasing and controlling boron doping, drawing on knowledge obtained with nitrogen-doped graphene as presented in Chapter 10.1. Owing to the development of a LPCVD apparatus capable of using liquid precursors, Chapter 10.2.1, future investigations are also possible into the synthesis of pure and hetero-atom doped LPCVD graphene using any suitable liquid precursor. Furthermore, future studies need not be limited to production of graphene, with synthesis into the growth of hexagonal boron nitride already being conducted using this apparatus.

List of References

1. Murdock, A. T.; Koos, A.; Britton, T. B.; Houben, L.; Batten, T.; Zhang, T.; Wilkinson, A. J.; Dunin-Borkowski, R. E.; Lekka, C. E.; Grobert, N. *ACS Nano* 2013, 7, (2), 1351-1359.

2. Koós, A. A.; Murdock, A. T.; Nemes-Incze, P.; Nicholls, R. J.; Pollard, A. J.; Spencer, S. J.; Shard, A. G.; Roy, D.; Biró, L. P.; Grobert, N. *Phys. Chem. Chem. Phys.* 2014.

3. Nicholls, R. J.; Murdock, A. T.; Tsang, J.; Britton, J.; Pennycook, T. J.; Koós, A.; Nellist, P. D.; Grobert, N.; Yates, J. R. *ACS Nano* 2013, 7, (8), 7145-50.

4. Kertész, K.; Koós, A. A.; Murdock, A. T.; Vértesy, Z.; Nemes-Incze, P.; Szabó, P. J.; Horváth, Z. E.; Tapasztó, L.; Hwang, C.; Grobert, N.; Biró, L. P. *Applied Physics Letters* 2012, 100, (21), 213103.

5. Grobert, N.; Murdock, A. T.; Koos, A. A. Producing two-dimensional nanomaterial (graphene) by chemical vapor deposition, used in e.g. display, comprises contacting substrate with flow of hydrogen and flow of precursor such that precursor forms material on surface of substrate. WO2013144640-A1, WO2013144640-A1 03 Oct 2013 C30B-025/16 201367, 2013.

6. Soldano, C.; Mahmood, A.; Dujardin, E. *Carbon* 2010, 48, (8), 2127-2150.

7. Kim, K.; Coh, S.; Kisielowski, C.; Crommie, M. F.; Louie, S. G.; Cohen, M. L.; Zettl, A. *Nat. Commun.* 2013, 4, 2723.

8. Robertson, A. W.; Warner, J. H. *Nanoscale* 2013, 5, (10), 4079-93.

9. Goerbig, M. O. *arXiv.org, e-Print Arch., Condens. Matter* 2010, cond-mat.mes-hall.

10. Castro Neto, A. H. C. *Mater. Today* 2010, 13, (3), 12-17.

11. Geim, A. K.; Novoselov, K. S. *Nat. Mater.* 2007, 6, (3), 183-191.

12. Novoselov, K. S.; Geim, A. K.; Morozov, S. V.; Jiang, D.; Zhang, Y.; Dubonos, S.; Grigorieva, I. V.; Firsov, A. *Science* 2004, 306, (5696), 666-669.

13. Zhang, Y.; Tang, T.-T.; Girit, C. l.; Hao, Z.; Martin, M. C.; Zettl, A.; Crommie, M. F.; Shen, Y. R.; Wang, F. *Nature* 2009, 459, (7248), 820-823.

14. Mak, K. F.; Shan, J.; Heinz, T. F. *Phys. Rev. Lett.* 2010, 104, (17), 176404.

15. Bao, W.; Jing, L.; Jr, J. V.; Lee, Y.; Liu, G.; Tran, D.; Standley, B.; Aykol, M.; Cronin, S. B.; Smirnov, D.; Koshino, M.; McCann, E.; Bockrath, M.; Lau, C. N. *Nature Physics* 2011, 7, (12), 948.

16. Brown, L.; Hovden, R.; Huang, P.; Wojcik, M.; Muller, D. A.; Park, J. *Nano Letters* 2012, 12, 1609-1615.

17. Koshino, M. *New Journal of Physics* 2013, 15, 015010.

18. Zhu, Z.; Hatori, H.; Wang, S.; Lu, G. *J. Phys. Chem. B* 2005, 109, (35), 16744-16749.

19. Terrones, M.; Ajayan, P. M.; Banhart, F.; Blase, X.; Carroll, D.; Charlier, J.-C.; Czerw, R.; Foley, B.; Grobert, N.; Kamalakaran, R.; Kohler-Redlich, P.; Ruhle, M.; Seeger, T.; Terrones, H. *Appl. Phys. A: Mater. Sci. Process.* 2002, 74, (3), 355-361.

20. Terrones, M.; Jorio, A.; Endo, M.; Rao, A. M.; Kim, Y. A.; Hayashi, T.; Terrones, H.; Charlier, J.-C.; Dresselhaus, G.; Dresselhaus, M. S. *Mater. Today* 2004.

21. Stephan, O.; Ajayan, P. M.; Colliex, C.; Redlich, P.; Lambert, J. M.; Bernier, P.; Lefin, P. *Science* 1994, 266, (5191), 1683-1685.

22. Wei, D.; Liu, Y. *Advanced Materials* 2010, 22, (30), 3225-41.

23. Rao, C. N. R.; Sood, A. K.; Subrahmanyam, K. S.; Govindaraj, A. *Angew. Chem., Int. Ed. Engl.* 2009, 48, (42), 7752-77.

24. Wei, D.; Liu, Y.; Wang, Y.; Zhang, H.; Huang, L.; Yu, G. *Nano Lett.* 2009, 9, (5), 1752-1758.

25. Usachov, D.; Vilkov, O.; Grüneis, A.; Haberer, D.; Fedorov, A. V.; Adamchuk, V. K.; Preobrajenski, A. B.; Dudin, P.; Barinov, A.; Oehzelt, M.; Laubschat, C.; Vyalikh, D. V. *Nano Lett.* 2011.

26. Novoselov, K. S.; Geim, A. K.; Morozov, S. V.; Jiang, D.; Grigorieva, I. V.; Dubonos, S.; Firsov, A. *Nature* 2005.

27. Zhang, Y.; Tan, Y.-W.; Stormer, H. L.; Kim, P. *Nature* 2005, 438, (7065), 201-204.

28. Mayorov, A. S.; Gorbachev, R. V.; Morozov, S. V.; Britnell, L.; Jalil, R.; Ponomarenko, L. A.; Blake, P.; Novoselov, K. S.; Watanabe, K.; Taniguchi, T.; Geim, A. K. *Nano Letters* 2011, 11, (6), 2396-9.

29. Castro Neto, A. H. C.; Guinea, F.; Peres, N. M. R.; Novoselov, K. S.; Geim, A. K. *Rev. Mod. Phys* 2009, 81, (1), 109-162.

30. Bolotin, K. I.; Sikes, K. J.; Jiang, Z.; Klima, M.; Fudenberg, G.; Hone, J.; Kim, P.; Stormer, H. L. *Solid State Commun.* 2008, 146, (9-10), 351-355.

31. Chen, J.-H.; Jang, C.; Xiao, S.; Ishigami, M.; Fuhrer, M. S. *Nat. Nanotechnol.* 2008, 3, (4), 206-9.

32. Du, X.; Skachko, I.; Barker, A.; Andrei, E. Y. *Nat. Nanotechnol.* 2008, 3, (8), 491-5.

33. Baringhaus, J.; Ruan, M.; Edler, F.; Tejeda, A.; Sicot, M.; Taleb-Ibrahimi, A.; Li, A.-P.; Jiang, Z.; Conrad, E. H.; Berger, C.; Tegenkamp, C.; de Heer, W. A. *Nature* 2014, 506, (7488), 349-54.

34. Moser, J.; Barreiro, A.; Bachtold, A. *Appl. Phys. Lett.* 2007, 91, 163513.

35. Novoselov, K. S.; Fal'ko, V. I.; Colombo, L.; Gellert, P. R.; Schwab, M. G.; Kim, K. *Nature* 2012, 490, (7419), 192-200.

36. Nair, R. R.; Blake, P.; Grigorenko, A. N.; Novoselov, K. S.; Booth, T. J.; Stauber, T.; Peres, N. M. R.; Geim, A. K. *Science* 2008, 320, (5881), 1308-1308.

37. Bonaccorso, F.; Sun, Z.; Hasan, T.; Ferrari, A. C. *Nat. Photonics* 2010, 4, (9), 611.

38. Lee, C.; Wei, X.; Kysar, J. W.; Hone, J. *Science* 2008, 321, (5887), 385-388.

39. The 2010 Nobel Prize in Physics- Advanced Information. www.nobelprize.org/nobel_prizes/physics/laureates/2010/advanced.html (2 April 2014),

40. Turner, A. H.; Makovicky, P. J.; Norell, M. A. *Science* 2007, 317, (5845), 1721.

41. Balandin, A. A.; Ghosh, S.; Bao, W.; Calizo, I.; Teweldebrhan, D.; Miao, F.; Lau, C. N. *Nano Lett.* 2008, 8, (3), 902-907.

42. Cai, W.; Moore, A. L.; Zhu, Y.; Li, X.; Chen, S.; Shi, L.; Ruoff, R. S. *Nano Lett.* 2010, 10, (5), 1645-51.

43. Balandin, A. A. *Nat. Mater.* 2011, 10, (8), 569-81.

44. Fuhrer, M. S.; Lau, C. N.; MacDonald, A. H. *MRS Bull.* 2010, 35, (4), 289-295.

45. Seol, J.; Jo, I.; Moore, A. L.; Lindsay, L.; Aitken, Z. H.; Pettes, M.; Li, X.; Yao, Z.; Huang, R.; Broido, D.; Mingo, N.; Ruoff, R. S.; Shi, L. *Science* 2010, 328, (5975), 213.

46. Pop, E.; Varshney, V.; Roy, A. K. *MRS Bull.* 2012, 37, 1273-1281.

47. Zheng, B.; Hermet, P.; Henrard, L. *ACS Nano* 2010.

48. Guo, B.; Liu, Q.; Chen, E.; Zhu, H.; Fang, L.; Gong, J. R. *Nano Lett.* 2010, 10, (12), 4975-4980.

49. Guo, B.; Fang, L.; Zhang, B.; Gong, J. R. *Insciences Journal* 2011, 1, (2), 80-89.

50. Wang, X.; Li, X.; Zhang, L.; Yoon, Y.; Weber, P. K.; Wang, H.; Guo, J.; Dai, H. *Science* 2009, 324, (5928), 768-771.

51. Calandra, M.; Mauri, F. *Phys. Rev. B* 2007, 76, (16), 161406.

52. Martins, T. B.; Miwa, R. H.; da Silva, A. J. R.; Fazzio, A. *Phys. Rev. Lett.* 2007, 98, (19), 196803.

53. Dai, J.; Yuan, J.; Giannozzi, P. *Appl. Phys. Lett.* 2009, 95, (23), 232105.

54. Panchakarla, L. S.; Subrahmanyam, K. S.; Saha, S. K.; Govindaraj, A.; Krishnamurthy, H. R.; Waghmare, U. V.; Rao, C. N. R. *Adv. Mater.* 2009, 21, (46), 4726-+.

55. Qu, L.; Liu, Y.; Baek, J.-B.; Dai, L. *ACS Nano* 2010.

56. Guillaume, S. O.; Zheng, B.; Charlier, J. C.; Henrard, L. *Phys. Rev. B* 2012, 85, (3), 035444.

57. Luo, Z.; Lim, S.; Tian, Z.; Shang, J.; Lai, L.; Macdonald, B.; Fu, C.; Shen, Z.; Yu, T.; Lin, J. *J. Mater. Chem.* 2011, 21, (22), 8038-8044.

58. Yan, Q.; Huang, B.; Yu, J.; Zheng, F.; Zang, J.; Wu, J.; Gu, B.-L.; Liu, F.; Duan, W. *Nano Lett.* 2007, 7, (6), 1469-1473.

59. Sun, Z.; Yan, Z.; Yao, J.; Beitler, E.; Zhu, Y.; Tour, J. M. *Nature* 2010, 468, (7323), 549-552.

60. Dai, J.; Yuan, J. *Phys. Rev. B* 2010, 81, (16), 165414.

61. Wang, H.; Maiyalagan, T.; Wang, X. *ACS Catalysis* 2012, 2, 781-794.

62. Lin, Y.-m.; Dimitrakopoulos, C.; Jenkins, K. A.; Farmer, D. B.; Chiu, H.-Y.; Grill, A.; Avouris, P. *Science* 2010, 327, (5966), 662-662.

63. Cheng, R.; Bai, J.; Liao, L.; Zhou, H.; Chen, Y.; Liu, L.; Lin, Y.-C.; Jiang, S.; Huang, Y.; Duan, X. *Proceedings of the National Academy of Sciences* 2012, 109, (29), 11588-92.

64. Sun, Z.; Hasan, T.; Torrisi, F.; Popa, D.; Privitera, G.; Wang, F.; Bonaccorso, F.; Basko, D. M.; Ferrari, A. C. *ACS Nano* 2010, 4, (2), 803-10.

65. Kumar, A.; Zhou, C. *ACS Nano* 2010, 4, (1), 11-4.

66. Wu, J.; Becerril, H. A.; Bao, Z.; Liu, Z.; Chen, Y.; Peumans, P. *Appl. Phys. Lett.* 2008, 92, (26), 263302.

67. Blake, P.; Brimicombe, P. D.; Nair, R. R.; Booth, T. J.; Jiang, D.; Schedin, F.; Ponomarenko, L. A.; Morozov, S. V.; Gleeson, H. F.; Hill, E. W.; Geim, A. K.; Novoselov, K. S. *Nano Lett.* 2008, 8, (6), 1704-1708.

68. Bae, S.; Kim, H.; Lee, Y.; Xu, X.; Park, J.-S.; Zheng, Y.; Balakrishnan, J.; Lei, T.; Ri Kim, H.; Song, Y. I.; Kim, Y.-J.; Kim, K. S.; Ozyilmaz, B.; Ahn, J.-H.; Hong, B. H.; Iijima, S. *Nat. Nanotechnol.* 2010, 5, 574-578.

69. Kim, K. S.; Zhao, Y.; Jang, H.; Lee, S. Y.; Kim, J. M.; Kim, K. S.; Ahn, J.-H.; Kim, P.; Choi, J.-Y.; Hong, B. H. *Nature* 2009, 457, (7230), 706-710.

70. Kim, B. J.; Jang, H.; Lee, S.-K.; Hong, B. H.; Ahn, J.-H.; Cho, J. H. *Nano Lett.* 2010.

71. Xia, F.; Mueller, T.; Lin, Y.-m.; Valdes-Garcia, A.; Avouris, P. *Nat. Nanotechnol.* 2009, 4, (12), 839-843.

72. Liu, M.; Zhang, X. *Nat. Photonics* 2013, 7, (11), 851.

73. Liu, J.; Xue, Y.; Zhang, M.; Dai, L. *MRS Bull.* 2012, 37, 1265-1272.

74. El-Kady, M. F.; Kaner, R. B. *Nat. Commun.* 2013, 4, 1475.

75. Chen, S.; Brown, L.; Levendorf, M. P.; Cai, W.; Ju, S.-Y.; Edgeworth, J.; Li, X.; Magnuson, C. W.; Velamakanni, A.; Piner, R. D.; Kang, J.; Park, J.; Ruoff, R. S. *ACS Nano* 2011, 5, (2), 1321-1327.

76. Meyer, J. C.; Girit, C. O.; Crommie, M. F.; Zettl, A. *Nature* 2008, 454, (7202), 319-322.

77. Regan, W.; Alem, N.; Alemán, B. n.; Geng, B.; Girit, C. l.; Maserati, L.; Wang, F.; Crommie, M. F.; Zettl, A. *Appl. Phys. Lett.* 2010, 96, (11), 113102.

78. Ling, X.; Xie, L.; Fang, Y.; Xu, H.; Zhang, H.; Kong, J.; Dresselhaus, M. S.; Zhang, J.; Liu, Z. *Nano Lett.* 2010, 10, (2), 553-561.

79. N'Diaye, A.; Bleikamp, S.; Feibelman, P. J.; Michely, T. *Phys. Rev. Lett.* 2006, 97, (21), 215501.

80. Gall', N.; Rut'kov, E.; Tontegode, A. *Phys. Solid State* 2004, 46, (2), 371-377.

81. Schedin, F.; Geim, A. K.; Morozov, S. V.; Hill, E. W.; Blake, P.; Katsnelson, M. I.; Novoselov, K. S. *Nat. Mater.* 2007, 6, (9), 652-655.

82. Stankovich, S.; Dikin, D. A.; Dommett, G. H. B.; Kohlhaas, K. A.; Zimney, E. J.; Stach, E. A.; Piner, R. D.; Nguyen, S. T.; Ruoff, R. S. *Nature* 2006, 442, (7100), 282-286.

83. Young, R. J.; Kinloch, I. A.; Gong, L.; Novoselov, K. S. *Composites Science and Technology* 2012, 72, (12), 1459-1476.

84. Kim, Y.; Lee, J.; Yeom, M. S.; Shin, J. W.; Kim, H.; Cui, Y.; Kysar, J. W.; Hone, J.; Jung, Y.; Jeon, S.; Han, S. M. *Nat. Commun.* 2013, 4, 2114.

85. Gomez, H.; Ram, M. K.; Alvi, F.; Villalba, P.; Stefanakos, E.; Kumar, A. *Journal of Power Sources* 2011, 196, (8), 4102-4108.

86. Zhao, L.; He, R.; Rim, K. T.; Schiros, T.; Kim, K. S.; Zhou, H.; Gutierrez, C.; Chockalingam, S. P.; Arguello, C. J.; Palova, L.; Nordlund, D.; Hybertsen, M. S.; Reichman, D. R.; Heinz, T. F.; Kim, P.; Pinczuk, A.; Flynn, G. W.; Pasupathy, A. N. *Science* 2011, 333, (6045), 999-1003.

87. Wang, Y.; Shao, Y.; Matson, D. W.; Li, J.; Lin, Y. *ACS Nano* 2010.

88. Reddy, A. L. M.; Srivastava, A.; Gowda, S. R.; Gullapalli, H.; Dubey, M.; Ajayan, P. M. *ACS Nano* 2010, 4, (11), 6337-6342.

89. Jeong, H. M.; Lee, J. W.; Shin, W. H.; Choi, Y. J.; Shin, H. J.; Kang, J. K.; Choi, J. W. *Nano Lett* 2011, 11, (6), 2472-7.

90. Obraztsova, A. N. *Nat. Nanotechnol.* 2009, 4, (4), 212-3.

91. Park, S.; Ruoff, R. S. *Nat. Nanotechnol.* 2009, 4, (4), 217-224.

92. Choi, W.; Lahiri, I.; Seelaboyina, R.; Kang, Y. S. *Crit. Rev. Solid State Mater. Sci.* 2010, 35, (1), 52-71.

93. Graphene Industries. http://grapheneindustries.com (29 April 2009),

94. Reina, A.; Son, H.; Jiao, L.; Fan, B.; Dresselhaus, M. S.; Liu, Z.; Kong, J. *J. Phys. Chem. C* 2008, 112, 17741-17744.

95. Eda, G.; Fanchini, G.; Chhowalla, M. *Nat. Nanotechnol.* 2008, 3, (5), 270-274.

96. Li, X.; Zhang, G.; Bai, X.; Sun, X.; Wang, X.; Wang, E.; Dai, H. *Nat. Nanotechnol.* 2008, 3, (9), 538-542.

97. Hernandez, Y.; Nicolosi, V.; Lotya, M.; Blighe, F. M.; Sun, Z.; De, S.; McGovern, I. T.; Holland, B.; Byrne, M.; Gun'ko, Y. K.; Boland, J. J.; Niraj, P.; Duesberg, G. S.; Krishnamurthy, S.; Goodhue, R.; Hutchison, J.; Scardaci, V.; Ferrari, A. C.; Coleman, J. N. *Nat. Nanotechnol.* 2008, 3, (9), 563-568.

98. Choucair, M.; Thordarson, P.; Stride, J. *Nat. Nanotechnol.* 2008, 4, (1), 30-33.

99. Hummers, W.; Offeman, R. *J. Am. Chem. Soc.* 1958, 80, (6), 1339-1339.

100. Stankovich, S.; Dikin, D. A.; Piner, R. D.; Kohlhaas, K. A.; Kleinhammes, A.; Jia, Y.; Wu, Y.; Nguyen, S. T.; Ruoff, R. S. *Carbon* 2007, 45, (7), 1558-1565.

101. Berger, C.; Song, Z.; Li, T.; Li, X.; Ogbazghi, A.; Feng, R.; Dai, Z.; Marchenkov, A. N.; Conrad, E. H.; First, P. N.; De Heer, W. A. *J. Phys. Chem. B* 2004, 108, (52), 19912-19916.

102. **Berger, C.; Song, Z.; Li, X.; Wu, X.; Brown, N.; Naud, C.; Mayou, D.; Li, T.; Hass, J.; Marchenkov, A. N.; Conrad, E. H.; First, P. N.; De Heer, W. A.** ***Science*** **2006, 312, (5777), 1191-1196.**

103. **Ohta, T.; Bostwick, A.; Seyller, T.; Horn, K.; Rotenberg, E.** ***Science*** **2006, 313, (5789), 951-954.**

104. **Emtsev, K. V.; Bostwick, A.; Horn, K.; Jobst, J.; Kellogg, G. L.; Ley, L.; McChesney, J. L.; Ohta, T.; Reshanov, S. A.; Roehrl, J.; Rotenberg, E.; Schmid, A. K.; Waldmann, D.; Weber, H. B.; Seyller, T.** ***Nat. Mater.*** **2009, 8, (3), 203-207.**

105. **Shelton, J. C.; Patil, H. R.; Blakely, J. M.** ***Surf. Sci.*** **1974, 43, (2), 493-520.**

106. **Marchini, S.; Guenther, S.; Wintterlin, J.** ***Phys. Rev. B*** **2007, 76, (7), 075429.**

107. **Zhang, C.; Fu, L.; Liu, N.; Liu, M.; Wang, Y.; Liu, Z.** ***Adv. Mater.*** **2011, 23, (8), 1020-1024.**

108. **Yu, Q.; Lian, J.; Siriponglert, S.; Li, H.; Chen, Y. P.; Pei, S. S. S.** ***Appl. Phys. Lett.*** **2008, 93, (11), 113103.**

109. **Gamo, Y.; Nagashima, A.; Wakabayashi, M.; Terai, M.; Oshima, C.** ***Surf. Sci.*** **1997, 374, (1-3), 61-64.**

110. **Gall', N.; Rut'kov, E.; Tontegode, A.** ***Int. J. Mod. Phys. B*** **1997, 11, (16), 1865-1911.**

111. **Obraztsova, A. N.; Tyurnina, A. V.; Zolotukhin, A. A.** ***Carbon*** **2007, 45, (10), 2017-2021.**

112. **Makarenko, I.; Titkov, A.; Waqar, Z.; Dumas, P.; Rut'kov, E.; Gall', N.** ***Phys. Solid State*** **2007, 49, (2), 371-376.**

113. **Land, T.; Michely, T.; Behm, R.; Hemminger, J.; Comsa, G.** ***Surf. Sci.*** **1992, 264, (3), 261-270.**

114. **Vaari, J.; Lahtinen, J.; Hautojärvi, P.** ***Catal. Lett.*** **1997, 44, (1), 43-49.**

115. **Sasaki, M.; Yamada, Y.; Ogiwara, Y.; Yagyu, S.; Yamamoto, S.** ***Phys. Rev. B*** **2000, 61, (23), 15653-15656.**

116. **Starr, D.; Pazhetnov, E.; Stadnichenko, A.; Boronin, A.; Shaikhutdinov, S.** ***Surf. Sci.*** **2006, 600, (13), 2688-2695.**

117. **Wintterlin, J.; Bocquet, M.-L.** ***Surf. Sci.*** **2009, 603, (10-12), 1841-1852.**

118. **Geim, A. K.** ***Science*** **2009, 324, (5934), 1530-1534.**

119. **Meyer, J. C.; Kurasch, S.; Park, H. J.; Skakalova, V.; Künzel, D.; GroÃ, A.; Chuvilin, A.; Algara-Siller, G.; Roth, S.; Iwasaki, T.; Starke, U.; Smet, J. H.; Kaiser, U.** ***arXiv.org, e-Print Arch., Condens. Matter*** **2010, cond-mat.mtrl-sci.**

120. **MTI Corp. www.mtixtl.com/tubefurnaceforgraphene.aspx (2 April 2014),**

121. **Kim, H.; Mattevi, C.; Calvo, M. R.; Oberg, J. C.; Artiglia, L.; Agnoli, S.; Hirjibehedin, C. F.; Chhowalla, M.; Saiz, E.** ***ACS Nano*** **2012, 6, (4), 3614-23.**

122. **Ago, H.; Ogawa, Y.; Tsuji, M.; Mizuno, S.; Hibino, H.** ***J. Phys. Chem. Lett.*** **2012, 3, 228-2236.**

123. **Robertson, J.** ***J. Mater. Chem.*** **2012, 22, (37), 19858.**

124. **Oshima, C.; Nagashima, A.** ***J. Phys.: Condens. Matter*** **1997, 9, 1-20.**

125. **Eizenberg, M.; Blakely, J. M.** ***Surf. Sci.*** **1979, 82, (1), 228-236.**

126. **Lang, B.** ***Surf. Sci.*** **1975, 53, (DEC), 317-329.**

127. **Coraux, J.; N'Diaye, A. T.; Busse, C.; Michely, T.** ***Nano Lett.*** **2008, 8, (2), 565-570.**

128. **N'Diaye, A. T.; Coraux, J.; Plasa, T. N.; Busse, C.; Michely, T.** ***New J. Phys.*** **2008, 10, 043033.**

129. **van Gastei, R.; N'Diaye, A. T.; Wall, D.; Coraux, J.; Busse, C.; Buckanie, N.; zu Heringdorf, F.-J. M.; von Hoegen, M. H.; Michely, T.; Poelsema, B.** ***Appl. Phys. Lett.*** **2009, 95, (12), 121901.**

130. Coraux, J.; N'Diaye, A. T.; Engler, M.; Busse, C.; Wall, D.; Buckanie, N.; Heringdorf, F.-J. M. z.; van Gastei, R.; Poelsema, B.; Michely, T. *New J. Phys.* 2009, 11, 023006.

131. Usachov, D.; Dobrotvorskii, A. M.; Varykhalov, A.; Rader, O.; Gudat, W.; Shikin, A. M.; Adamchuk, V. K. *Phys. Rev. B* 2008, 78, (8), 085403.

132. Ueta, H.; Saida, M.; Nakai, C.; Yamada, Y.; Sasaki, M.; Yamamoto, S. *Surf. Sci.* 2004, 560, (1-3), 183-190.

133. Pan, Y.; Shi, D.-X.; Gao, H.-j. *Chin. Phys.* 2007, 16, (11), 3151-3153.

134. Vazquez de Parga, A. L.; Calleja, F.; Borca, B.; Passeggi Jr, M. C. G.; Hinarejos, J. J.; Guinea, F.; Miranda, R. *Phys. Rev. Lett.* 2008, 100, (5), 56807.

135. Sutter, P.; Flege, J.; Sutter, E. A. *Nat. Mater.* 2008, 7, (5), 406-411.

136. Sutter, E. A.; Albrecht, P.; Sutter, P. *Appl. Phys. Lett.* 2009, 95, (13), 133109.

137. Pan, Y.; Zhang, H.; Shi, D.-X.; Sun, J.; Du, S.; Liu, F.; Gao, H.-j. *Adv. Mater.* 2009, 21, (27), 2777-+.

138. Cui Yi, Y.; Fu Qiang, Q.; Zhang, H.; Tan DaLi, D.; Bao XinHe, X. *J. Phys. Chem. C* 2009, 113, (47), 20365-20370.

139. Reina, A.; Jia, X.; Ho, J.; Nezich, D.; Son, H.; Bulovic, V.; Dresselhaus, M. S.; Kong, J. *Nano Lett.* 2009, 9, (1), 30-35.

140. Cao, H.; Yu, Q.; Pandey, D.; Zemlyanov, D.; Colby, R.; Childres, I.; Drachev, V.; Stach, E. A.; Lian, J.; Li, H.; Pei, S. S. S.; Chen, Y. P. *arXiv.org, e-Print Arch., Condens. Matter* 2009.

141. Reina, A.; Thiele, S.; Jia, X.; Bhaviripudi, S.; Dresselhaus, M. S.; Schaefer, J. A.; Kong, J. *Nano Res.* 2009, 2, (6), 509-516.

142. Thiele, S.; Reina, A.; Healey, P.; Kedzierski, J.; Wyatt, P.; Hsu, P.-L.; Keast, C.; Schaefer, J. A.; Kong, J. *Nanotechnology* 2010, 21, (1), 015601.

143. Weatherup, R. S.; Dlubak, B.; Hofmann, S. *ACS Nano* 2012, 6, (11), 9996-10003.

144. Li, X.; Cai, W.; An, J.; Kim, S.; Nah, J.; Yang, D.; Piner, R. D.; Velamakanni, A.; Jung, I.; Tutuc, E.; Banerjee, S. K.; Colombo, L.; Ruoff, R. S. *Science* 2009, 324, (5932), 1312-1314.

145. Li, X.; Cai, W.; Colombo, L.; Ruoff, R. S. *Nano Lett.* 2009, 9, (12), 4268-72.

146. Li, X.; Zhu, Y.; Cai, W.; Borysiak, M.; Han, B.; Chen, D.; Piner, R. D.; Colombo, L.; Ruoff, R. S. *Nano Lett.* 2009, 9, (12), 4359-4363.

147. Cao, H.; Jauregui, L. A.; Tian, J.; Liu, Z.; Jalilian, R.; Benjamin, D. K.; Jiang, Z.; Bao, J.; Pei, S. S. S.; Chen, Y. P. *arXiv.org, e-Print Arch., Condens. Matter* 2009, cond-mat.mes-hall.

148. Levendorf, M. P.; Ruiz-Vargas, C. S.; Garg, S.; Park, J. *Nano Lett.* 2009, 9, (12), 4479-4483.

149. Bae, S.; Kim, H. K.; Balakrishnan, J.; Lei, T.; Song, Y. I.; Kim, Y. J.; Ozyilmaz, B.; Ahn, J.-H.; Hong, B. H.; Iijima, S. *arXiv.org, e-Print Arch., Condens. Matter* 2009, cond-mat.mtrl-sci.

150. Lee, Y.; Bae, S.; Jang, H.; Jang, S.; Zhu, S.-E.; Sim, S. H.; Song, Y. I.; Hong, B. H.; Ahn, J.-H. *Nano Lett.* 2010, 10, (2), 490-3.

151. Lee, Y.-H.; Lee, J.-H. *Appl. Phys. Lett.* 2010, 96, (8), 083101.

152. Cao, H.; Yu, Q.; Jauregui, L. A.; Tian, J.; Wu, W.; Liu, Z.; Jalilian, R.; Benjamin, D. K.; Jiang, Z.; Bao, J.; Pei, S. S. S.; Chen, Y. P. *Appl. Phys. Lett.* 2010, 96, (25), 259901.

153. Bae, S.; Kim, H. K.; Lee, Y.; Park, J.-S.; Zheng, Y.; Balakrishnan, J.; Lei, T.; Song, Y. I.; Kim, Y. J.; Kim, K. S.; Ozyilmaz, B.; Ahn, J.-H.; Hong, B. H.; Iijima, S. *arXiv.org, e-Print Arch., Condens. Matter* 2010, cond-mat.mtrl-sci.

154. Ihm, K.; Lee, K.-j.; Lim, J. T.; Kwon, J. W.; Kang, T.-H.; Chung, S.; Bae, S.; Kim, J. H.; Hong, B. H.; Yeom, G. Y. *arXiv.org, e-Print Arch., Condens. Matter* 2010, cond-mat.mtrl-sci.

155. Ismach, A.; Druzgalski, C.; Penwell, S.; Schwartzberg, A.; Zheng, M.; Javey, A.; Bokor, J.; Zhang, Y. *Nano Lett.* 2010, 10, (5), 1542-1548.

156. Papasimakis, N.; Luo, Z.; Shen, Z. X.; De Angelis, F.; Di Fabrizio, E.; Nikolaenko, A. E.; Zheludev, N. I. *Opt. Express* 2010, 18, (8), 8353-8359.

157. Srivastava, A.; Galande, C.; Ci, L.; Song, L.; Rai, C.; Jariwala, D.; Kelly, K. F.; Ajayan, P. M. *Chem. Mater.* 2010, 22, (11), 3457-3461.

158. Verma, V. P.; Das, S.; Lahiri, I.; Choi, W. *Appl. Phys. Lett.* 2010, 96, (20), 203108.

159. Pal, A. N.; Bol, A. A.; Ghosh, A. *arXiv.org, e-Print Arch., Condens. Matter* 2010, cond-mat.mes-hall.

160. Bae, S.; Kim, H.; Lee, Y.; Xu, X.; Park, J.-S.; Zheng, Y.; Balakrishnan, J.; Lei, T.; Ri Kim, H.; Song, Y. I.; Kim, Y.-J.; Kim, K. S.; Ozyilmaz, B.; Ahn, J.-H.; Hong, B. H.; Iijima, S. *Nat. Nanotechnol.* 2010.

161. Alemán, B. n.; Regan, W.; Aloni, S.; Altoe, V.; Alem, N.; Girit, C. l.; Geng, B.; Maserati, L.; Crommie, M. F.; Wang, F.; Zettl, A. *ACS Nano* 2010.

162. Kasry, A.; Kuroda, M. A.; Martyna, G. J.; Tulevski, G. S.; Bol, A. A. *ACS Nano* 2010.

163. Güneş, F.; Shin, H.-J.; Biswas, C.; Han, G. H.; Kim, E. S.; Chae, S. J.; Choi, J.-Y.; Lee, Y. H. *ACS Nano* 2010.

164. Gao, L.; Guest, J. R.; Guisinger, N. P. *Nano Lett.* 2010.

165. Yu, Q.; Lian, J.; Siriponglert, S.; Li, H.; Chen, Y.; Pei, S. S. S. *arXiv.org, e-Print Arch., Condens. Matter* 2008, cond-mat.mtrl-sci.

166. Di, C.-a.; Wei, D.; Yu, G.; Liu, Y.; Guo, Y.; Zhu, D. *Adv. Mater.* 2008, 20, (17), 3289-+.

167. Bhaviripudi, S.; Jia, X.; Dresselhaus, M. S.; Kong, J. *Nano Lett.* 2010, 10, 4128-4133.

168. Li, X.; Magnuson, C. W.; Venugopal, A.; An, J.; Suk, J. W.; Han, B.; Borysiak, M.; Cai, W.; Velamakanni, A.; Zhu, Y.; Fu, L.; Vogel, E. M.; Voelkl, E.; Colombo, L.; Ruoff, R. S. *Nano Lett.* 2010, 10, (11), 4328-4334.

169. Wu, W.; Liu, Z.; Jauregui, L. A.; Yu, Q.; Pillai, R.; Cao, H.; Bao, J.; Chen, Y. P.; Pei, S.-s. *Sensor Actuat B-Chem* 2010, 150, (1), 296-300.

170. Gao, L.; Bode, M.; Guest, J. R.; Guisinger, N. P. *American Physical Society* 2010, 21003.

171. Lee, S.; Lee, K.; Zhong, Z. *Nano Lett.* 2010, 10, (11), 4702-7.

172. May, J. *Surf. Sci.* 1969, 17, (1), 267-&.

173. Sutter, P.; Sadowski, J. T.; Sutter, E. *Phys. Rev. B* 2009, 80, (24), 245411.

174. Gao, M.; Pan, Y.; Huang, L.; Hu, H.; Zhang, L. Z.; Guo, H. M.; Du, S. X.; Gao, H.-J. *Appl. Phys. Lett.* 2011, 98, (3), 033101.

175. Gao, T.; Xie, S.; Gao, Y.; Liu, M.; Chen, Y.; Zhang, Y.; Liu, Z. *ACS Nano* 2011, 5, (11), 9194-201.

176. Gao, L.; Ren, W.; Xu, H.; Jin, L.; Wang, Z.; Ma, T.; Ma, L.-P.; Zhang, Z.; Fu, Q.; Peng, L.-m.; Bao, X.; Cheng, H.-M. *Nat. Commun.* 2012, 3, 699.

177. Lin, Y.-C.; Lin, C.-Y.; Chiu, P.-W. *Appl. Phys. Lett.* 2010, 96, (13), 133110.

178. Shao, Y.; Zhang, S.; Engelhard, M. H.; Li, G.; Shao, G.; Wang, Y.; Liu, J.; Aksay, I. A.; Lin, Y. *J. Mater. Chem.* 2010, 20, (35), 7491.

179. Zhao, W.; Höfert, O.; Gotterbarm, K.; Zhu, J. F.; Papp, C.; Steinrück, H.-P. *J. Phys. Chem. C* 2012, 116, 5062-5066.

180. Deng, D.; Pan, X.; Yu, L.; Cui, Y.; Jiang, Y.; Qi, J.; Li, W.-X.; Fu, Q.; Ma, X.; Xue, Q.; Sun, G.; Bao, X. *Chemistry of Materials* 2011, 23, 1188-1193.

181. Qu, L.; Liu, Y.; Baek, J.-B.; Dai, L. *ACS Nano* 2010, 4, (3), 1321-1326.

182. Park, H. J.; Skakalova, V.; Meyer, J. C.; Lee, D. S.; Iwasaki, T.; Bumby, C.; Kaiser, U.; Roth, S. *Phys. Status Solidi B* 2010, 247, (11-12), 2915-2919.

183. Lv, R.; Li, Q.; Botello-Méndez, A. R.; Hayashi, T.; Wang, B.; Berkdemir, A.; Hao, Q.; Elías, A. L.; Cruz-Silva, R.; Gutiérrez, H. R.; Kim, Y. A.; Muramatsu, H.; Zhu, J.; Endo, M.; Terrones, H.; Charlier, J.-C.; Pan, M.; Terrones, M. *Scientific Reports* 2012, 2.

184. Jin, Z.; Yao, J.; Kittrell, C.; Tour, J. M. *ACS Nano* 2011, 5, 4112-4117.

185. Xue, Y.; Wu, B.; Jiang, L.; Guo, Y.; Huang, L.; Chen, J.; Tan, J.; Geng, D.; Luo, B.; Hu, W.; Yu, G.; Liu, Y. *J. Am. Chem. Soc.* 2012, 134, (27), 11060-3.

186. Gao, H.; Song, L.; Guo, W.; Huang, L.; Yang, D.; Wang, F.; Zuo, Y.; Fan, X.; Liu, Z.; Gao, W.; Vajtai, R.; Hackenberg, K.; Ajayan, P. M. *Carbon* 2012, 50, (12), 4476-4482.

187. Meyer, J. C.; Kurasch, S.; Park, H. J.; Skakalova, V.; Künzel, D.; Gross, A.; Chuvilin, A.; Algara-Siller, G.; Roth, S.; Iwasaki, T.; Starke, U.; Smet, J. H.; Kaiser, U. *Nat. Mater.* 2011, 10, (3), 209-15.

188. Das, A.; Pisana, S.; Chakraborty, B.; Piscanec, S.; Saha, S. K.; Waghmare, U. V.; Novoselov, K. S.; Krishnamurthy, H. R.; Geim, A. K.; Ferrari, A. C.; Sood, A. K. *Nat. Nanotechnol.* 2008, 3, (4), 210.

189. Kidambi, P. R.; Ducati, C.; Dlubak, B.; Gardiner, D.; Weatherup, R. S.; Martin, M.-B.; Seneor, P.; Coles, H.; Hofmann, S. *J. Phys. Chem. C* 2012, 116, 22492-22501.

190. Sheng, Z.-H.; Gao, H.-L.; Bao, W.-J.; Wang, F.-B.; Xia, X.-H. *J. Mater. Chem.* 2012, 22, (2), 390-395.

191. Tang, Y.-B.; Yin, L.-C.; Yang, Y.; Bo, X.-H.; Cao, Y.-L.; Wang, H.-E.; Zhang, W.-J.; Bello, I.; Lee, S.-T.; Cheng, H.-M.; Lee, C.-S. *ACS Nano* 2012, 6, (3), 1970-8.

192. Lü, X.; Wu, J.; Lin, T.; Wan, D.; Huang, F.; Xie, X.; Jiang, M. *J. Mater. Chem.* 2011, 21, (29), 10685-10689.

193. Wu, T.; Shen, H.; Sun, L.; Cheng, B.; Liu, B.; Shen, J. *New J. Chem.* 2012, 36, (6), 1385-1391.

194. Li, X.; Fan, L.; Li, Z.; Wang, K.; Zhong, M.; Wei, J.; Wu, D.; Zhu, H. *Adv. Energy Mater.* 2012, 2, (4), 425-429.

195. Cattelan, M.; Agnoli, S.; Favaro, M.; Garoli, D.; Romanato, F.; Meneghetti, M.; Barinov, A.; Dudin, P.; Granozzi, G. *Chem. Mater.* 2013, 25, 1490-1495.

196. Zhao, L.; Levendorf, M.; Goncher, S.; Schiros, T.; Pálová, L.; Zabet-Khosousi, A.; Rim, K. T.; Gutiérrez, C.; Nordlund, D.; Jaye, C.; Hybertsen, M.; Reichman, D.; Flynn, G. W.; Park, J.; Pasupathy, A. N. *Nano Lett* 2013, 13, (10), 4659-65.

197. Schneider, G. g. F.; Calado, V. E.; Zandbergen, H.; Vandersypen, L. M. K.; Dekker, C. *arXiv* 2010, cond-mat.mes-hall.

198. Wang, Y.; Zheng, Y.; Xu, X.; Dubuisson, E.; Bao, Q.; Lu, J.; Loh, K. P. *ACS Nano* 2011, 5, (12), 9927-9933.

199. Yao, Y.; Li, Z.; Lin, Z.; Moon, K.-S.; Agar, J.; Wong, C. *J. Phys. Chem. C* 2011, 115, (13), 5232-5238.

200. Liu, W.; Li, H.; Xu, C.; Khatami, Y.; Banerjee, K. *Carbon* 2011, 49, (13), 4122-4130.

201. Hwang, C.; Yoo, K.; Kim, S. J.; Seo, E. K.; Yu, H.; Biró, L. s. P. t. *J. Phys. Chem. C* 2011, 115, 22369-22374.

202. Regmi, M.; Chisholm, M. F.; Eres, G. *Carbon* 2012, 50, 134-141.

203. Liu, L.; Zhou, H.; Cheng, R.; Chen, Y.; Lin, Y.-C.; Qu, Y.; Bai, J.; Ivanov, I. A.; Liu, G.; Huang, Y.; Duan, X. *J. Mater. Chem.* 2012, 22, (4), 1498.

204. **Wu, W.; Yu, Q.; Peng, P.; Liu, Z.; Bao, J.; Pei, S.-s.** ***Nanotechnology*** **2012, 23, (3), 035603.**

205. **Li, X.; Magnuson, C. W.; Venugopal, A.; Tromp, R. M.; Hannon, J. B.; Vogel, E. M.; Colombo, L.; Ruoff, R. S.** ***J. Am. Chem. Soc.*** **2011, 133, (9), 2816-2819.**

206. **Petrone, N.; Dean, C. R.; Meric, I.; Zande, A. M. v. d.; Huang, P. Y.; Wang, L.; Muller, D.; Shepard, K. L.; Hone, J.** ***Nano Lett*** **2012, 12, 2751-2756.**

207. **Wofford, J. M.; Nie, S.; McCarty, K. F.; Bartelt, N. C.; Dubon, O. D.** ***Nano Lett.*** **2010, 10, (12), 4890-4896.**

208. **Zhang, Y.; Zhang, L.; Kim, P.; Ge, M.; Li, Z.; Zhou, C.** ***Nano Lett*** **2012, 12, 2810-2816.**

209. **Vlassiouk, I.; Regmi, M.; Fulvio, P.; Dai, S.; Datskos, P.; Eres, G.; Smirnov, S.** ***ACS Nano*** **2011, 5, (7), 6069-76.**

210. **Robertson, A. W.; Warner, J. H.** ***Nano Lett.*** **2011.**

211. **Yu, Q.; Jauregui, L. A.; Wu, W.; Colby, R.; Tian, J.; Su, Z.; Cao, H.; Liu, Z.; Pandey, D.; Wei, D.; Chung, T. F.; Peng, P.; Guisinger, N. P.; Stach, E. A.; Bao, J.; Pei, S.-s.; Chen, Y. P.** ***Nat. Mater.*** **2011, 10, (6), 443-449.**

212. **Luo, Z.; Kim, S.; Kawamoto, N.; Rappe, A. M.; Johnson, A. T. C.** ***ACS Nano*** **2011, 5, (11), 9154-60.**

213. **Fan, L.; Li, Z.; Li, X.; Wang, K.; Zhong, M.; Wei, J.; Wu, D.; Zhu, H.** ***Nanoscale*** **2011, 3, (12), 4946-4950.**

214. **Geng, D.; Wu, B.; Guo, Y.; Huang, L.; Xue, Y.; Chen, J.; Yu, G.; Jiang, L.; Hu, W.; Liu, Y.** ***Proc. Natl. Acad. Sci. USA*** **2012, 109, 7992-7996.**

215. **Wu, Y. A.; Fan, Y.; Speller, S.; Creeth, G. L.; Sadowski, J. T.; He, K.; Robertson, A. W.; Allen, C. S.; Warner, J. H.** ***ACS Nano*** **2012, 6, (6), 5010-5017.**

216. **Cho, J.; Gao, L.; Tian, J.; Cao, H.; Wu, W.; Yu, Q.; Yitamben, E. N.; Fisher, B.; Guest, J. R.; Chen, Y. P.; Guisinger, N. P.** ***ACS Nano*** **2011, 5, (5), 3607-13.**

217. **Huang, P. Y.; Ruiz-Vargas, C. S.; van der Zande, A. M.; Whitney, W. S.; Levendorf, M. P.; Kevek, J. W.; Garg, S.; Alden, J. S.; Hustedt, C. J.; Zhu, Y.; Park, J.; McEuen, P. L.; Muller, D. A.** ***Nature*** **2011, 469, 389-392.**

218. **Kim, K.; Lee, Z.; Regan, W.; Kisielowski, C.; Crommie, M. F.; Zettl, A.** ***ACS Nano*** **2011, 5, (3), 2142-6.**

219. **Wang, H.; Wang, G.; Bao, P.; Yang, S.; Zhu, W.; Xie, X.; Zhang, W.-J.** ***Journal of the American Chemical Society*** **2012.**

220. **Paronyan, T. M.; Pigos, E. M.; Chen, G.; Harutyunyan, A. R.** ***ACS Nano*** **2011, 5, (12), 9619-27.**

221. **Lu, A.-Y.; Wei, S.-Y.; Wu, C.-Y.; Hernandez, Y.; Chen, T.-Y.; Liu, T.-H.; Pao, C.-W.; Chen, F.-R.; Li, L.-J.; Juang, Z.-Y.** ***RSC Adv.*** **2012, 2, (7), 3008.**

222. **Vlassiouk, I.; Fulvio, P.; Meyer, H.; Lavrik, N.; Dai, S.; Datskos, P.; Smirnov, S.** ***Carbon*** **2013, 54, (C), 58-67.**

223. **Fan, L.; Zou, J.; Li, Z.; Li, X.; Wang, K.; Wei, J.; Zhong, M.; Wu, D.; Xu, Z.; Zhu, H.** ***Nanotechnology*** **2012, 23, (11), 115605.**

224. **Howsare, C. A.; Weng, X.; Bojan, V.; Snyder, D.; Robinson, J. A.** ***Nanotechnology*** **2012, 23, (13), 135601.**

225. **Luo, Z.; Lu, Y.; Singer, D. W.; Berck, M. E.; Somers, L. A.; Goldsmith, B. R.; Johnson, A. T. C.** ***Chem. Mater.*** **2011, 23, (6), 1441-1447.**

226. **Han, G. H.; Güneş, F.; Bae, J. J.; Kim, E. S.; Chae, S. J.; Shin, H.-J.; Choi, J.-Y.; Pribat, D.; Lee, Y. H.** ***Nano Lett.*** **2011, 11, (10), 4144-8.**

227. Nie, S.; Wofford, J. M.; Bartelt, N. C.; Dubon, O. D.; McCarty, K. F. *Phys. Rev. B* 2011, 84, (15), 155425.

228. Chavez, K.; Hess, D. *J. Electrochem. Soc.* 2001, 148, (11), G640-G643.

229. Yu, V.; Whiteway, E.; Maassen, J.; Hilke, M. *Phys. Rev. B* 2011, 84, (20), 205407.

230. Lahiri, I.; Verma, V. P.; Choi, W. *Carbon* 2011, 49, (5), 1614-1619.

231. Zhang, B.; Lee, W. H.; Piner, R.; Kholmanov, I.; Wu, Y.; Li, H.; Ji, H.; Ruoff, R. S. *ACS Nano* 2012, 6, (3), 2471-2476.

232. Wood, J. D.; Schmucker, S. W.; Lyons, A. S.; Pop, E.; Lyding, J. W. *Nano Lett.* 2011, 11, (11), 4547-4554.

233. Tao, L.; Lee, J.; Chou, H.; Holt, M.; Ruoff, R. S.; Akinwande, D. *ACS Nano* 2012.

234. Tao, L.; Lee, J.; Holt, M.; Chou, H.; Mcdonnell, S. J.; Ferrer, D. A.; Babenco, M. G.; Wallace, R. M.; Banerjee, S. K.; Ruoff, R. S.; Akinwande, D. *J. Phys. Chem. C* 2012, 116, 24068-24074.

235. Grantab, R.; Shenoy, V. B.; Ruoff, R. S. *Science* 2010, 330, (6006), 946-948.

236. Batzill, M. *Surface science reports* 2012, 67, 83 - 115.

237. Wang, B.; Bocquet, M.-L.; Marchini, S.; Guenther, S.; Wintterlin, J. *Phys. Chem. Chem. Phys.* 2008, 10, (24), 3530-3534.

238. Walter, A. L.; Nie, S.; Bostwick, A.; Kim, K. S.; Moreschini, L.; Chang, Y. J.; Innocenti, D.; Horn, K.; McCarty, K. F.; Rotenberg, E. *Phys. Rev. B* 2011, 84, (19), 195443.

239. Ogawa, Y.; Hu, B.; Orofeo, C. M.; Tsuji, M.; Ikeda, K.-i.; Mizuno, S.; Hibino, H.; Ago, H. *J Phys Chem Lett* 2012, 3, (2), 219-226.

240. Hu, B.; Ago, H.; Ito, Y.; Kawahara, K.; Tsuji, M.; Magome, E.; Sumitani, K.; Mizuta, N.; Ikeda, K.-i.; Mizuno, S. *Carbon* 2012, 50, (1), 57-65.

241. Rasool, H. I.; Song, E. B.; Allen, M. J.; Wassei, J. K.; Kaner, R. B.; Wang, K. L.; Weiller, B. H.; Gimzewski, J. K. *Nano Lett.* 2011, 11, (1), 251-6.

242. Rasool, H. I.; Song, E. B.; Mecklenburg, M.; Regan, B. C.; Wang, K. L.; Weiller, B. H.; Gimzewski, J. K. *J. Am. Chem. Soc.* 2011, 133, (32), 12536-43.

243. Zhao, L.; Rim, K. T.; Zhou, H.; He, R.; Heinz, T. F.; Pinczuk, A.; Flynn, G. W.; Pasupathy, A. N. *Solid State Commun.* 2011, 151, (7), 509-513.

244. Gao, L.; Guest, J. R.; Guisinger, N. P. *Nano Lett.* 2010, 10, (9), 3512-3516.

245. Orofeo, C. M.; Hibino, H.; Kawahara, K.; Ogawa, Y.; Tsuji, M.; Ikeda, K.-i.; Mizuno, S.; Ago, H. *Carbon* 2012, 50, (6), 2189-2196.

246. Bi, H.; Huang, F.; Zhao, W.; Lü, X.; Chen, J.; Lin, T.; Wan, D.; Xie, X.; Jiang, M. *Carbon* 2012, 50, (8), 2703-2709.

247. Zhu, Y.; Murali, S.; Cai, W.; Li, X.; Suk, J. W.; Potts, J. R.; Ruoff, R. S. *Adv. Mater.* 2010, 22, (35), 3906-24.

248. Kim, J.; Kim, F.; Huang, J. *Mater. Today* 2010, 13, (3), 28-38.

249. Gao, L.; Ren, W.; Li, F.; Cheng, H.-M. *ACS Nano* 2008, 2, (8), 1625-1633.

250. De Marco, P.; Nardone, M.; Del Vitto, A.; Alessandri, M.; Santucci, S.; Ottaviano, L. *Nanotechnology* 2010, 21, (25), 255703.

251. Jung, I.; Pelton, M.; Piner, R.; Dikin, D. A.; Stankovich, S.; Watcharotone, S.; Hausner, M.; Ruoff, R. S. *Nano Lett.* 2007, 7, (12), 3569-3575.

252. NanoFocus NanoFocus: µsurf technology. www.nanofocus.com/technology/measurement-principles/usurf-technology (2 April 2014),

253. Ferrari, A. C.; Meyer, J. C.; Scardaci, V.; Casiraghi, C.; Lazzeri, M.; Mauri, F.; Piscanec, S.; Jiang, D.; Novoselov, K. S.; Roth, S. *Phys. Rev. Lett.* 2006, 97, (18), 187401.

254. Graf, D.; Molitor, F.; Ensslin, K.; Stampfer, C.; Jungen, A.; Hierold, C.; Wirtz, L. *Nano Lett.* 2007, 7, (2), 238-242.

255. Gupta, A.; Chen, G.; Joshi, P.; Tadigadapa, S.; Eklund, P. C. *Nano Lett.* 2006, 6, (12), 2667-2673.

256. Ferrari, A. C. *Solid State Commun.* 2007, 143, (1-2), 47-57.

257. Graf, D.; Molitor, F.; Ensslin, K.; Stampfer, C.; Jungen, A.; Hierold, C.; Wirtz, L. *Solid State Commun.* 2007, 143, (1-2), 44-46.

258. Dresselhaus, M. S.; Jorio, A.; Hofmann, M.; Dresselhaus, G.; Saito, R. *Nano Lett.* 2010, 10, (3), 751-8.

259. Malard, L. M.; Pimenta, M. A.; Dresselhaus, G.; Dresselhaus, M. S. *Phys. Rep.* 2009, 473, (5-6), 51-87.

260. Cancado, L. G.; Jorio, A.; Martins Ferreira, E. H.; Stavale, F.; Achete, C. A.; Capaz, R. B.; Moutinho, M. V. O.; Lombardo, A.; Kulmala, T. S.; Ferrari, A. C. *Nano Lett.* 2011, 11, (8), 3190-3196.

261. Kim, Y. A.; Fujisawa, K.; Muramatsu, H.; Hayashi, T.; Endo, M.; Fujimori, T.; Kaneko, K.; Terrones, M.; Behrends, J.; Eckmann, A.; Casiraghi, C.; Novoselov, K. S.; Saito, R.; Dresselhaus, M. S. *ACS Nano* 2012, 6, (7), 6293-300.

262. Krauss, B.; Nemes-Incze, P. t.; Skakalova, V.; Biró, L. s. P. t.; von Klitzing, K.; Smet, J. H. *Nano Lett.* 2010, 10, (11), 4544-4548.

263. Ni, Z. H.; Chen, W.; Fan, X. F.; Kuo, J. L.; Yu, T.; Wee, A. T. S.; Shen, Z. X. *Phys. Rev. B* 2008, 77, (11), 115416.

264. Lee, D. S.; Riedl, C.; Krauss, B.; von Klitzing, K.; Starke, U.; Smet, J. H. *Nano Lett.* 2008, 8, (12), 4320-4325.

265. Calizo, I.; Balandin, A. A.; Bao, W.; Miao, F.; Lau, C. N. *Nano Lett.* 2007, 7, (9), 2645-2649.

266. Huang, M.; Yan, H.; Chen, C.; Song, D.; Heinz, T. F.; Hone, J. *P Natl Acad Sci Usa* 2009, 106, (18), 7304-7308.

267. Cancado, L. G.; Reina, A.; Kong, J.; Dresselhaus, M. S. *Phys. Rev. B* 2008, 77, (24), 245408.

268. Podila, R.; Chacon-Torres, J.; Spear, J. T.; Pichler, T.; Ayala, P.; Rao, A. M. *Appl. Phys. Lett.* 2012, 101, 123108.

269. Paredes, J. I.; Villar-Rodil, S.; Solis-Fernandez, P.; Martinez-Alonso, A.; Tascon, J. M. D. *Langmuir* 2009, 25, (10), 5957-5968.

270. Instruments, O. EBSD electron backscatter diffraction. www.ebsd.com (2 April 2014),

271. Wilkinson, A. J.; Britton, T. B. *Materials Today* 2012, 15, (9), 366-376.

272. Alemán, B. n.; Regan, W.; Aloni, S.; Altoe, V.; Alem, N.; Girit, C. l.; Geng, B.; Maserati, L.; Crommie, M. F.; Wang, F.; Zettl, A. *ACS Nano* 2010, 4, (8), 4762 - 4768.

273. Meyer, J. C.; Geim, A. K.; Katsnelson, M. I.; Novoselov, K. S.; Booth, T. J.; Roth, S. *Nature* 2007, 446, (7131), 60-63.

274. Meyer, J. C.; Geim, A. K.; Katsnelson, M. I.; Novoselov, K. S.; Obergfell, D.; Roth, S.; Girit, C. O.; Zettl, A. *Solid State Commun.* 2007, 143, (1-2), 101-109.

275. Wu, T.; Ding, G.; Shen, H.; Wang, H.; Sun, L.; Jiang, D.; Xie, X.; Jiang, M. *Adv. Funct. Mater.* 2012, 23, (2), 198-203.

276. Tsen, A. W.; Brown, L.; Levendorf, M. P.; Ghahari, F.; Huang, P. Y.; Havener, R. W.; Ruiz-Vargas, C. S.; Muller, D. A.; Kim, P.; Park, J. *Science* 2012, 336, (6085), 1143-6.

277. Hashimoto, A.; Suenaga, K.; Gloter, A.; Urita, K.; Iijima, S. *Nature* 2004, 430, (7002), 870-873.

278. Meyer, J. C.; Kisielowski, C.; Erni, R.; Rossell, M. D.; Crommie, M. F.; Zettl, A. *Nano Lett.* 2008, 8, (11), 3582-3586.

279. Warner, J. H.; Ruemmeli, M. H.; Gemming, T.; Buechner, B.; Briggs, G. A. D. *Nano Lett.* 2009, 9, (1), 102-106.

280. Liu, Z.; Suenaga, K.; Harris, P. J. F.; Iijima, S. *Phys. Rev. Lett.* 2009, 102, (1), 015501.

281. Warner, J. H.; Margine, E. R.; Mukai, M.; Robertson, A. W.; Giustino, F.; Kirkland, A. I. *Science* 2012, 337, (6091), 209-12.

282. Wang, H.; Wang, Q.; Cheng, Y.; Li, K.; Yao, Y.; Zhang, Q.; Dong, C.; Wang, P.; Schwingenschlögl, U.; Yang, W.; Zhang, X. X. *Nano Lett* 2012, 12, (1), 141-4.

283. Lu, C.-C.; Lin, Y.-C.; Liu, Z.; Yeh, C.-H.; Suenaga, K.; Chiu, P.-W. *ACS Nano* 2013, 7, (3), 2587-94.

284. Rasool, H. I.; Ophus, C.; Klug, W. S.; Zettl, A.; Gimzewski, J. K. *Nat. Commun.* 2013, 4, 2811.

285. Robertson, A. W.; Montanari, B.; He, K.; Allen, C. S.; Wu, Y. A.; Harrison, N. M.; Kirkland, A. I.; Warner, J. H. *ACS Nano* 2013, 7, (5), 4495-502.

286. Pennycook, S. J.; Chisholm, M. F.; Lupini, A. R.; Varela, M.; Borisevich, A. Y.; Oxley, M. P.; Luo, W. D.; Benthem, K. v.; Oh, S.-H.; Sales, D. L.; Molina, S. I.; Garcia-Barriocanal, J.; Leon, C.; Santamaria, J.; Rashkeev, S. N.; Pantelides, S. T. *Phil. Trans. R. Soc. A* 2009, 367, 3709–3733.

287. Pennycook, S. J.; Lupini, A. R.; Varela, M.; Borisevich, A. Y.; Peng, Y.; Oxley, M. P.; van Bentham, K.; Chisholm, M. F. *in Scanning microscopy for nanotechnology- techniques and applications* 2006, 152-191.

288. Krivanek, O. L.; Chisholm, M. F.; Nicolosi, V.; Pennycook, T. J.; Corbin, G. J.; Dellby, N.; Murfitt, M. F.; Own, C. S.; Szilagyi, Z. S.; Oxley, M. P.; Pantelides, S. T.; Pennycook, S. J. *Nature* 2010, 464, (7288), 571-574.

289. Zhou, W.; Kapetanakis, M. D.; Prange, M. P.; Pantelides, S. T.; Pennycook, S. J.; Idrobo, J.-C. *Phys. Rev. Lett.* 2012, 109, (20), 206803.

290. Ramasse, Q. M.; Seabourne, C. R.; Kepaptsoglou, D.-M.; Zan, R.; Bangert, U.; Scott, A. J. *Nano Lett* 2013, 13, (10), 4989-95.

291. Egerton, R. F., *Electron energy-loss spectroscopy in the electron microscope*. 3rd ed.; Springer publishing: 2011.

292. Egerton, R. F. *Rep. Prog. Phys.* 2009, 72, 016502.

293. Nicholls, R. J.; Sader, K.; Warner, J. H.; Plant, S. R.; Porfyrakis, K.; Nellist, P. D.; Briggs, G. A. D.; Cockayne, D. J. H. *ACS Nano* 2010, 4, (7), 3943-8.

294. Kidambi, P. R.; Bayer, B. C.; Blume, R.; Wang, Z.-J.; Baehtz, C.; Weatherup, R. S.; Willinger, M.-G.; Schloegl, R.; Hofmann, S. *Nano Lett* 2013, 13, 4769-4778.

295. Koos, A. A.; Dowling, M.; Jurkschat, K.; Crossley, A.; Grobert, N. *Carbon* 2009, 47, (1), 30-37.

296. Amelinckx, S.; van Dyck, D.; van Landuyt, J.; van Tendeloo, G. *Wiley-VCH* 2008, 1-517.

297. Damascelli, A. *Phys Scripta* 2004, T109, 61-74.

298. Enderlein, C.; Kim, Y. S.; Bostwick, A.; Rotenberg, E.; Horn, K. *New Journal of Physics* 2010, 12, 033014.

299. Zhang, Y.; Li, Z.; Kim, P.; Zhang, L.; Zhou, C. *ACS Nano* 2011.

300. Meysami, S. S.; Dillon, F.; Koos, A. A.; Aslam, Z.; Grobert, N. *Carbon* 2013, 58, 151-158.

301. Han, Z.; Kimouche, A.; Kalita, D.; Allain, A.; Arjmandi-Tash, H.; Reserbat-Plantey, A.; Marty, L.; Pairis, S.; Reita, V.; Bendiab, N.; Coraux, J.; Bouchiat, V. *Adv. Funct. Mater.* 2013, 24, (7), 964-970.

302. Van Hove, M. A.; Somorjai, G. A. *Surf. Sci.* 1980, 92, (2-3), 489-518.

303. Giovannetti, G.; Khomyakov, P. A.; Brocks, G.; Karpan, V. M.; van den Brink, J.; Kelly, P. J. *Phys. Rev. Lett.* 2008, 101, (2), 026803.

304. Ren, Y.; Chen, S.; Cai, W.; Zhu, Y.; Zhu, C.; Ruoff, R. S. *Appl. Phys. Lett.* 2010, 97, (5), 053107.

305. Varykhalov, A.; Scholz, M. R.; Kim, T. K.; Rader, O. *Phys. Rev. B* 2010, 82, (12), 121101.

306. Wang, W. X.; Liang, S. H.; Yu, T.; Li, D. H.; Li, Y. B.; Han, X. F. *Journal of Applied Physics* 2011, 109, (7), 07C501.

307. Mohiuddin, T. M. G.; Lombardo, A.; Nair, R. R.; Bonetti, A.; Savini, G.; Jalil, R.; Bonini, N.; Basko, D. M.; Galiotis, C.; Marzari, N.; Novoselov, K. S.; Geim, A. K.; Ferrari, A. C. *Phys. Rev. B* 2009, 79, (20), 205433.

308. Zabel, J.; Nair, R. R.; Ott, A.; Georgiou, T.; Geim, A. K.; Novoselov, K. S.; Casiraghi, C. *Nano Lett.* 2012, 12, (2), 617-621.

309. Frank, O.; Tsoukleri, G.; Parthenios, J.; Papagelis, K.; Riaz, I.; Jalil, R.; Novoselov, K. S.; Galiotis, C. *ACS Nano* 2010, 4, (6), 3131-3138.

310. He, R.; Zhao, L.; Petrone, N.; Kim, K. S.; Roth, M.; Hone, J.; Kim, P.; Pasupathy, A.; Pinczuk, A. *Nano Lett* 2012, 12, (5), 2408-13.

311. Tsen, A. W.; Brown, L.; Havener, R. W.; Park, J. *Accounts of chemical research* 2013, 46, (10), 2286-2296.

312. Biro, L. P.; Lambin, P. *New J. Phys.* 2013, 15, 035024.

313. Yan, Z.; Peng, Z.; Tour, J. M. *Accounts of Chemical Research* 2013, 47, 1327-1337.

314. Lee, G.-H.; Cooper, R. C.; An, S. J.; Lee, S.; van der Zande, A.; Petrone, N.; Hammerberg, A. G.; Lee, C.; Crawford, B.; Oliver, W.; Kysar, J. W.; Hone, J. *Science* 2013, 340, (6136), 1073-6.

315. Zhang, X.; Xu, Z.; Hui, L.; Xin, J.; Ding, F. *J. Phys. Chem. Lett.* 2012, 3, 2822-2827.

316. Papageorgiou, D.; Evangelakis, G. *Surf. Sci.* 2000, 461, (1-3), L543-L549.

317. Liu, Y.; Dobrinsky, A.; Yakobson, B. I. *Phys. Rev. Lett.* 2010, 105, (23), 235502.

318. Datta, S. S.; Strachan, D. R.; Khamis, S. M.; Johnson, A. T. C. *Nano Lett* 2008, 8, (7), 1912-5.

319. Campos, L. C.; Manfrinato, V. R.; Sanchez-Yamagishi, J. D.; Kong, J.; Jarillo-Herrero, P. *Nano Lett* 2009, 9, (7), 2600-4.

320. Cairns, J. A.; Keep, C. W.; Bishop, H. E.; Terry, S. *Journal of Catalysis* 1977, 46, (1), 120-123.

321. Hao, Y.; Bharathi, M. S.; Wang, L.; Liu, Y.; Chen, H.; Nie, S.; Wang, X.; Chou, H.; Tan, C.; Fallahazad, B.; Ramanarayan, H.; Magnuson, C. W.; Tutuc, E.; Yakobson, B. I.; Mccarty, K. F.; Zhang, Y.-W.; Kim, P.; Hone, J.; Colombo, L.; Ruoff, R. S. *Science* 2013, 342, (6159), 720-723.

322. Babenko, V.; Murdock, A. T.; Koos, A. A.; Britton, J.; Crossley, A.; Holdway, P.; Moffat, J.; Alexander-Webber, J.; Huang, N.; Nicholas, R.; Grobert, N. *Submitted for publication* 2014.

323. Koos, A. A.; Dillon, F.; Obraztsova, E.; Crossley, A.; Grobert, N. *Carbon* 2010, 48, (11), 3033-3041.

324. Martins Ferreira, E. H.; Moutinho, M. V. O.; Stavale, F.; Lucchese, M. M.; Capaz, R. B.; Achete, C. A.; Jorio, A. *Phys. Rev. B* 2010, 82, 125429.

325. Vickerman, J. C.; Gilmore, I. S., *Surface analysis- the principal techniques*. 2nd ed.; Wiley: 2009.

326. **Moulder, J. F.; Stickle, W. F.; Sobol, P. E.; Bombden, K. D., *Handbook of X-ray photoelectron spectroscopy*. Perkin-Elmer Corp: 1992.**

327. **Lambin, P.; Amara, H.; Ducastelle, F.; Henrard, L. *Phys. Rev. B* 2012, 86, 045448.**

328. **Rutter, G. M.; Crain, J. N.; Guisinger, N. P.; Li, T.; First, P. N.; Stroscio, J. A. *Science* 2007, 317, (5835), 219-222.**

329. **Brihuega, I.; Mallet, P.; Bena, C.; Bose, S.; Michaelis, C.; Vitali, L.; Varchon, F.; Magaud, L.; Kern, K.; Veuillen, J. Y. *Physical Review Letters* 2008, 101, 206802.**

330. **Suenaga, K.; Akiyama-Hasegawa, K.; Niimi, Y.; Kobayashi, H.; Nakamura, M.; Liu, Z.; Sato, Y.; Koshino, M.; Iijima, S. *Journal of Electron Microscopy* 2012, 61, (5), 285-291.**

331. **Zhang, X.; Li, H.; Ding, F. *Adv. Mater.* 2014, 26, (31), 5488-95.**

332. **Bartelt, N.; Mccarty, K. *MRS Bulletin* 2012, 37, (12), 1158-1165.**

333. **Artyukhov, V. I.; Liu, Y.; Yakobson, B. I. *Proceedings of the National Academy of Sciences of the United States of America* 2012, 109, (38), 15136-40.**

334. **Tagawa, H.; Sugawara, H. *Bull. Chem. Soc. Japan.* 1962, 35, (8), 1276-1279.**

335. **Merino, P.; Svec, M.; Pinardi, A. L.; Otero, G.; Martín-Gago, J. A. *ACS Nano* 2011, 5, (7), 5627-34.**

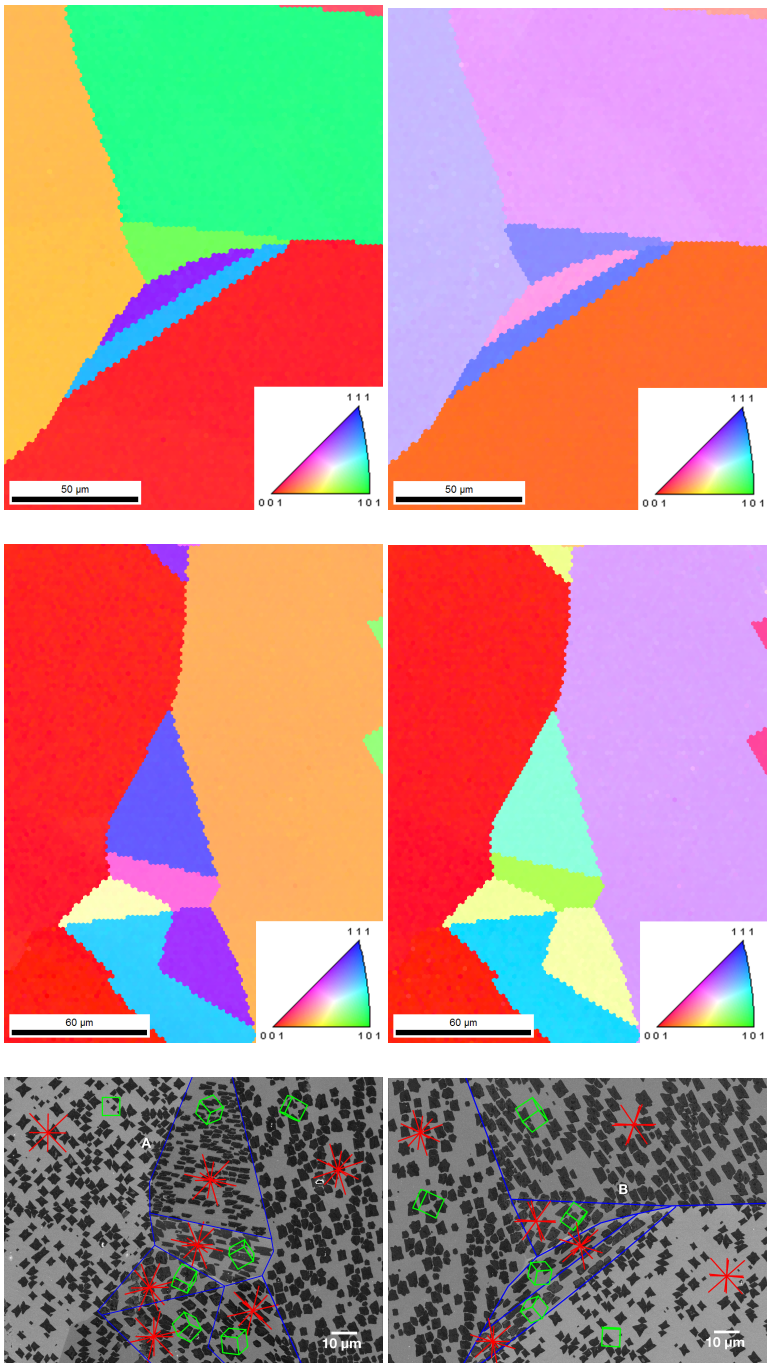
336. **Seah, C. M.; Chai, S. P.; Mohamed, A. R. *Carbon* 2014, 70, 1-21.**

337. **Merino, P.; Rodrigo, L.; Pinardi, A. L.; Méndez, J.; López, M. F.; Pou, P.; Pérez, R.; Martín Gago, J. A. *ACS Nano* 2014, 8, (4), 3590-6.**

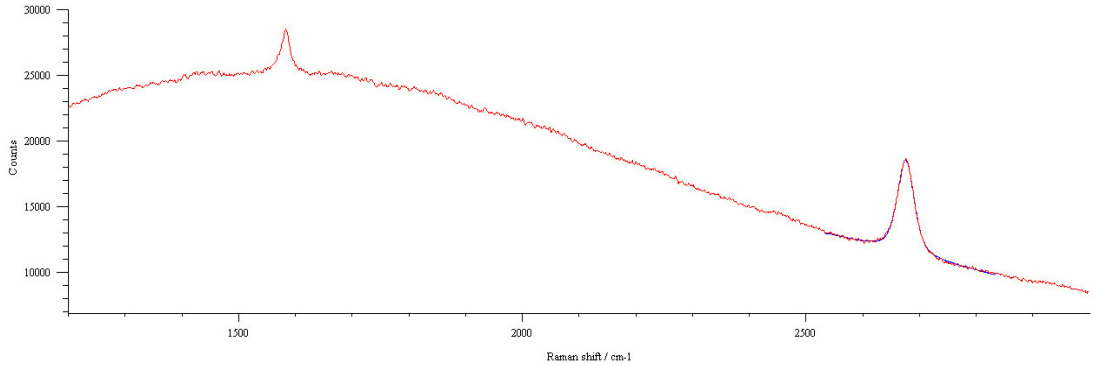
338. **Ito, Y.; Christodoulou, C.; Nardi, M. V.; Koch, N.; Sachdev, H.; Müllen, K. *ACS Nano* 2014.**

Appendix

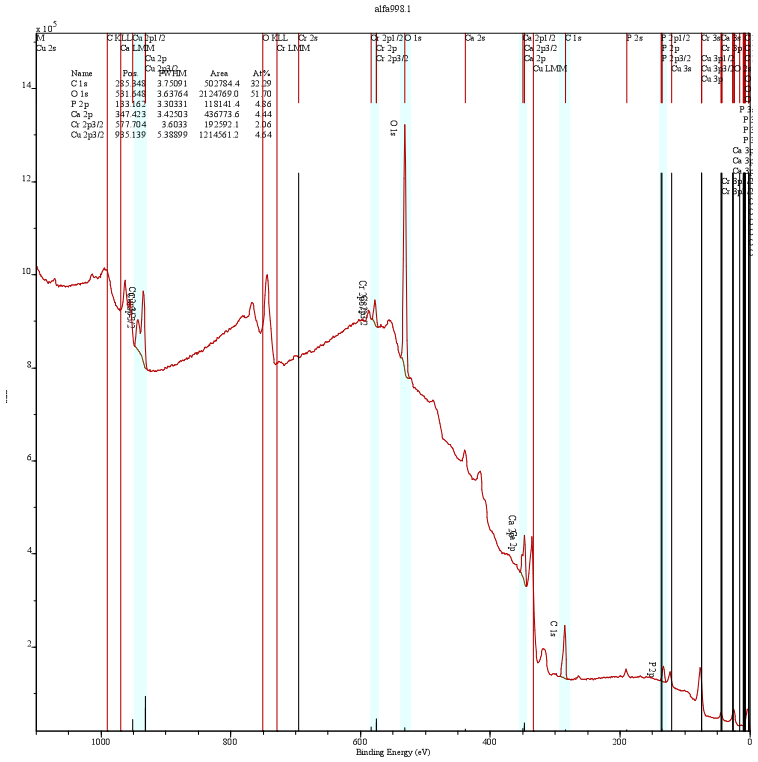
EBSD data from analysis of influence of Cu crystallographic orientation on graphene



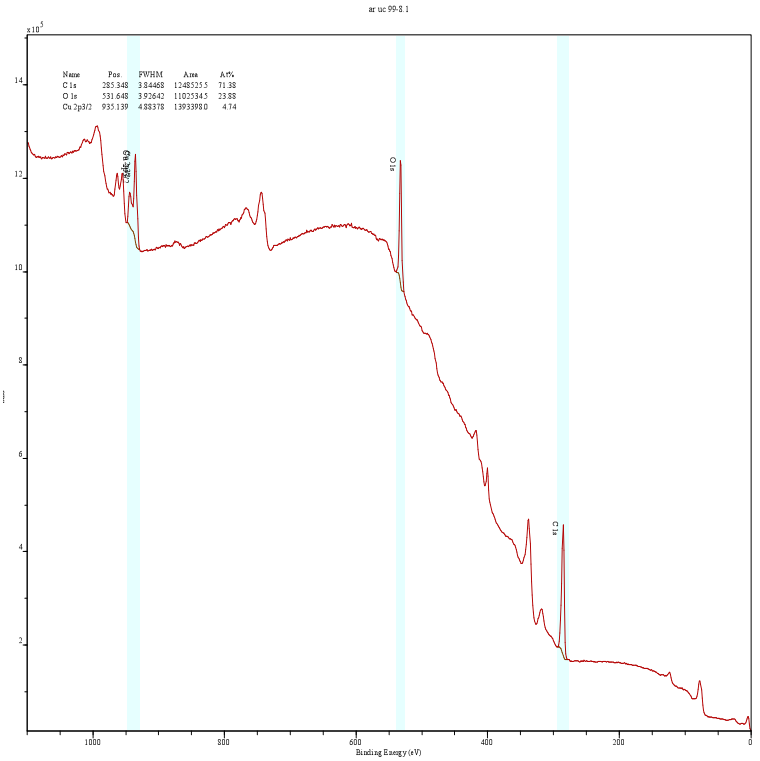
Representative Raman spectra from analysis of influence of Cu crystallographic orientation on LPCVD graphene



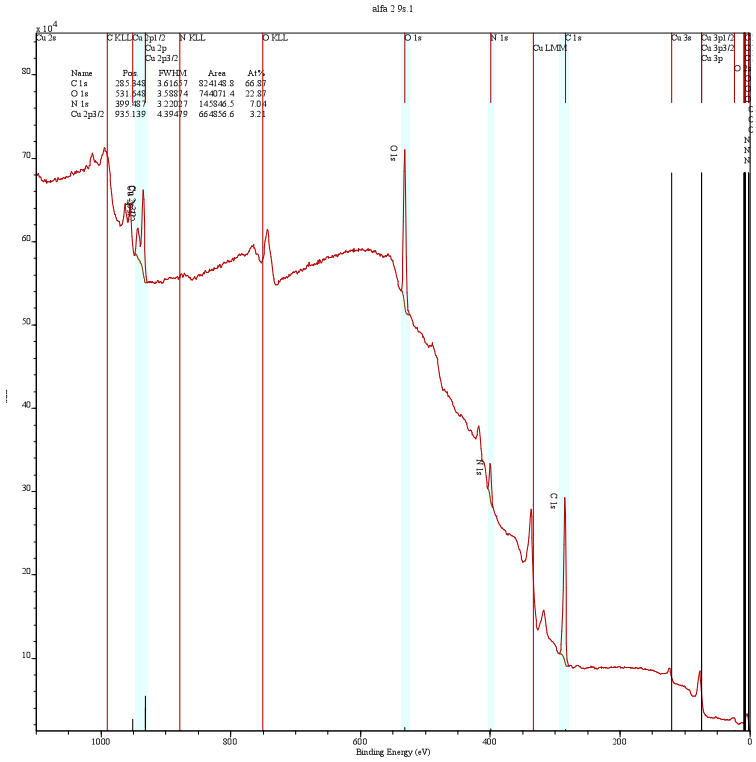
XPS analysis of Cu foils



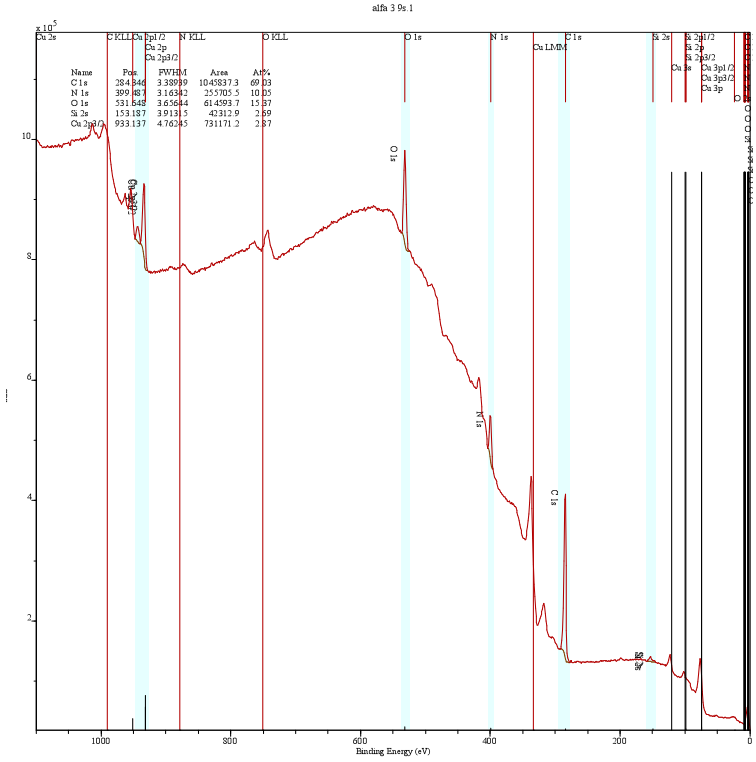
Coated 99.8 % Alfa Aesar



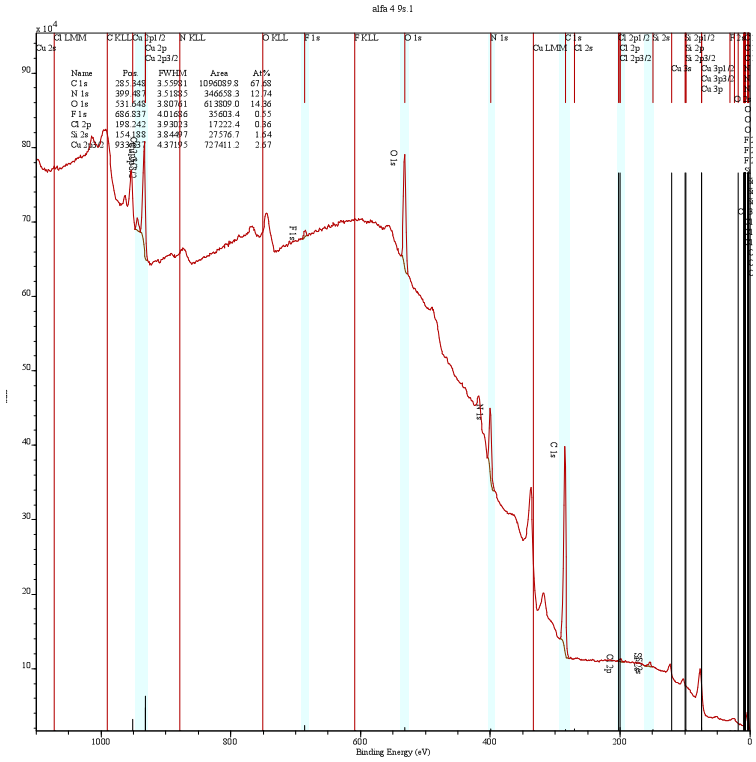
Uncoated 99.8 % Alfa Aesar



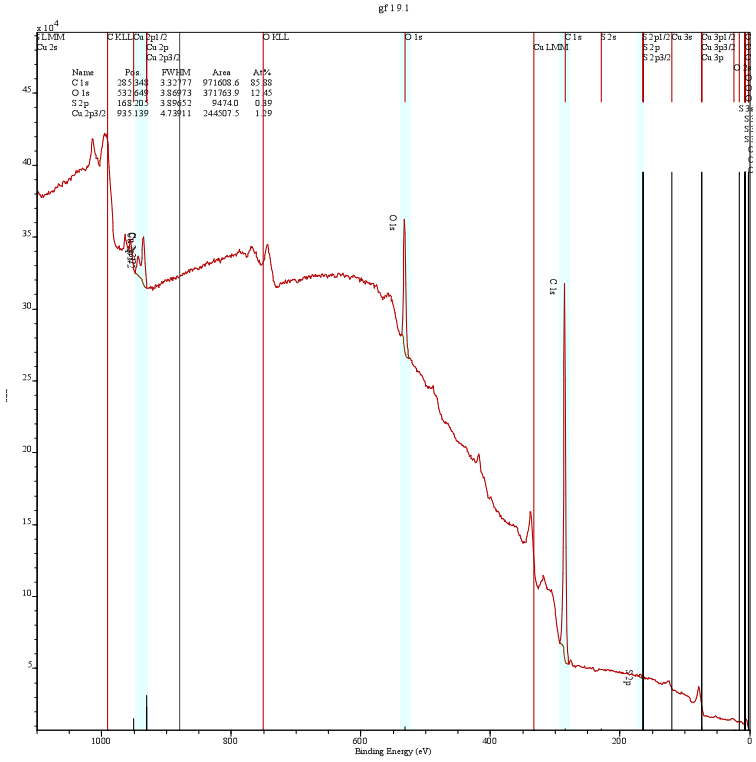
99.99+ % Alfa Aesar



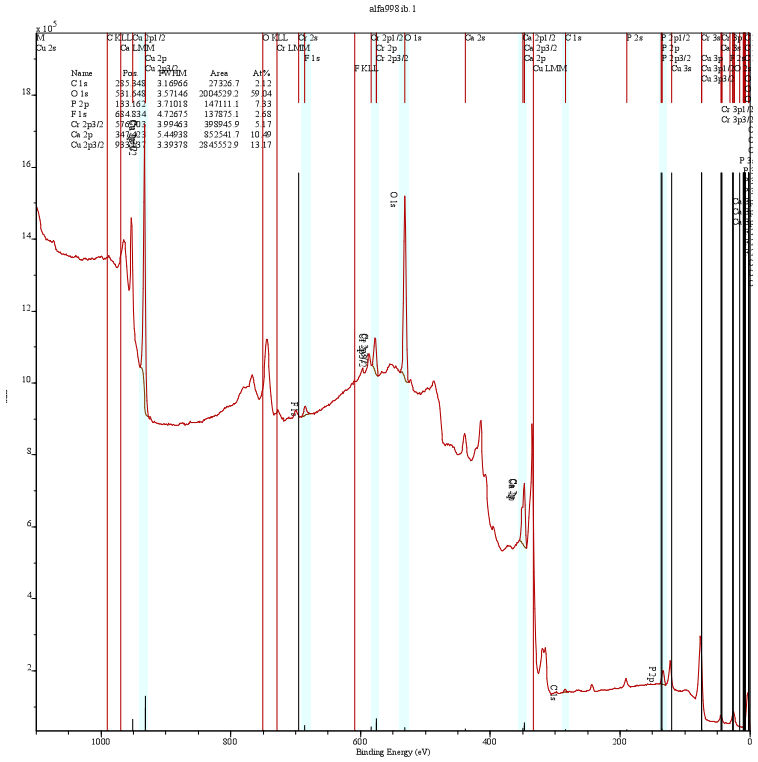
99.999 % Alfa Aesar



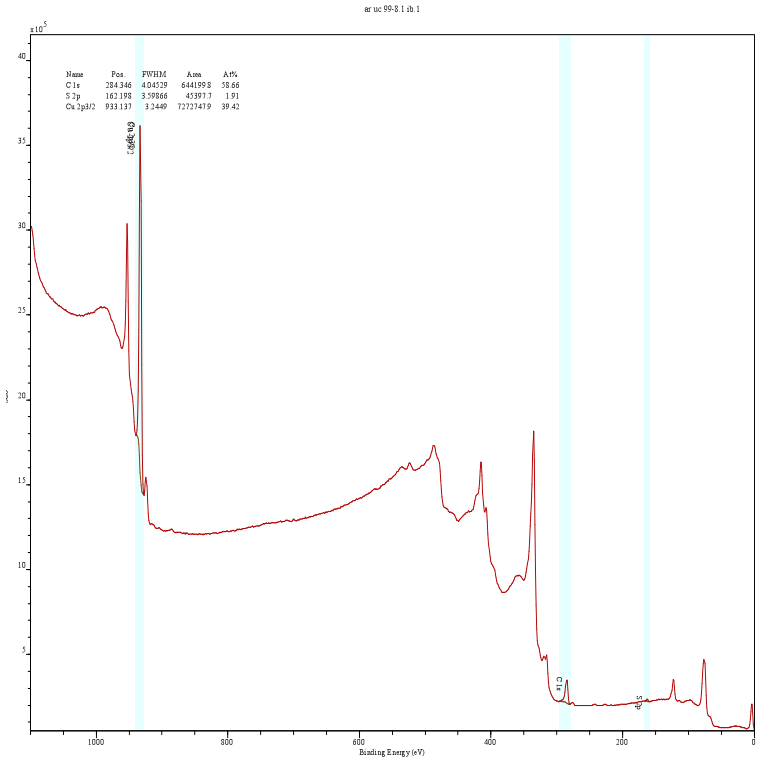
99.9999 % Alfa Aesar



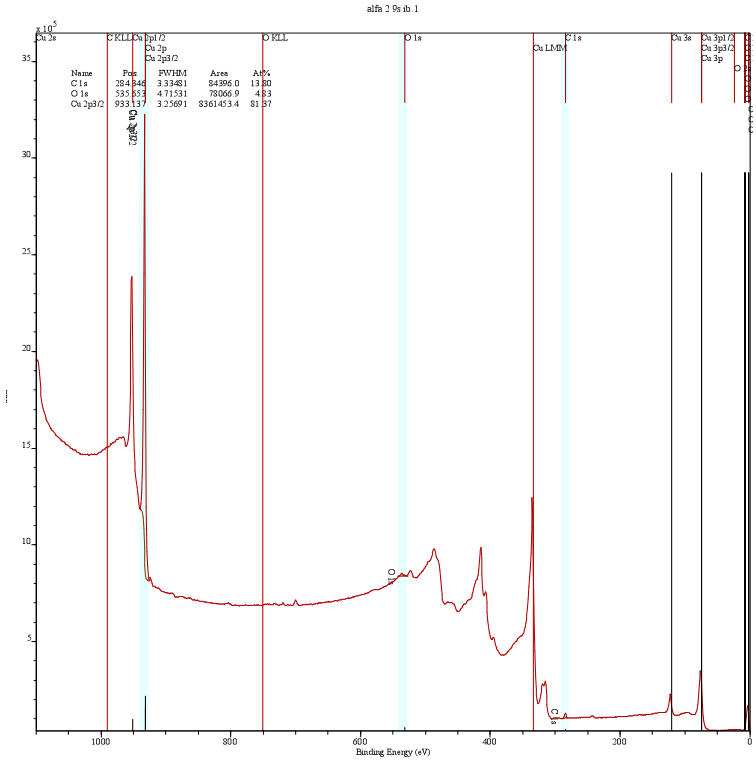
99.9 % Goodfellow



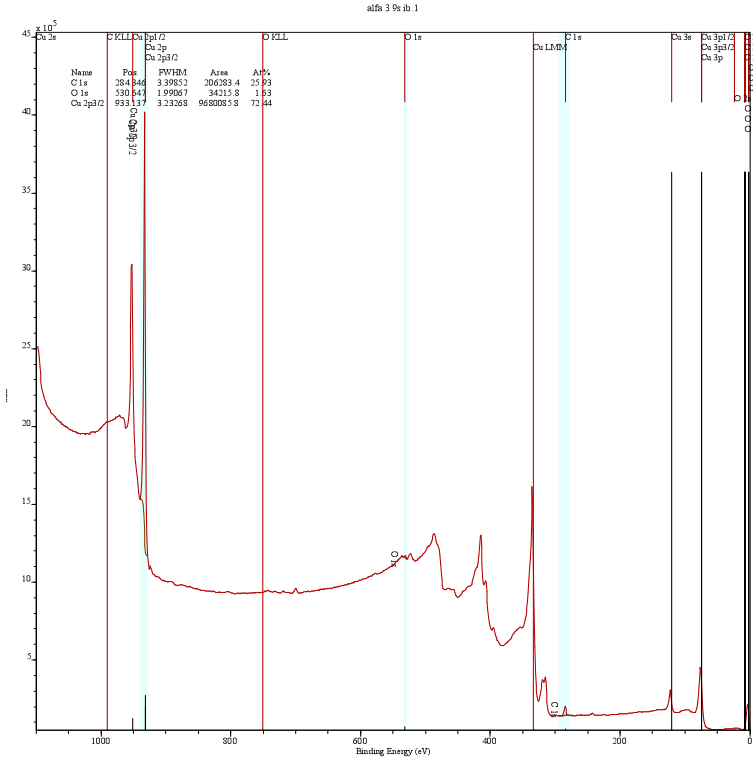
~2 nm ion bombarded Coated 99.8 % Alfa Aesar



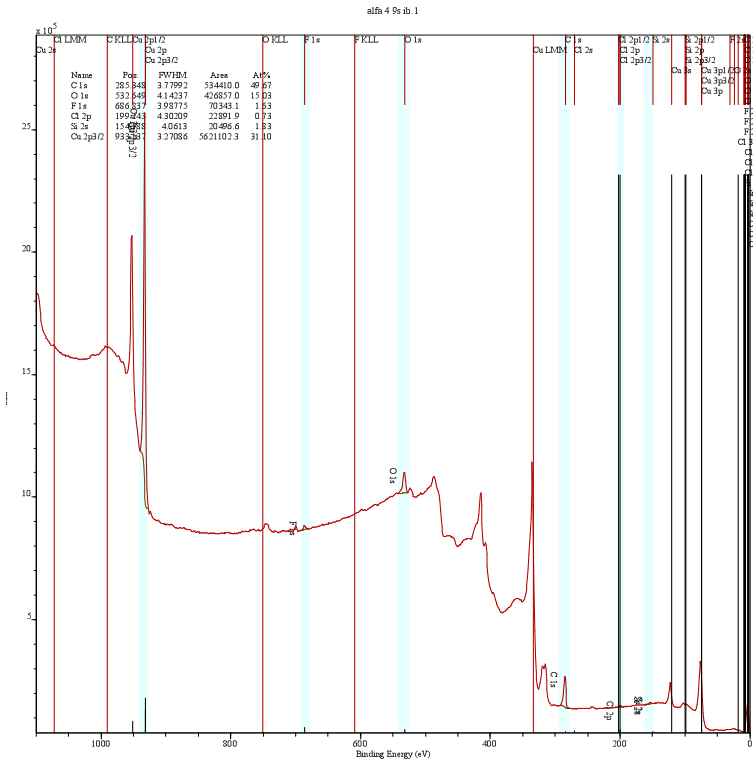
~2 nm ion bombarded Uncoated 99.8 % Alfa Aesar



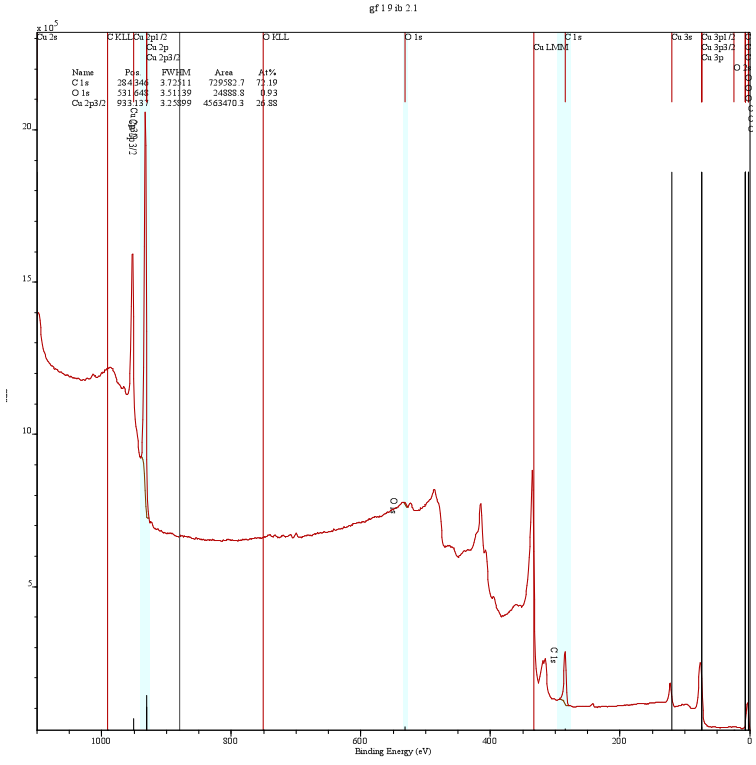
~2 nm ion bombarded 99.99+ % Alfa Aesar



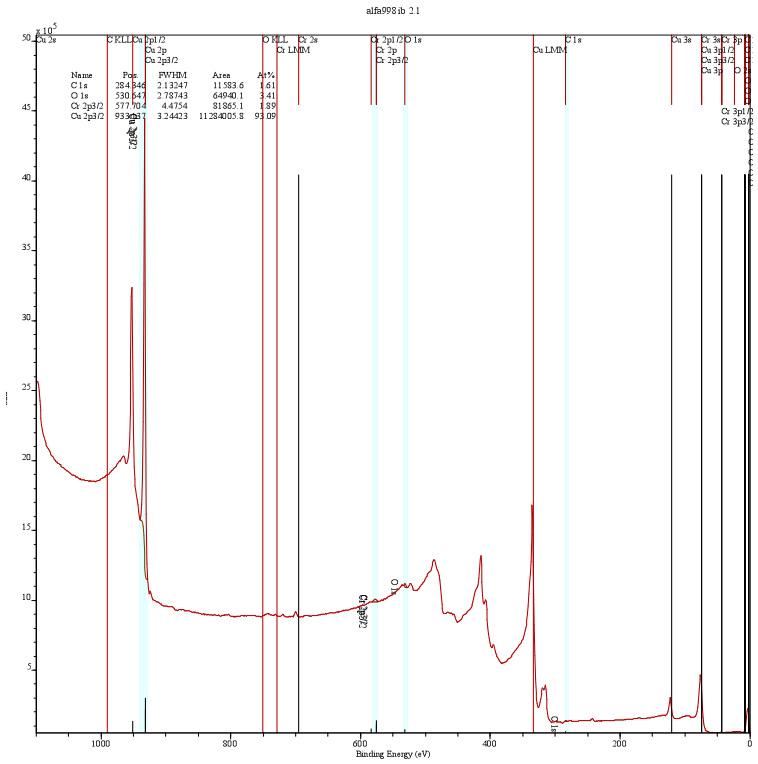
~2 nm ion bombarded 99.999 % Alfa Aesar



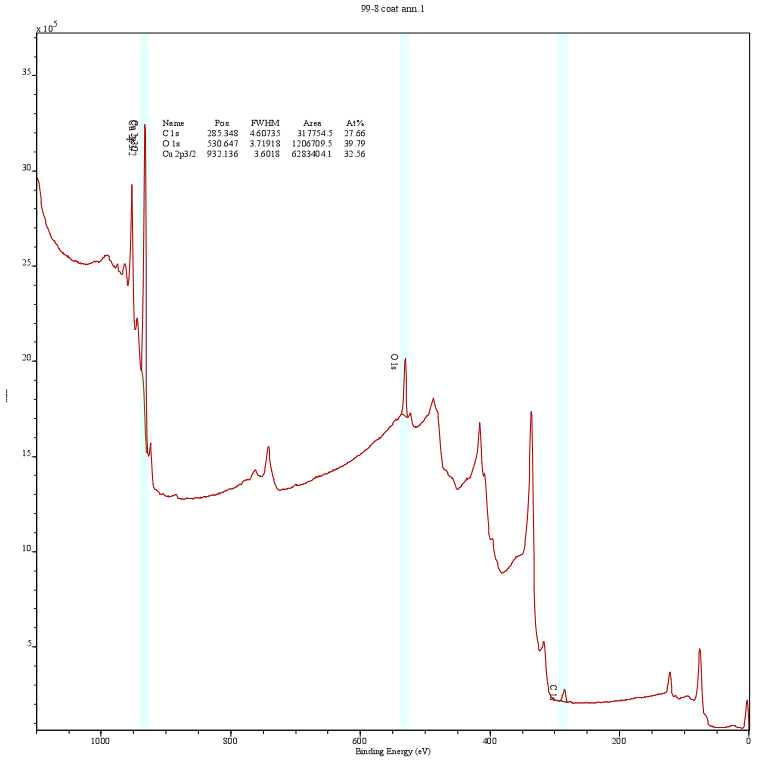
~2 nm ion bombarded 99.9999 % Alfa Aesar



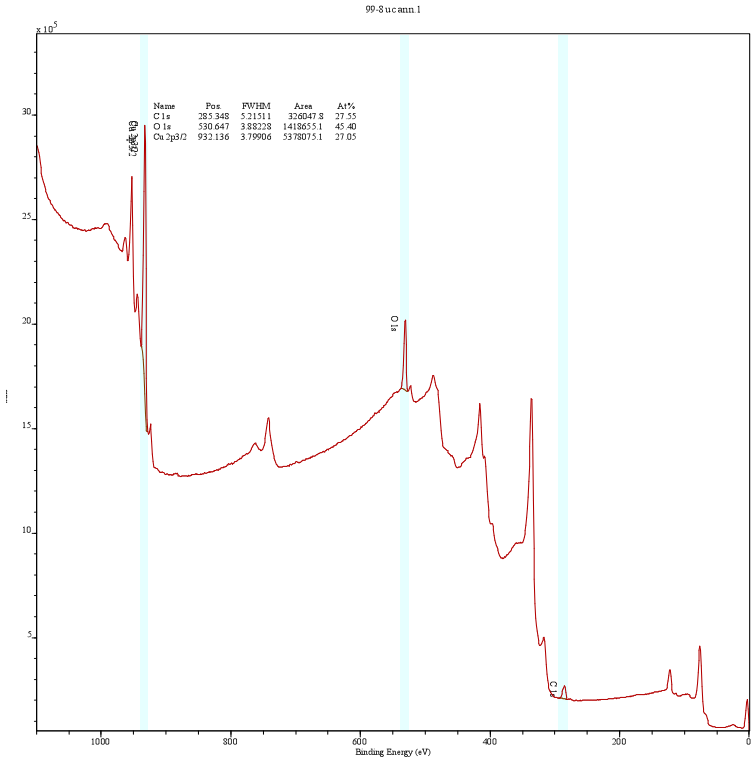
~2 nm ion bombarded 99.9 % Goodfellow



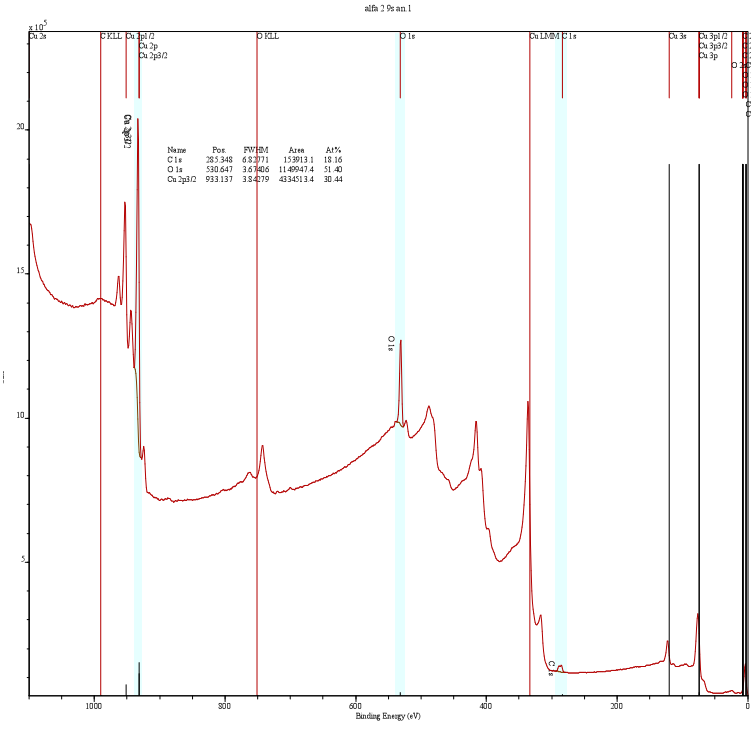
~5 nm ion bombardment Coated 99.8 % Alfa Aesar



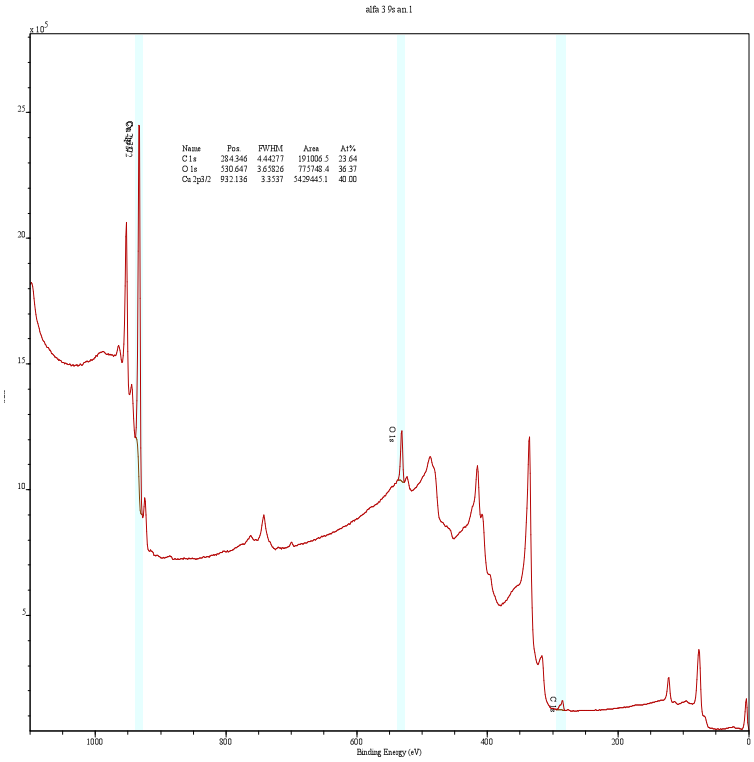
Annealed Coated 99.8 % Alfa Aesar



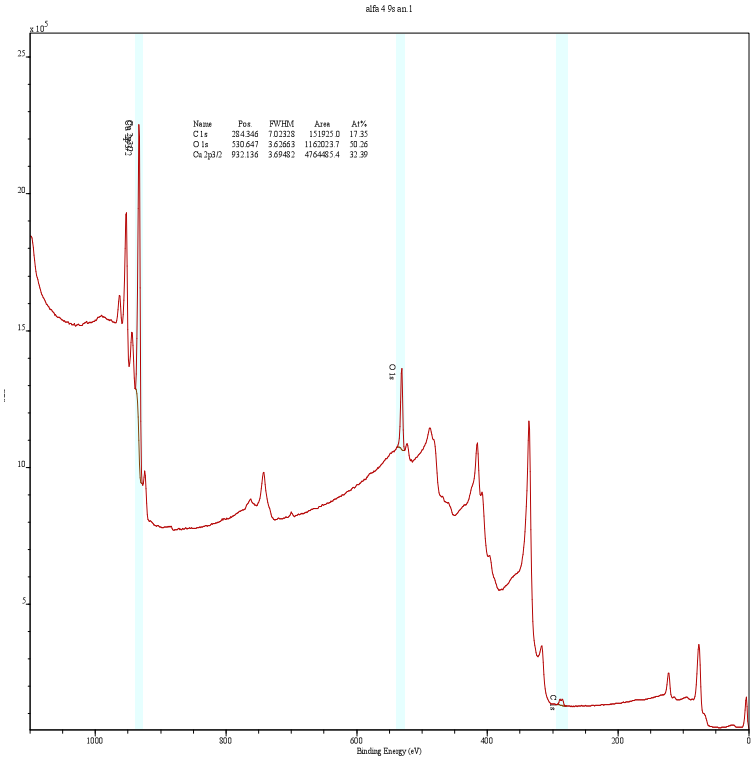
Annealed Uncoated 99.8 % Alfa Aesar



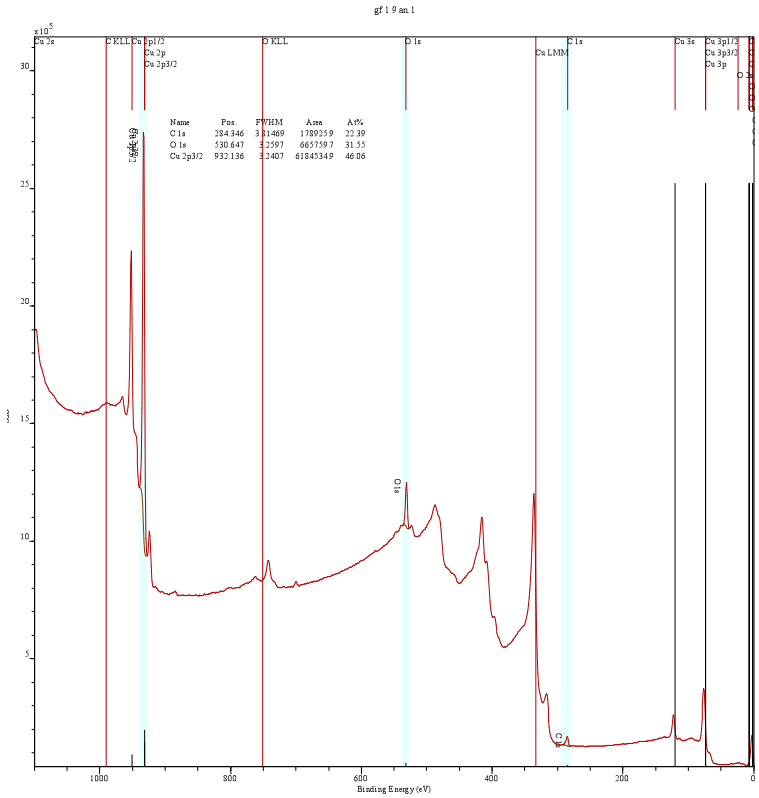
Annealed 99.99+ % Alfa Aesar



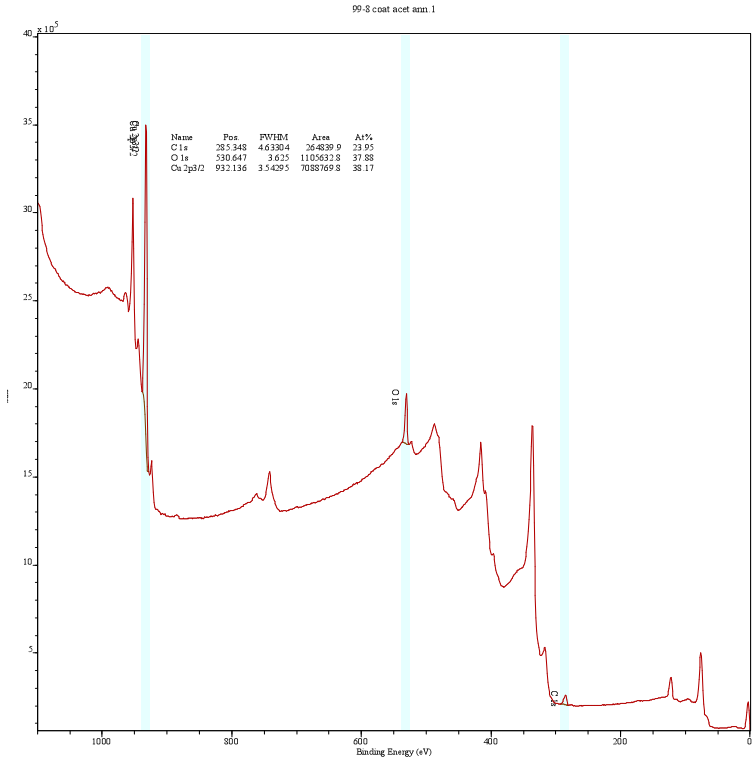
Annealed 99.999 % Alfa Aesar



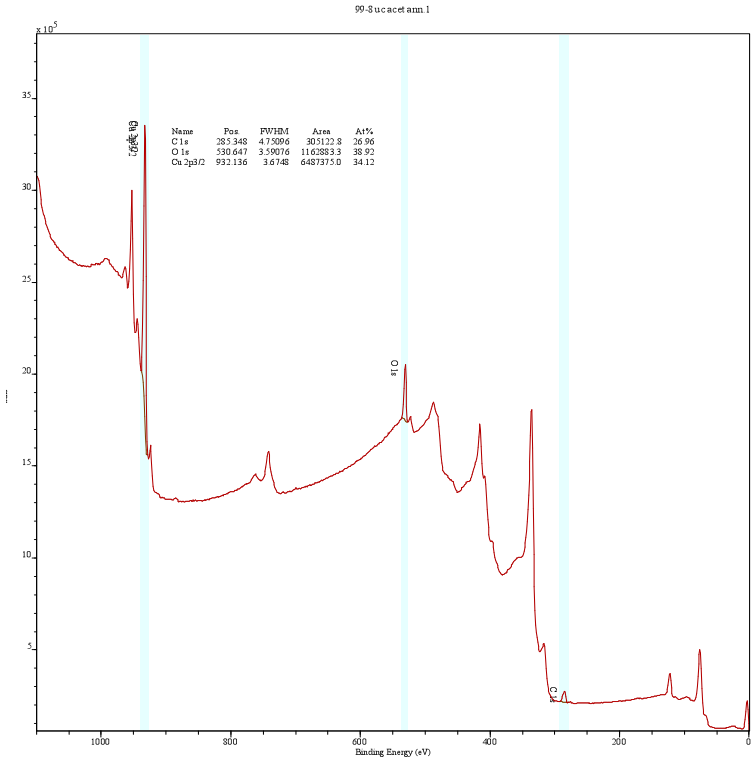
Annealed 99.9999 % Alfa Aesar



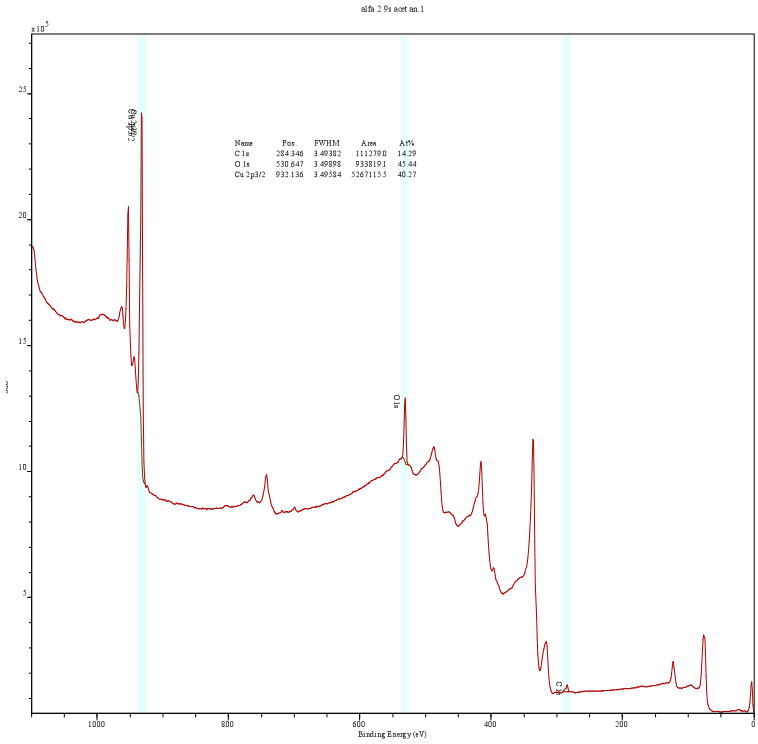
Annealed 99.9 % Goodfellow



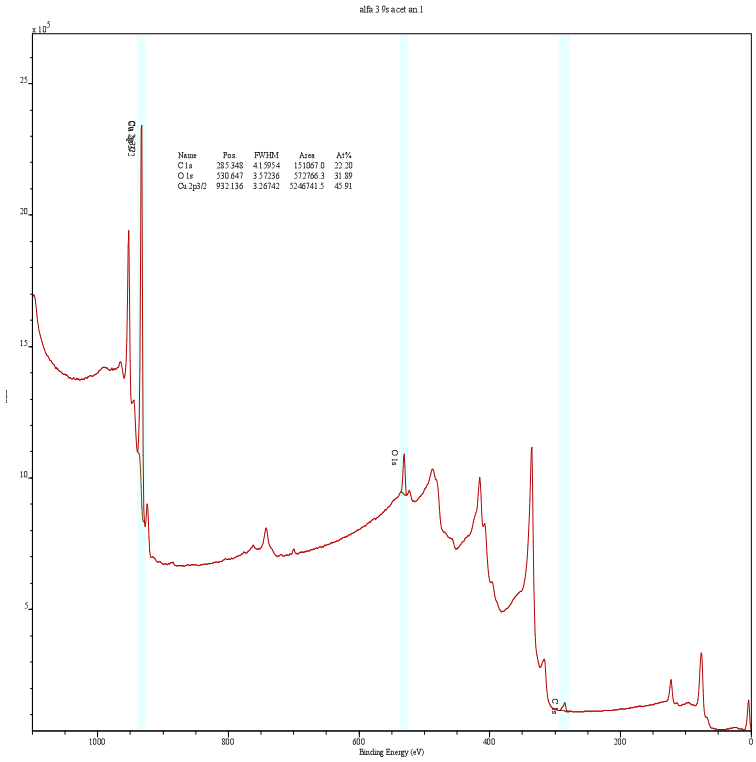
Acetic acid cleaned annealed Coated 99.8 % Alfa Aesar



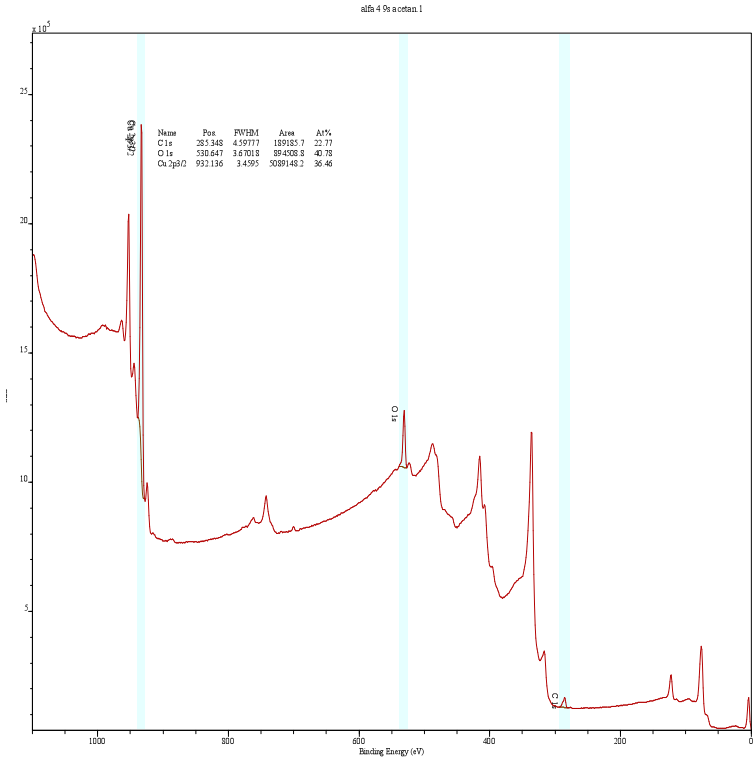
Acetic acid cleaned annealed Uncoated 99.8 % Alfa Aesar



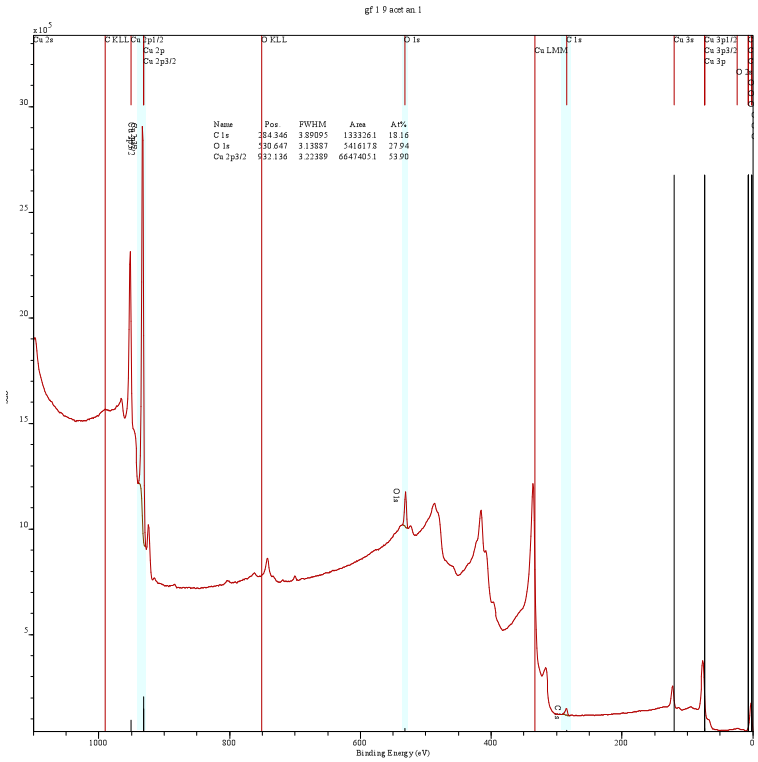
Acetic acid cleaned annealed 99.99+ % Alfa Aesar



Acetic acid cleaned annealed 99.999 % Alfa Aesar

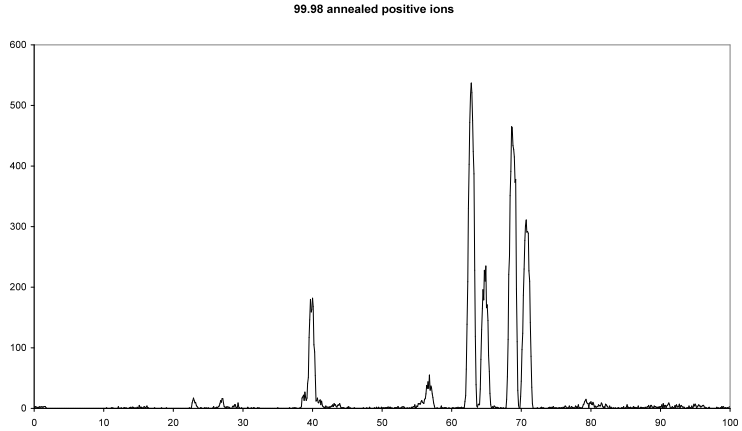


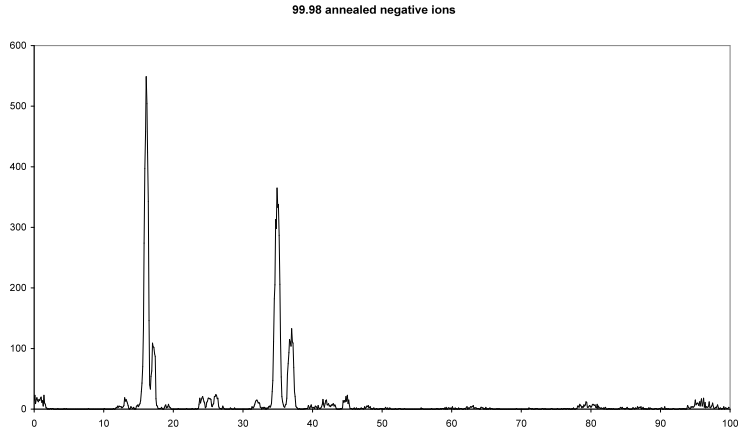
Acetic acid cleaned annealed 99.9999 % Alfa Aesar



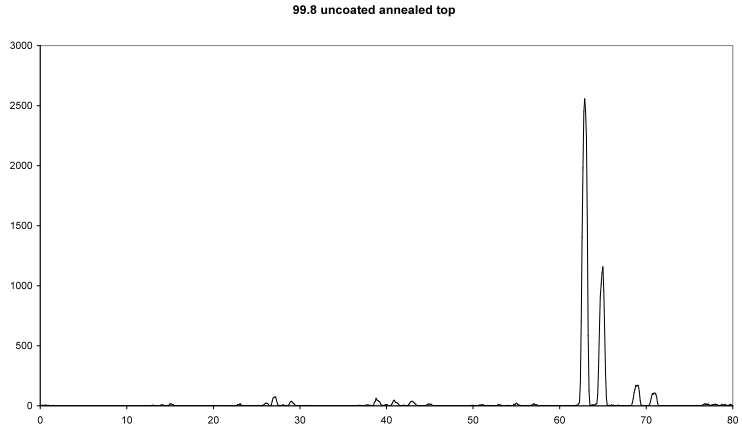
Acetic acid cleaned annealed 99.9 % Goodfellow

SIMS data from analysis of Cu foils

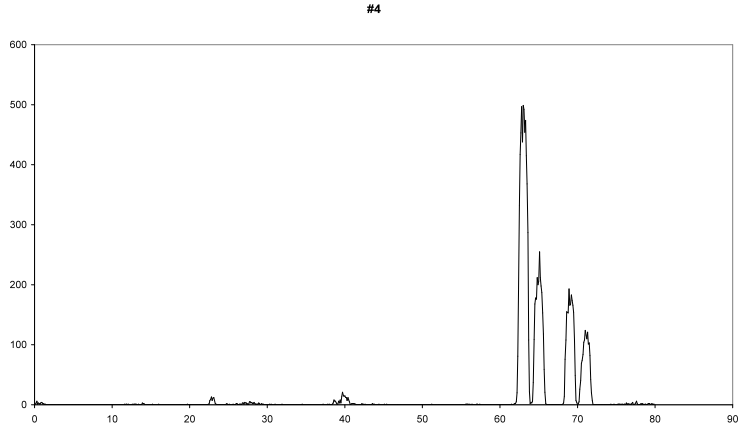




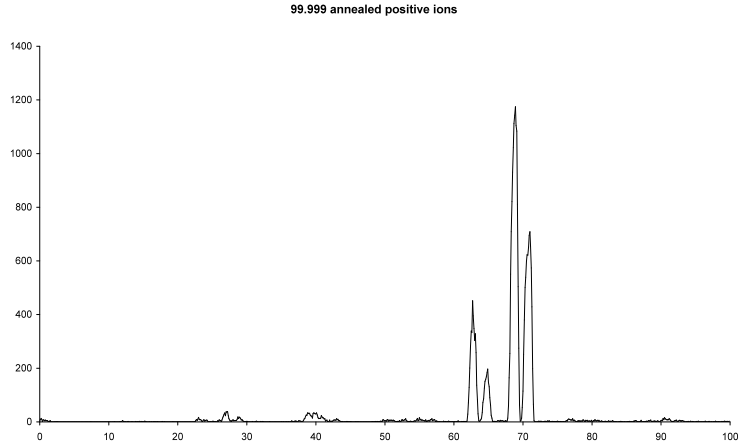
Annealed coated 99.8 % Alfa Aesar Cu foil -Masses; 40 Ca; 63, 65 Cu; 69, 71 implanted Ga**,** Main peaks; 16 O; 17 OH; 24 C2; 25 C2H; 26 C2H2 and CN; 35,37 Cl



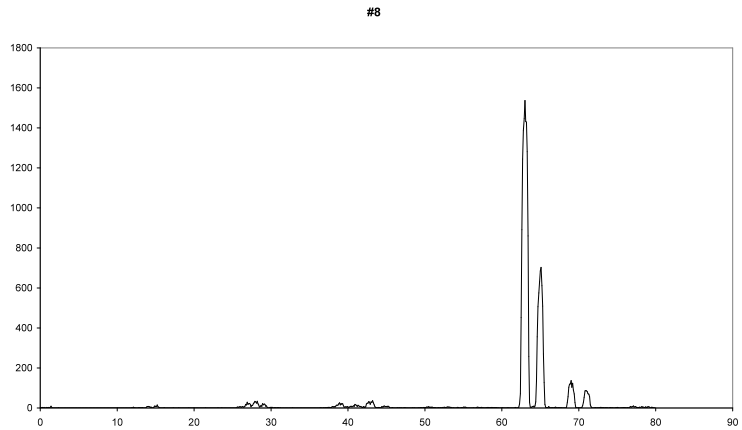
Annealed uncoated 99.8 % Alfa Aesar Cu foil- Masses; 40 Ca; 63, 65 Cu; 69, 71 implanted Ga



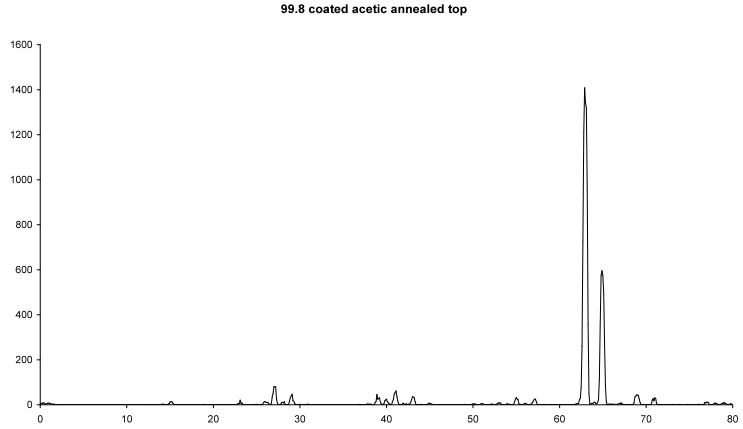
Annealed 99.99+ % Alfa Aesar Cu foil



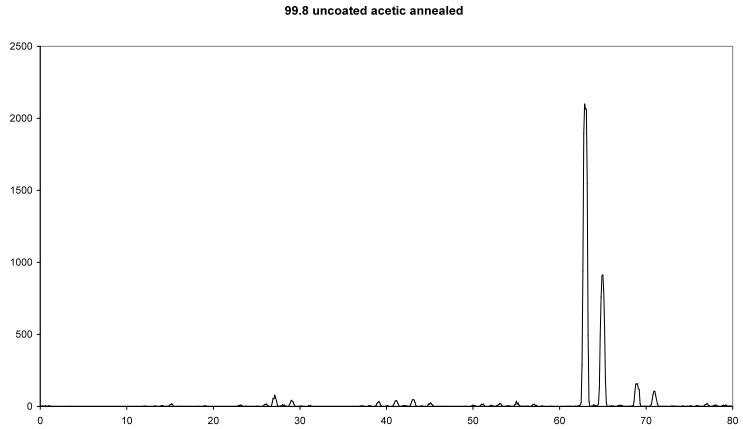
Annealed 99.999 % Alfa Aesar Cu foil- Masses; 40 Ca; 63, 65 Cu; 69, 71 implanted Ga



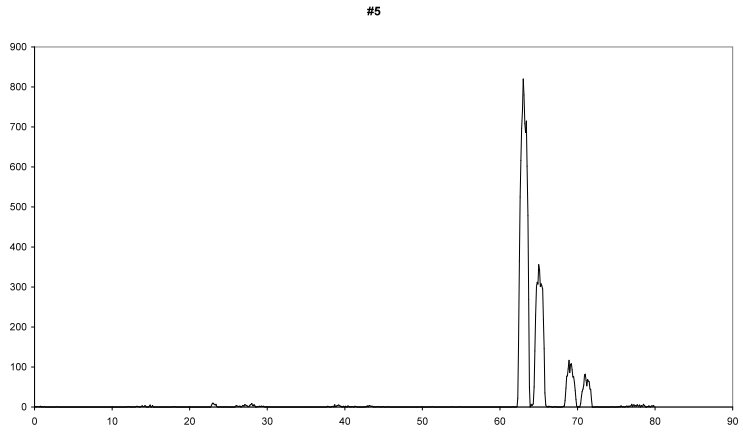
Annealed 99.9 % Goodfellow Cu foil



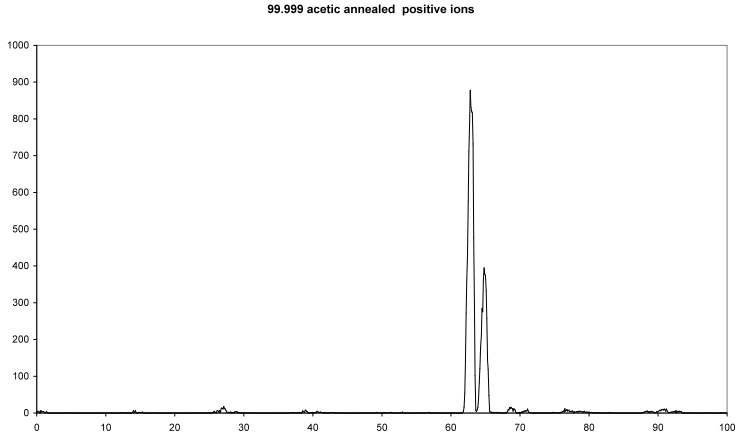
Acetic acid cleaned and annealed Coated 99.8 % Alfa Aesar Cu foil



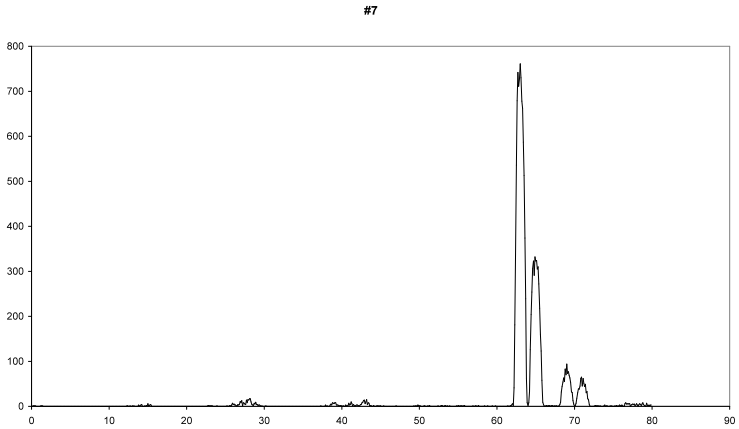
Acetic acid cleaned and annealed Uncoated 99.8 % Alfa Aesar Cu foil



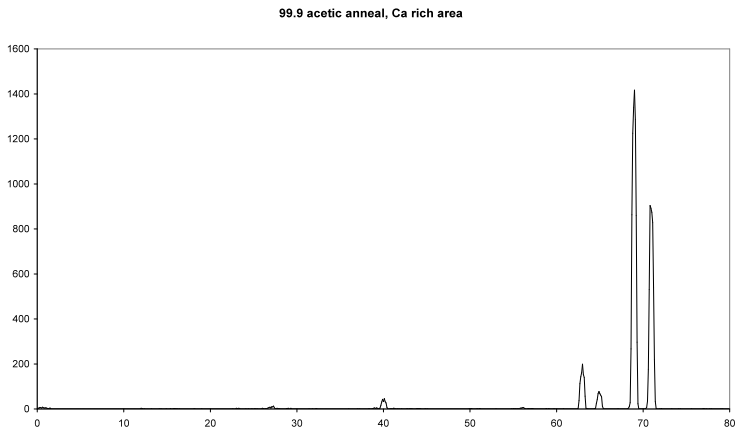
Acetic acid cleaned and annealed 99.99+ % Alfa Aesar Cu foil



Acetic acid cleaned and annealed 99.999 % Alfa Aesar Cu foil

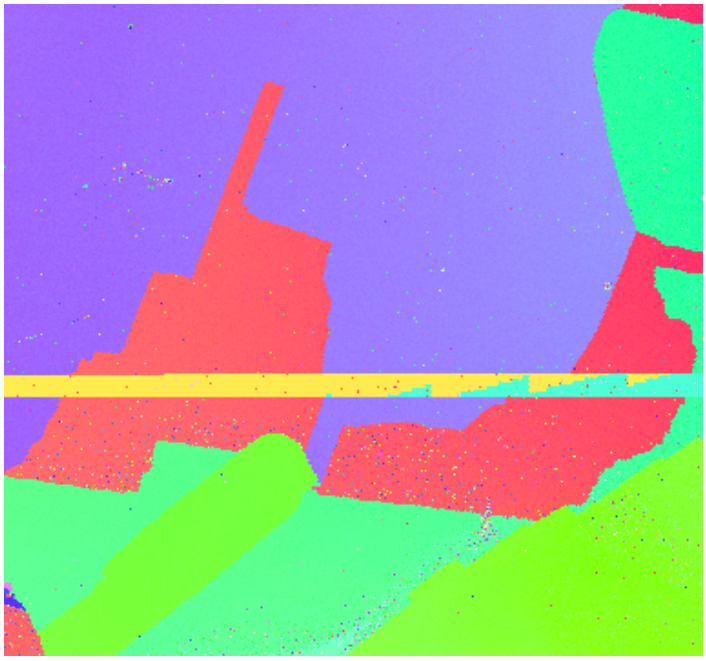


Acetic acid cleaned and annealed 99.9999 % Alfa Aesar Cu foil



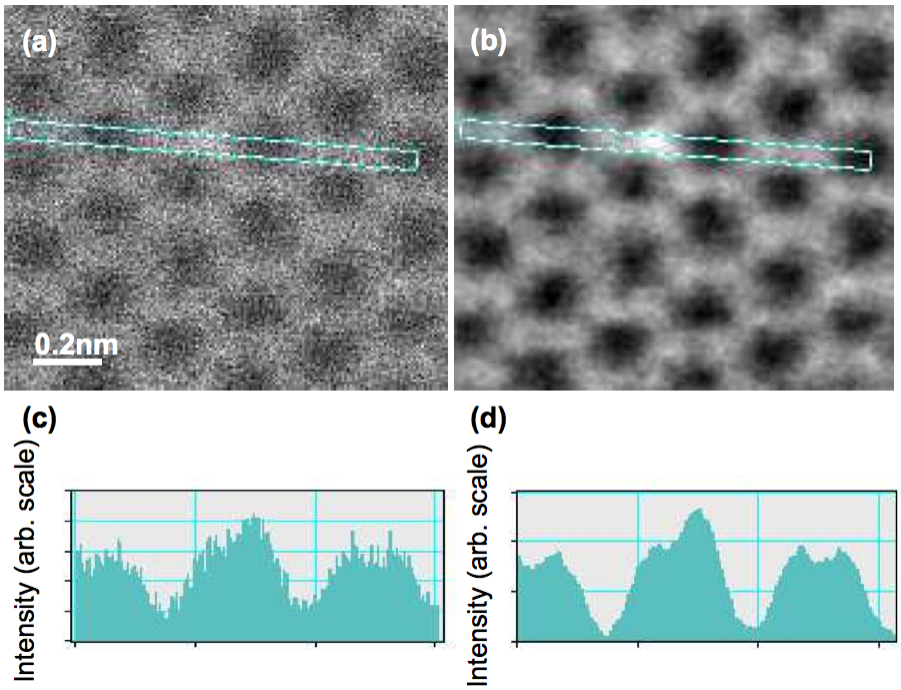
Acetic acid cleaned and annealed 99.9 % Goodfellow Cu foil

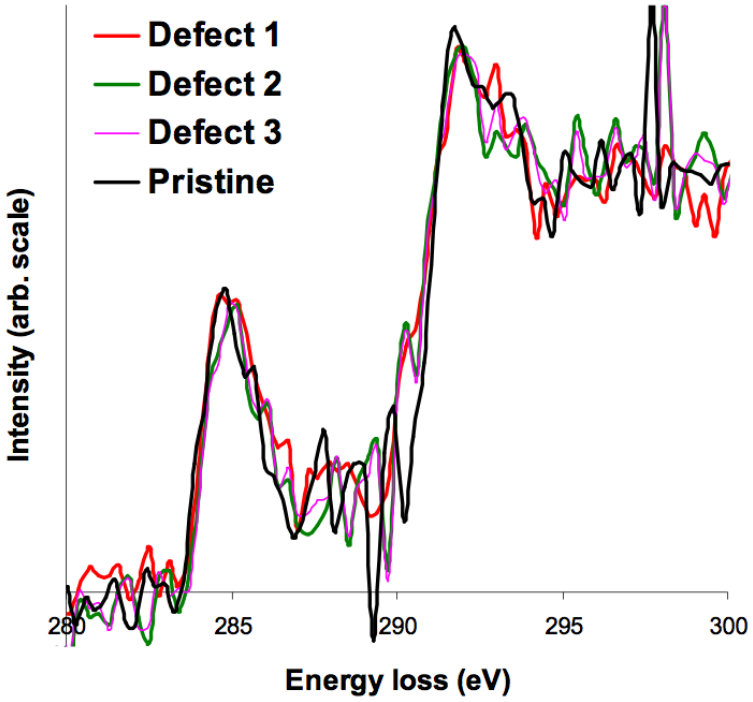
Large area EBSD map of annealed 99.9999 % Alfa Aesar Cu foil



900 x 900 µm EBSD map. Strip of yellow crystallographic orientations should be ignored.

STEM and EELS data of nitrogen-doped graphene




Defect 1
Defect 2
Defect 3
Pristine
Intensity (arb. scale)
280
285
290
295
300
Energy loss (eV)